UNIVERSIDAD POLITÉCNICA DE MADRID
Escuela Técnica Superior de Ingenierios Industriales

Adaptive Modelling and Control of a Membraneless Micro Redox Flow Battery

DOCTORAL THESIS

Submitted for the degree of Doctor by:

Alberto Bernaldo de Quirós Sanz
Ingeniero Electrónica Industrial y Automática

Madrid, 2023

UNIVERSIDAD POLITÉCNICA DE MADRID
Escuela Técnica Superior de Ingenierios Industriales

Doctoral Degree in Electrical and Electronic Engineering

Adaptive Modelling and Control of a Membraneless Micro Redox Flow Battery

DOCTORAL THESIS

Submitted for the degree of Doctor by:

Alberto Bernaldo de Quirós Sanz
Ingeniero Electrónica Industrial y Automática

Under the supervision of:
Dr. Javier Uceda Antolín(Supervisor)

Madrid, 2023

Title: Adaptive Modelling and Control of a Membraneless Micro Redox Flow Battery

Author: Alberto Bernaldo de Quirós Sanz

Doctoral Programme: Electrical and Electronic Engineering

Thesis Supervision:

Dr. Javier Uceda Antolín, Director Centro de Electrónica Industrial, Universidad Politécnica de Madrid(Supervisor)

External Reviewers:

Thesis Defense Committee:

Thesis Defense Date:

This thesis has been partially supported by the Industrial Doctorate Program of the Comunidad de Madrid under Grant IND2018/AMB-9616.

A mis padres

Acknowledgement

First of all, I would like to thank my advisor, Javier Uceda, for trusting me and allowing me the opportunity to pursue this PhD. His support and vision have guided me throughout the research process, especially in the moments of greatest uncertainty.

Secondly, I would like to thank Enrique Serrano for his commitment to this industrial doctorate project, without his firm belief in research and progress in new energy storage technologies this thesis would not exist, nor would the company B5tec, where I have been able to work and carry out the industrial part of the work during these 5 years.

On the academic side, I would like to thank the people at the CEI with whom I have been able to share and discuss the aspects of this work. In particular, I would like to thank Airán Francés for his attentive availability, attention and advice whenever I needed his experience.

On behalf of B5tec, I would like to acknowledge the support of my colleagues with whom I have been working since the beginning of the company. Alberto Quintero, for his broad and scientific outlook, Beatriz Oraá, a companion of doctoral hardships, and María José Torres, for her diligent help. Also to the rest of my colleagues: Miguel, Jorge, Percy, Óscar, Laura, Sonia, Mayte, Dani, Miguel and Celia.

I would also like to give my personal thanks to my friends Hugo, Yepes, David, Mikel and Alfredo.

My family has shown me the constant and greatest support from the beginning, my parents always willing to give me more than I can imagine, my brothers with their complicity, and my grandparents with their affection, two of whom I have lost during this work.

Finally, I would like to thank Yaiza for making me feel that all my effort makes sense and for making me trust again that things can work out well.

Abstract

Green energy transition is pressing global demand for renewable energy solutions, leading to extensive research in the field of energy storage technologies in order to integrate them with intermittent renewable energy sources. In this context, redox flow batteries (RFBs) are significantly relevant due to the characteristics they can offer, including scalability, long cycle life, low degradation, high depth-of-discharge and ability to decouple energy and power. Therefore, RFBs can provide large-scale, flexible, and long-duration energy storage solutions that do not suffer as much degradation as other technologies from intermittent operation.

An alternative design for traditional RFBs are micro-scale membraneless redox flow reactors (MRFB), whose development has been led by the advances in microfabrication together with the growing interest in microfluidics. These designs are defined by the absence of a membrane, which is possible by passing the electrolytes through the reactors in a laminar regime which prevents the flows from mixing and creates an interface between the two species that minimizes the advective mixing. The lack of membrane reduces costs and optimizes the battery performance, as it decreases internal electrical resistance. Besides these advantages, microfluidics also allows to raise the efficiency and rate of electrochemical energy conversion through enhanced mass transport. Similarly, using microfabrication provides a flexible cell design using a cheaper and simpler manufacturing method.

However, MRFBs also have drawbacks and unfavourable intrinsic characteristics that have stopped their industrial application. They need a very precise control of the electrolyte interface within the reactor. Otherwise, their mixing and self-discharge losses are significantly larger than for conventional RFBs due to crossover, plummeting their coulombic efficiency, reactant conversion ratio and cycle life. In order to handle this, it is necessary to deal with inherent microfluidics behaviour: limited instrumentation, stochasticity and changes in system properties. All this casuistic is why, regardless several designs and scientific works being developed in the last decade, until recently there was not any of them that proved a complete true battery system (continuous charge and discharge cycles with electrolyte recirculation). The project in which this thesis takes place in the form of industrial PhD has been the first to accomplish this milestone and its currently working towards its scaling and industrialization.

Modelling of batteries is a key factor to study its properties and response. Battery models are valuable from design research and optimization until its integration in an electric grid. Therefore they should cover a wide range of dimensions (electrochemical, thermal, fluidic, electrical). This works has been done for traditional RFBs, but for MRFB it has been bounded to study its primary electrochemical processes and its design optimization. Hence, there is a lack of this models in the membraneless micro scale scenario, whose peculiarities do not allow to extend the ones from conventional RFBs.

Electrical modelling allows to characterize the electrical output of batteries under different working conditions. It can be used to compare and optimize these working conditions and the control applied. These models parametrize charge and discharge cycles and give and equivalent electrical model useful also for future grid integration.

Fluidic dynamic modelling is critical in any system using moving liquids for the purpose of guaranteeing safe and proper operation. In the context of batteries is even more important due to energy efficiency considerations of the pumping system. Moreover, MRFB depend on proper positioning of the liquid interface between electrolytes in a microscale reactor with no physical separation. This makes the MRFB case unique, and its modelling vital. This model shall be used to characterize response to different working conditions, and to optimize its fluidic control. Fluidic control strategies that optimize the modelled fluidic dynamics define the efficiency of the whole battery system, reaching the point of making the battery viable or not, and limiting its possible applications. Strategies can vary from flowing the electrolytes at the fixed maximum flow to assure always maximum power availability, to model-free strategies (such as basic PID algorithm) or model based (different optimal control algorithms, predictive control).

The objective of this thesis is to propose MRFB models that precisely represent their behaviour and can be used for its working conditions effects study, reactor design optimization, grid integration and fluidic control design. These models are applied to its electrical and fluid dynamics characteristics. Electrical model defines an equivalent electrical circuit, studying the parametrization of the elements of this circuit, and measuring its fitness with electrochemical tests. It also accounts for the fluid dynamic influence on this electrical part. Besides, the fluid dynamic model presents equations describing flows at the reactor based on system active elements action. In summary, the final goal is to obtain a fluidic model that can be used to design a proper control strategy of the operation of the active elements, and to validate it with the electrical model which also is needed for the future grid integration of the battery.

The methodology used in this work has consisted in, first, defining the fluidic system architecture to work with the battery cells. To do this it was necessary to study the state of the art previous works and their microfluidic setup, together with the instrumentation ready to use in the market and adapt or develop any missing element. When these devices were already integrated in a working microfluidic solution, other topics were reviewed in the state of the art. These topics include existing fluidic models for MRFB, electrical equivalent circuits for RFB, greybox modelling, parameter identification, real time correction and estimation filters, and control strategies. Then, electrochemical experiments were performed to learn about the electrical behaviour and propose an electrical model for the equivalent circuit, and to model metrics such as power and mixing and self-discharge losses. Equivalently, for the fluidic modelling there was an experimental and data gathering phase, followed with the proposal of the dynamic equations. For this model, there was also a real time correction study, based on heuristics and from stochasticity observed that is incorporated to the model with estimation filters. Fluidic model is used to design new state-space control strategies, which are then compared and evaluated using the electrical model.

Resumen

La transición energética está presionando la demanda mundial de soluciones de energía renovables, lo que ha dado lugar a una amplia investigación en el campo de las tecnologías de almacenamiento de energía con el fin de integrarlas con aquellas fuentes de energía renovables intermitentes. En este contexto, las baterías de flujo redox (RFB) adquieren una relevancia significativa debido a las características que pueden ofrecer, como escalabilidad, larga ciclabilidad, baja degradación, alta profundidad de descarga y capacidad para desacoplar energía y potencia. Por lo tanto, las RFB pueden proporcionar soluciones de almacenamiento de energía a gran escala, flexibles y de larga duración que no sufren tanta degradación como otras tecnologías durante el funcionamiento intermitente.

Un diseño alternativo a las RFB tradicionales son los micro reactores de flujo redox sin membranas (MRFB), cuyo desarrollo se ha visto impulsado por los avances en microfabricación junto con el creciente interés en microfluídica. Estos diseños se definen por la ausencia de membrana, lo que es posible haciendo pasar los electrolitos a través de los reactores en un régimen laminar que impide que los flujos se mezclen y crea una interfaz entre las dos especies que minimiza la mezcla advectiva. La ausencia de membrana reduce los costes y optimiza el rendimiento de la batería, ya que disminuye la resistencia eléctrica interna. Además de estas ventajas, la microfluídica también permite aumentar la eficiencia y la tasa de conversión electroquímica de energía gracias a la mejora en el transporte de masa. Del mismo modo, el uso de microfabricación proporciona un diseño de celda flexible utilizando métodos de fabricación más baratos y sencillos.

Sin embargo, las MRFB también presentan inconvenientes y características intrínsecas desfavorables que han frenado su uso a escala industrial. Necesitan un control muy preciso de la interfaz de electrolitos en el reactor. De lo contrario, sus pérdidas por mezcla y autodescarga son significativamente mayores que las de las RFB convencionales debido al cruce de especies, lo que desploma su eficiencia coulómbica, la relación de conversión de reactante y la ciclabilidad. Para mitigar esto es necesario lidiar con problemática inherente a la microfluídica: instrumentación limitada, estocasticidad y cambios en las propiedades del sistema.

Toda esta casuística es la razón por la que, a pesar de que en la última década se han desarrollado varios diseños y trabajos científicos, hasta hace poco no había ninguno de ellos que demostrara ser un verdadero sistema de batería completo (ciclos continuos de carga y descarga con recirculación del electrolito). El proyecto en el que se enmarca esta tesis, en forma de doctorado industrial, ha sido el primero en lograr este hito y actualmente trabaja para su escalado e industrialización. El modelado de las baterías es un factor clave para estudiar sus propiedades y su respuesta. Los modelos de baterías son valiosos en todo el ámbito de trabajo, desde la investigación del diseño y su optimización hasta la integración en la red eléctrica. Por lo tanto, deben abarcar una amplia gama de dimensiones (electroquímica, térmica, fluídica, eléctrica). Estos trabajos se han realizado para las RFB tradicionales, pero para las MRFB se han limitado a estudiar sus procesos electroquímicos primarios y la optimización de su diseño. Por lo tanto, existe una carencia de estos modelos en el caso de los diseños micro sin membrana, cuyas peculiaridades no permiten extender los de las RFBs convencionales.

El modelado eléctrico permite caracterizar el rendimiento eléctrico de las baterías en diferentes condiciones de trabajo. Puede utilizarse para comparar y optimizar estas condiciones de trabajo así como el control aplicado. Estos modelos parametrizan los ciclos de carga y descarga y proporcionan un modelo eléctrico equivalente útil también para la futura integración en red.

El modelado fluidodinámico es fundamental en cualquier sistema que utilice líquidos en movimiento para garantizar un funcionamiento seguro y adecuado. En un contexto de uso en baterías es aún más importante debido a las consideraciones de eficiencia energética del sistema de bombeo. Aún más, las MRFB dependen del posicionamiento adecuado de la interfaz líquida entre electrolitos en un reactor micro sin separación física. Esto hace que el caso MRFB sea único, y su modelado crítico. Este modelo se utilizará para caracterizar la respuesta en diferentes condiciones de trabajo, y para optimizar su control fluídico.

Las estrategias de control fluídico para optimizar la fluido dinámica modelada definen la eficiencia del conjunto del sistema de la batería, hasta el punto de hacerla viable o no, y limitar sus posibles aplicaciones. Las estrategias pueden variar desde hacer fluir los electrolitos a un caudal máximo fijo para garantizar siempre la máxima disponibilidad de potencia eléctrica, hasta estrategias de control sin modelo (como un algoritmo PID básico) o basadas en modelo (diferentes algoritmos de control óptimo, control predictivo).

El objetivo de esta tesis es proponer modelos de MRFB que representen con precisión su comportamiento y puedan ser utilizados para el estudio de los efectos de las condiciones de operación, la optimización del diseño del reactor, la integración en red y el diseño del control fluídico. Estos modelos se aplican a sus características eléctricas y fluidodinámicas. El modelo eléctrico define un circuito eléctrico equivalente, estudiando la parametrización de los elementos de este circuito, y midiendo su idoneidad con ensayos electroquímicos. También tiene en cuenta la influencia fluidodinámica en esta parte eléctrica. Además, el modelo fluidodinámico presenta ecuaciones que describen los flujos en el reactor en función de la acción de los elementos activos del sistema. En resumen, el objetivo final es obtener un modelo fluidodinámico que pueda ser utilizado para diseñar una estrategia de control adecuada del funcionamiento de los elementos activos, y que es validado con el modelo eléctrico, que también es necesario para la futura integración en red de la batería.

La metodología empleada en este trabajo ha consistido, en primer lugar, en definir la arquitectura del sistema fluídico para trabajar con las celdas de la batería. Para ello fue necesario estudiar el estado del arte de trabajos previos y su configuración microfluídica, junto con la instrumentación en el mercado y adaptar o desarrollar cualquier elemento que faltase. Cuando estos dispositivos ya estaban integrados en una solución microfluídica en funcionamiento, se revisaron otras temáticas del estado de la técnica. Estas temáticas incluyen los modelos fluídicos existentes para MRFB, los circuitos eléctricos equivalentes para RFB, la modelización de caja gris, la identificación de parámetros, los filtros de corrección y estimación en tiempo real y las estrategias de control. A continuación, se realizaron experimentos electroquímicos para conocer el comportamiento eléctrico y proponer un modelo eléctrico para el circuito equivalente, así como para modelizar métricas como la potencia y las pérdidas por mezcla y autodescarga. De forma equivalente, para la modelización fluídica hubo una fase experimental y de recopilación de datos, seguida de la propuesta de las ecuaciones dinámicas.

Para este modelo, también hubo un estudio de corrección en tiempo real, basado en heurísticos y a partir de la estocasticidad observada, que se incorpora al modelo con filtros de estimación. El modelo fluídico se utiliza para diseñar nuevas estrategias de control en espacio de estados, que luego son comparadas y evaluadas con el modelo eléctrico.

Contents

Acknowledgement . . . iii
Abstract . . . iv
Resumen . . . vi
List of Figures . . . xii
List of Tables . . . xix
Abbreviations . . . xx

1 Introduction **1**
1.1 Energy storage . . . 1
1.1.1 Redox Flow Batteries . . . 7
1.2 Membraneless Redox Flow Batteries . . . 12
1.3 Thesis Outline . . . 14

2 Study of the state of the art **17**
2.1 Microfluidic Membraneless Redox Flow Bateries . . . 17
2.1.1 Previous Designs: Cell Reactors and Microfluidic System . . . 17
2.2 Redox Flow Batteries Models . . . 26
2.2.1 Electrochemical . . . 26
2.2.2 Hydraulic . . . 29
2.2.3 Thermal . . . 32
2.2.4 Electric . . . 33
2.3 Model Definition and Identification Techniques . . . 36
2.3.1 Analytical Models . . . 36
2.3.2 Blackbox Model Techniques . . . 37
2.3.3 Greybox Model Techniques . . . 39
2.3.4 Real Time Filters and Estimators . . . 40
2.4 Control Design Methods . . . 44
2.4.1 Model Free Methods . . . 47
2.4.2 Model Based Strategies . . . 48
2.5 Conclusions . . . 52

3 System configuration for microfluidic membraneless redox flow batteries operation **55**
3.1 Cell Reactor . . . 55
3.2 Instrumentation selection and development . . . 58

3.2.1 Pumps . . . 58
3.2.2 Valves . . . 61
3.2.3 Sensors Selection . . . 62
3.2.4 Tanks Monitoring . . . 63
3.3 Electronics . . . 64
3.3.1 Hardware: Electronic Board . . . 64
3.3.2 Software: Embedded and SCADA . . . 65
3.4 Full Microfluidic Setup . . . 66
3.5 Conclusions . . . 68

4 Electrical model: fluid-dynamic influence 69
4.1 Electric Equivalent Circuit . . . 69
4.2 Available Steady State Power . . . 73
4.3 Power Dynamic Response . . . 80
4.4 Mixing Losses . . . 83
4.5 Conclusions . . . 86

5 Fluid dynamic modelling 89
5.1 System Configuration . . . 89
5.2 Equations Definition . . . 90
5.3 Correction Factors Definition . . . 94
5.4 Extended Kalman Filter Correction . . . 97
5.5 Conclusions . . . 100

6 System control 103
6.1 Model-Free Control Strategy . . . 104
6.1.1 Multiple Independent PID-Controllers . . . 104
6.2 Model Based Strategies . . . 108
6.2.1 LQR with Integral Action . . . 108
6.2.2 Optimal with Incremental State . . . 113
6.2.3 Adaptive Nonlinear Model Predictive Control . . . 116
6.2.4 Adaptive Incremental Model Predictive Control . . . 122
6.3 Conclusions . . . 125

7 Control strategies evaluation 131
7.1 Power Profile Definition . . . 131
7.2 Control Strategies Evaluation . . . 133
7.2.1 Available Relative Cell Power . . . 133
7.2.2 Mixing Losses . . . 137
7.2.3 Actuators Consumption . . . 139
7.3 Conclusions . . . 143

8 Conclusions and outlook 147
8.1 Summary of Contributions . . . 150
8.2 Future Work . . . 151
8.3 Dissemination . . . 152

8.3.1 Direct Contributions 152
8.3.2 Other Works and Collaborations 152

List of Figures

1.1 Wind and solar increase in global energy production [5]. 2
1.2 Centralized vs decentralized electricity grid system [6]. 2
1.3 Daily supply and demand with storage of renewable energy, 11–17 July 2007, Minnesota as referenced in [7]. 3
1.4 Classification of energy storage technologies by the form of stored energy [8]. 3
1.5 RFB structure during charge process [17]. 9
1.6 Detail of reactions taking place in the RFB cell during charge [18]. 9
1.7 The cost breakdowns of all-Vanadium battery systems [23]. 11
1.8 a) Schematic representation of a membraneless battery design based on immiscible redox electrolytes b) Membrane-free flowbattery with a horizontal design to favor the formation of the two immiscible phases [38]. 13
1.9 (Left) Schematic of the microfluidic reaction cell with electrolytes interface (diffusion is not depicted) and electrodes. (Right) Actual cell during operation. 13

2.1 Shematic design of the first microfluidic membraneless cell, presented by Ferrigno et al. in [39]. 18
2.2 Schematic of the membraneless fuel cell [41], with regions of fuel/oxidant depletion and diffusional fuel/oxidant crossover indicated (not drawn to scale). Double syringe pump PHD2000 by Harward Apparatus also represented to show injection at the inlets. 19
2.3 Microfluidic membranelss cell with three-dimensional vanadium-based microfluidic fuel cell with the graphite rods architecture [43] 20
2.4 Schematics of design and operation (left) of the microfluidic membraneless cell with flow-through electrodes, and cross-sectional geometry (right) of the architecture [44] 21
2.5 (a) Exploded view; and (b) assembly of the proposed microfluidic cell with gold current collectors (not to scale) [45] 21
2.6 Scheme of the microfluidic pumping system and annotated image of the microfluidic redox battery operating from [46] in discharge mode. 22
2.7 Microfluidic setup and cell from [47], with herringbone pattern promoting mass transport, “X” shape cell structure and syringe pumps at the inlets. 23
2.8 Real time image from [48] of the cell discharging the vanadium electrolytes. . 24
2.9 Schematic of the flow battery architecture demonstrated in [50], with dotted lines indicating the possibility of using the peristaltic pumps for recirculating. 25

2.10 Membraneless microfluidic rector used in [54] with absorbent pad to create a capillary flow. . . . 25
2.11 Schemes of fuel concentrations profiles at different flow rates from the model from [56]. . . . 27
2.12 Scheme of a reactor with the mass transport of the species represented with colours and distances of the reactor indicated, from [49]. . . . 28
2.13 Schematic of a reaction cell with planar electrodes and detail of the studied mixing region in a 2-dimensional model in [61], where effects of the self-discharge diffusion on concentration change are indicated. . . . 29
2.14 Experimental measurements of the self-discharge losses from [66], at different equal inlet flow rates from 0.1 to 300 $\mu L/min$ and at 90% states of charge. . 30
2.15 Charts from [74] demonstrating battery performance enhancement from flow rate variable operation. (Left) Different constant and variable flow configurations. (Right) Charge-discharge reactor voltage versus time for different flow rates. . . . 31
2.16 Figures from [78], where the microfluidic RFB with heat dissipation concepts is represented (left) and the relationship between heat dissipation and power delivered is plotted (right). . . . 32
2.17 Electrical equivalent model from [80]. . . . 33
2.18 Electrical equivalent model from [81], with two half cells equivalent impedances joined in one equivalent group, and parasitic loads represented with one resistance and current source. . . . 34
2.19 Electric and thermal coupled models from [82]. . . . 34
2.20 Stack electrical model from [83] where a simple cell equivalent circuit is repeated. 35
2.21 Equivalent electric circuit from [84]. . . . 35
2.22 Equivalent electric circuit from [85] for the battery, with load connected and indications for where terminal voltage and cell current are measured. . . . 36
2.23 Kalman Filter scheme with state X at different time steps (k, k-1). . . . 42
2.24 Control scheme for an i-PID approach from [110] using an optimization algorithm for a high order system. This scheme is general to any i-PID methodology by substituting the optimization algorithm with the concrete adaptation technique and applying it to the specific plant. . . . 48
2.25 Time horizon strategy for MPC as depicted in [123], with the moving prediction and control horizons, the set of control actions u, the measured and expected outputs (y and $\hat{y}$) and the state constraints w. . . . 50
2.26 Fuzzy system process scheme from [128] where an input variable is converted to a fuzzy value that may be composed by several sets, evaluated following the rule-based inference, and then defuzzified to a composed output variable. . . 51
2.27 Representation of the switching mechanism for the VSC from [130], with the trajectory on the state space, the sliding surface and the chattering produce around the switching region. . . . 52

3.1 Soft lithography in PDMS process. . . . 56
3.2 Microfluidic membraneless redox flow cell negative mould made with 3D DLP printing additive manufacturing, and PDMS block after curing in this mould. 56

3.3 Carbon paper-porous sheets that are cut to obtain the electrodes. 56
3.4 Plasma cleaner used for bounding and its inside process with oxygen plasma. 57
3.5 Mould, PDMS block and complete reactor cell for the microfluidic membraneless RFB. 57
3.6 System microfluidic setup for recirculation with syringe pumps (left) and long term flow rate for one electrolyte, with pulsation and switching discontinuities (right). 58
3.7 Gear pump prototype and design made with DLP 3D printer. 59
3.8 Pressure driven flow (PDF) pumping principle (left), and setup for recirculation with valve (right), from Elveflow products. 59
3.9 Piezoelectric pump from Bartels Mikrotechnik GmbH (left) and working principle steps (right). 60
3.10 Piezoelectric pumps flow response compared to syringe pumps and PDF systems, tested at different flowrates in the range of 1-1000µL/min, and stability test for several days. 60
3.11 Scheme of the pneumatic valve including liquid inlet (1), air inlets (2) and membrane (3) (left) and young modulus calculations and real experiments measurements (right). 61
3.12 Thermal working principle of liquid flow meters, from [132]. 62
3.13 Tanks monitoring application with real time calculation of leakage and flowmeters compensation. 63
3.14 Hardware scheme of the board developed for the microfluidic setup integration. 64
3.15 Image of the control board, with the drivers for the piezoelectric pumps (1 and 2), the piezoelectric pump itself connected (3), the flowmeters with their connections (4), the air pump driver (5) and the micro pump itself (6), and the micro USB connector (7). 65
3.16 Screen capture from computer SCADA application during operation of the microfluidic membraneless RFB. Values from actuators, sensors, control and operation configuration and logging are shown. 66
3.17 System scheme, with actuators and flowmeters for both electrolytes circuits. Flows at the negative and positive inlets are Q_1 and Q_2, and Q_3 and Q_4 at the outlets. 67
3.18 Real image of the system, with reaction cell, liquid pumps, air compressor pumps, valves, flowmeters, tanks, control boards and electrical contacts highlighted. 67

4.1 The proposed electric equivalent circuit for the microfluidic membraneless RFB. 70
4.2 Nyquist plot of the collection of EIS experiments performed to measure the battery response under different flow conditions. 72
4.3 Experiment showing microfluidic influence on electric response. Constant voltage (0.7V) discharge, with different flow configurations represented on the left axis by the three flows, and the maximum given electric current on the right axis. 74

4.4 Constant voltage discharge experiment, with one of minimum inlet flow rates constant and modifying the fluidic interface by changing the other inlet flow (left axis), and relative current output (right scale). 76
4.5 Simulated response for the model of equation (4.9) and real experimental data. The goodness of fit measurement is performed and indicated in the legend in percentage. 78
4.6 Simulated response for the proposed model from equations (4.10)-(4.12) with parameters from Table 4.1, and actual steady-state relative current experimental data. The fitness measure is indicated in the legend. 79
4.7 Simulated response for the proposed model from equations (4.10)-(4.12) with parameters from Table 4.1, and actual steady-state relative current experimental data in different experiment. The fitness measure is indicated in the legend. 79
4.8 Simulated responses for the dynamic model and three real experimental transient power data. The fitness measure is indicated in each legend. 82
4.9 Experimental measurements of the self-discharge losses from [66], at different equal inlet flow rates from 0.1 to 300 $\mu l/min$ and at 90% states of charge, using logarithmic scale. 83
4.10 System configuration scheme for correlation between flow and mixing and self-discharge, with pumping system, reaction cell, flowmeters, and spectrophotometers. The cell outlets are not recirculated to preserve SOC at the tanks. 85
4.11 Relation between SOC losses and mixed volume, with experimental points and linear curve model fit indicated. Root-mean-square error and R^2 measurements are shown in the legend. 85

5.1 System output for model with grey box identified parameters compared to real experimental data for the same experiment as used for identification. Fitness measurement is indicated for each dataset. 93
5.2 System output for model with grey box identified parameters compared with real data for a different experiment. Fitness measurement is indicated for each dataset. 94
5.3 Experimental data compared with models with and without factor correction calculated in an offline regression. Fitness measurement is indicated for each dataset. 96
5.4 Comparison of real data system response with the model with online EKF factor correction and the model without factor correction. Fitness measurement is indicated for each dataset. 99
5.5 Random factor values fed to the simulated model of the system and EKF online estimation of these values. Estimated values are adjusted precisely to random changes in the factors fed to the model. 100

6.1 Model-free control architecture based on three independent SISO PID controllers by assigning one input for the actuators to one measured output of the system. 105
6.2 Simulated response for the control architecture with 3 PIDs controllers. . . . 106
6.3 Real response for the control architecture with 3 PIDs controllers. 107

6.4 Control scheme of the LQR with integral action, with factors from the EKF estimation for the adaptive model of the control calculation, and the iteratively calculated control gains. . . . 110
6.5 Simulated response for the LQR with integral action control architecture. . . 111
6.6 Real response for the LQR with integral action control architecture. 112
6.7 Scheme for the optimal controller with incremental state, with factors from the EKF estimation for the adaptive model of the control calculation, and the iteratively calculated control gains. . . . 114
6.8 Simulated response for the optimal control with incremental state architecture. 115
6.9 Real experiment response for the optimal control with incremental state architecture. . . . 116
6.10 Time horizon strategy for general MPC with the moving prediction and control horizons, the set of control actions u, and the reference and expected outputs. 117
6.11 Scheme for the adaptive nonlinear MPC, with factors from the EKF estimation for the adaptive model of the control calculation, and the calculated manipulated variables. Note that saturations for the inputs are marked to indicate that are not necessary since the MPC calculation already considers the operation range as a constraint. . . . 119
6.12 Simulated response for the adaptive nonlinear MPC architecture. 120
6.13 Real experiment response for the adaptive nonlinear MPC architecture. . . . 121
6.14 Scheme for the adaptive incremental MPC, with factors from the EKF estimation for the adaptive model of the control calculation, and the calculated increment in the manipulated variables. . . . 122
6.15 Simulated response for the adaptive incremental MPC architecture. 124
6.16 Real experiment response for the adaptive incremental MPC architecture. . . 125
6.17 Simulated response to a single reference step. Comparison of all the proposed control methods. . . . 127
6.18 Real experiments response to a single reference step. Comparison of all the proposed control methods. . . . 128
6.19 Real experiments response to a sequence of different steps. Comparison of all the proposed control methods. . . . 129

7.1 Profiles from [149] where energy production, load, energy import, and export are presented for a sunny day of July 2020 (a) and a partly cloudy day of July 2020 (b). . . . 132
7.2 Benchmark power profile defined for control strategies electric evaluation. . . 133
7.3 Benchmark power profile with the relative power response of each of the control strategies. . . . 134
7.4 Detail of the benchmark power profile with a single step increasing the reference and the relative power response of each of the control strategies. 135
7.5 Detail of the benchmark power profile with a single step decreasing the reference and the relative power response of each of the control strategies. 136
7.6 Volume mixed evolution in benchmark power profile experiment for the different designed control strategies. . . . 138
7.7 Pump driver power data points and curve from equation (7.2). 140

7.8 Pump driver power data points and curve from equation (7.3). 141
7.9 Inputs actions from all control strategies during real experiment performing the benchmark power profile. 142

List of Tables

1.1 Battery technologies comparison. Own elaboration based on [27],[28],[29],[30],[31],[32]. Note that values are approximate to give a comparative reference since the sources differ from each other and the technologies are in continuous evolution. 12

4.1 Values of the parameters of the proposed equations 78

5.1 Parameters of the proposed equations 91

6.1 Values of the parameters of the proposed PID controllers 105

7.1 Percentage of power under demanded reference power for each control method 137
7.2 Volume mixed during benchmark operation for each control method 137
7.3 Increment in state of charge losses during benchmark operation for each control method 138
7.4 Consumption of pump drivers 139
7.5 Consumption of valve driver 141
7.6 Total equivalent action consumption for each control method 143
7.7 Summary of Control Strategies Electrical Evaluation 145

Abbreviations

AR Auto-Regressive

ARIMA Auto-Regressive Integrated Moving Average

CAES Compressed Air Energy Storage

CFD Computational Fluid Dynamics equations

COP Conference of the parties

CSP Concentrated Solar Power

DLP Digital Light Processing

EIS Electrochemical Impedance Spectroscopy

EKF Extended Kalman Filter

FES Flywheel Energy Storage

GDE Gas Diffusion Electrode

i-PID Intelligent PID

LED Light Emitting Diode

LNG Liquefied Natural Gas

LQR Linear Quadratic Regulator

MA Moving Average

MFPC Model-Free Predictive Control

MIMO Multiple Input Multiple Output

MISO Multiple Input Single Output

MPC Model Predictive Control

PCM Phase Change Material

PDF Pressure Driven Flow

PDMS PolyDiMethylSiloxane

PID Proportional-Integral-Derivative

PHS Pumped Hydro Storage

PLS Partial Least Squares

RFBs Redox Flow Batteries

SCADA System Control And Data Acquisition

SIMO Single Input Multiple Output

SISO Single Input Single Output

SMA Shape Memory Alloy (SMA)

SMES Superconducting Magnetic Energy Storage

SOC State Of Charge

SVR Support Vector Regression

UKF Unscented Kalman Filter

UNFCCC United Nations Climate Change Conference

VSC Variable Structure Control

VSF Variable Structure Filter

VRFB Vanadium Redox Flow Batteries

Chapter 1

Introduction

This chapter describes the context and motivation of this thesis. First, an introduction of the global energy transition context and the vital role energy storage plays is detailed, reviewing different technologies with the focus on redox flow batteries and their working principles. Second, membraneless redox flow batteries are introduced, briefly detailing their background (that is covered more in depth in chapter 2) and delving deeper into the challenges of their design and operation. It is also identified which of them are solved within the scope of this thesis. Finally, the content of the thesis is outlined.

1.1 Energy storage

Human prosperity depends on our capacity to harness higher amounts of energy and utilize it efficiently. During the last century, the significant rise in living standards was fuelled with fossil resources [1]. However, with the advent of the 21st century and growing concerns about climate change, coupled with the declining cost and competitiveness of renewable power sources, the electrical mix has progressively increased the share of these new technologies [2]. Wind and solar energy, being the fastest-growing sources, are inherently intermittent [3]. Thus, the need for large-scale energy storage becomes critical to align the availability of their generated power with energy demand [4].

Energy transition is being pushed not only technologically but also institutionally, especially to fight climate change. Conference of the parties (COP) is the annual United Nations Climate Change Conference (UNFCCC), where negotiators and delegates from around the world gather to discuss climate-related issues and negotiate agreements. The COP conferences have resulted in significant milestones, such as the adoption of the Kyoto Protocol in 1997 and the Paris Agreement in 2015, which set international targets for reducing greenhouse gas emissions and promoting global climate action. They have emphasized the importance of reducing reliance on fossil fuels and transitioning to cleaner and more sustainable energy sources to mitigate the impact of climate change. This integration of renewable energy sources has led to a more decentralized and distributed energy system, where power generation occurs at various locations, including rooftop solar panels, community wind farms, and small-scale hydro plants.

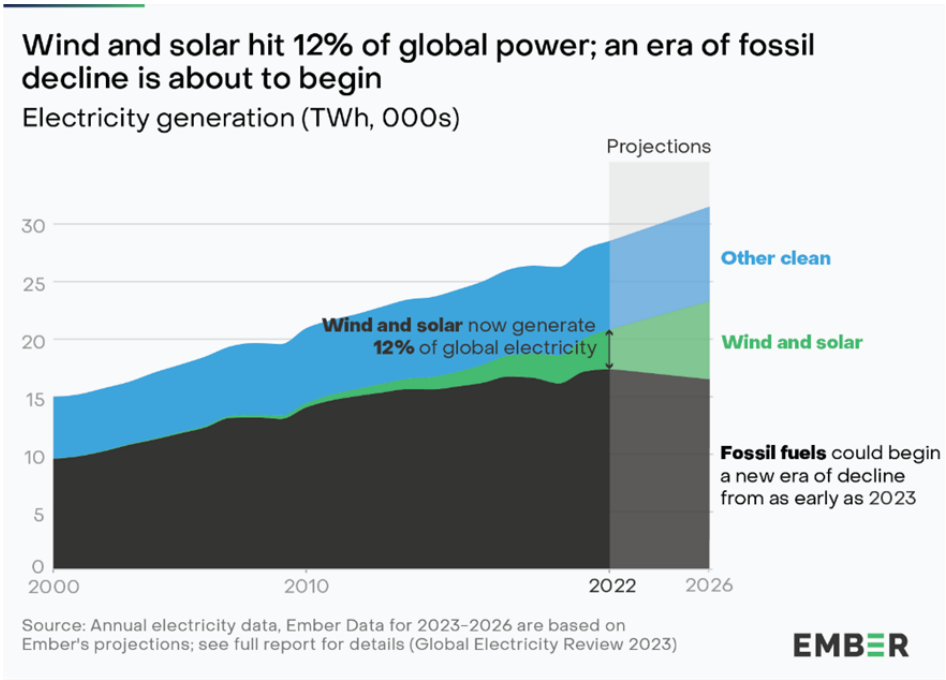

Figure 1.1: Wind and solar increase in global energy production [5].

Energy storage systems plays a crucial role in this new grid paradigm. They store excess energy generated during peak times and release it when demand is high or when renewable energy generation is low. This helps stabilize the grid, ensure a steady and reliable energy supply, and maximize the utilization of renewable energy resources.

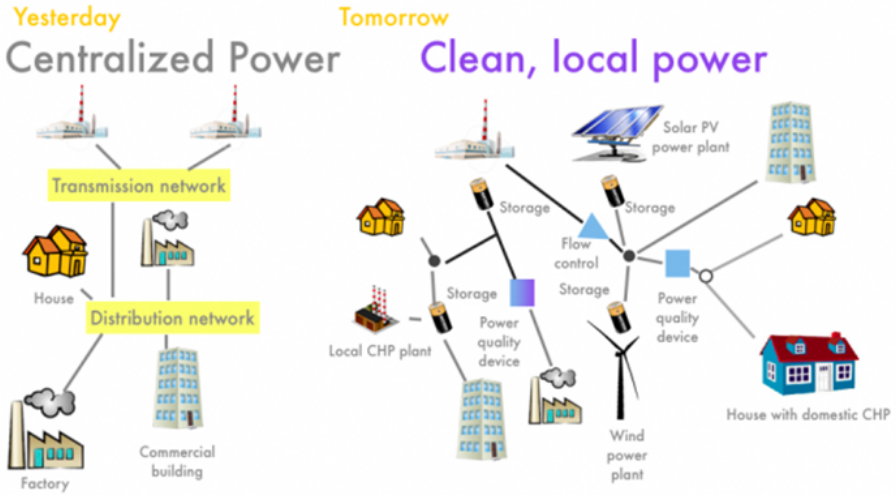

Figure 1.2: Centralized vs decentralized electricity grid system [6].

Moreover, energy storage facilitates the integration of renewable energy into the grid, as it enables grid operators to overcome the challenges posed by variable generation. By deploying

energy storage systems strategically, grid operators can optimize the use of renewable energy, reduce curtailment (wasting excess renewable energy), and enhance the grid's flexibility and resilience.

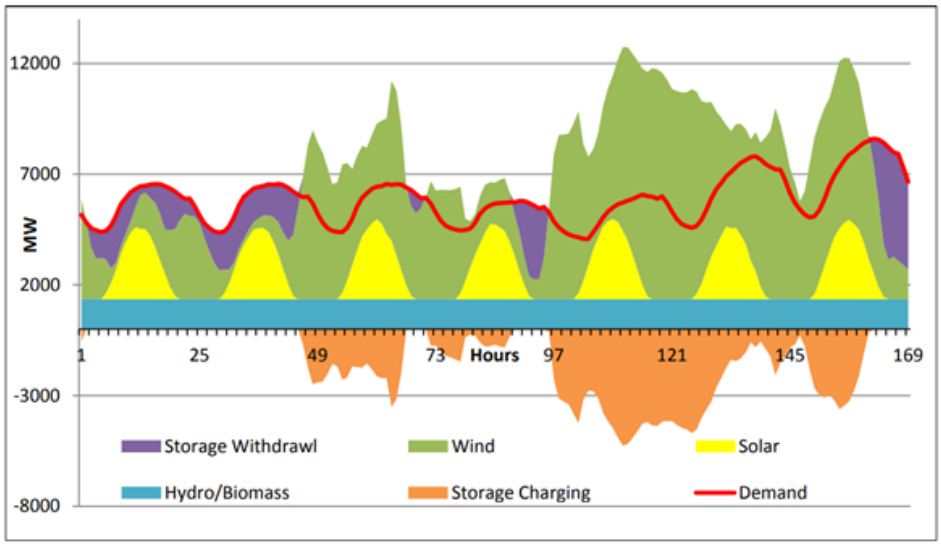

Figure 1.3: Daily supply and demand with storage of renewable energy, 11–17 July 2007, Minnesota as referenced in [7].

At the same time, COPs have also emphasized the importance of electrification and the decarbonization of various sectors, such as transportation and heating. The new grid paradigm envisions a shift towards electrifying these sectors, relying on electricity generated from renewable sources and stored in energy storage systems. This transition not only reduces carbon emissions but also increases the efficiency and sustainability of energy use across different applications.

Energy storage technologies are diverse, and they can be classified by their underlying principles, which defines the form of their stored energy. The main forms are mechanical, electrochemical, electrical, chemical and thermal.

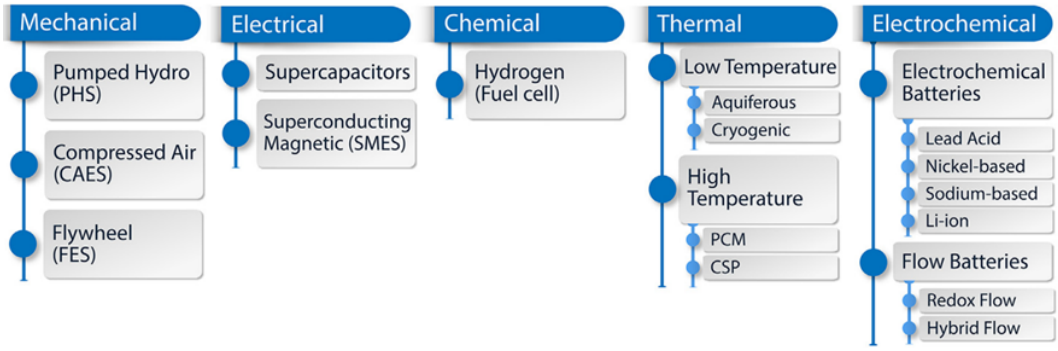

Figure 1.4: Classification of energy storage technologies by the form of stored energy [8].

Mechanical Energy Storage

Mechanical storage systems store energy in the form of potential or kinetic energy and they rely on mechanical processes to convert and release stored energy as needed. These systems have been utilized for centuries and are among the most established and efficient methods of large-scale energy storage.

Pumped Hydro Storage (PHS) consist of two water reservoirs at different elevations. During periods of excess electricity generation, surplus electricity is used to pump water from the lower reservoir to the higher reservoir. When electricity demand rises or during peak hours, the stored water is released back to the lower reservoir through turbines, generating electricity. PHS is the most widely deployed and mature form of large-scale energy storage. It offers high round-trip efficiency, typically exceeding 80-90%, making it an essential component of grid stability and peak load management. PHS can quickly respond to fluctuations in demand, acting as a reliable and cost-effective method to balance supply and demand.

Compressed Air Energy Storage (CAES) use excess electricity to compress air and store it in underground caverns or above-ground tanks. During periods of high electricity demand, the compressed air is released, expanded through turbines, and used to generate electricity. CAES is another large-scale energy storage option that provides grid flexibility and can help manage intermittent renewable energy sources. Advanced adiabatic CAES systems aim to increase efficiency by capturing and reusing waste heat during the compression and expansion processes.

Flywheel Energy Storage (FES) systems store energy as rotational kinetic energy by spinning a rotor at high speeds. When electricity needs to be stored, the motor accelerates the rotor, and during discharge, the rotor acts as a generator, slowing down and releasing the stored energy as electricity. Flywheel energy storage provides fast response times, high power density, and high efficiency. It is often used in short-duration energy storage applications and can help regulate frequency and voltage on the grid, particularly during transient events.

Electrical Energy Storage

Electrical storage systems store energy in the form of an electrical or magnetic field. These systems use various principles, such as charge separation, magnetic induction, or superconductivity. Supercapacitors store electrical energy by the separation of charges at the interface between an electrode and an electrolyte. They store energy through electrostatic forces and do not involve chemical reactions like batteries. Supercapacitors are known for their rapid charge and discharge capabilities, making them suitable for applications requiring high-power performance and short-duration energy storage. They are commonly used in conjunction with batteries to enhance their performance.

Superconducting Magnetic Energy Storage (SMES) store energy in the magnetic field created by a superconducting coil. The coil is cooled to extremely low temperatures, allowing it to conduct electricity without resistance, resulting in minimal energy losses. SMES systems offer high-power densities and ultra-fast response times, making them valuable for applications that require quick and precise power delivery, such as improving power quality and grid stability.

Chemical Energy Storage

Chemical energy storage involves converting electrical energy into chemical potential energy through chemical reactions and then converting it back to electrical energy when needed. Hydrogen is the most common compound due to its potential as an energy carrier, a source of other storage chemicals like methane, and a feedstock for the chemical industry. Chemical storage shows promise for large-scale seasonal storage required for future high levels of renewable energy generation and applications that benefit from its high energy density. However, it has drawbacks, such as low energy efficiency in successive conversion steps. Electrolyzers and fuel cells are essential in hydrogen energy conversion. Electrolyzers use water electrolysis to produce and store hydrogen, while fuel cells generate electricity through redox reactions of fuel (hydrogen) and oxidant (oxygen). Fuel cells offer high theoretical energy densities (over 400 Wh kg-1) but have low power density (60 W kg-1), limiting their energy storage applications. Their specific energy cost is low due to external tank storage. However, the need for two reactors and expensive electrochemical cells hinders their feasibility and efficiency.

Thermal Energy Storage

Thermal energy storage is a method of storing and releasing thermal energy for later use. Aquiferous systems store thermal energy by injecting water into an underground aquifer during the cooling season and extracting it during the heating season. The stored water acts as a thermal reservoir, absorbing or releasing heat as needed. ATES is commonly used for heating and cooling buildings, providing a sustainable and efficient solution for temperature regulation.

Cryogenic thermal energy systems store thermal energy in the form of cryogenic fluids, such as liquefied air or nitrogen, at extremely low temperatures. During the discharge phase, these cryogenic fluids vaporize and expand, releasing stored energy. It is employed in various industries, such as Liquefied Natural Gas (LNG) plants, where excess cold energy during liquefaction is stored and later used for power generation or cooling.

Phase Change Material (PCM) store thermal energy by undergoing a phase change (e.g., solid to liquid or liquid to gas) at a specific temperature. During charging, the PCM absorbs heat and changes its phase, and during discharging, it releases heat while transitioning back to its original phase. PCMs are used in building envelopes, solar thermal systems, and electronics cooling to maintain temperature stability and enhance energy efficiency.

Concentrated Solar Power (CSP) concentrate sunlight onto a receiver, heating a heat transfer fluid (e.g., molten salt or oil). The hot fluid is then stored in a thermal energy storage system and used to generate steam, driving a turbine and producing electricity when needed, including during periods without sunlight. CSP with thermal energy storage is utilized in large-scale solar power plants to provide continuous and dispatchable electricity generation, even after sunset, improving grid stability and renewable energy integration.

Electrochemical Energy Storage

Electrochemical energy storage systems are a class of energy storage technologies that utilize reversible electrochemical reactions to store and release energy. These systems involve the conversion of electrical energy into chemical energy during charging and the reverse process during discharging.

Lead-acid batteries use lead plates as electrodes and a sulfuric acid electrolyte to store energy. During charging, lead oxide and lead react to form lead sulfate and store electrical energy. During discharging, lead sulfate is converted back to lead oxide and lead, releasing stored energy. Lead-acid batteries are commonly used in automotive applications, backup power systems, and renewable energy storage for smaller-scale applications.

Nickel-based batteries, such as nickel-cadmium (NiCd) and nickel-metal hydride (NiMH) batteries, use nickel-based compounds as positive electrodes. During charging, nickel oxide or hydroxide is formed, and during discharging, it reverts to nickel ions, releasing stored energy. NiCd batteries were widely used in portable electronics, but their use has declined due to environmental concerns. NiMH batteries are still used in some consumer electronics and power tools.

Sodium-based batteries, such as sodium-sulfur (NaS) batteries and sodium-ion batteries, use sodium compounds as active materials. During charging, sodium ions are stored in the anode material, and during discharging, they migrate to the cathode, releasing stored energy. Sodium-ion batteries are being researched as potential alternatives to lithium-ion batteries for large-scale energy storage due to the abundance of sodium.

Lithium-ion batteries use lithium-based compounds (e.g., lithium cobalt oxide, lithium iron phosphate) as cathode materials and carbon-based materials as anodes. During charging, lithium ions move from the cathode to the anode, and during discharging, they move back to the cathode, releasing stored energy. Lithium-ion batteries are widely used in portable electronics, electric vehicles, renewable energy storage, and grid-scale energy storage due to their high energy density and efficiency.

Redox Flow Batteries (RFBs) store energy in chemical solutions (electrolytes) in separate tanks. During charging and discharging, the electrolytes flow through electrochemical cells, where reversible redox reactions occur, converting chemical energy to electrical energy. This technology is the base for the microscale membraneless reactors explored in this thesis, and it is further discussed later on. They are suitable for large-scale energy storage applications, especially in grid-scale storage and renewable energy integration, due to their scalable and flexible nature.

Hybrid Flow batteries combine aspects of RFBs with other types of electrochemical cells. They use different active materials for the positive and negative electrodes, leading to improved energy density and performance. They are being researched as potential solutions for long-duration and high-power energy storage applications.

1.1.1 Redox Flow Batteries

This technology has been exploited for the last few decades and it is experimenting a remarkable increase in interest, but its research and development process has been ongoing since the beginning of the previous century.

During the first half of the 20th century there were several experiments of systems using metal-ion couples for energy storage. For example, Kangro's experiments [9], particularly in the late 1950s, using redox pairs as chromium, iron, titanium, and chlorine showcased the reversible nature of the electrochemical processes, as metal ions transitioned between different oxidation states. Although these early experiments were conducted on a relatively small scale, they provided crucial insights into the principles of redox reactions as a means of storing and releasing energy.

Similarly, Piper's work [10] delved into the exploration of iron-based redox reactions as a potential avenue for energy storage. Piper's research focused on understanding the electron transfer mechanisms. These investigations not only contributed to the fundamental understanding of redox reactions but also highlighted the challenges associated with efficiency and practical application.

A significant turning point in RFB development occurred during the 1970s with NASA's research on regenerative fuel cells for space applications. Lawrence Thaller and his team at NASA's Lewis Research Center investigated RFBs that could store energy for space missions [11]. Their work led to the development of the first practical redox flow battery, which utilized a chromium and iron couple, and first introduced the term "redox flow battery".

In the late 1980s, Dr. Maria Skyllas-Kazacos, an Australian researcher, made significant contributions to the advancement of RFB technology [12]. She introduced the use of vanadium as a symmetric redox couple (symmetrical redox flow battery makes that physical crossover of electro-active species does not result in permanent battery damage and simplifies charge rebalancing). Vanadium Redox Flow Batteries (VRFB) designs use four different oxidation states on carbon-based electrodes. This work refined the design of the VRFB and investigated various chemistries, including the use of sulfuric acid and other supporting electrolytes. Her research laid the groundwork for the commercialization of VRFBs and their potential applications in large-scale energy storage systems. Vanadium is now the most common electrolyte in these applications.

After this significant milestone, the research on RFBs gained momentum and expanded into various directions. One significant direction of research involved optimizing RFB designs and system components to enhance overall efficiency and durability. This included developing advanced electrode materials, ion-selective membranes, and flow cell configurations that could enhance reaction kinetics, minimize crossover, and improve energy conversion efficiency.

Furthermore, research efforts aimed at addressing challenges related to scalability and cost-effectiveness. As RFBs moved from lab-scale demonstrations to practical applications, researchers worked on developing manufacturing processes that could produce reliable and cost-efficient components for large-scale deployment.

The integration of RFBs into renewable energy systems, grid applications, and microgrid

scenarios also gained attention. Researchers aimed to demonstrate the compatibility of RFBs with intermittent renewable energy sources, such as solar and wind, by enabling energy storage and grid stabilization. This work contributed to the RFB's role in enhancing the reliability and resilience of modern energy infrastructure.

Simultaneously, efforts were directed towards optimizing system control, monitoring, and management to ensure efficient operation and maximize the lifespan of RFB systems. The development of sophisticated control strategies, state-of-charge estimation algorithms, and predictive maintenance techniques further improved the overall performance and economic viability of RFB installations.

However, research of non-vanadium chemistries has continued. Different redox-active species, such as organic molecules [13], metal ions, and other transition metals, are currently being developed at laboratory scale, and used in new non-aqueous [14] or hybrid solutions [15]. These efforts aim to identify chemistries that could offer improved performance characteristics while potentially reducing material costs.

Other remarkable research lines are the use of redox mediators [16] that use a solid active material introduced into the external tanks in order to increase energy density, or the concept used in this thesis of membraneless reactors for redox flow batteries.

Redox Flow Batteries Working Principles

It has already been introduced that RFBs consist of two electrolyte solutions containing different redox-active species. Electrolytes contains a pair of redox couples: one species capable of being oxidized (losing electrons, gaining positive charge) and another species capable of being reduced (gaining electrons, losing positive charge). These redox couples should undergo reversible reactions with minimal degradation over many charge-discharge cycles.

An RFB cell typically consists of two compartments separated by an ion-selective membrane. Each compartment contains one of the electrolytes with its corresponding redox species. The electrodes, usually made of porous materials are placed in contact with the electrolytes on either side of the membrane.

During the charging process, electrical energy from an external source is used to drive the redox reactions. At the positive electrode, the positive species in the electrolyte undergoes oxidation (vanadium goes from oxidation state 4+ to 5+), releasing electrons and forming an oxidized species. Simultaneously, at the negative electrode, the species in the other electrolyte undergoes reduction, gains electrons and forming a reduced species (vanadium goes from oxidation state 3+ to 2+). This process store energy in the form of an electrochemical potential. These reactions are represented in the following expressions:

$$V^{(V)}O_2 + 2H^+ + e^- \rightarrow V^{(IV)}O^{2+} + H_2O \quad E^0 = 0.99V \tag{1.1}$$

$$V^{2+} \rightarrow V^{3+} + e^- \quad E^0 = -0.26V \tag{1.2}$$

The ions (protons) generated during the redox reactions move through the ion-selective membrane that separates the two compartments. The membrane allows only ions to pass

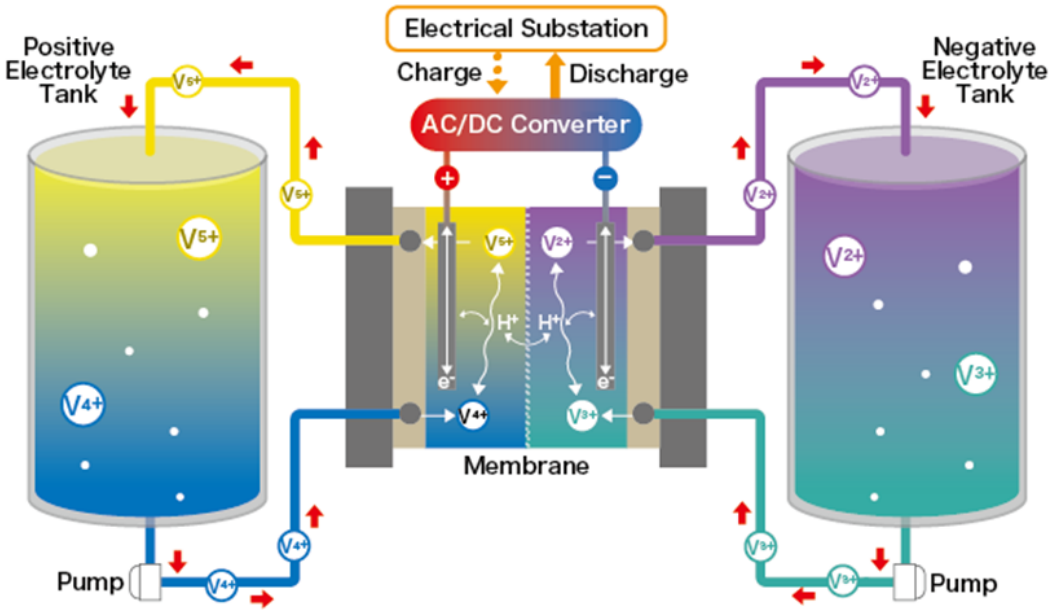

Figure 1.5: RFB structure during charge process [17].

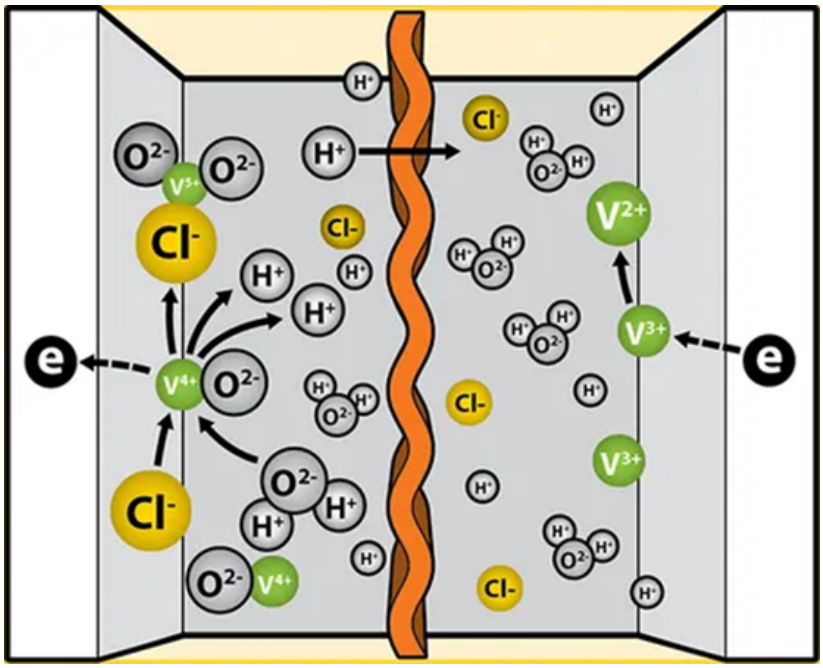

Figure 1.6: Detail of reactions taking place in the RFB cell during charge [18].

through, preventing the mixing of the two electrolytes. This movement of ions balances the charge and maintains electrical neutrality in both compartments.

During discharge, the process is reversed. At the positive electrode, the positive species in the electrolyte undergoes reduction (vanadium goes from oxidation state 5+ to 4+), gaining

electrons. While at the negative electrode, the species undergoes oxidation, donating electrons (vanadium goes from oxidation state 2+ to 3+). This process releases energy in the form of an electric current.

The reactions take place at the electrode surface, so its active area is directly proportional to the amount of species that react per unit of time, and therefore is a key element defining cell power. Electrodes are typically carbon based to not be damaged by the acid media of the electrolytes [19]. Also, the electrode electric conductivity conditions the internal ohmic resistance, together with the contact between these electrodes and the current collector that drives electrons out of the reactor to the electric circuit. There is also a trade-off between active area (usually linked to material porosity) and pumping consumption, as the energy needed for pumping the liquids may increase significantly [20].

The hydraulic system of the battery keeps the electrolytes at the cell being continuously renewed with new liquid from the tank. This is made using pumps which inherently increase energy losses and which operation conditions system efficiency. However, this liquids flow provides RFB with the capacity of decoupling energy capacity and power, which is one of the significant advantages of this systems. The amount of energy stored is determined by the volume of the electrolyte tanks, allowing for easy scalability and adjustment of capacity without affecting power output, which is defined by reactor design and number of them. This also makes RFBs suitable for applications requiring long-duration energy storage, as electrochemical potential in the tanks can be isolated one from an another, and therefore energy preserved.

Their intrinsic properties make RFBs able to undergo numerous charge-discharge cycles without significant degradation, making them suitable for applications requiring frequent energy storage and retrieval. This is caused by the mentioned symmetry of the electrolytes for the vanadium case, where liquid mixing between the circuits causes state of charge loss but not a permanent damage to the electrolytes. This mixing can happen because membrane damage or just during normal operation, as these membranes have certain permeability to the species, and this permeability is also different between them, so that the reagents concentrations become unbalanced over time. Rebalancing the tanks by mixing completely them and compensating their volume to be equivalent would make the battery electrolytes ready to be used again.

Besides pumps, that require a preventive maintenance, membrane are the elements that suffer the most damage. As the polymeric membrane is continuously exposed to the oxidative and acidic environment of the vanadium electrolyte it may suffer deterioration over time. This deterioration results in poorer membrane selectivity towards vanadium permeability, which causes faster discharge times and less efficiency of the battery [21]. The quality of the membrane also determines internal electric ohmic resistance of the cell, which not only increases energy losses but also limits maximum power of the reactor. This resistance is related with ionic conductivity, which increases with larger pore size, higher pore interconnectivity, lower thickness, and higher hydrophilicity [22]. The lower resistance can result in higher voltage efficiency, but if it also leads to lower selectivity it may sacrifice columbic efficiency.

All cited membrane casuistic makes them be responsible of much share of the battery system

costs. Total system costs can be divided in capital cost and life cycle cost that include operation and maintenance, replacement and end of life costs. The membrane percentage cost can reach more than 40% of the capital cost [23]. Total costs are a critical point for battery selection criteria for industrial applications and therefore should be carefully analysed.

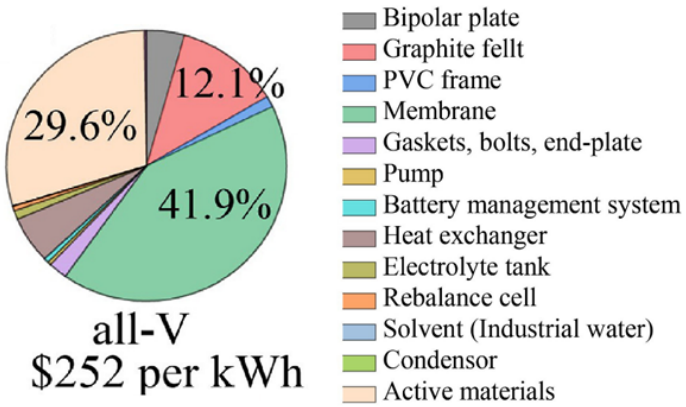

Figure 1.7: The cost breakdowns of all-Vanadium battery systems [23].

Life cycle cost takes into account not only the initial capital investment but also the ongoing costs associated with the entire life span of the RFB system. These costs are subject to more different factors and their analysis methodologies are more diverse [24]. This includes operational and maintenance costs, as well as replacement of components that might wear out over time, so preventive maintenance becomes indispensable. Another forward approach for saving life cycle costs is increasing efficiency. RFBs energy efficiency depends on factors such as redox couples, electrode materials, and system design, so optimizing these aspects can improve overall performance.

Other important share of capital cost is represented by active materials. Therefore, capital costs can not only be decreased with reductions of cell stack materials costs, but also with higher power densities. The power density can be raised using other chemistries and also increasing species concentration in the electrolyte. This concentration is defined by redox species solubility, as high concentrations reach a limit where solid precipitation occurs [25]. Although there are efforts in improving its solubility and stability, vanadium solubility is low and it results in specific energy densities around 20-25 Wh kg-1, which is substantially lower than other technologies [26]. This limits its applications and is another reason why it has been implemented for stationary solutions, as integration with renewable energy sources, where space is not so limiting.

To summarize, RFBs are battery system that need a complex operation system, and which energy density is limited. Nevertheless, they offer a low degradation, high cyclability, long cycle life and safe solution, that do not suffer at high depths of discharge, that can be rebalanced to regenerate its electrolytes, and a flexible solution as they are highly scalable, cost-effective and their energy and power are decoupled.

A comparison of its main properties with respect to other extended battery technologies is provided in the following table.

Battery Type	VRFB	Lithium	Lead Acid	NiCd	Ni-MH
Life Span	15-25 years	3-5 years	2-3 years	5-7 years	7-10 years
Power-Energy Decoupl.	Yes	No	No	No	No
Number of Cycles	10,000+	1000-2500	300-700	300-1000	700-2000
Depth of Discharge	100%	80%	50%	50%	40-50%
Energy Density (Wh/l)	20-25	300-600	50-90	50-70	40-75
Cost ($/kWh)	200-400	120-300	600-1000	400∼	83∼
Operational Risk	Low	Mod.-High	Moderate	Moderate	Moderate
Coulombic Efficiency	80-95%	95-99%	70-85%	70-90%	95-98%
Energy Efficiency	75-90%	85-95%	70-80%	70-80%	80-90%

Table 1.1: Battery technologies comparison. Own elaboration based on [27],[28],[29],[30],[31],[32]. Note that values are approximate to give a comparative reference since the sources differ from each other and the technologies are in continuous evolution.

1.2 Membraneless Redox Flow Batteries

RFBs are already implemented in many large-scale applications, and they can be considered a mature technology. However, research is currently not limited to improve performance of these designs and their integration, but also different alternatives are being studied [33]. These alternatives include the research of chemistries beyond vanadium (inorganic such as the bromine-hydrogen RFB [34], or organic such as the methyl viologen–TEMPO designs [35]). Another line of research is the inclusion of solid materials, such as the already mentioned mediators/boosters [36] or using suspension of solid particles to increase power density [37]. Alternative reactor concepts and configurations are also being studied, pursuing to surpass traditional RFB limitations, such as manufacturing and materials costs, energy density or resistive physical barriers.

Membraneless redox flow batteries are one of these remarkable designs that can extend traditional RFB properties. They are defined by their reactor lacking a physical barrier between the two electrolytes, this is removing the ion selective membrane. There are two main strategies for maintaining electrolytes separated even without this barrier, the use of immiscible liquids for the electrolytes and the use of laminar flow.

Immiscible concepts rely on the use of a biphasic system that is constrained by the chemistries used for the redox species and their solvent properties. Therefore, this concept can also be applied to certain chemistries, which excludes for example the all-vanadium one.

Laminar flow allows to create an interface of two liquids through a channel. This interface allows to keep the two electrolytes separated and to dispense with the membrane. Microfluidics operate with laminar flows and is a field that has raised interest and progress in the recent years. Together with advances in microfabrication has allowed to create micro scale reactors and RFB designs without membrane, extending traditional concepts properties. This concept has no chemistries limitations, and although it should be adapted for each specific liquid properties it can be used with the most common species. Such is the case for vanadium that

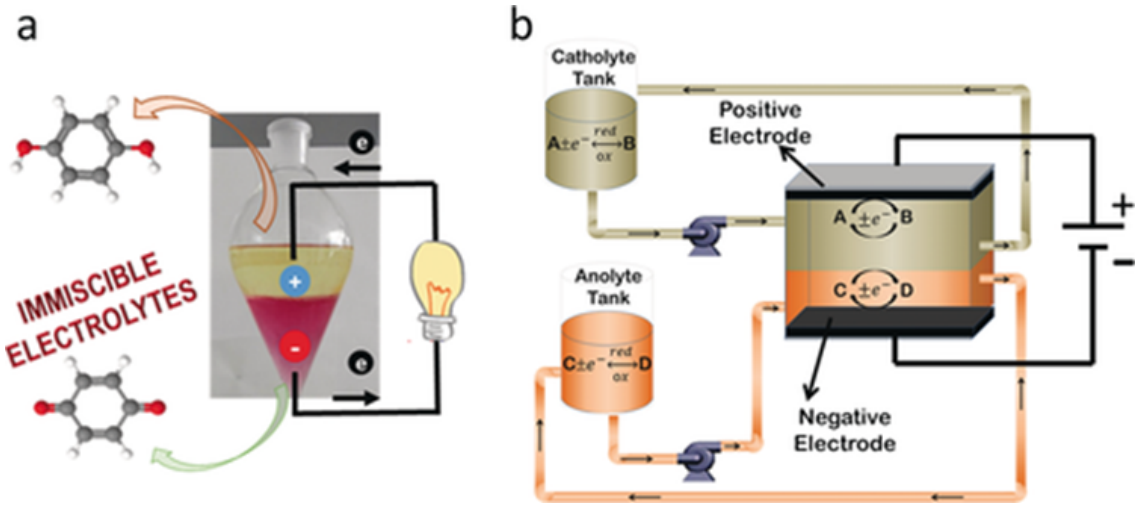

Figure 1.8: a) Schematic representation of a membraneless battery design based on immiscible redox electrolytes b) Membrane-free flowbattery with a horizontal design to favor the formation of the two immiscible phases [38].

is the most extended and is the one used in this thesis.

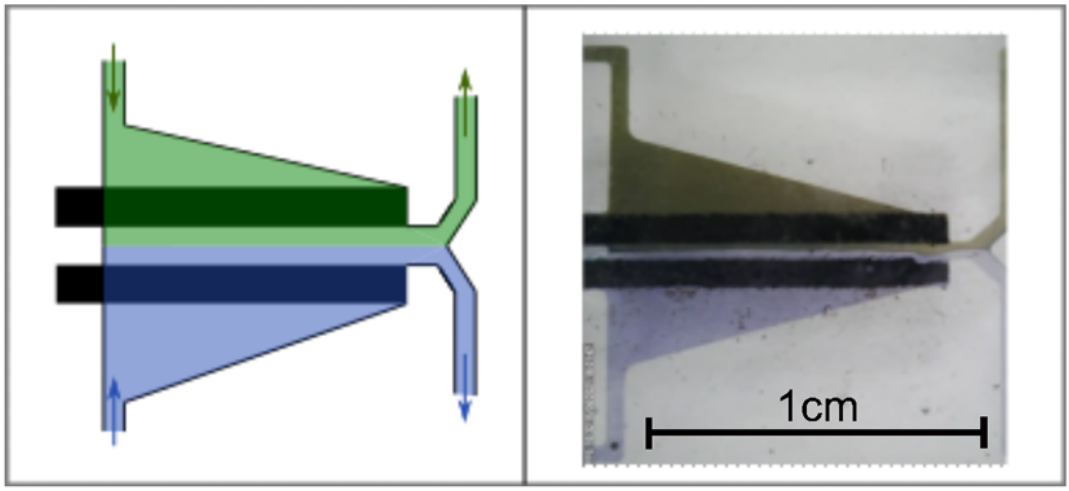

Figure 1.9: (Left) Schematic of the microfluidic reaction cell with electrolytes interface (diffusion is not depicted) and electrodes. (Right) Actual cell during operation.

Microfluidic membranesless RFB benefit from avoiding membrane use, hence, saving the high costs of this element, reducing electrical internal resistance, and increasing power density. Moreover, there are advantages of using a microfluidic scale reactor: higher surface to volume ratio, enhanced mass transport and more flexible design.

It has been mentioned that traditional RFB can be scaled-up for large scale applications. However, scaling down their design for smaller grids integration is more complex. Microfabrication of membranelles reactors can overcome this limitation by reproducing and stacking multiple single simple reactors. It also provides miniaturization and on-chip integration capabilities,

and a simpler and cheaper manufacturing method.

Microfluidic membraneless RFB face some intrinsic problems as diffusive self-discharge and mixing within the reactor, or distribution of the reactants among the stacked cells. However, the factor that has been limiting their performance the most has been the imprecise microfluidic operation. The lack of proper microfluidic instrumentation and complete fluid-dynamics modelling is responsible for this. As it is further reviewed in Chapter 2, state of the art works have been using imprecise instrumentation such as syringe pumps, in an open-loop control strategy that does not allows to adapt liquid flows at the reactor. Obviously, these strategies do not rely on any microfluidic modelling. What is more, proper fluidic operation influence on electric response has not been modelled in previous works. This has caused that it has not been reported before any work that both continuous recirculates electrolytes and is able to make a complete battery operation (charge and discharge).

This works covers the mentioned problematic. Hence, it presents for the first time and electric model, including an equivalent electrical circuit for future integration and an analysis of the fluid dynamic influence on this electric response. It also provides a microfluidic model that represents electrolytes flow within the reactor and their response to active elements instrumentation of the microfluidic circuit. This adaptive model considers inherent microfluidic variability and stochasticity. Finally, it presents several control strategies based on this model to assure that microfluidic operation is optimal for the battery, using the electrical model to analyse quantitatively them.

These efforts have led the project where this thesis takes part to become the first reported microfluidic membraneless complete battery, able to recirculate electrolytes for several charge and discharge cycles.

1.3 Thesis Outline

In summary, the main ideas that motivate this thesis are:

- Climate change and energy transition is accelerating the adoption of renewable energy sources. Wind and solar sources are experiencing the faster increase in their deploy.
- These are intermittent energy sources that need energy storage solutions to synchronize production and demand, stabilizing the grid.
- Redox flow batteries have properties such as power-energy decoupling, high cyclability, low degradation, high depth of discharge, scalability, cost-effectiveness and long cycle life, that make them an excellent solution to work with this intermittent energy sources.
- Redox flow batteries have some limitations such as low energy and power densities that are trying to be extended with different approaches. One alternative concept is membraneless redox flow batteries, which can also benefit from saving material and manufacturing costs.
- Microfluidic membraneless redox flow batteries rely on a precise control of the liquid interface by adjusting the electrolytes flows to keep them separated.

- There are no existing models of the microfluidic dynamics and influence on the electrical response, which has led to inappropriate microfluidic instrumentation use and operation.

The research questions that this thesis tries to solve are:

- is it possible to obtain an equivalent electrical model of these batteries that includes microfluidic influence on its electrical response?
- is it possible to obtain a microfluidic model that reproduces electrolytes flow behaviours in the reactor from instrumentation operation?
- is it possible to design control strategies that optimize microfluidic operation based on previous dynamic modelling and evaluate and compare them with the electrical model?

In this context, this thesis explores a methodology to obtain an electrical equivalent circuit, and electrical and microfluidic dynamic models, design microfluidic control strategies and evaluate their suitability. It is divided in the following chapters:

- Chapter 2 studies the state of microfluidic membraneless RFB, general RFB existing models, modelling identification techniques, and control design methods.
- Chapter 3 explains the system configuration used in this work, and the instrumentation selected. It also explains the electronics development needed for its operation and the hardware and software implementations made.
- Chapter 4 proposes a new equivalent electrical circuit for membraneless RFB. It also analyses the influence of microfluidic operation on three key metrics of the electrical model (power steady state, power dynamics and mixing and self-discharge losses).
- Chapter 5 introduces equations that model microfluidic dynamic response. It proposes an adaptive modelling methodology where these equations are corrected in real time with some factors that account for stochasticity. The real time estimation filter for these factors is also explained.
- Chapter 6 present different control strategies for microfluidic control. It is studied keeping electrolytes at maximum flow renovation, traditional model-free strategies, or advanced techniques using the proposed microfluidic model from Chapter 5.
- Chapter 7 details the performance of the different control strategies, evaluating and comparing them based on the electrical modelling of Chapter 4.
- Chapter 8 summarizes the contributions, future work and the importance of the work presented in this thesis.

Chapter 2

Study of the state of the art

This chapter details the state of the art in the topics concerning this works. Therefore, it reviews the main microfluidic membraneless redox flow batteries, describing their reactor cell designs and their system instrumentation and operation. It also explains existing RFB models, divided in the physical process they represent and distinguishing between microfluidic and traditional ones. Then, model identification techniques are reviewed to show the different available modelling approaches. Finally, there is a discussion of the main control techniques in the literature that can be applied to microfluidic control, whether or not a model is available.

2.1 Microfluidic Membraneless Redox Flow Bateries

Microfluidic membraneless RFB have been a disruptive design that has showed interesting performance metrics at the laboratory scale for the last two decades. Here, it is presented a review of the main works in this technology, explaining how their reactor design, and with special focus on their operation, describing the pumping system (its instrumentation and configuration).

It should be noted that some of the microfluidic membraneless reactors are described as "fuel-cells" even when their chemistry (redox couple species) could operate in charge-discharge cycles. This is because they only use these redox species as fuels that discharge through the reactor in a single pass. They are limited by its own reactor design and mainly by the microfluidic system that is not able to control a continuous recirculation. This is a clear indicator of the need to develop a more precise microfluidic system, including its instrumentation, modelling and control.

2.1.1 Previous Designs: Cell Reactors and Microfluidic System

First Reactor Design with Planar Electrodes (Syringe Pumps at the Inlets)

The first development of a microfluidic electrochemical reactor removing membrane by using flow streams in a laminar regime was presented by Ferrigno et al. [39] in 2002. This development was inspired by the use some years before of these low Reynolds number flow

streams for microfabrication [40]. This first electrochemical reactor used vanadium pair (charged in states 5+ and 2+) as a fuel to be discharged through an "Y" shaped channel with planar electrodes.

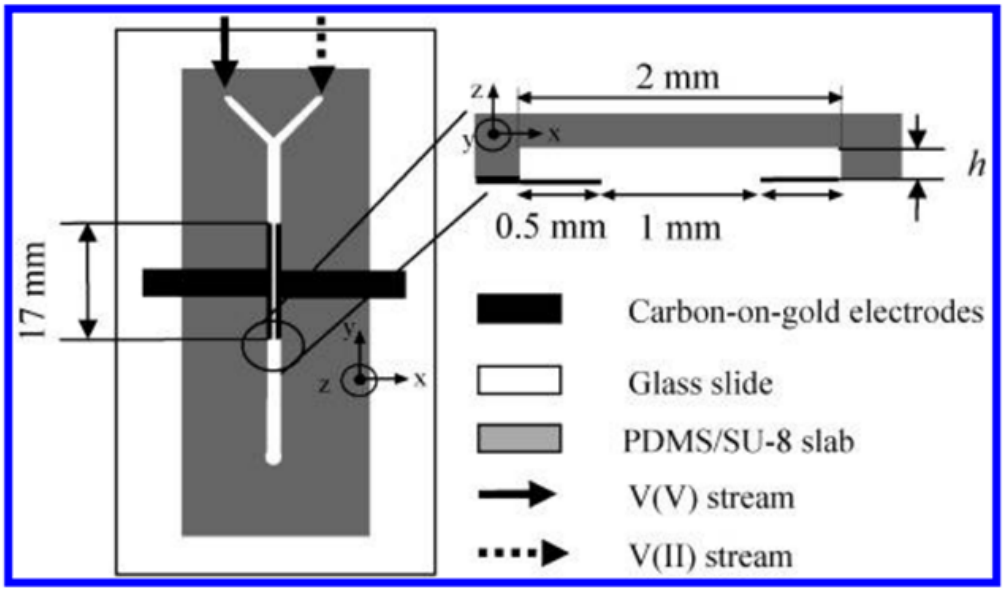

Figure 2.1: Shematic design of the first microfluidic membraneless cell, presented by Ferrigno et al. in [39].

It can be observed that this reactor design mixes the two electrolytes after being discharged through the electrodes. This means it can only be used to discharge and in a single pass, as the amount of charge left after this single discharge is lost when liquids mix at the output. Therefore, although using vanadium as chemistry the scope of the work is only to prove it as a fuel-cell, explicitly explaining that coupled regeneration of the fuels is not demonstrated.

The microfluidic system for this work operation is only described as using alternatively syringe pumps or gravity for injecting the solutions at the inlets. Therefore, there is not any control of the laminar interface and its proper positioning within the reactor. This, together with the use of low active area planar electrodes, makes that using three of these cells only supplies 192mW/cm2, the amount of power used to light a Light Emitting Diode (LED).

Other Design using Planar Electrodes (Syringe Pumps at the Inlets)

Two years later, in 2004, work by Choban et al. [41] used the same "Y" shaped reactor to operate as a conventional hydrogen fuel cell, using formic acid as the fuel. The electrodes were also plain but in this work were catalyst covered. It explained the formation of depletion boundary layers near the electrodes, as well as the diffusional crossover.

Although this design removed all typically associated to the proton-exchange membrane (PEM) as drying out, it questioned the viability for practical applications, due to fuel conversion efficiency and to pumping and recirculation issues. These issues, together with the mentioned depletion and diffusion layers formation, make the authors explicitly highlight the need for

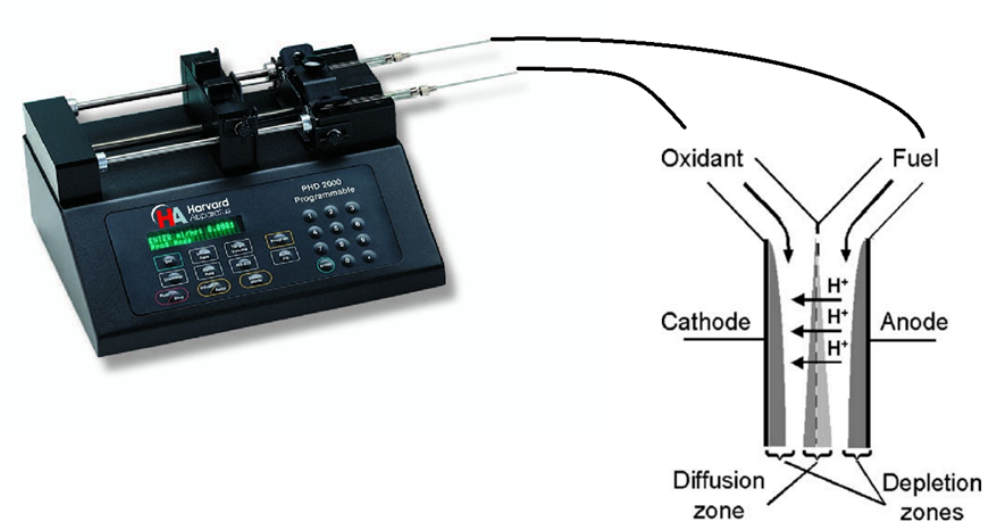

Figure 2.2: Schematic of the membraneless fuel cell [41], with regions of fuel/oxidant depletion and diffusional fuel/oxidant crossover indicated (not drawn to scale). Double syringe pump PHD2000 by Harward Apparatus also represented to show injection at the inlets.

a precise microfluidic control. However, the microfluidic setup only consisted again in the technology available at that time, the use of syringe pumps at a fixed injecting speed in an open loop. They used the model PHD 2000 of Harward Apparatus working 0.3 and 0.8 ml/min.

First use of Porous Elctrodes (Syringe Pumps at the Inlets)

Other remarkable work in fuel cells was [42], in 2005. Although again being adjusted to work as a traditional fuel cell with formic acid, the importance of this design for membraneless microfluidic reactors is being the first to use porous electrodes. Particularly, it used a Gas Diffusion Electrode (GDE) at the cathode, in an attempt to avoid limitations of oxygen solubility in the oxidant. It increased the current density until 130 mA/cm^2 using an "F" shaped reactor where two liquids enter the cell from one side and are mixed at the output, preventing any possible recirculation. The "F" shaped reactor tries to help to avoid that one electrolyte reaches the opposite electrode, as the microfluidic system is limited again to use the same PHD2000 Harward Apparatus syringe pumps.

Graphite Rods within the Channel (Syringe Pumps at the Inlets)

Next development continued with the idea of migrating from planar electrodes to three dimensional structures. This was the case for the first design by Kjeang et al. group [43] where 0.5mm graphite rods formed an array within the cell cavity. There, they were used as electrodes and also as separators as some of them were not electrically connected at the end plate. This central rods space is the path for the co-laminar flows of the electrolytes, that were again vanadium as in the first microfluidic reactor in [39]. This design demonstrated an increase of almost one order of magnitude in power density compared to a planar electrode

design, and reached a 78% of fuel utilization.

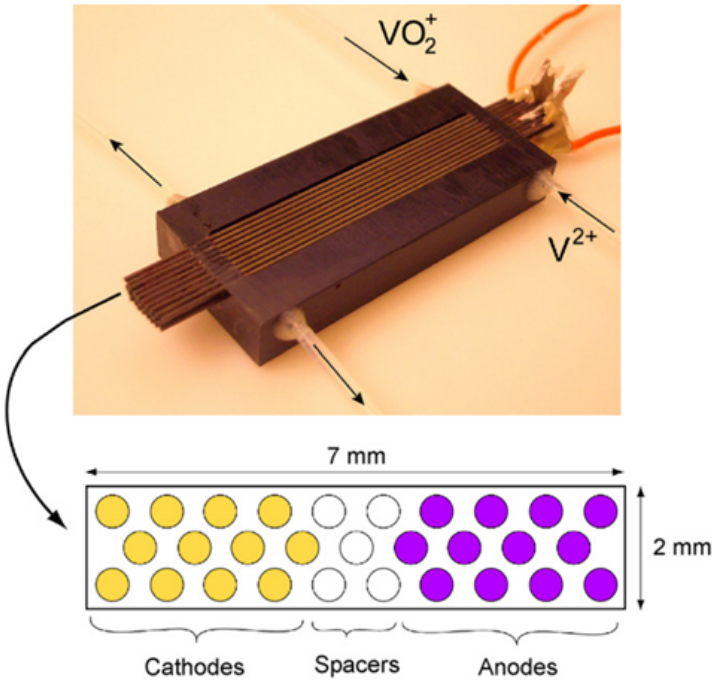

Figure 2.3: Microfluidic membranelss cell with three-dimensional vanadium-based microfluidic fuel cell with the graphite rods architecture [43]

This work microfluidic setup consisted of using again syringe pumps (PHD 2000; Harvard Apparatus, Holliston, MA) and not controlling the electrolytes at the outlets producing their mixture and making recirculation impossible.

Flow-Through Porous Electrodes (Syringe Pumps at the Inlets)

Following this previous work, Kjeang et al. also presented a new design using three dimensional structures, and carbon porous electrodes [44] for vanadium. It was first presented a flow-through design where electrolyte is forced to pass through the porous electrodes before going into the central channel where the liquid interface between them is created. This design allows to avoid concentration boundary problems since electrochemical species are forced to be renewed continuously. It reached an improved power density of 131 mW/cm^2 and a fuel utilization of 94%.

This design was operated using again syringe pumps PHD2000 by Harward Apparatus, flowing in the range from 1 to 300 $\mu l/min$. The microfluidic outlet is again just one evacuating the waste, and therefore it is not possible to recirculate and operate as a battery. However, in this work it was first demonstrated reversible operation by using the pumping microfluidic system in reverse, and proving that waste was converted again to the original charged electrolytes. It reported a current density of 45 $mA/cm2$ in this operation mode, and it explicitly explained that complete integration of regenerative mode and investigation of its roundtrip efficiency *"will require development of supporting infrastructure beyond the scope of this work"* [44].

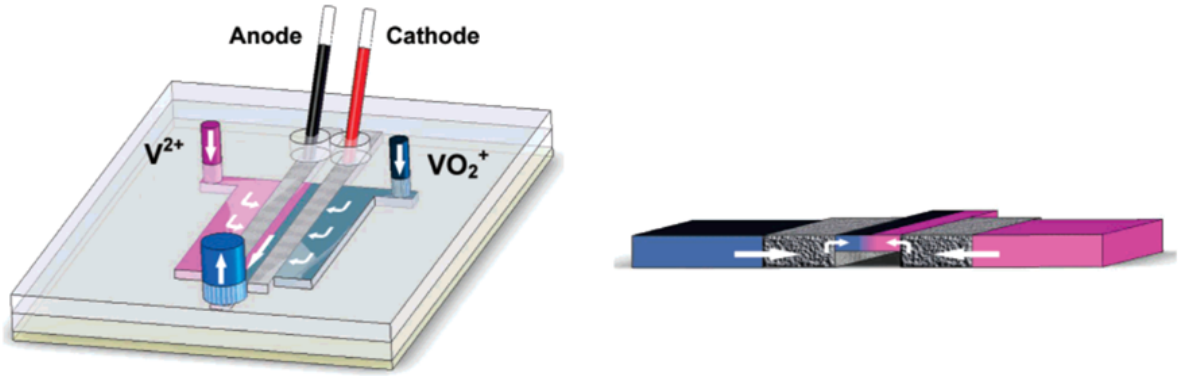

Figure 2.4: Schematics of design and operation (left) of the microfluidic membraneless cell with flow-through electrodes, and cross-sectional geometry (right) of the architecture [44]

Gold Current Collector (Syringe Pumps at the Inlets)

Next work [45] was focused on improving electrical contact of the porous electrodes to the external electrical circuit, specifically using improved gold current collectors for the vanadium microfluidic cell reactor of [44]. The use of this current collector induced to an increase of the 78% in power density, boosted by a decrease in ohmic contact resistance of 7.9Ω.

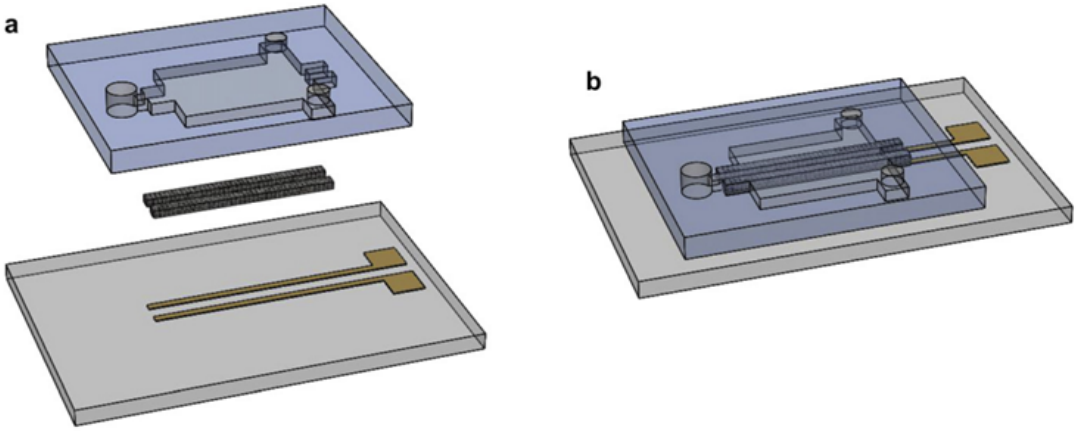

Figure 2.5: (a) Exploded view; and (b) assembly of the proposed microfluidic cell with gold current collectors (not to scale) [45]

There was no improvement in the microfluidic setup of [45], using just a different model of syringe pump (MA1 70-2209, Harvard Apparatus).

First Charge-Discharge Cycle: X shaped cell (Syringe Pumps at Inlets and Outlets)

Improvement in the design and operation that led to the first battery mode operation (charge and discharge) was developed in [46] in 2013. In this work the reactor structure is modified to a dual-pass one where electrolytes go through the porous electrodes two times within the cell.

Also, now there are two outlets so each electrolyte can remain separated at the output. This separation at the outlet, together with the symmetric "X" structure of the cell that make inlets and outlets interchangeable, are key to allow a charge-discharge process. This cycle for the all-vanadium chemistry used is reported to have an efficiency of around 20%, and the power density of the reactor is 300 mW/cm^2.

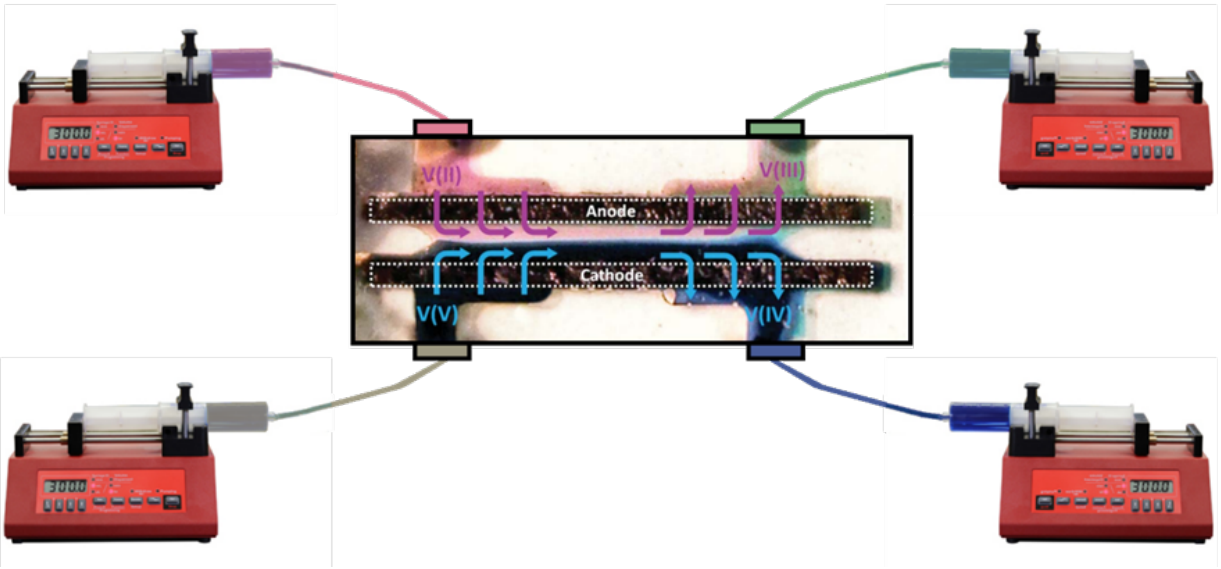

Figure 2.6: Scheme of the microfluidic pumping system and annotated image of the microfluidic redox battery operating from [46] in discharge mode.

The microfluidic system of this work incorporates syringe pumps at the outlets, withdrawing electrolytes separately. This withdrawing syringe pumps work simultaneously with the inlet ones, and when operation changes from charge to discharge the ones injecting start to withdraw and vice versa. This is an approach that allows to use two single-pass operations together to operate like in recirculation, although electrolytes are not really going back to the same tank. Obviously, it is not possible neither to make electrolytes flow through the cell several times for a charge or discharge alone. The use of syringe pumps also has the limitations of adding pulsation to the flow, and working in an open-loop not having feedback of the real flow rate produced. Flow rates used in this work are in the range 1 to 10$\mu l/min$. In conclusion, this microfluidic system and control is still rudimentary and have problems that limit operability and efficiency of the battery.

Design to Enhance Mass Transport (Syringe Pumps at the Inlets)

After this milestone, later designs continued to use the "X" shape for the reactor. This is the case for [47] in 2017, where herringbones pattern structures in the cell channels are used to enhance mass transport. This work also tests new chemistries for the microfluidic design, as organic anthraquinone and iron as electrolytes. It obtained a peak power density of around 24,4 mW/cm^2.

The operation of this design is again as a fuel cell, and therefore it only uses syringe pumps at the inlets, and considering waste at the outlets although there are two of them, one for

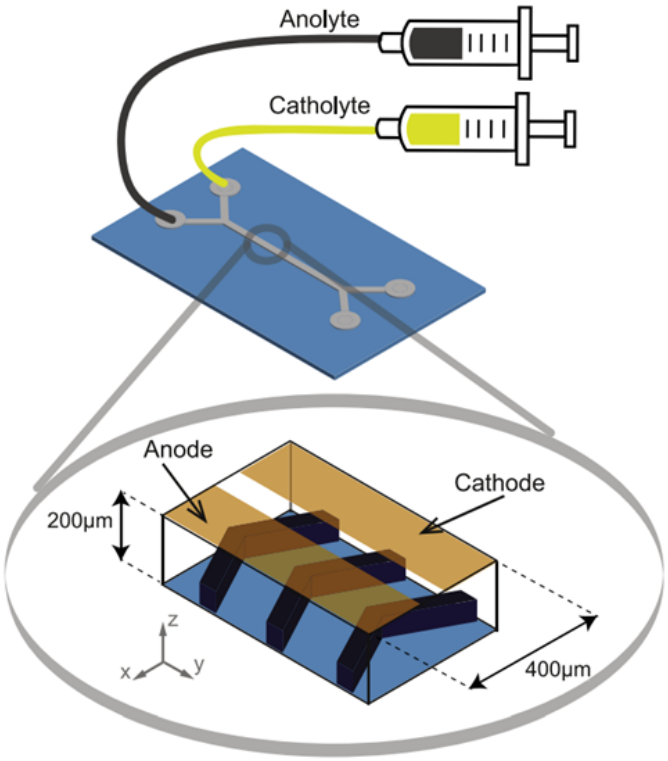

Figure 2.7: Microfluidic setup and cell from [47], with herringbone pattern promoting mass transport, "X" shape cell structure and syringe pumps at the inlets.

each electrolyte. The model used for the syringe pumps are Cetoni neMESYS equipped with two glass syringes (SGE Analytical Science, $25ml$). Flow rates are in the range from 0.48 to $3.6ml/min$.

Other X Cell Design (Syringe Pumps at Inlets and Outlets)

Other contribution is the one presented in 2017 in [48]. This is a continuation of the work from [46], where carbon nanotubes are dispersed in the solution of the vanadium electrolytes, boosting power densities up to $2W/cm^2$. The cell is "X" shape and electrolytes go through the porous electrodes only one time in this design.

This work does not include any enhancement or difference in the microfluidic setup, using the same structure of syringe pumps as in [46]. The model used in this work was Harvard Apparatus MA1 70-2209, with injection and withdrawn operated in unison at flow rates ranging from 10 to $200\mu l/min$. However, this work does not report it usage in charge-discharge cycles, as it is only focused on enhancing discharge power.

Theoretical studies for membraneless microfluidics reactors have also been applied, not covering or giving any information about microfluidic setup, such as in [49].

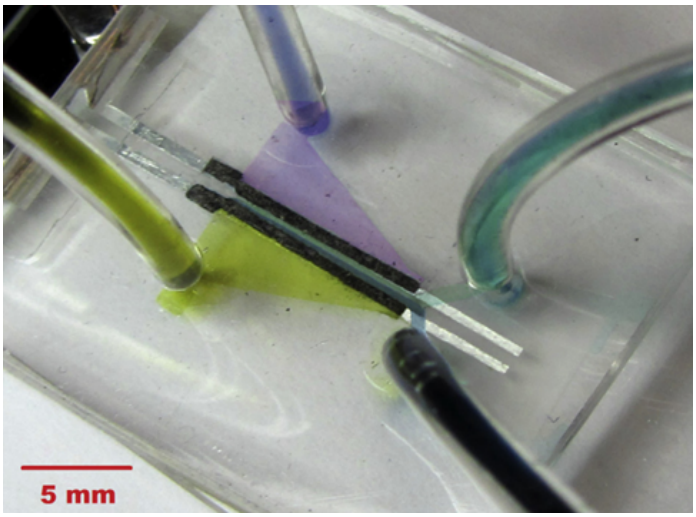

Figure 2.8: Real time image from [48] of the cell discharging the vanadium electrolytes.

Other Chemistries for Flow Batteries (Peristaltic Pumps at the Inlets)

Since the work from [46], there has been other works using different approaches as not using vanadium but other chemistries. This is the example of [50] that uses bromine/hydrobromic acid as the oxidant through a porous media and hydrobromic acid solution flowing through an open channel.

The microfluidic setup of this work does not use syringe pumps but regular peristaltic pumps (Harvard Apparatus, MA), which introduce much more pulsation. Nevertheless, this kind of pump could be used for recirculation, although in this work it was used a single pass for charge and another single pass for discharge. The flow rates used are from 0.6 to $2ml/min$.

Other recent work using other chemistry is [51], consisting in a Hydrogen-Iron battery. In this work one of the reaction components is a gas (the hydrogen), so there is a liquid-gas interphase to control at the cell. This work also uses a peristaltic pump (Cole Parmer Masterflex L/S) for the liquid electrolyte.

Other Microfluidic Reactor Examples (Capillary flow)

Other later examples of microfluidic membraneless reactors worth mentioning are electrolyzers [52], metal-air batteries [53], or paper-based electrochemical flow cells [54]. These designs use capillary forces for self-pumping reactant flows, so the reaction volume is limited by the absorbent pad capacity.

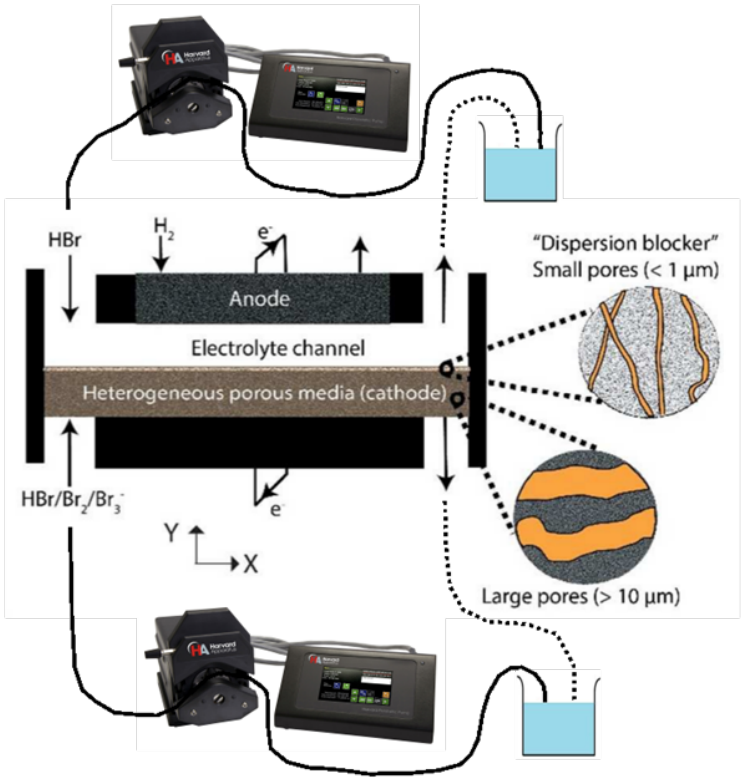

Figure 2.9: Schematic of the flow battery architecture demonstrated in [50], with dotted lines indicating the possibility of using the peristaltic pumps for recirculating.

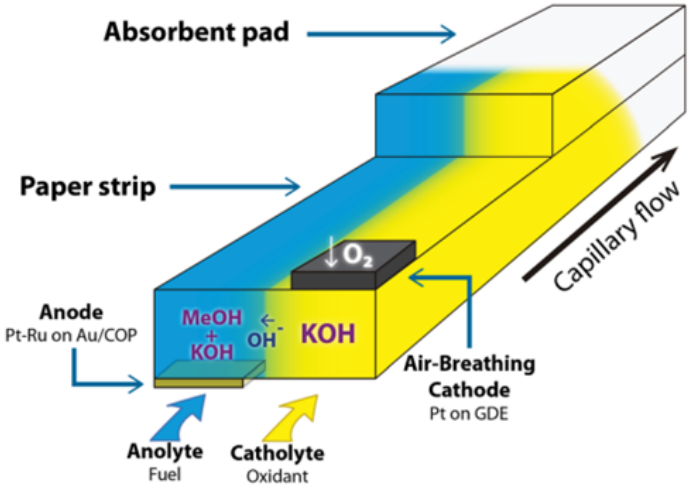

Figure 2.10: Membraneless microfluidic rector used in [54] with absorbent pad to create a capillary flow.

2.2 Redox Flow Batteries Models

Membraneless microfluidic redox flow batteries are complex systems that can benefit from a precise modelling of their processes. In this section, it is studied the existing models in the state of the art, applied to different relevant dimensions of these batteries.

Models refer to microfluidic membraneless works, but there are references to other conventional RFB works in case the discussed dimension has not been thoroughly studied, and these conventional models are the closer examples.

2.2.1 Electrochemical

Battery performance is mainly described by the electrochemical process during charge and discharge, storing and releasing energy in an electrical-chemical energy conversion. Therefore, most of works are focused on this dimension when presenting a new reactor design or demonstrating an enhancement on existing ones.

Here, main used methodologies for these electrochemical models, together with several examples of applying them are described. The main electrochemical processes modelled are fluid flows for concentration profiles, mass transport (species transportation), and the diffusive mixing in self-discharge reactions, which described together can model the electrochemical response of the microfluidic RFB and the evolution of its state of charge.

Fluid Flows for Concentration Profiles

Reactor concentration profiles are usually modelled with a 2-dimensional approximation of the cell geometry. This geometry tries to model the concentration of the species in the liquids interface and at the walls/electrodes where depletion zones appear.

Finite elements methods are used to numerically obtain solutions to the model where analytical expressions for the reactions and the boundary conditions are used. Concentration profiles use fluid flow Computational Fluid Dynamics equations (CFD) for a representation of the distribution of the liquids within the cell.

The equations defining the analytical solution are standard steady-state continuity and Navier-Stokes equations for incompressible flow with constant physical properties.

$$\nabla.\vec{v} = 0 \tag{2.1}$$

$$\frac{\partial \vec{v}}{\partial t} + (\vec{v}.\nabla\vec{v}) = -\frac{1}{p}\nabla p + \frac{\mu}{\rho}\nabla^2\vec{v} \tag{2.2}$$

When porous electrodes are used, the Darcy equation for continuity and momentum becomes relevant:

$$\nabla.p = -\frac{\mu}{K}.\vec{v} \tag{2.3}$$

In these expressions v is the superficial fluid velocity vector, p is the pressure in the liquid, μ is the dynamic viscosity and K is the permeability of the electrode material in the in-plane direction. Some examples of works using this CFD numerical methodology are [49], [55], [56].

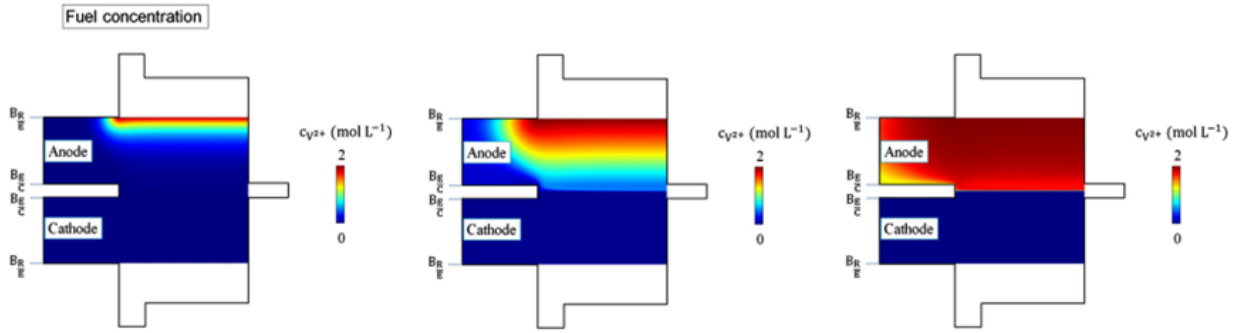

Figure 2.11: Schemes of fuel concentrations profiles at different flow rates from the model from [56].

Mass Transport

Mass transport of the species is modelled expressions that represent diffusion of the species within the electrolytes, its concentration, the velocity components (from the fluid flow model part), and the electrochemical potential from the reaction. These reactions are again for the vanadium case:

$$V^{(V)}O_2 + 2H^+ + e^- \rightarrow V^{(IV)}O^{2+} + H_2O \quad E^0 = 0.99V \tag{2.4}$$

$$V^{2+} \rightarrow V^{3+} + e^- \quad E^0 = -0.26V \tag{2.5}$$

Then, for diffusivity there are more than one option, as the model of diluted species with constant diffusivity, used in [49] and [57], that is based on the statement:

$$v.\nabla.c = \frac{4}{Pe}.\nabla^2 c \tag{2.6}$$

Where c is the dimensionless molar concentration of the species and Pe is the Péclet number. The convection-diffusion equation for each species is defined in works as [58] with the equation:

$$\frac{\partial c_t}{\partial t} = -\nabla - [D_i \nabla c_i + c_i.u] \tag{2.7}$$

where c_i is the concentration of the ith species, t is the time, D_i is the diffusivity of the ith species and again v is the velocity flow field. Then, boundary conditions of the concentration are defined depending on each reactor design, including fixing the constant concentration at the inlets or concentration impermeability at the walls.

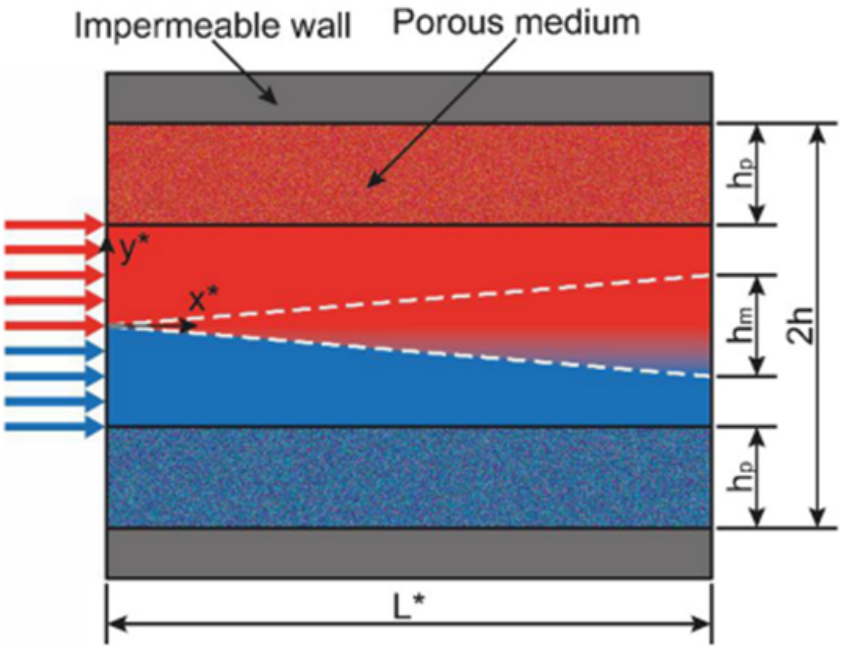

Figure 2.12: Scheme of a reactor with the mass transport of the species represented with colours and distances of the reactor indicated, from [49].

The transportation of mass relies on these convection and diffusion mechanisms, so various approaches benefit from these models to enhance this transport. This may include raising the mean flow velocity and reactant concentrations, minimizing the average distance a reactant molecule needs to travel to reach the electrode surface, or utilizing reactant species with higher diffusivity [59]. In cases where mass transfer is restricted by a depletion boundary layer, this limitation can be rapidly restored by increasing the flow rate, especially in single-pass systems. This higher flow rates also aid in the removal of bubbles. However, there's a limit to increasing flow rates to maintain laminar flow conditions. Fuel crossover can also be analysed, together with its diffusive mixing zone.

Introducing new flow configurations for fluids reaching the electrodes offers an avenue for enhancing fuel utilization and power density within the cell. Several works on mass transport use the knowledge and conclusions from these models to perform a geometry optimization such as in [60].

Diffusive Mixing in Self-Discharge

Estimation for the crossover rates can help complete the electrochemical modelling of the microfluidic membraneless RFBs. These losses can be explained by the combination of active species diffusion and homogeneous self-discharge reactions [61], and some works include this mechanism as part of the electrochemical model.

Diffusive mixing is studied partially when analysing mass transport, but it is usually limited to the charge/discharge associated reactions. Nevertheless, there is a diffusive mixing region between the two laminar flows. For the microfluidic membraneless case, assumptions made

for the conventional models that this self-discharge is instantaneous [62], [63], [64] or is not considered [65], are not enough. Proper modelling of this process can help understand how design and operation can be enhanced.

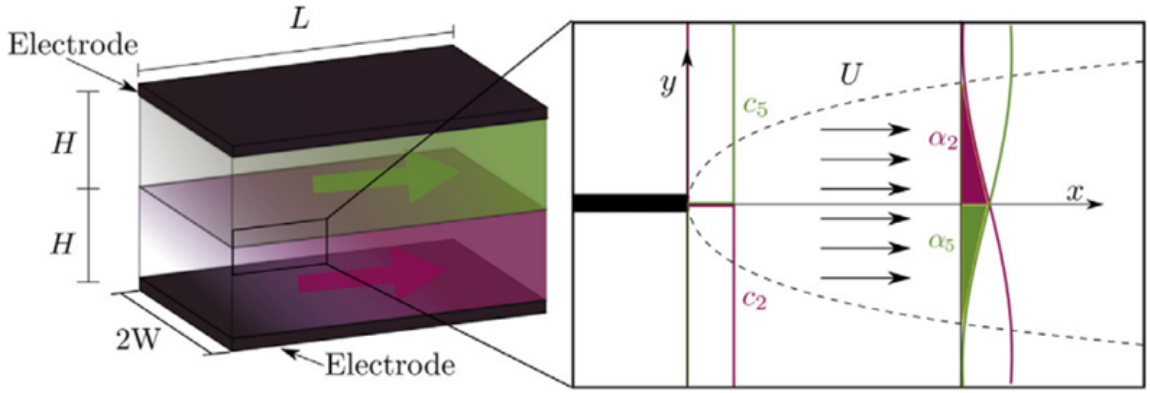

Figure 2.13: Schematic of a reaction cell with planar electrodes and detail of the studied mixing region in a 2-dimensional model in [61], where effects of the self-discharge diffusion on concentration change are indicated.

Experimental measures of the crossover losses have been made in order to complete and validate the models. For example, in [66] experimental measurements were performed to study the viability of the reactant recirculation. These measurements are repeated at different equal inlet flow rates and state of charges. The measurements of the self discharge loss are made using open circuit potential (OCV) values from a saturated calomel reference electrode (SCE, Fisher Scientific) and compared to previously measured titration curves. This OCV measurements have limited precision due to impurities in the reference electrode, temperature variations and the instability of its potential [67],[68].

2.2.2 Hydraulic

This section is focused on the models representing hydraulic behaviour along all the liquid circuit, from the tanks to the pumping method and through the reactor. Note that in previous section electrolytes behaviour within the reactor has been already discussed, but considering ideal flow at the inlets and not disturbances or pressure differences at the outlets.

This topic has not been studied in depth for the microfluidic case, since published works relevance was acquired by enhancing the reactor properties, and consequently the efforts have been made to improve its inside flow distribution. Models considering how the pumping system can help to maintain this proper distribution have not been reported previously.

However, for any device that uses pumping liquids, as any RFB, pumping power and active fluidic modelling are very relevant. Conventional RFB models are the most similar reference available, so they are used for these state of the art description when microfluidic membraneless are not available.

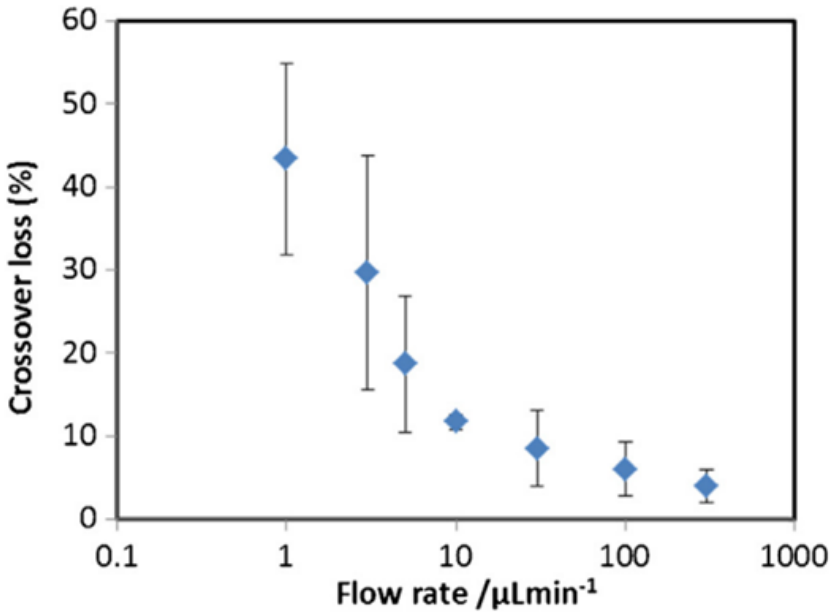

Figure 2.14: Experimental measurements of the self-discharge losses from [66], at different equal inlet flow rates from 0.1 to 300 $\mu L/min$ and at 90% states of charge.

Pumping Power

Pumping power models use pressure drop metrics and pumping power curves for modelling power consumption and optimization. Microfluidic membraneless RFB works have studied the first ones, pressure drop of the cell and how it changes in its different designs. Specifically, it has been analysed in the context of using porous materials for the electrodes [69]. In this work, a channel width optimization of pressure drop losses versus ohmic electrical losses between electrodes is also given.

Equations defining pressure drop are Navier-Stokes (2.2) and the Brinkman equation, that states:

$$\rho(v.\nabla)v\frac{1}{\epsilon^2} = -\nabla p + \frac{\mu}{\epsilon}\nabla^2.v - (\frac{\mu}{K} + \beta\epsilon\rho\,|v|)v, \qquad \beta = \frac{c_i}{\sqrt{K}} \tag{2.8}$$

where, v is the superficial flow velocity, p is the pressure, ρ is the density, μ is the dynamic viscosity, ϵ is the porosity, K is the permeability of the porous medium, and C_i is the concentration of the ith species (mol/m^3). Therefore, it can be deduced that the power loss due to the pressure drop of the porous media is:

$$P_{pd} = \frac{\mu A\,|v|^2\,h}{K} \tag{2.9}$$

where $|v|$ is the average velocity of the reactant entering the porous area, A is the cross-sectional area of the channel/porous electrode, and h is the length of the channel. Nevertheless,

microfluidic works do not include in the model the active pumping element curves, that typically show a non-linear relationship between its power consumption and the pressure drop power to push. This is obviously highly dependent on the chosen pumping system and the active elements, which as it has been discussed has been typically syringe pumps that are not a valid solution for recirculating circuits.

Conventional batteries have studied abundantly this pumping losses including the real pump power, with its performance curves and efficiency taken into account to make economic cost estimations [70], [71].

Fluidic Control of Active Elements

For the membraneless microfluidic case, as it has been explored in the state of the art section dedicated to its previous developments, microfluidic operation has been based in open loop operation of pumps, with no model or feedback of the actual flow rates through the cell. Also, analytical electrochemical models considered flowrates at the inlets and outlets ideal, with no deviation to the desired setpoint and no pulsation. However, it is known that microfluidics requires precise control of its active elements to obtain this proper operation, and that is subject to high variability and stochastic processes [72], [73]. Consequently, for a precise operation in recirculation of reactants electrolytes, with charge and discharge cycles of a microfluidic membraneless RFB, fluidic dynamic modelling of the behaviour of the microfluidic active elements and its effect in the cell response are needed. This is one of the motivations and contributions of the current thesis as it is explained in subsequent sections.

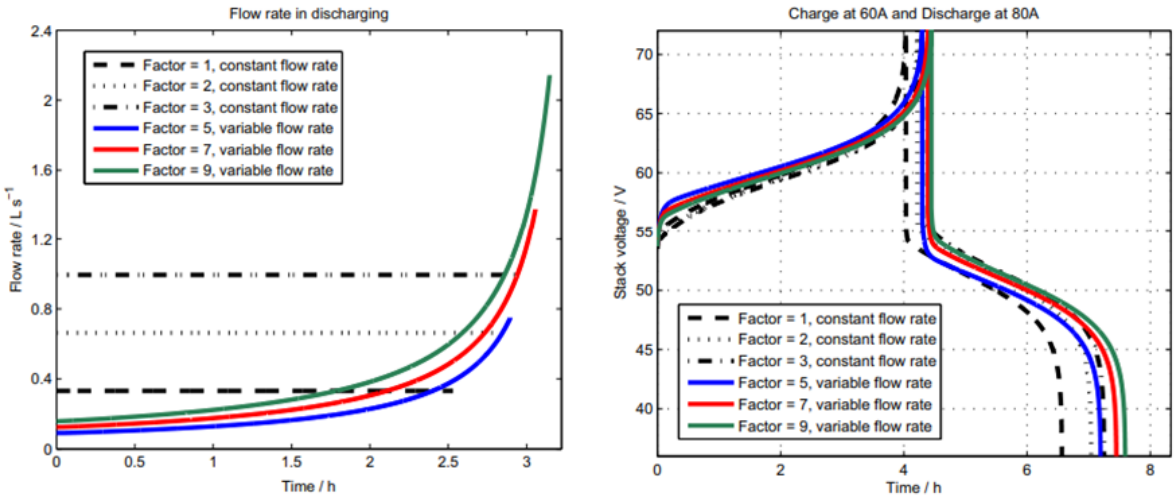

Figure 2.15: Charts from [74] demonstrating battery performance enhancement from flow rate variable operation. (Left) Different constant and variable flow configurations. (Right) Charge-discharge reactor voltage versus time for different flow rates.

Conventional RFB use a membrane to keep electrolytes separated in the cells, however it is still important as in the microfluidic case to control pressure of the pumping system to make sure crossover is minimized (small volumes that cross the membrane are increased with higher pressure differences), avoid damage in the membrane and specially to optimize

pumps consumption. Therefore, model of this fluidic response has been done and there are conventional works available as the only reference in literature. However, these models are not control oriented, but more focused on power optimization. This is due to the difference between conventional and microfluidic operation requirements, as large-scale RFB flow operation can operate without precise control and models, and microfluidic reactors need very accurate ones.

For example, in [74] it is studied how adapting the flow rate actively can improve not only power consumption but also cell performance, concluding the importance of a sophisticated flow control system even for large-scale RFB. Similarly, in [75] a dynamic model strategy for adapting the flow rate during operation is presented to optimize the power losses during varying charge and discharge conditions.

Other example for conventional RFB is [76], where a hydraulic model including pumps operations is presented in an space-state representation together with the thermal response.

2.2.3 Thermal

Microfluidic membraneless RFB properties make them suitable to remove heat by flowing the electrolytes through the area to cool down. This idea of using the electrolyte has both an energy carrier and as a coolant has been explored in some works [47],[77],[78], which are oriented to its integration with electronic microprocessors that can benefit from both uses. In these works, a study of the electrolytes specific heat is performed to estimate the overall heat removal capacity.

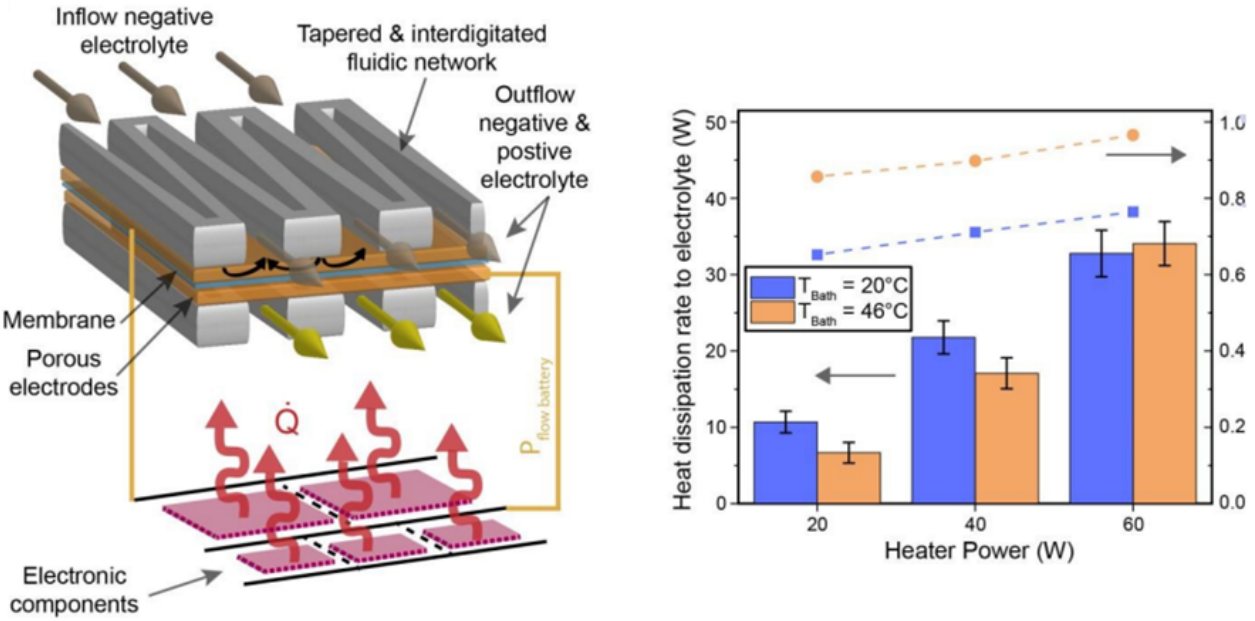

Figure 2.16: Figures from [78], where the microfluidic RFB with heat dissipation concepts is represented (left) and the relationship between heat dissipation and power delivered is plotted (right).

Conventional RFB have made more exhaustive studies including thermal models as part of the

hydraulic and efficiency analysis, and also as an electrolyte temperature estimator [76],[79].

2.2.4 Electric

Before this thesis work there was not any existent model including the electrical response or an equivalent electrical circuit for future integration of the microfluidic membraneless RFB, since these devices where still in a research stage where efforts where focused on improving the reactor response. Hence, one of the main contributions of this thesis has been to propose the first electric model for this battery type, including an equivalent electrical circuit and an analysis of the microfluidic operation on it.

In order to make a study of the most similar existing electric models, works on conventional RFB are presented. Equivalent circuit models of several references are presented below, considering the structural differences with microfluidic membraneless designs.

One of these conventional models is [80], where the electric circuit includes elements including voltage source representing cell power depending on State Of Charge (SOC), current sources that are equivalent to diffusion and shunt losses, two set of impedances representing each half-cell physical structure, and an auxiliar model that derives part of the output power to the pumping system and correlates it with the SOC.

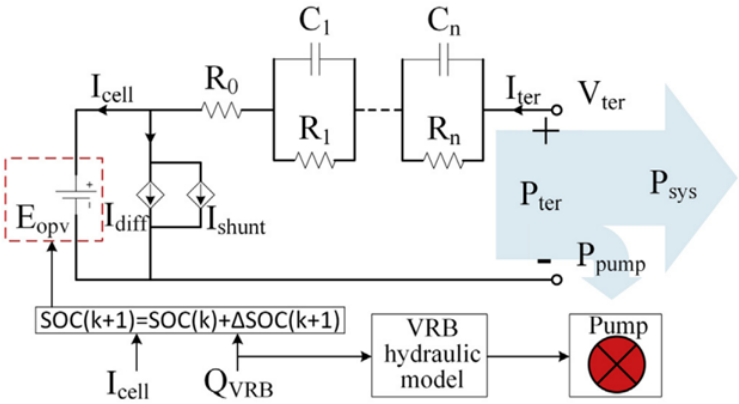

Figure 2.17: Electrical equivalent model from [80].

Similar to this model, in [81] it is proposed an equivalent circuit that modifies the two current sources with one resistor and one current source accounting for all parasitic losses, also changing the disposition of these loads, and joining the sets of resistances and capacitors for each cell in just one equivalent set.

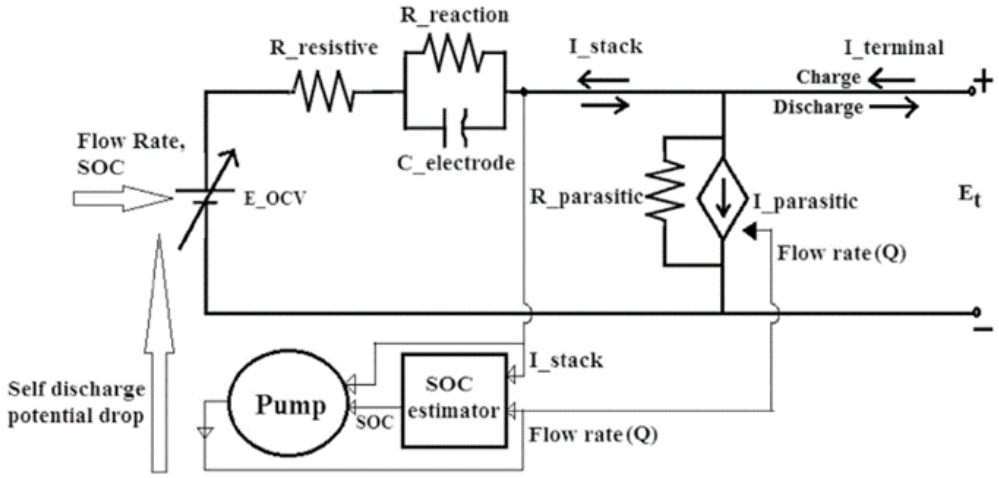

Figure 2.18: Electrical equivalent model from [81], with two half cells equivalent impedances joined in one equivalent group, and parasitic loads represented with one resistance and current source.

In [82], diffusion and shunt losses are not represented with current sources as in [80], but with resistances. Also, this works couples the electric circuit with a thermal model that modifies the voltage source that depends on the cell SOC and temperature.

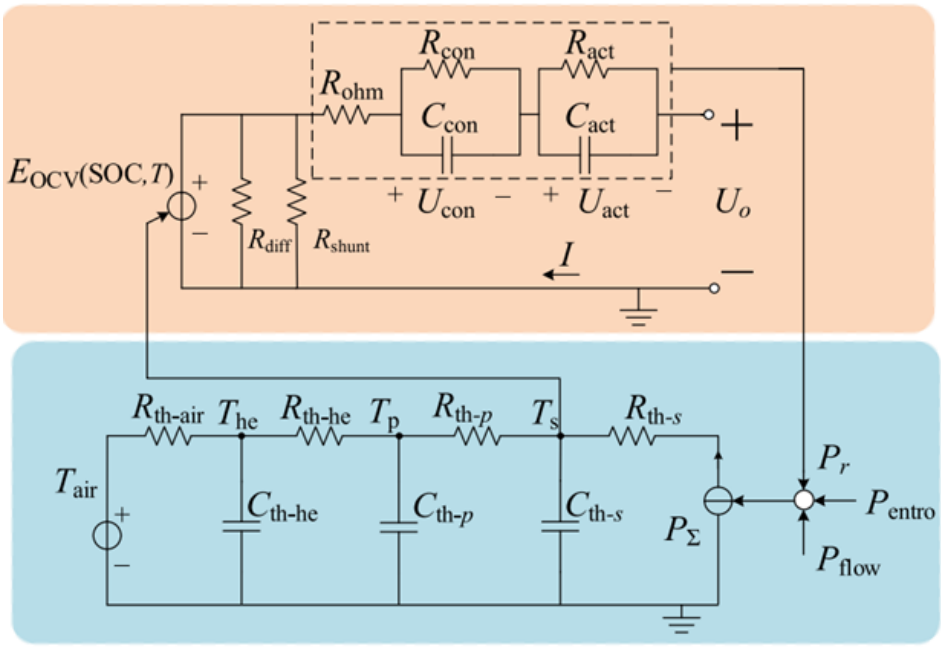

Figure 2.19: Electric and thermal coupled models from [82].

A simplified stack electric model is presented in [83], where a simple cell equivalent circuit is repeated the same number of times as the number of cells there are.

In [84], a different approach is presented. As seen in 2.21, U_d is the open-circuit voltage of the cell, i_d is the terminal current, i_{pump} is the pump current equivalent source, V_{stack} is the stack

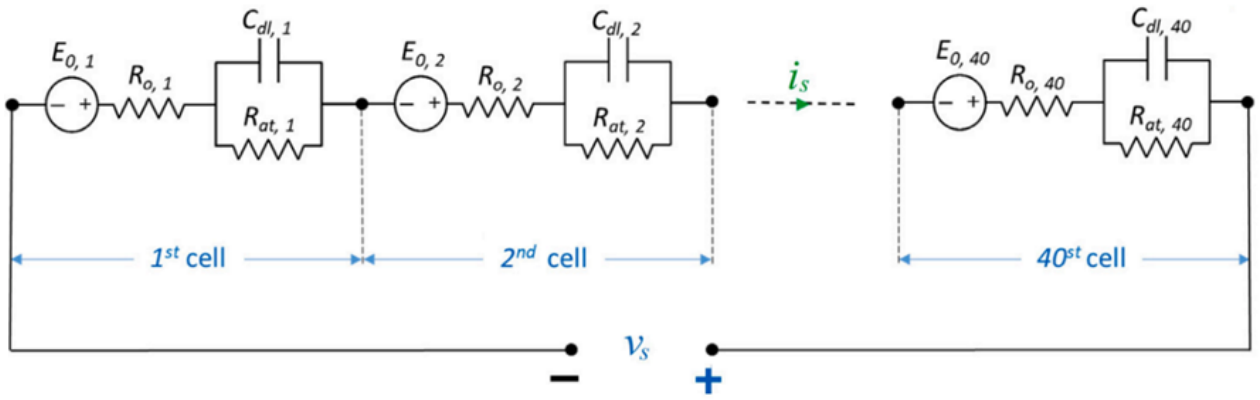

Figure 2.20: Stack electrical model from [83] where a simple cell equivalent circuit is repeated.

voltage, C_{elec} is the dynamic response capability, R_{reac} is the resistance caused by reaction kinetics, R is the fixed resistance losses, and R_{res} is the resistance caused by mass migration, membrane, electrode, and bipolar plate.

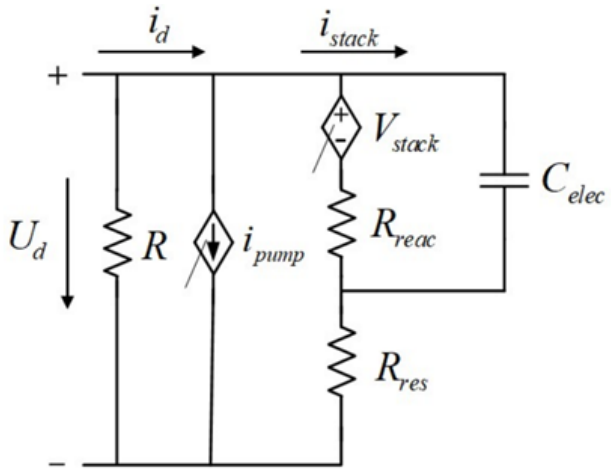

Figure 2.21: Equivalent electric circuit from [84].

Finally, the last presented model is [85], where self-discharge and shunt losses are represented again as current sources, and internal cell resistance with R_{SOC}. The set of impedances also includes a resistance R_{CTR} standing for the charge transfer resistance that can simulate electrode degradation.

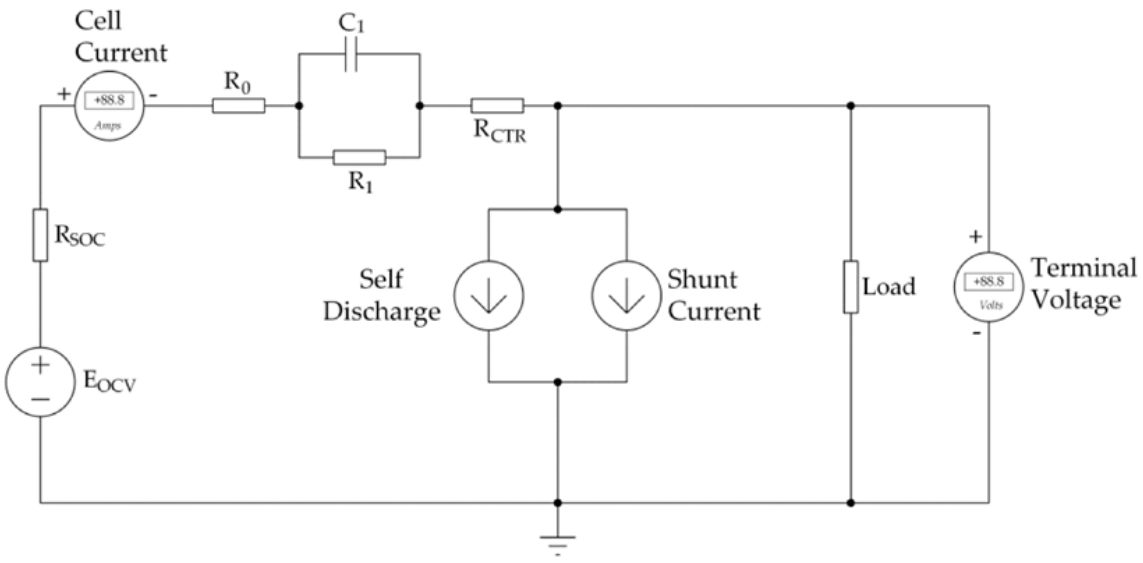

Figure 2.22: Equivalent electric circuit from [85] for the battery, with load connected and indications for where terminal voltage and cell current are measured.

2.3 Model Definition and Identification Techniques

Modelling can be divided using several different types of categorizations. For physical system modelling, it can be classified depending on the prior knowledge about the system and the experimental data used. This criterion is the one used for explaining the different possible approaches to be applied to the microfluidic membraneless RFB. It is also important to introduce the existing methodologies for real time adaptation of the system model, this is filters and estimators to adjust the parameters or structure of the offline defined expressions.

2.3.1 Analytical Models

Classical definition of a system comes from using all available knowledge from the system internal principles and defining all physical processes that are responsible for the system behaviour. Therefore, system's physics laws, principles, and governing equations are explored, and an analytical solution is proposed. They are also called white-box or transparent models. White box modelling aims to provide insights into the inner workings of a system and is often used for in-depth analysis, optimization, and understanding causality.

This approach can be applied to multiple dimensions of the system, and often requires the integration of more than one of these dimensions due to the coupling of the physical processes involved. All previous existing model described in Section 2.2 used this approach to explain at low level system processes, and as it could be deduced they are applied to electrochemical dimensions, hydraulic, electrical, thermal, etc; or to more than one simultaneously (electrical-thermal [82]). These models are transparent in that they provide a clear understanding of how different factors contribute to the system's behaviour. Also, this prior knowledge can be

extract backwards from relationships and equations used in the model, as they are explicitly known and understood.

Although it is based on fundamental principles, it may still involve simplifications and assumptions to make the model mathematically tractable. Including all involved processes would make the model not manageable, so boundary conditions are defined. These assumptions need to be carefully considered for their impact on model accuracy. Other limitation is that they can become complex, especially for systems with intricate interactions and nonlinear behaviour. Simulating them may require extensive computational resources, depending on the complexity of the equations involved.

They can provide accurate and precise predictions when the underlying principles are well understood. However, they are still highly dependent on the assumptions made, and the fidelity of the underlying physics. As in any model they can not represent precisely real behaviour if input data has noise in the measurement or is biased.

White box models applicable when a deep understanding of the system's behaviour is required or defined mathematical equations want to be evaluated. They can be used to gain insights on the working principles, perform sensitivity analyses, or optimize designs.

2.3.2 Blackbox Model Techniques

Opposite to the analytical approach, blackbox model techniques are based on available data from the real system. In this approach, the internal workings or mechanisms of the system are not explicitly known or modelled. These models use data to fit a mathematical structure that should reproduce the output of the system when it is excited with the same input. Hence, there is not any internal knowledge of the system that is reproduced in the internal model definition, but it is just acting as a black box that provides the desired output for the specific inputs. It captures the relationships between inputs and outputs without understanding the underlying processes.

It is a strategy that has been used in various fields beside modelling, including machine learning, deep learning and data analysis and classification.

It relies heavily on data, and the real experiment performed to collect it. The obtained dataset contains input-output pairs from the system working in the regions to be modelled. The mathematical representation should describe patterns, trends, and relationships in the data that can be used to make predictions or decisions reproducing real system behaviour.

Unlike analytical descriptions, black box modelling does not aim to understand or represent the internal mechanisms of the system using equations or known principles of its mechanisms. It's just concerned with mapping inputs to outputs. However, they can capture complex and nonlinear relationships between inputs and outputs that might be difficult to represent analytically. This makes them suitable for systems with intricate interactions.

Black box models can handle diverse types of data and problems. They can be applied to a wide range of problems and domains, and they are not constrained by the need for explicit expert or physical laws knowledge.

Nevertheless, this opacity in their internal structure can be a problem when it is desired any interpretability. Their lack of transparency makes it challenging to explain why a certain output response was made.

Other problem, common to machine learning or any data driven fitting algorithm, is the possible overfitting. This happens when the model is configured to fit perfectly the experimental provided to it. This can lead to measurement noise reproduction in the model, becoming a high order dimension model that is too flexible and reproduces not desired patterns, and makes the model bad for generalization. It can be reduced with regularization of the data, and proper dataset selection, that cover all the workspace and divided for cross-validation. Therefore, these models heavily rely on data quality, as inaccurate or biased data can lead to misleading results, and its previous treatment and selection.

The mathematical structure for the model can vary. Some of the commonly used are:

- Transfer Functions: Expressions in the Laplace domain that are ratios of polynomials relating the output to the input in a linear time-invariant system. Their structure is defined by its number of poles and zeros, and then the blackbox model identifies their values.
- Polynomial Models: Simple polynomial equations can be used. to capture relationships between variables. The polynomial order is defined and then the value of each term is identified.
- State-Space: These representation takes system in terms of state variables, input, and output. The, the relation matrices are identified in the blackbox algorithm.
- Differential Equations: Differential equations describe how variables change with respect to time or other variables and their derivatives. The order of the equations is defined previous to the identification of the parameters.
- Difference Equations: Similar to differential equations, but used in discrete-time systems instead of continuous time.
- Auto-Regressive (AR) Models: A type of time-series model where the output variable is modelled as a linear combination of past outputs and inputs. The polynomial order is defined and then identified.
- Moving Average (MA) Models: Another type of time-series model where the output depends on a linear combination of past output errors and input errors.
- Auto-Regressive Integrated Moving Average (ARIMA) Models: Combines AR and MA models with differencing that can handle non-stationary time-series data.
- Neural Networks: Artificial neural networks are used for linear and nonlinear system identification. The structure of the network and number of neurons is defined and then trained with a back-propagation algorithm.
- Nonlinear Differential Equations: For systems where linear models are insufficient, nonlinear differential equations can capture more complex behaviour.

- Wiener, Hammerstein, and Wiener-Hammerstein Models: They consist of the combination of simpler linear and nonlinear models to compose a structure that represents a more complex nonlinear system. They can be a nonlinear model followed by a linear model, a linear model followed by a nonlinear one, or a structure of a linear-nonlinear-linear models respectively.
- Time-Delay Systems: System that incorporate delays to reproduce inherent time delays in their responses.

Also, partial models can be combined to cover different working points, using fuzzy logic, polytopic structures or other aggregation operators that follow rules or conditions to decide with of the single model of combination of them are applicable every instant.

After the model structure is defined regression algorithms are used for the identification of the parameters. Depending on the structure or other desired properties of the identification some of the algorithms are: linear regression (least square method [86]), generalized linear models (Gaussian [87], Poisson [88]), nonlinear regression [89], regularized regression (Lasso, Ridge, Elastic Net) [90], kernel regression [91], Support Vector Regression (SVR) [92], Partial Least Squares (PLS) regression [93], neural network regression [94].

2.3.3 Greybox Model Techniques

Greybox modelling is an intermediate solution between the analytical and blackbox model. In this solution, some knowledge of the system is used and expressed in the mathematical equations of the system and is corrected or completed with data driven identification.

Analytical model can be limited or imprecise for several reasons, as it was discussed in its previous section. Therefore, completing the model for the unknown physical processes, hidden variables that are approximated with new expressions, or parameters identification of properties that are not accessible, can be very useful for many real practical systems [95].

Grey box models can adapt to different levels of available information. They can start with a basic understanding and refine the model as more data is collected. They strike a balance between the complexity of analytical box models and the flexibility of black box models to capture intricate patterns. It also allows to leverage both domain expertise and data-driven insights to create models that lead to better results than both approaches.

There are several ways for combining both sources of knowledge: physical laws and data. One classification of them is provided in [96]:

- Constrained black box: It uses a black box identification where specific parameters are constrained based on physical laws and known relations.
- Semi Physical Modelling: It uses of physical insights to transform the input and outputs variables to new variables where the regression is applied.
- Mechanistic Modelling: Starts from fundamental knowledge of the process and then some of the parameters are unknown and are estimated from experimental data. In some cases, not only parameters but also some of the structures are redefined.

- Hybrid Modelling: It is the combination of analytical and blackbox models. The configurations can vary: serial, parallel or a combination of them.
- Distributed Parameter Modelling: Spatially distributed phenomena are important in many chemical and biochemical processes, and include for instance any process involving mass or energy transport by convection or diffusion. For such processes, a priori knowledge will result in a model structure involving partial differential equations (PDE).

Greybox models use all the mathematical structures and regression algorithms already cited for the blackbox case.

2.3.4 Real Time Filters and Estimators

Estimators and filters are crucial components in real-time correction of models to adapt and update them based on incoming data. These techniques are often used to improve the accuracy of predictions and ensure that the model remains relevant as new information becomes available. They can be necessary due to model imprecision or to correct parameters or condition that change over time in a stochastic or unpredictable way.

The primary objective of the estimation task is to reduce the error associated with state or parameter estimation, all while maintaining resilience in the face of uncertainties and disturbances. These uncertainties and disturbances naturally emerge during the measurement process, stemming from instruments and environmental factors. System uncertainties, on the other hand, typically are caused by inaccuracies in process modelling, approximations, nonlinearity, and variations in the physical attributes of the system.

There are plenty of filters and estimating algorithms that can be used for real time correction, as discussed in [97]. Some of the most common are detailed as follows. The choice of estimator or filter depends on the specific characteristics of the system, the available data, and the requirements of the real-time correction process. Each technique has its strengths and limitations, and selecting the most suitable one requires careful consideration of the application context.

Bayes Estimator

Bayes estimator involves using prior information, often represented as a prior probability distribution, to make inferences about unknown parameters in a statistical model based on observed data. Bayesian estimation incorporates prior knowledge, handles complex models, and quantifies uncertainty in parameter estimates. It provides a principled framework for making statistical inferences that goes beyond point estimates and probability values, allowing for a more complete understanding of the uncertainty inherent in modelling [98].

This prior information, knowledge before observing any data, is quantified in the form of a prior probability distribution. The prior distribution encapsulates beliefs, assumptions or uncertainties about the parameter's possible values. Then, a likelihood function that represents the probability of observing the data given different parameter values is formulated.

Bayes' theorem is used to relate the prior distribution, the likelihood function, and the

posterior distribution. It is expressed as:

$$P(\theta|x) = \frac{P(x|\theta) \cdot P(\theta)}{P(x)} \tag{2.10}$$

$P(\theta|x)$ is what we want to estimate, the posterior distribution of the parameter θ given the observed data x. $P(x|\theta)$ is the likelihood function, representing the probability of observing the data x given a specific value of the parameter θ. $P(\theta)$ is the prior distribution, representing your prior beliefs about the parameter θ. $P(x)$ is the marginal likelihood or evidence, which acts as a normalizing constant.

Finally, the posterior distribution is the updated probability distribution of the parameter of interest after observing the data. It can be used to obtain point estimates and measures of uncertainty for the parameter. The process is repeated iteratively.

Recursive Least Squares (RLS)

It is a method that also updates model parameters iteratively, adapting to changing data. It's useful when the model parameters themselves change over time. It estimates the parameters of a linear model in the form:

$$y = X\theta + \epsilon \tag{2.11}$$

Where y is the observed data or output, X is the matrix of input features, θ is the vector of unknown parameters to be estimated, and ϵ represents the error or noise.

RLS estimator processes data sequentially and updates parameter estimates at each time step. It maintains an estimate of the parameter vector θ with new data measurements. At each time step the RLS algorithm performs a prediction of the next observation based on the current estimate and a correction updating the estimate based on the prediction error (the difference between the predicted and observed values) and the information from the new data point.

The recursive formulas to update the estimate are designed to minimize the mean squared error of the estimates [99].

Wiener-Kolmogorov Filter

This estimator aims to extract an estimate of a signal sequence from an observable data sequence. It is oriented with the goal of minimizing the mean square error between the estimated signal and the true signal.

It's a linear filter that operates in the frequency domain. It uses the power spectral densities of the signal and noise to determine filter coefficients that optimize the trade-off between noise reduction and signal preservation [100].

The Wiener-Kolmogorov filter is typically non-recursive or non-sequential manner, it doesn't inherently maintain memory of past observations. It was the historical predecessor of the Kalman Filter.

Kalman Filter

A widely used recursive algorithm that estimates the state of a dynamic system while accounting for measurement noise, combining predictions from a system model with real measurements to provide optimal and continuously updated estimates.

The state represents the system's current condition or configuration and the prior knowledge about its uncertainty. Then, the prediction step, a known mathematical model of the system's dynamics predicts how the state will evolve from the previous time step to the current time step. It also estimates its uncertainty. In the update step, measurements from real data are made, the predicted state with the actual measurements are compared and the state estimate adjusted. At this step the estimate of uncertainty is also updated. It works recursively, continuously updating the state estimate with new measurements, and maintaining a running estimate of the state and its uncertainty.

In the prediction and correction steps, the filter minimizes the mean squared error of the state estimate, making it an optimal estimator.

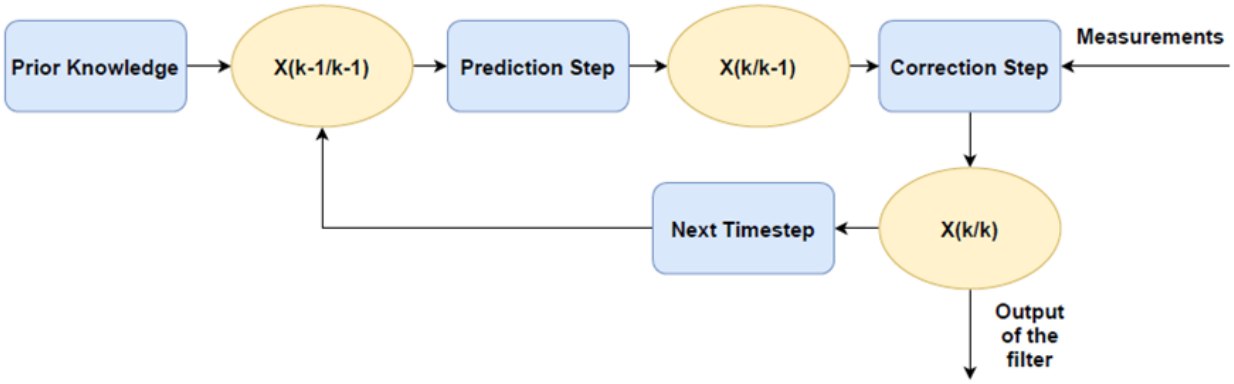

Figure 2.23: Kalman Filter scheme with state X at different time steps (k, k-1).

Extended Kalman Filter (EKF)

It is an extension of the Kalman filter to be used with nonlinear systems by linearizing the system dynamics around the current estimate. EKF takes dynamic nonlinear equations and calculates its linearized jacobian matrix, that is used in the prediction and correction steps, and allows to use the same mean square error optimization as in the regular Kalman Filter [101].

Unscentend Kalman Filter (UKF)

Another extension of the Kalman Filter that tries to reproduce the system nonlinearity using the unscented transform for substituting linearization with this sampling technique [102]. It is useful for system that need to reproduce strong nonlinearities, where this methodology tries to preserve mean and covariance of the nonlinearities.

Particle Filter (Monte Carlo Filter)

This filter estimates the state of the system by representing it with a set of particles or samples. Each sample represents a possible value for the state. It is a probabilistic estimation that maintains these several states using Monte Carlo methods [103]. It propagates them (the equivalent to the prediction for a single estimation), and then in the correction step weights each state depending on how different to the real measurements is each one. For the next step a resampling is made, emphasizing particles with higher weights and discarding the ones with lower performance.

H_∞ Filter

This approach is specifically designed to deal with the possibility of an imperfect model, by minimizing the effects of the worst-case scenario of disturbances and uncertainties. While the workflow is again like the one described for the Kalman Filter, but the function to minimize is not a least square error, but instead is the H_∞ norm. The function to minimize, as in [104], is defined as:

$$J^* = \min_{(\hat{x}^k)} \max_{(x^0, w^k, y^k)} J \tag{2.12}$$

$$J = \frac{\sum_{k=0}^{N-1} \|z_k - \hat{z}_k\|_2^2}{\|x_0 - \hat{x}_0\|_2^2 + \sum_{k=0}^{N-1} \left(\|w_k\|_2^2 + \|v_k\|_2^2 \right)} \tag{2.13}$$

where the tracked target is Z_k, and its estimated value is $\hat{z}_k$, x_0 represents the initial state, and $\hat{x}_0$ denotes the estimation of x_0 . Then, w_k and v_k are the input and measurement noises respectively.

Variable Structure Filter (SVF)

This estimator uses the common workflow to make an estimation of the state restricted to a subspace in the vicinity of the actual system states [105]. This is made by defining a hyperplane or switching surface between two or more subspaces or structures. The asymptotic stability condition of this switching surface forces the error in state estimation to be reduced, and therefore the estimated states to move closer to the actual system states.

This is possible by switching between the different subspaces and applying for each its control law. This may lead to chattering due to fast switching from one to another, that can be filtered defining a boundary layer increasing the switching surface [105].

Gauss Hermite Filter

The Gauss-Hermite filter assumes that both the process noise and the measurement noise are Gaussian in nature and have zero mean and unit variance, which implies that, on average, the noise does not introduce any bias into the system [97].

The probability density functions of the filter state and measurements are expressed with Hermite polynomials, which are a sequence of orthogonal polynomials that approximate Gaussian distributions accurately. These polynomials can be operated with the Gauss-Hermite quadrature method, an efficient numerical method for evaluating integrals whose terms are in this polynomial form [106].

Finally, like all the other filters, it uses a recursive estimation process, first formulating the predicted state of the system based on the previous one and then updating the estimation with new measurements. This estimation propagates the shape and spread of the probability density functions defined with the Hermite polynomials. It also accounts for uncertainty by keeping an estimate of the error covariance.

2.4 Control Design Methods

Automatic control and its associated control design techniques are a fundamental pillar of modern engineering, technology, and industrial processes. In a world increasingly dependent on complex systems and automation, the ability to regulate optimally processes, machines, and devices efficiently is vital. Automatic control, or control engineering, encapsulates a wide array of methods, tools, and strategies designed to manipulate and manage actuators and its variables, ensuring that systems operate reliably, safely, and with optimal performance.

Regarding micro membraneless RFB, control methods must be used for the regulation of the pumping actuators, and its proper operation is crucial for the stabilization of the two liquids interface, and in consequence maximization of the power of the battery, minimization of the mixing and self-discharge losses, and optimization of the energy consumption and utilization.

Automatic control involves the manipulation of actuators in a system to maintain desired states with changing conditions or achieve specific different ones. The goal of automatic control is to ensure that a system's output remains within predefined limits or follows a predetermined trajectory, regardless of disturbances or uncertainties.

It must be considered that control techniques are system dependent, and it does not exist a single methodology that can be applied to every system with the most optimal performance. They are tailored to the specific needs of the system they govern and how the optimal response is defined for it: in a trade-off between fast response, stability, robustness, or power consumption depending on how each one is weighted in the particular system. Also, the control methodology is selected based on system characteristics, such as the existence of a model for the system, the presence of noise and disturbances, the existence of delays, stochasticity of system variables or other unpredictability, inertias and complexity among other characteristics.

These control techniques can be broadly categorized depending on some general characteristics

they may meet:

Continuous time vs Discrete Time: The first evident classification for any control method is whether it uses continuous or discrete time. In continuous-time control, the system's state and control inputs are considered as continuous functions of time. The controller continuously adjusts the control input to maintain or optimize the system's behaviour in real-time. Naturally physical systems such as analogue electronics or mechanical systems operate in continuous time. Discrete-time control, on the other hand, implies dividing time into discrete intervals or samples. At each time step, the controller calculates and applies control inputs based on the system's discrete-time state measurements. This is the natural time for digital systems or any computer-based control. The choice between discrete and continuous-time control depends on various factors, first of all the nature of the system, but also computational resources available, and the desired control performance. In practice, may continuous-time systems are discretized for digital control implementation, with time steps balancing between accuracy and computational power.

Single/Multiple Input/Output: The number of inputs that can be operated in a control system, and the number of outputs to be regulated define the control strategy to apply. Single Input Single Output (SISO) systems are the simpler applications where one input is adapted to make the output match the reference. Multiple Input Multiple Output (MIMO) systems are the other end of complexity as more than one input should be operated to control more than one output. These systems have complex interactions between multiple variables. Sometimes they can be simplified using the approach to divide one MIMO system in multiple SISO ones. Also, they can be divided into Single Input Multiple Output (SIMO) or Multiple Input Single Output (MISO) systems. SIMO systems may have problems of control compatibility between the multiple outputs or trade-off conflicts for some specifications of their responses. MISO systems on their behalf, may have problems of coordination of the different inputs, or determination as there are more than one combination that leads to the desired reference. Regarding modelling, MISO and MIMO systems are more difficult for identification, as it is necessary to isolate the action of each input.

Feedback vs Open Loop Control: This is the most common form of control, where a system continuously compares the actual output to a desired reference and adjusts the control input accordingly. Open loop strategies do not measure the output to rectify the action of the actuators, just operate the system inputs depending on the reference and assume the output will be the expected based on models, operation tables or actuator curves.

Linear vs Nonlinear: Based on the mathematical expression describing their behaviour this distinction can be made. Linear control systems have relationships between inputs, outputs, and the system's dynamics described by linear mathematical equations. The principle of superposition holds, meaning that the response to a sum of multiple inputs is the same as the sum of the responses to each input individually. The system's transfer functions, state-space equations or differential equations are linear with respect to the variables involved. They have the advantages of mathematical simplicity, well-established theory and predictable behaviour. However, there might be systems that exhibit a more complex or nonlinear systems which are not able to represent correctly even after using linearization around the working point. In this scenarios, nonlinear control models are used. Nonlinear control systems

do not hold superposition, meaning that the response to a sum of multiple inputs may be significantly different from the sum of responses to individual inputs. They can also exhibit other complex behaviours, including oscillations, chaos, and bifurcations. These allow to a more accurate and flexible representation of real-world systems. On the other hand, using this type of representation means higher efforts in mathematical analysis, more limited analytical techniques and tools, and they may exhibit more sensitivity to initial conditions and parameter variations, requiring robust control strategies.

Feedforward Control: It is an option for incorporating system state measure to the regulation, just as feedback control, but these designs use measures that anticipate disturbances or changes in the system and applies corrective actions before they affect the output. This can be done through modelling and measure of system conditions that will influence the response in the near future and are not still present.

Optimal Control: Optimal control is any technique that operates seeking to find the best possible control input to minimize a predefined cost function. The cost function can consider the previously mentioned properties (error to reference, input power, etc) weighted depending on the particular application requirements.

Robust Control: Robust control techniques are defined as any approach that deals in its design with uncertainty explicitly, this is incorporating it to the modelling of the system or input control. They are focused on maintaining system performance under uncertainty and variations, assuming some variables are unknown (although they are bounded to some limits).

Adaptive Control: These methods continually adjust their control parameters based on real-time measurements and system dynamics. Like robust control, adaptive control approach can deal with uncertainty and variations, but it always implies a dynamic modification of the control parameters, while robust control usually has a static control policy. This is useful in situations where the system's characteristics change over time, due to aging or wearing, evolving environmental conditions or stochasticity due to non-measurable or known variables.

Predictive Control: This approach considers not only the current state of the system but also its expected future behaviour. This technique goes beyond simple feedback control by employing the model of the system to predict future outputs of the system and optimize control inputs by comparing the real with the modelled results. Like in optimal control, a cost function defines the system's performance goals, and the controller then calculates control inputs over a future prediction horizon, aiming to minimize this cost function while adhering to system constraints. Now, an introduction of some relevant and extended control strategies is presented and its application in RFBs discussed. However, the previous characteristics are not used for classification but just for describing the strategies. Since this work proposes for the first time a microfluidic dynamic model for micro membraneless RFB, the review on control techniques and methods is divided based on strategies that require this modelling and model-free methods that could be applied to the system control without the need for a model.

2.4.1 Model Free Methods

Usually, in practical engineering problems the knowledge about the system is limited and it is difficult to have a precise model of the plant [107]. In other applications, noise and disturbances may produce that model differs from real behaviour and any control technique based on a model not considering them may have stability and robustness issues. Therefore, many control techniques are not based on any model or use an over simplified one. Other recent works rely only on input-output data and a continuously updated local relation for them.

Classical Proportional-Integral-Derivative (PID)

Classical approach of Proportional-Integral-Derivative (PID) is the simplest technique for model-free control. It is true that it can also be designed more precisely with a complete model of the plant, but it is a good alternative when the system knowledge is reduced and it is used a simplification. Design, tunning and implementation have been extensively studied and it's a well-stablished and known method that do not requires further examination. Many references as [108] can be found for more detailed information.

$$u(t) = k_p e(t) + k_i \int_0^t e(\tau)d\tau + k_d \frac{d}{dt} e(t) \tag{2.14}$$

In equation 2.14 it is presented the general equation for the control action u when an error e of the feedback signal to the reference is used, and the constants for proportional k_p, integral k_i, and derivative k_d are adjusted.

Intelligent PID (i-PID) Techniques

It is considered an intelligent PID controller (i-PID) any method where unknown parts of the plant are considered for control and gains calculation and adaptation without any plant modelling [109].

The techniques for adapting the control gains are numerous and wide, and have been proposed since the first approaches of using Ziegler-Nichols formula [111], to use genetic algorithms [112], particle-swarm optimization [113], neuronal networks [114], or fuzzy logic composition [115].

Other Modern Approaches

There are multiple modern approaches for model-free scenarios. These techniques have gained significant attention and relevance in recent years, especially in applications where system dynamics are complex, poorly understood, or constantly changing.

One of the strategies is use reinforcement learning. These methods rely on defining a state representing the internal conditions of the plant, the possible actions of the actuators, and a reward mechanism that evaluates how each action contributes or not to reach the desired outcome. A learning algorithm is proposed based on this architecture to weight the set of

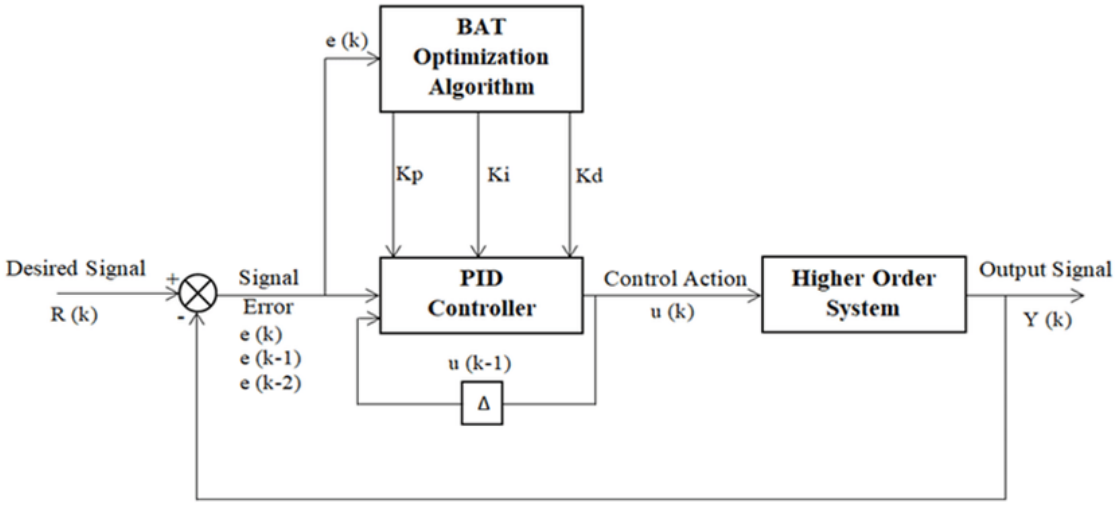

Figure 2.24: Control scheme for an i-PID approach from [110] using an optimization algorithm for a high order system. This scheme is general to any i-PID methodology by substituting the optimization algorithm with the concrete adaptation technique and applying it to the specific plant.

available actions for each state, and then the control algorithm uses this training to select the best action at each time. An example of this method is described in [116].

Similar control schemes that use a previous learning can use genetic algorithms [117], neuronal networks [118] or other machine learning methods, where the learning or training can be applied to different control law architectures.

Other common approach is the Model-Free Predictive Control (MFPC), where only using input and output data a mathematical relationship is constructed to work as a model identified in real time. Then, predictive control is applied similar to a Model Predictive Control (MPC) that is discussed further on in the text. A complete review on its principles and some applications is featured in [119].

Also, some methods that do not require previous learning or training are the use of fuzzy logic together with linguistic variables that mimic human expertise rules [120], or systems that resemble collective behaviour by using multiple agents, such as in particle swarm or ant colony optimizations [121].

2.4.2 Model Based Strategies

Control design can be more precise when a model of the system is available or the modelling efforts are reasonable. Also, these techniques can be used to guarantee an optimal response and a more efficient use of computational resources. Also, it is easier to make stable and robust controllers with the model information, and their response can be easier predicted, what is paramount in safety-critical applications.

Linear Quadratic Regulator (LQR)

This wide used technique is designed for linear dynamic systems and can optimize input control to a cost function that considers the output error and the input power used. This optimization achieves desired performance objectives while taking into account system dynamics and noise. It is characterized by the use of quadratic cost functions to formulate control objectives, which LQR controllers are designed to minimize. The most typical cost function for the discrete time case is:

$$J = \sum_{x=0}^{\infty}((X(k) - X_r)^T Q(X(k) - X_r)) + (U(k)^T RU(k)) \tag{2.15}$$

Where X is the state represented in space-state in the time instant k, U is the control action, and Q and R matrices are defined to weight error versus action in the cost function. Therefore, this cost function combines control effort and system state deviations from desired values. The resulting control law provides a mathematically elegant and efficient means of regulating dynamic systems.

However, in the presence of model imprecisions, disturbances or any other uncertainty this method can not guarantee zero steady-state error. Therefore, there are some control techniques that incorporate an integral action to the LQR control to compensate for this possible deviation [122].

Model Predictive Control (MPC)

This is the name for a range of control methods, that make a prediction of the system response in a time restricted horizon by considering the effect of the applied inputs into a model of the system. Using this model dynamics, a defined cost function and current state knowledge it calculates the optimal future actions on the manipulated variables to reach the desired state.

It is also known as receding horizon control or moving horizon control because each time step the prediction time frame and the control action for the next period are updated for the next equivalent time.

The control action and state are usually constrained to stay in certain limits that assure the safety operation of the plant. The cost function can be defined in several ways, although for reference it can be considered a similar function to the one defined in (2.15) for the LQR case. This function together with how precisely the model captures the system dynamics will condition the controller response.

In summary, MPC uses a explicit model to predict the plant output along a future time horizon, calculates a control sequence optimal to a defined cost function, and updates the time horizons with a receding horizon strategy, so that time frame is moved towards the future (including the control action applied during this horizon).

There exist modifications of the simple method, that include using a nonlinear model [124] or using an adaptive strategy for the model [125].

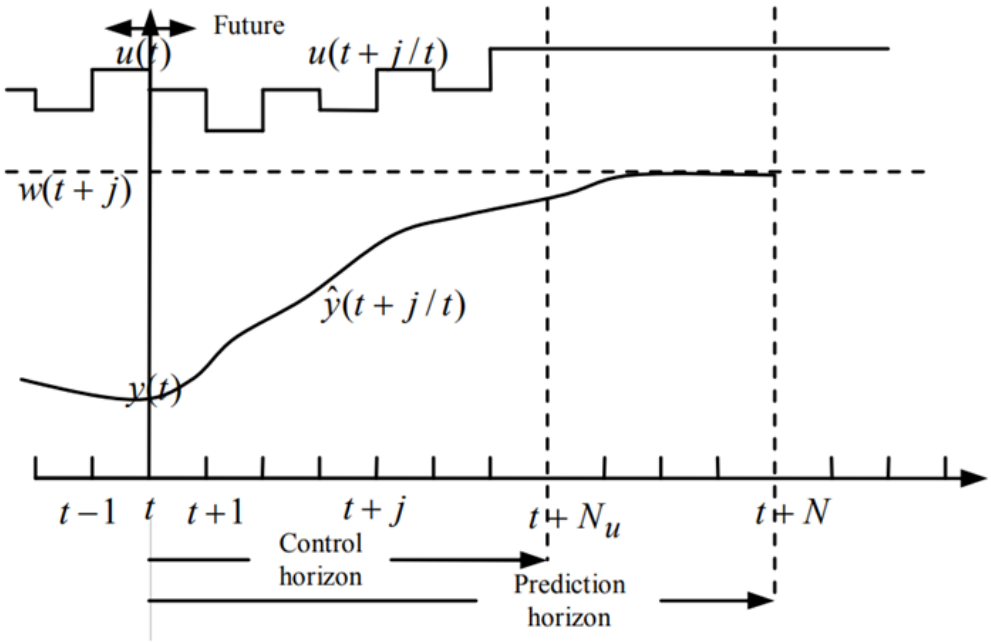

Figure 2.25: Time horizon strategy for MPC as depicted in [123], with the moving prediction and control horizons, the set of control actions u, the measured and expected outputs (y and $\hat{y}$) and the state constraints w.

Robust H_∞ Control

H_∞ control is a robust control methodology that consist of using the definition of the closed loop system with a control gain applied to the state feedback so that the controller is stable and satisfies a H-infinity norm constraint [126]. The controller has the form:

$$U(s) = kX(s) \tag{2.16}$$

The transfer function of the system with the feedback control ($W(s)$) must satisfy that its h-infinity norm is smaller than an index γ, which implies that the maximum gain of the system over a range of frequencies (the h-norm) is minimized under a certain value, ensuring robustness to disturbances:

$$\|W(s)\|_\infty < \gamma \tag{2.17}$$

This implies solving a mathematical optimization problem to find the minimum h-infinity norm and the feedback control gain that satisfies it. It also can be fixed a higher index which implies less robustness to improve performance.

This control aims to minimize the "worst-case" scenario in terms of system performance and robustness. It considers the most unfavourable combination of disturbances and uncertainties to ensure that the controlled system remains stable and performs satisfactorily under all conditions.

Fuzzy Control

Although first historical controllers using fuzzy logic emerged to be used without model and based on expert knowledge (Mamdami controllers), it can also be used to combine several subspaces models and their different control laws based on rules and the fuzzy composition (Tkagi-Sugeno controllers) [127]. This composition can be helpful to deal with nonlinearities and changing conditions thanks to its adaptability.

In general, fuzzy control is a control that defines a set of fuzzy submodels and membership functions and assigns a weight to each submodel depending on the values of the states of the systems. The membership to each model is defined using rules of the type IF-THEN. Then, the membership is not all or nothing but gradual using fuzzy logic, this is a logic that allows to have degrees of membership between 0 and 1.

As several fuzzy sets may be present at the same time these controllers perform a fuzzification process (convert variables to fuzzy set values), rule evaluation to activate each submodel, aggregation of all the active outputs, and defuzzification (converting fuzzy sets to a composed output).

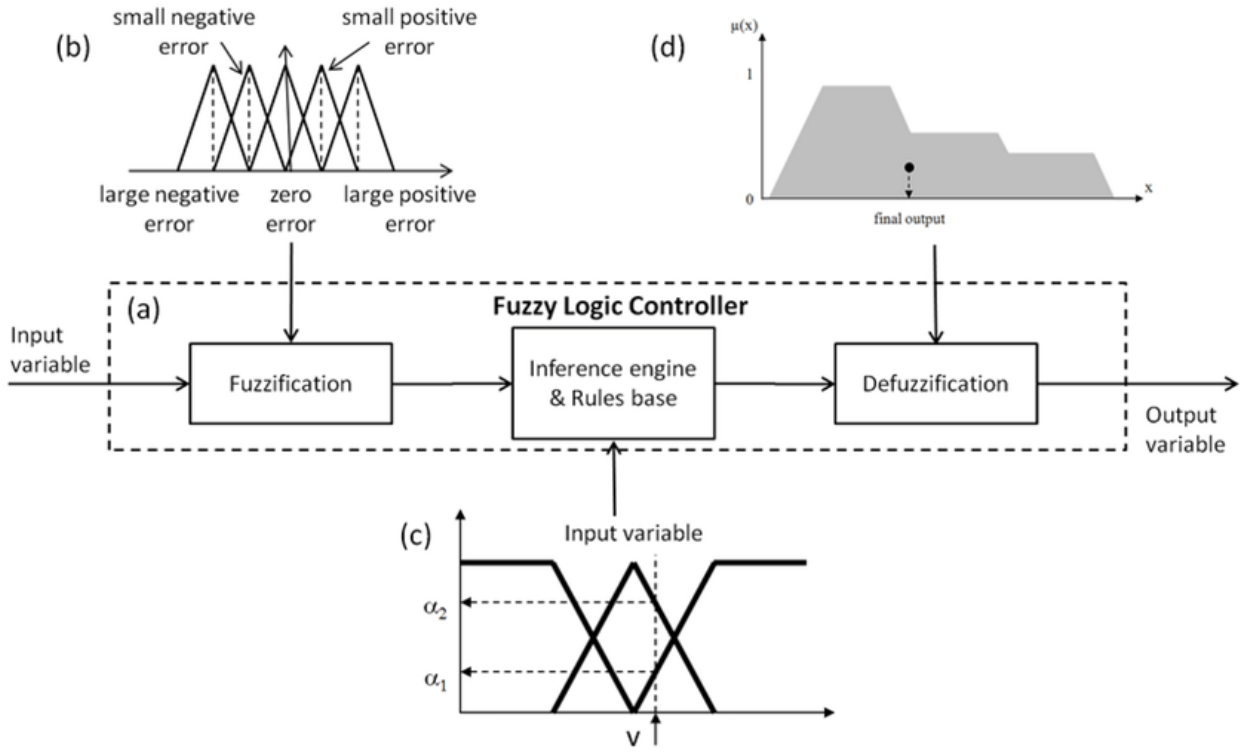

Figure 2.26: Fuzzy system process scheme from [128] where an input variable is converted to a fuzzy value that may be composed by several sets, evaluated following the rule-based inference, and then defuzzified to a composed output variable.

Fuzzy controllers can apply the process from fig. 2.26 to compose parameters of models with similar structure and then calculate one control action to the result, to aggregate different control laws depending on the state to the same model, or directly to compose the control

actions based on different models. In any case, these are generally considered model-based fuzzy controllers. There are also other methods for composing more than one model or control law.

Variable Structure Control (VSC)

Other strategy for combining different control strategies for the same plant, as fuzzy logic controllers, is Variable Structure Control (VSC). This technique consists of high frequency switching between two or more control structures in a discontinuous way. The switching is based on prior knowledge of the system, and it is specified using laws [129]. The VSC control can define a sliding surface in the state space, where the switching occurs and to guide the state to the desired target. This is typically called the sliding mode of the controller.

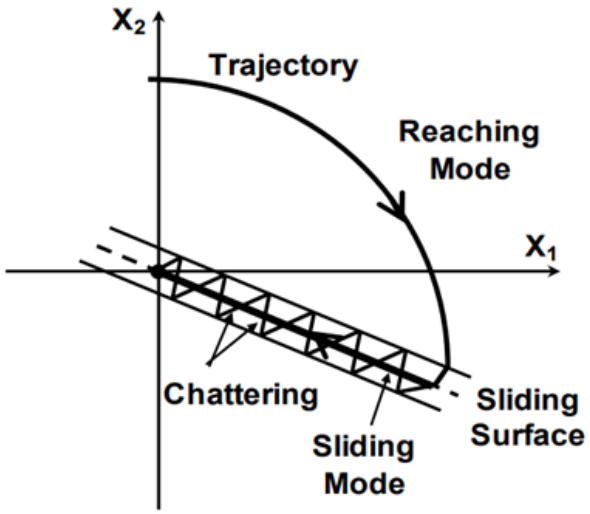

Figure 2.27: Representation of the switching mechanism for the VSC from [130], with the trajectory on the state space, the sliding surface and the chattering produce around the switching region.

The high frequency switching can lead to producing chattering, this is excessive commuting between the different controllers. In order to reduce it, the sliding area can be defined wider around the switching region.

2.5 Conclusions

In this chapter a complete revision of the state of the art is presented. First, all relevant previous works on microfluidic membraneless RFB are described, explaining the different designs, studies and chemistries, with emphasis on describing their microfluidic setup and operation. This gives important context about how the instrumentation selection, its lack of model and control, and limited ability to recirculate has constrained these previous works and prevented them to achieve a full battery process: charge-discharge cycles with electrolytes recirculation. In this thesis, the microfluidic operability is the first problem to be addressed

so that the whole project where this thesis takes place can work and iterate with its designs of reactors.

Then, previous modelling on the different dimensions of RFB is reviewed. This includes electrochemical, hydraulic, thermal and electrical previous models. These models are usually specific for microfluidic membraneless batteries, but when there are no references available (such as for the electrical dimension) conventional RFB models are described. This allows to have the closer references for the electrical and microfluidic dynamics modelling that will be performed in this thesis. These models are vital for future electrical integration and microfluidic operation respectively.

Following modelling state of the art, identification and model categorization are detailed based on the knowledge and transparency of the system physical internal processes. Analytical models using physical laws and principles, blackbox composed of mathematical expressions with no internal relation, and greybox as a hybrid approach are presented. Identification tools and methods for blackbox and greybox techniques are also mentioned. This thesis uses a greybox approach for its modelling, where equations from system behaviour knowledge are proposed and then completed with parameters identified from real data. Also, a review on real time estimators and filters is introduced. These filters allow to adjust in real time some model parameters and adapt their values and state estimation. In order to deal with microfluidic stochastic and variable nature, microfluidic dynamics model uses correction factors adjusted in real time using this filtering in this thesis.

Finally, control techniques are reviewed, explaining general properties that controllers can meet. Then, control design methods are divided into model-free and model based, so that it can be understood the alternatives that having a precise modelling allows. Relevant control techniques are briefly introduced, as specific controllers developed for microfluidic control will be further discussed and detailed later in this thesis.

The review presented in this chapter about the topics related with this research is one of the contributions of this thesis.

Chapter 3

System configuration for microfluidic membraneless redox flow batteries operation

This chapter introduces the complete microfluidic setup developed for the microfluidic membraneless RFB operation. It starts by detailing the cell reactor design used for all experimental test and measures, and for which the instrumentation and setup has been selected and optimized. Its dimensional and manufacturing properties do not only condition the operation ranges, but also must be taken into account when selecting the pumping instrumentation principles (watertightness, pressure drop and endurance). After that, the microfluidic instrumentation is described, and its selection compared to other alternatives justified. This includes pumps, valves, tanks (and its monitoring) and flow and pressure sensors. Electronics integrating all this instrumentation is also described. First, for the hardware, the developed electronic board interfacing with the pumps and valves drivers and the sensors is sketched. Then, the software scheme is also presented briefly, both the embedded in the board and the System Control And Data Acquisition (SCADA) in the monitoring and logging computer. The full microfluidic setup is shown in a final scheme with all elements.

3.1 Cell Reactor

In the previous chapter (Section 2.1) different designs for the reactor cell of a microfluidic membraneless RFB are described. Here, the one used in this thesis is explained in more detail, and its manufacturing process and the different elements that are part of it are presented.

The design is a continuation of the work already done in [66], specifically what is called Y-junction single pass cell in this paper. The flow distributor of the cell is made using PolyDiMethylSiloxane (PDMS), a silicone polymer optically clear, inert, non-toxic and non-flammable. This characteristic made it one of the most common materials used in microfluidics. This polymer is synthetized in liquid state, but after a curing process it becomes solid, so it maintains the shape of its recipient. Therefore, precision and resolution of the flow distributor

made on this PDMS block will depend on the ones of the recipient used as mould.

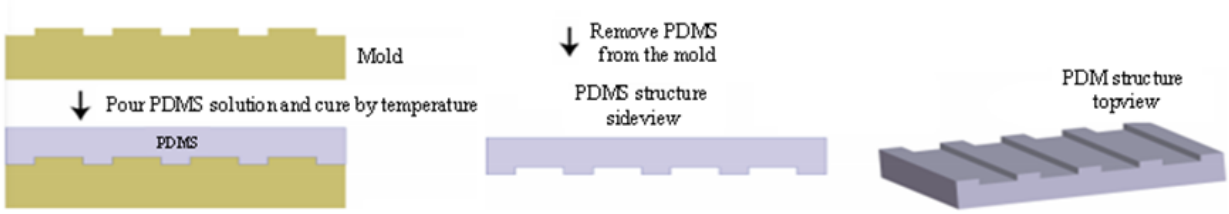

Figure 3.1: Soft lithography in PDMS process.

This moulding for the PDMS is manufactured using 3D additive printing. The most resolution and precision for this task is offered by Digital Light Processing (DLP) printers. These printers are based on the selective exposure of the liquid resin to a light source (a laser or most commonly a digital image projector) that induces polymerization in a photosensitive liquid resin. This polymerization forms solid and very thin layers that are stacked to create a solid object. This is how the negative block of the flow distributor is made.

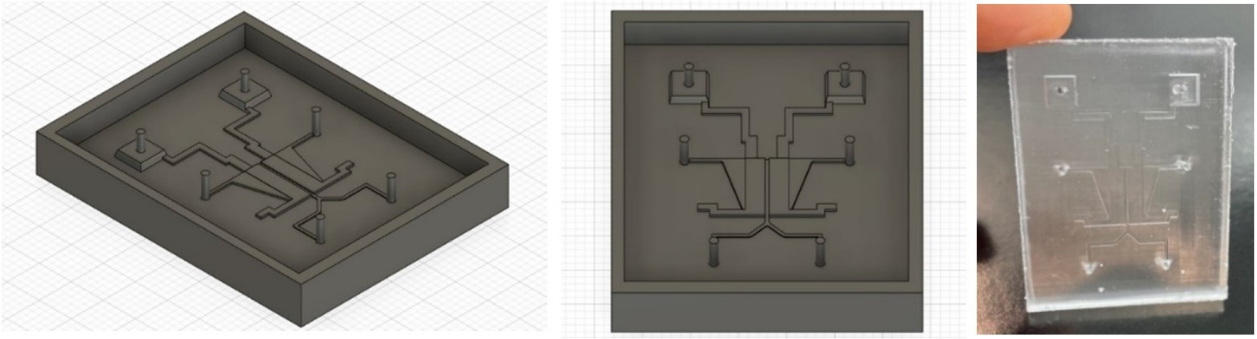

Figure 3.2: Microfluidic membraneless redox flow cell negative mould made with 3D DLP printing additive manufacturing, and PDMS block after curing in this mould.

This flow distributor also has a space where the porous electrodes are placed and go out to the external electric contacts. These porous electrodes are cut from a carbon paper bigger sheet.

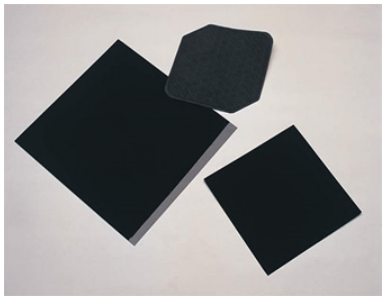

Figure 3.3: Carbon paper-porous sheets that are cut to obtain the electrodes.

Then, the PDMS block is sealed to a glass sheet with the electrodes putted inside. This process is made with plasma-bounding, which can produce a permanent bond between PDMS and glass by applying an oxygen plasma to the surfaces to be in contact. This plasma treatment in PDMS increases hydrophilic groups (-OH) on its surface, that eventually form strong covalent bonds with glass. The covalent bonds form the basis of a strong seal between the two materials that avoids leaking and also improves hydrophilicity and therefore flow on the PDMS.

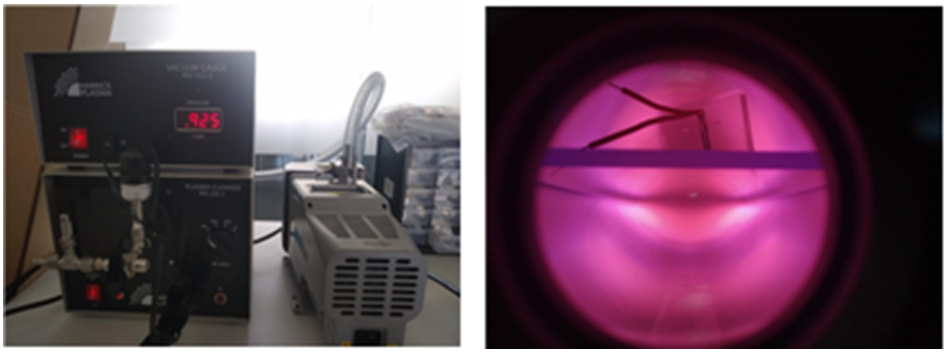

Figure 3.4: Plasma cleaner used for bounding and its inside process with oxygen plasma.

Finally, electrical contacts are made using wires glued with silver epoxy to the porous electrodes, and microfluidic tubing inserted in the PDMS orifices used as inlets and outlets for the electrolytes.

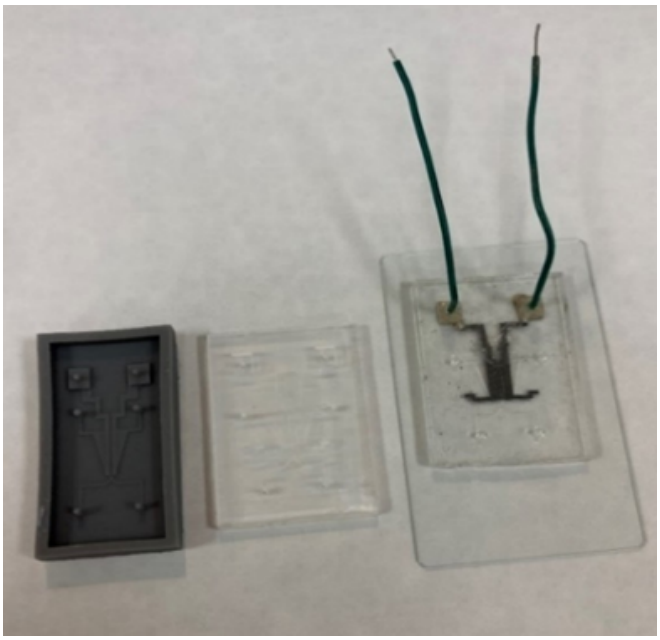

Figure 3.5: Mould, PDMS block and complete reactor cell for the microfluidic membraneless RFB.

3.2 Instrumentation selection and development

The microfluidic instrumentation, especially the pumping method, conditions not only battery performance but also limits how it can be operated. Other elements for control and monitoring as valves and sensors are also vital for this practical implementation. As it has been discussed, previous state of the art references had a limited operability, so in order to build a complete workbench, it was necessary to evaluate, select and combine all the new instruments from scratch.

3.2.1 Pumps

Electrolyte recirculation was a major requirement for the battery operation. This makes syringe pumps to be problematic since the setup becomes more complex in order to allow the recirculation. Nevertheless, it was tested using New Era Pump models and dual check valves for two syringes at each circuit. These valves allow to withdraw and infuse into different lines, which produce a circular fluidic circuit. This a very complex setup, that suffers from pulsation in the flow because of the pumping principle and at the switching instant between infusion and withdraw. This switching also produces desynchronization between the negative and positive circuits as liquid can cross from one circuit to the other in the cell and syringes may empty at different times.

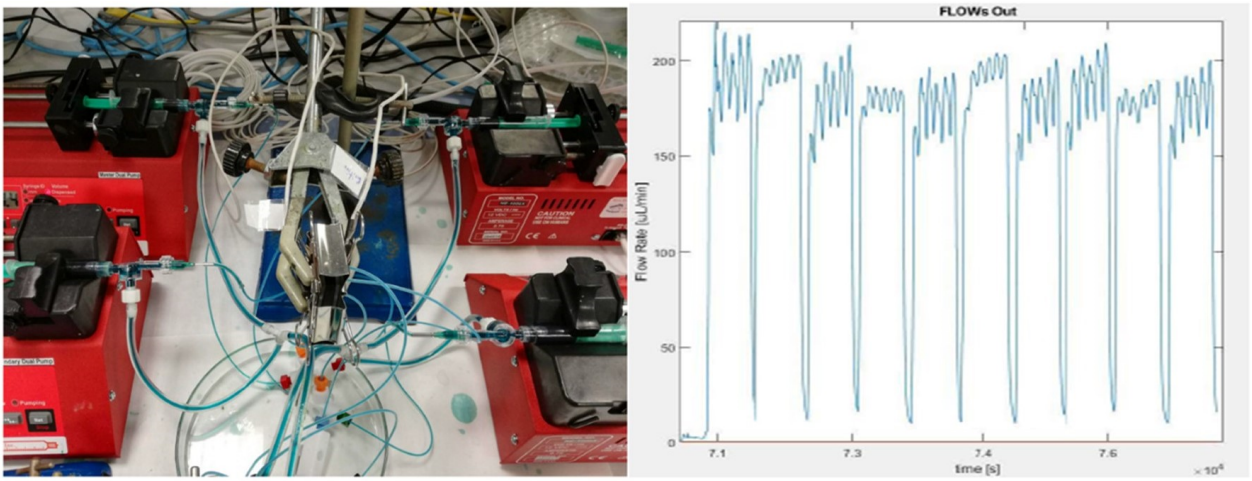

Figure 3.6: System microfluidic setup for recirculation with syringe pumps (left) and long term flow rate for one electrolyte, with pulsation and switching discontinuities (right).

As an alternative it was considered to use gear pumps. This technology allows for an ease close fluidic circuit, but commercial products were not suitable for use with the vanadium electrolyte (which is dissolved in sulfuric acid), as they have wetted metallic materials. Some prototypes were designed and manufactured using the DLP 3D printer so that the gears were polymeric and did not have any damage. However, the gears did not have a proper interlock, and the produced flow was not smooth (either the flow rate range is oversized or the flow was intermittent).

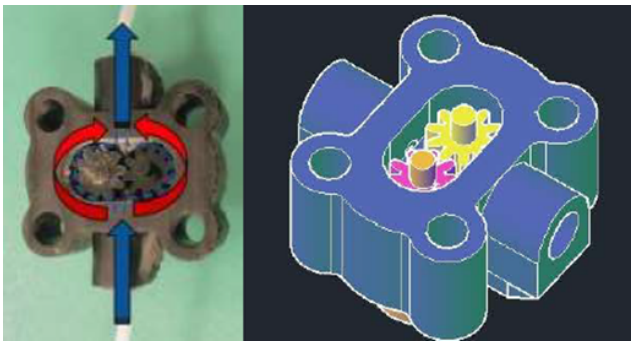

Figure 3.7: Gear pump prototype and design made with DLP 3D printer.

In microfluidics, generally it is considered the most precise and modern pumping system the ones that generate a Pressure Driven Flow (PDF). This method consists of pressurizing with air the tanks or the liquid reservoirs so that the liquids will start flowing out through the circuit. This is obvious to have drawbacks for the recirculation. Similar to syringe systems, it is necessary to use two tanks for each circuit that alternatively produce the pressure and receive the flow, and some valves that change the circuit configuration. Even knowing this it was acquired one system from the company Elveflow to test if the high precision of the flow compensated for the complex setup.

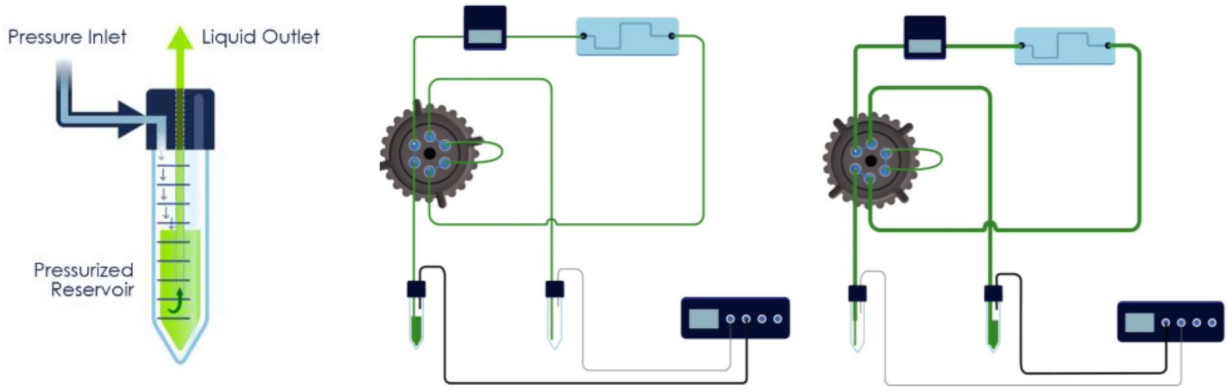

Figure 3.8: Pressure driven flow (PDF) pumping principle (left), and setup for recirculation with valve (right), from Elveflow products.

The experience was that the flow was certainly more precise than using syringe pumps. Complexity of the operation and setup was a problem, but the characteristic that discarded even more this alternative was the problems for controlling the pressure of the tanks receiving the electrolytes. This pressure determines the flow at the outlets of the cell, and interacted with the pressure at the inlets making the interface instable. This instability produced mixing and tanks desynchronization for the switching manoeuvre, which itself produced more mixing.

The last alternative was to try a special type of micro-peristaltic pumps. This kind of pump uses a piezoelectric to produce small displacement and high frequency pulsations on a membrane in contact with the liquid, and therefore propelling it. Classical peristaltic pumps

suffer from pulsation that would make the flow at the interface in the reactor oscillate and therefore produce mixing. However, this actuators from the company Bartels Mikrotechnik GmbH take advantage of this small piezoelectric displacement (in the order of micrometers) and high frequency (>100Hz), to produce small pulsation that the fluidic tubing itself can damp. They have two piezoelectric in series acting alternatively as peristaltic forces, which increases their working force, and produce less pulsation that it would make only one (there are other products as the ones from Takasago Fluidics Systems that use only one piezoelectric and has been checked to produce more pulsation).

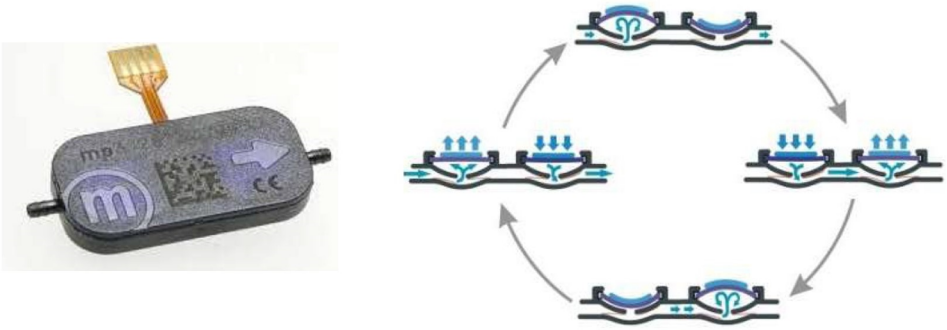

Figure 3.9: Piezoelectric pump from Bartels Mikrotechnik GmbH (left) and working principle steps (right).

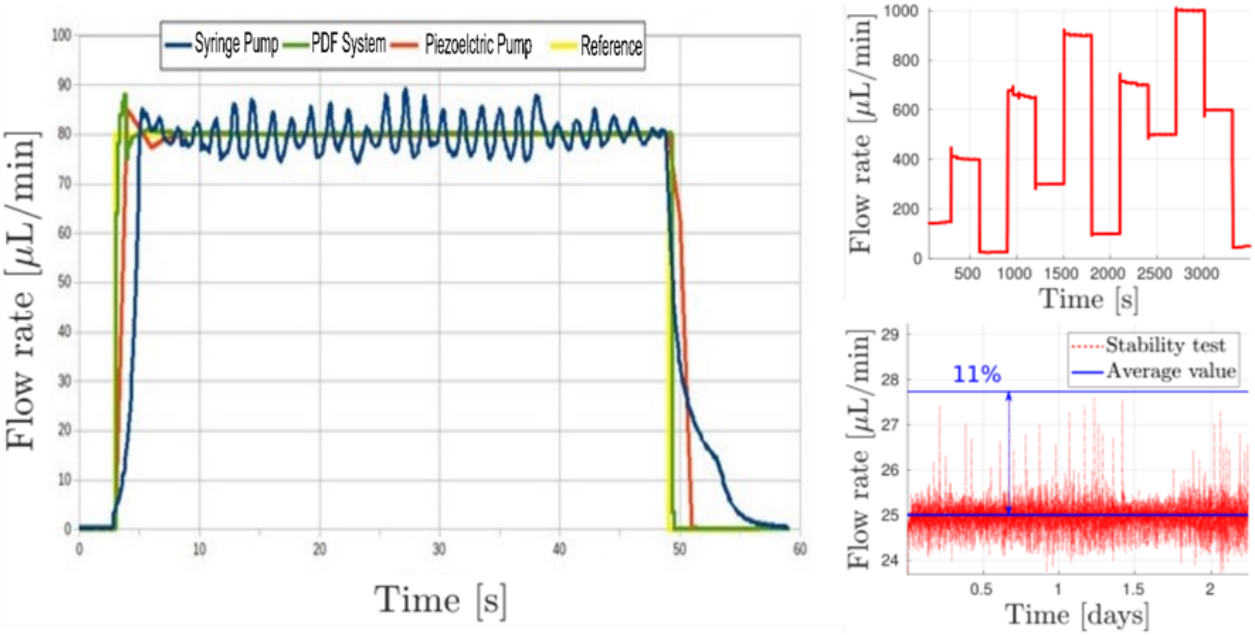

Figure 3.10: Piezoelectric pumps flow response compared to syringe pumps and PDF systems, tested at different flowrates in the range of 1-1000µL/min, and stability test for several days.

Testing and experimental data showed the best flow response, with easy recirculation, low pulsation and precise flow when integrated with flow sensors for a closed loop, and commercial drivers properly operated as it will be discussed in the electronic hardware section. These pumps also offer a reduced price compared to other systems, smaller size, higher and more flexible integrability, and lower power consumption.

3.2.2 Valves

Interface control in the reactor cell requires to control not only the flow at the inlets but to make sure that the outlets have the same flowrate. For this task, it was tried to regulate the flow using piezoelectric pump similarly to the inlets. However, they created perturbances when they suck from the reactor, especially at the joints of the PDMS block with the external tubing they can introduce air, as this joint is not perfectly watertight. Consequently, it was decided to use valves that equal the pressure drop at the outlets and therefore the flow rates can be adjusted and the interface is more easily controlled.

Available commercial valves were not proportional but all or nothing, so they can not be used for regulating directly. Nevertheless, some valve technologies have some proportional behaviour although are meant to be used as full open-close. This is the case for Shape Memory Alloy (SMA) technology, that use a shape memory alloy material as a membrane, changing it shape with temperature. Some units of this type of valve were tested from the company Memetis. They were operated heating them using electrical current and varying their deformation regulating this current. Using a closed loop with flow or pressure sensors feedback it was possible to achieve intermediate positions of the membrane, increasing pressure drop in the line but not closing completely it. Unfortunately, the intermediate positions were not stable, and even with the feedback, due to temperature and mechanical hysteresis, produced inertias in the positioning. Specifically, when it was needed to cool down the actuator it was not controllable in the short term.

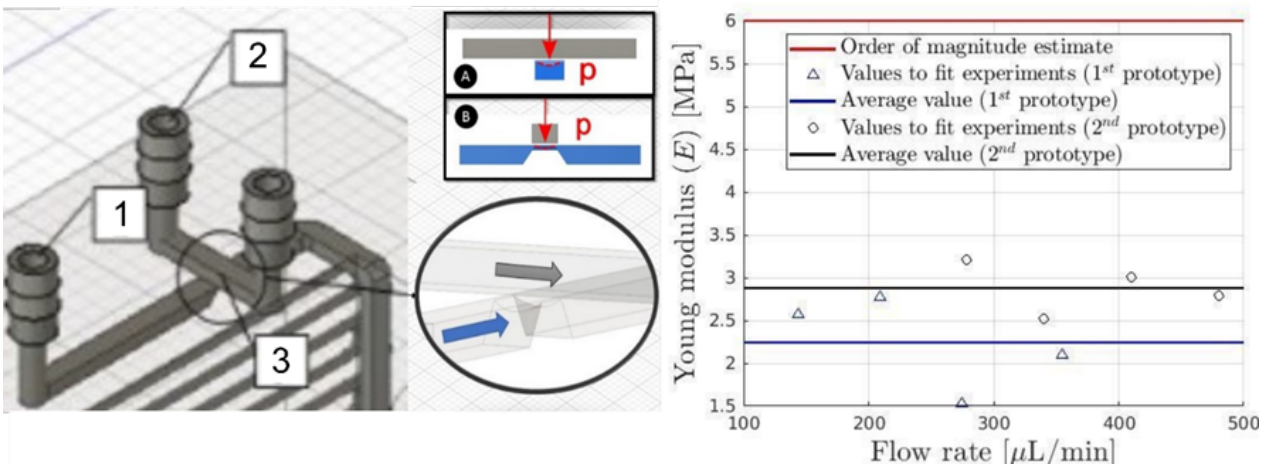

Figure 3.11: Scheme of the pneumatic valve including liquid inlet (1), air inlets (2) and membrane (3) (left) and young modulus calculations and real experiments measurements (right).

Although not commercially available, there are plenty of references of pneumatic activated valves that use some membrane or flexible material to narrow hydraulic conductions [131]. Based on this principle, it was studied and designed some prototypes of this type of valve, but using a slightly more rigid material that allows to control intermediate strangling proportionally. Using 3D DLP printing the membrane between pneumatic and hydraulic channels was iteratively adjusted, testing also different printer resins. During this testing, young modulus was selected to fit the estimated optimal.

The pneumatic line for actuating the designed valve was generated using TTPVentus micro air compressor. Based also on piezoelectric high frequency movement, these air pumps are able to regulate the applied pressure in the range 0-800 mBar. Their driver was integrated in the electronic board where all actuators are embedded.

3.2.3 Sensors Selection

The main variables to measure in a microfluidic membraneless RFB are flow, pressure and temperature. The most critical is flow, and flow sensors from the company Sensirion were integrated. This product works in the desired range of 0-1000 $\mu l/min$, and it is cheaper than the other available alternative that are Coriolis flow sensors. Their working principle is based on thermal measurements. They calculate thermal gradient measuring temperature before and after a microheater. Flow through this microchannel modifies this gradient that can be transduced into a flow rate estimation.

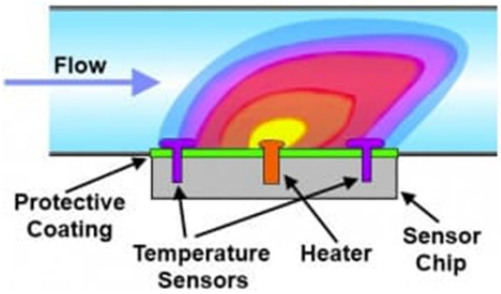

Figure 3.12: Thermal working principle of liquid flow meters, from [132].

These sensors are precise enough, with 0.2% of the full-scale accuracy and 0.02% repeatability. They are calibrated for water, and since the temperature gradient is specific heat dependant, they were calibrated for the different used electrolytes. This calibration process consisted of maintaining a continuous stable flow through the sensor for a period of time, and collecting the volume in a high precision weighing scale. This process showed little but significant deviation between vanadium electrolytes and water, and more importantly that this deviation does not barely change with state of charge changes.

Pressure sensors have been used for measuring the air pressure applied to the valves (Honeywell models for air in the range 0-1 Bar), and to measure the inline pressure of the liquid pipes (TE Connectivity model MS5837-30BA Ultra-Small 0-2 Bar). This second measurements have been mainly used to check that there are not clogging during operation or any other

problem in the reactor when first used. For example, the porous electrodes blocking the flow conductions.

Regarding temperature, both flow and pressure sensors have internal temperature measurements to compensate for the possible deviation on their main variables, and these values can be accessed. Therefore, there is no need to add extra sensors. Other variables that could be relevant to measure, as viscosity or electrochemical potential (both of which can be used for state of charge estimation) have been tried to measure. There has been attempts to develop prototypes from own designs, but the results were not satisfactory yet.

3.2.4 Tanks Monitoring

Regular different glass recipients have been used as tanks at different stages of the work. When it was not certain enough that sensors calibration was stable during long periods of time, microfluidic control was not adjusted to avoid mixing, or evaporation or leakages were not discarded, it was useful to have a continuous monitoring of the tanks level.

A simple computer vision application was developed that automatically calculated the tanks level. It compares the real time level of the tank with the initial, and extracts calculation of a possible leakage if the total volume has decrease. It also compared the relative change between the tanks with the one expected from the flowmeters measures (integrating the flow rate differences for a volume estimation) and calculates a compensation factor to be applied to the flowmeters of one line if necessary.

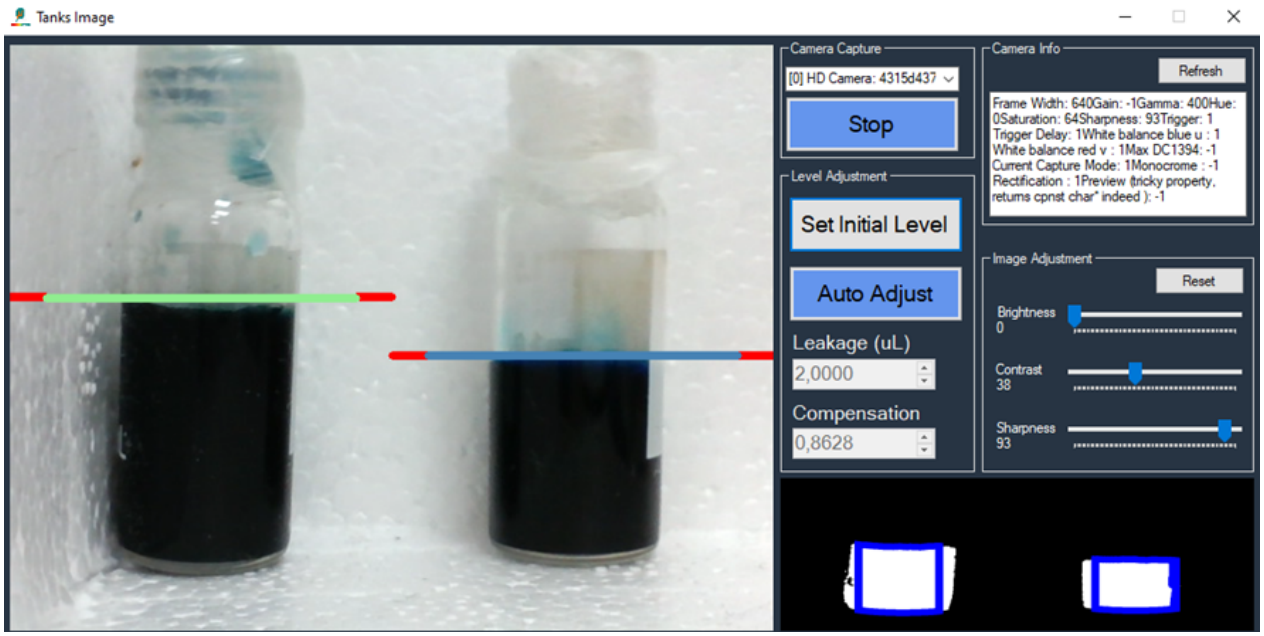

Figure 3.13: Tanks monitoring application with real time calculation of leakage and flowmeters compensation.

3.3 Electronics

All described instrumentation has been integrated by developing the proper electronics. This is the hardware including the electronic board where all actuator drivers and sensors are connected for power and data, and the software including the embedded in the board and a computer application to be used as system control and data acquisition (SCADA), with the regulation algorithms and the logging.

3.3.1 Hardware: Electronic Board

Components hardware have been tested using prototyping boards separately, and after being commissioned they have been integrated in a control board designed ad-hoc for this purpose. The selected microprocessor has been the Atmel SAM3X8E ARM Cortex-M3 CPU. The selected USB to serial converter for communication with the external computer is the ATmega16U2.

This board includes the connection and spaces for the actuator drives. In the case of the piezoelectric liquid pump, there are two drivers simultaneously integrated. This is because the manufacturer offers two models, one with an output voltage range of 0-150V, and the other within the range 77.5-260V. In order to have the wider operation range both are ready to be used, and activated. One is interfaced using an analogue signal from a digital-analogue converter of the microprocessor, and the other using I2C communication protocol. This protocol is also used to read the flowmeters. Regarding the air pump manufacturer driver, UART protocol is used.

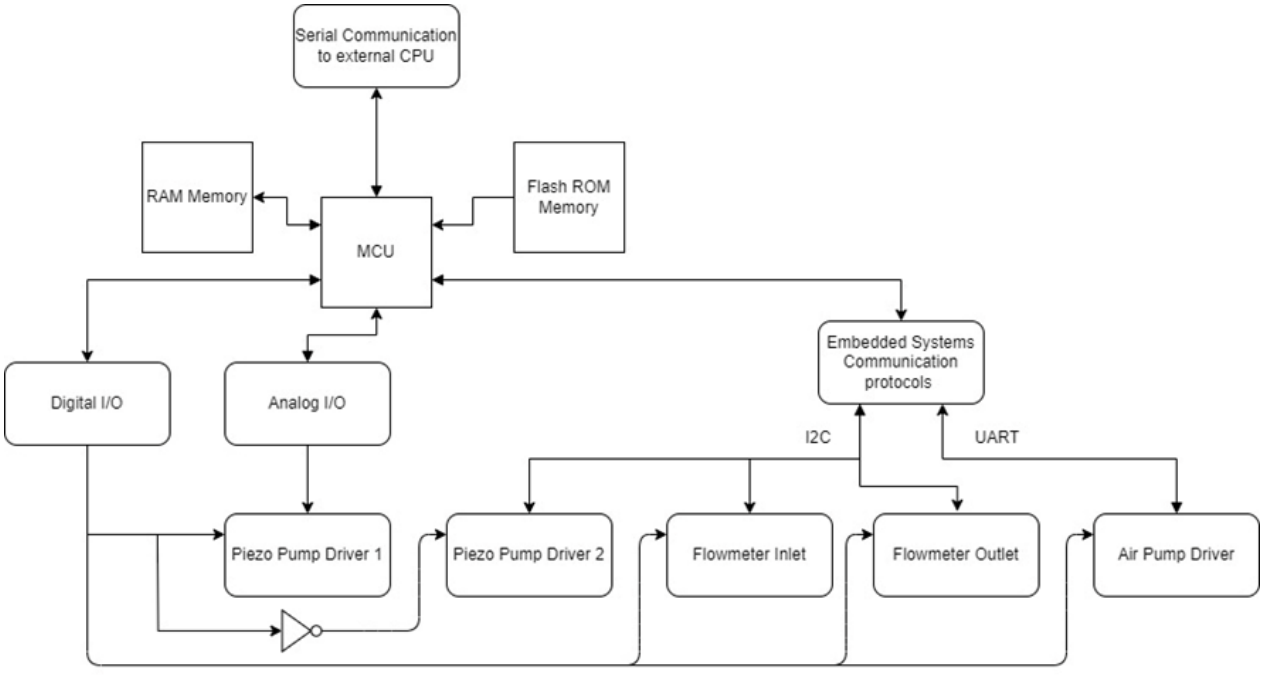

Figure 3.14: Hardware scheme of the board developed for the microfluidic setup integration.

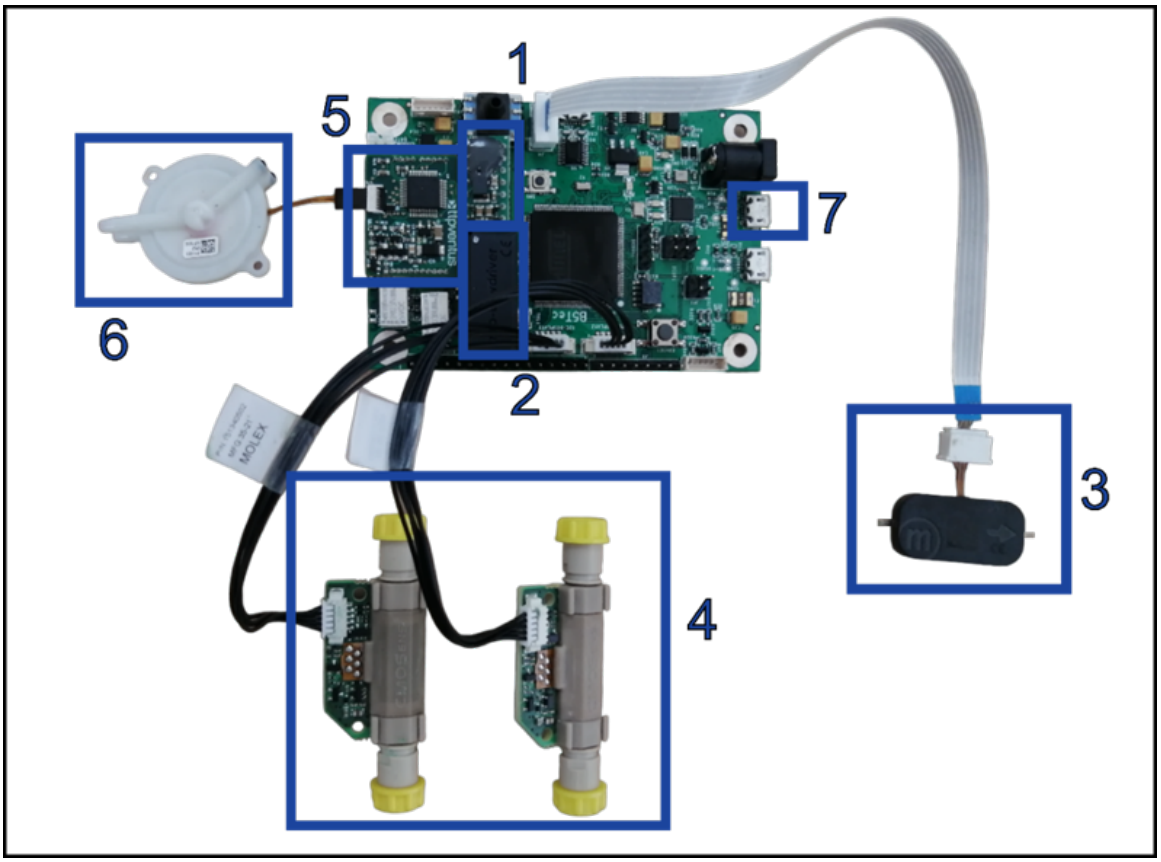

Figure 3.15: Image of the control board, with the drivers for the piezoelectric pumps (1 and 2), the piezoelectric pump itself connected (3), the flowmeters with their connections (4), the air pump driver (5) and the micro pump itself (6), and the micro USB connector (7).

One board has all the elements to control one microfluidic circuit, therefore there will be two of them. These boards are also configurable to connect other different sensors via I2C, such as pressure sensors, and the connectors are already prepared for adding them. Also, in all connectors the power for the element can be switched off/on to use the board in different configurations.

3.3.2 Software: Embedded and SCADA

The two control boards are programmed to interface with the sensors, read their values and send them to the computer after applying filters to the raw measurements. The value for the actuators to the boards comes from the computer, and the boards communicate with the actuator drivers with these references. The internal loop for the board takes less than $20ms$.

The computer receives data from both boards, applies the control algorithms and sends them to the boards. The communication loop is fixed to last $200ms$, as microfluidics dynamics are not very fast and need this time to see changes. The software for the computer application is developed as a Windows Form in the Microsoft .NET framework using C#. The application is prepared for using up to eight processes at the same time to parallelize battery testing.

Also, it logs all the data involved and its graphs can be visualized in real time. It is prepared to manage auxiliar sensors as the pressure ones when they are added to the boards.

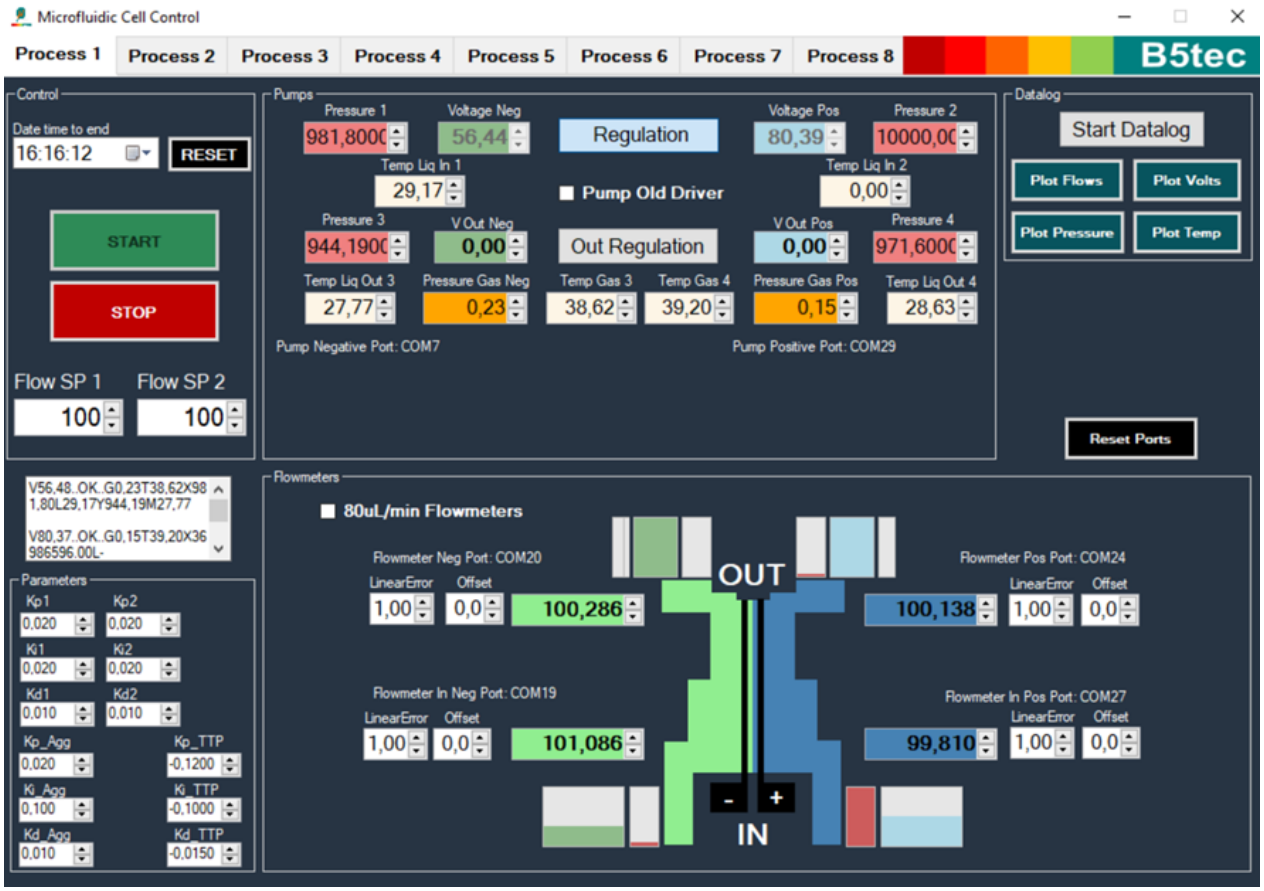

Figure 3.16: Screen capture from computer SCADA application during operation of the microfluidic membraneless RFB. Values from actuators, sensors, control and operation configuration and logging are shown.

3.4 Full Microfluidic Setup

The complete setup develop is shown in the following figures as a scheme and a real image of the system.

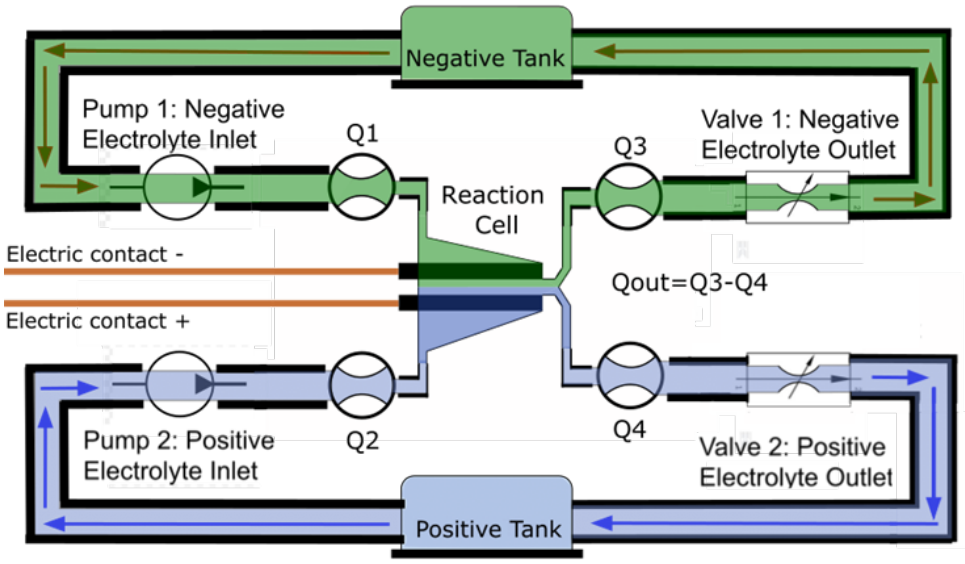

Figure 3.17: System scheme, with actuators and flowmeters for both electrolytes circuits. Flows at the negative and positive inlets are Q_1 and Q_2, and Q_3 and Q_4 at the outlets.

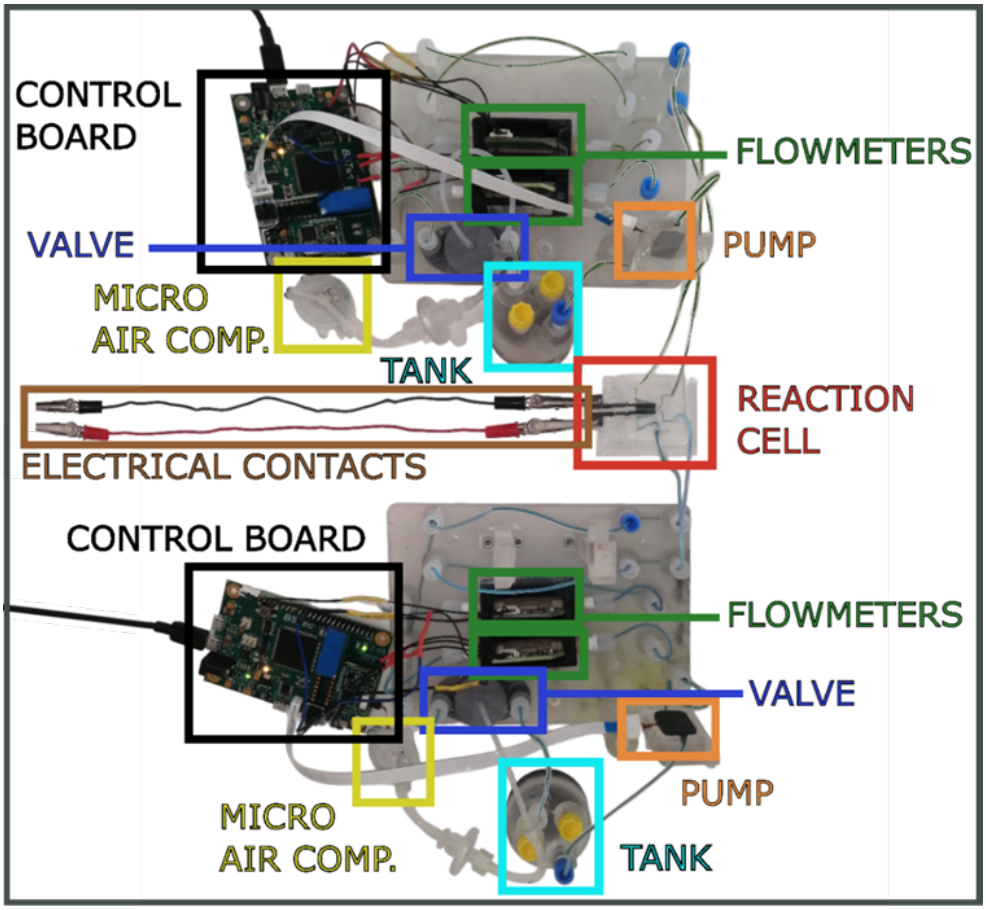

Figure 3.18: Real image of the system, with reaction cell, liquid pumps, air compressor pumps, valves, flowmeters, tanks, control boards and electrical contacts highlighted.

3.5 Conclusions

This chapter details the complete developed microfluidic setup needed for the membraneless battery operation. First, the design of the reaction cell is described, with references to previous works on which it is based. The manufacturing process is detailed, explaining the different elements that form the reactor and the machines and methods needed for each of them. The characteristics of the assembly are described.

Then, the study and the selection of the instrumentation and its electronics is presented. The liquid pumps are the most critical elements of the microfluidic system, and the one that conditions more its performance. Hence, alternatives tested (syringe and gear pumps and PDF systems) are briefly mentioned to explain their particularities and distinctive features, which helps to comprehend the decision of using for the first time in this type of batteries piezoelectric peristaltic pumps. Results of stability, regulation and pulsation tests are presented for these pumps.

Valves have been selected for having control not only of the flow at the inlets but also at the outlets of the cell. Again, commercially available options are briefly mentioned to explain the reason to develop an own design that has proportional regulation of the narrowing of the liquid channel. The 3D printing additive manufacturing method for the valve is cited, and the use of a micro air pump as compressor for activating pneumatically it is also described.

Flow sensors are the most compact, integrable and cost-effective solution available in the market, with enough precision and accuracy. They have integrated measure of temperature, as it also has the pressure sensors which have been used for measuring the air pressure for the valves and the liquid inline pressure in the tubing. Flow sensors are calibrated, and a small computer vision application has been developed to check for any unexpected volume that could mean leakage or flowmeter decompensation.

An electronic control board has been designed to integrate all the instruments of each electrolyte circuit, and the two of them are controlled with the SCADA application ready to operate them via USB communication from a computer. Full system and hardware schemes, together with real images of the system and hardware components are shown.

The selection of the pumping system, valve development and manufacturing, control board design, and integration and software programming of the instruments in the proposed setup is an important contribution of this thesis.

Chapter 4

Electrical model: fluid-dynamic influence

It has already been discussed the lack of electrical models for the microfluidic membraneless RFB, and the similar existing references for conventional models. In this chapter, it is proposed an equivalent circuit for this type of device. This circuit is proposed with special focus on the microfluidic operation influence on its response. This can help to study the importance of a proper regulation, by quantifying the available power differences between different strategies or the mixing and self-discharge losses. It is also a key element in the study of its possible future integration with dedicated power electronics, as the power dynamic response is also modelled using this equivalent circuit. The methodology steps for making this study will be proposing the equivalent circuit structure based on conventional references, analyse experimentally the influence on the different elements of the circuits, experimentally measure in changing conditions the desired metrics, include in the model the variations due to the microfluidic response, and evaluate the model with experimental data.

4.1 Electric Equivalent Circuit

The most common architecture for conventional RFB, and the shared basic elements present in the existing references, is proposed as the electric equivalent circuit basis for the microfluidic design. In particular, the single cell architecture used in [83] is the one that applied for the electric circuit elements distribution.

This circuit depicted in Fig. 4.1, consist of a voltage source that emulates the electromotive force of the battery (E_s), an ohmic resistance (R_0), that models the internal ohmic losses of all the electrical contacts (the electrodes, the electrolytes, and differently from conventional models not the membrane in this case), and an impedance pair in parallel, consisting of a resistance (R_{at}), that takes into account the concentration and activation overpotentials, and a capacitance (C_{dl}), that models the electrical double layers at the contacts between the porous electrodes and the liquid electrolytes. The voltage marked as V_c corresponds to the accessible output of the battery cell. The used architecture is a simple model accounting for

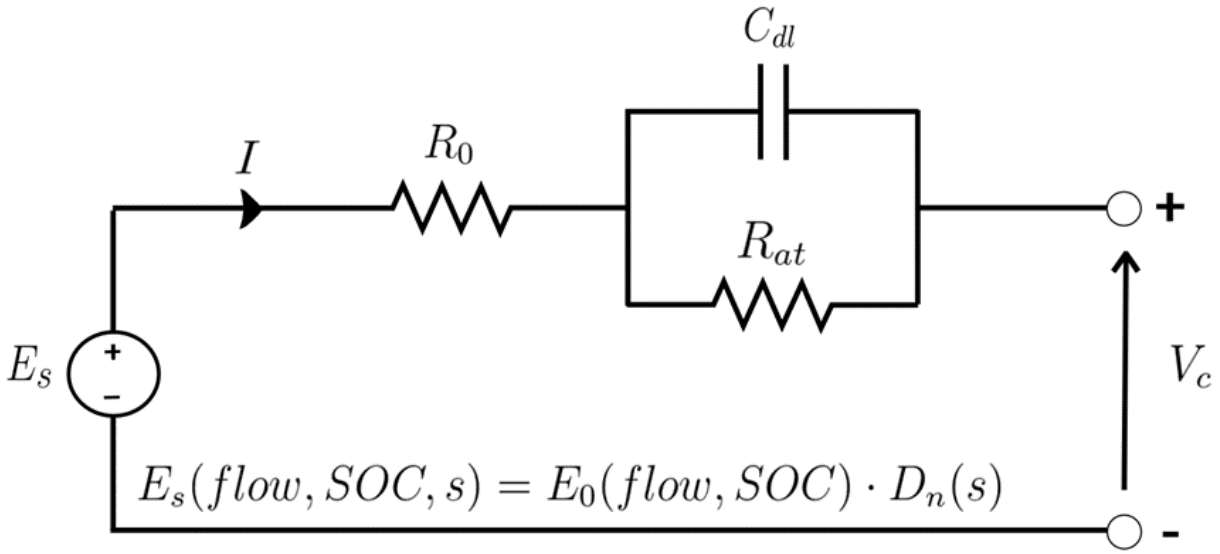

Figure 4.1: The proposed electric equivalent circuit for the microfluidic membraneless RFB.

the more straight-forward effects. It also considers that other processes like shunt currents and auxiliary power consumption (mainly the pumping power), take place independently to this equivalent circuit. This is the same strategy used in [83]. In addition, mass transfer diffusion is excluded, which has been sometimes modelled with a Warburg impedance for other battery models. Electromotive force (E_s), is defined as a function of microfluidic flows configuration, state of charge and time. Also, it is divided into the steady-state value (E_0), that is dependent on flows configuration and state of charge, and the time-dependent dynamics, described with the transfer function (D_n). The functions and dependencies are justified in this chapter.

There are operating conditions that have an impact in the parameters of the circuit. For example, temperature affects the voltage source (E_s). State of charge and concentration also influence not only the voltage source but can divert the resistance R_{at} and capacitance C_{dl}. This can be seen in the expression for the value of the voltage source in open circuit. It is specified by the Nernst´s equation, that in the simplified form as referred in [82] is:

$$E_{OCV} = E^{\theta} + \frac{2RT}{F} ln\left(\frac{SOC}{1 - SOC}\right) \tag{4.1}$$

where E^{θ} is the standard reduction potential for the given electrode, R is the universal gas constant (8.314 $Jmol^{-1}K^{-1}$), T the temperature in Kelvin, F the Faraday constant (96487 $Cmol^{-1}$), and SOC the state of charge of the battery which varies from 0 to 1. This state of charge present in the Nernst´s equation has to be defined. Usually, the definition for any battery [133] is the stored capacity (Q_{stored}) over the total theoretical capacity (Q_{total}):

$$SOC = \frac{Q_{stored}}{Q_{total}} \tag{4.2}$$

Experimentally, it can be measured in the negative electrolyte (SOC_-) as the concentration of the most negative vanadium oxidation state (C_{neg}) over the total concentration of all vanadium species (C_{tot-}) in this negative electrolyte; or equivalently in the positive tank (SOC_+) as the concentration of the most positive vanadium oxidation state (C_{pos}) over the concentration of all vanadium species (C_{tot+}) in the positive electrolyte:

$$SOC_- = \frac{C_{neg}}{C_{tot-}} \tag{4.3}$$

$$SOC_+ = \frac{C_{pos}}{C_{tot+}} \tag{4.4}$$

There might be differences between the two measurements. This can be explained because of imbalances in the reaction. In the ideal scenario, with a device with membrane only protons are exchanged across the membrane, so that concentrations vary at the same rate for both electrolytes. This would be the case where the two equations should express the same SOC. However, in real operation the mentioned imbalances, which are more pronounced in the membraneless case, make the values of the SOC differ. This makes it useful to consider both SOC calculations and use the more limiting one.

Regarding the other variables that modify the electric parameters according to the proposed electric model, flow configuration is now studied in order to determine how best to incorporate the microfluidic effects into the equivalent model structure.

Experiments varying the microfluidic configuration are performed, and to isolate its effects from other operating conditions, the temperature and state of charge are considered constant. Therefore, all the following experiments are performed in a controlled room temperature of 25 ºC and working with an electrolyte at the same state of charge (measured with an open circuit voltage of 1.42 V in all experiments).

In order to identify the values of electrical elements of the equivalent circuit it is used Electrochemical Impedance Spectroscopy (EIS). This experiment makes it possible to identify them model by measuring the electrical impedance response ff a circuit under different excitation frequencies. The measurements are usually presented on a Nyquist plot portraying the real and imaginary part of the impedance. Using identification techniques, the parameters of the selected equivalent electrical circuit architecture can be quantified to fit the curve.

EIS experiment can be used to see which of the circuit elements that modulate the impedance response, i.e. R_0, R_{at}, and C_{dl}, depend on flow configuration. For this aim, the EIS experiment is repeated with several different flow configurations to compare their Nyquist responses in 15 excitation frequencies, starting at 20 kHz and lowering it until 1 Hz. This minimum frequency is not set below because noise starts to be present in the measurement, with diffusion effects becoming relevant, and therefore EIS values being not reliable for a reactor with flow through it, as it is the case. This effect has already been reported in the literature, as for example in [134], where frequency dependence of EIS measurement accuracy is explained. Furthermore, this frequency range is the commonly used for EIS experiments with microfluidic redox reactors [44].

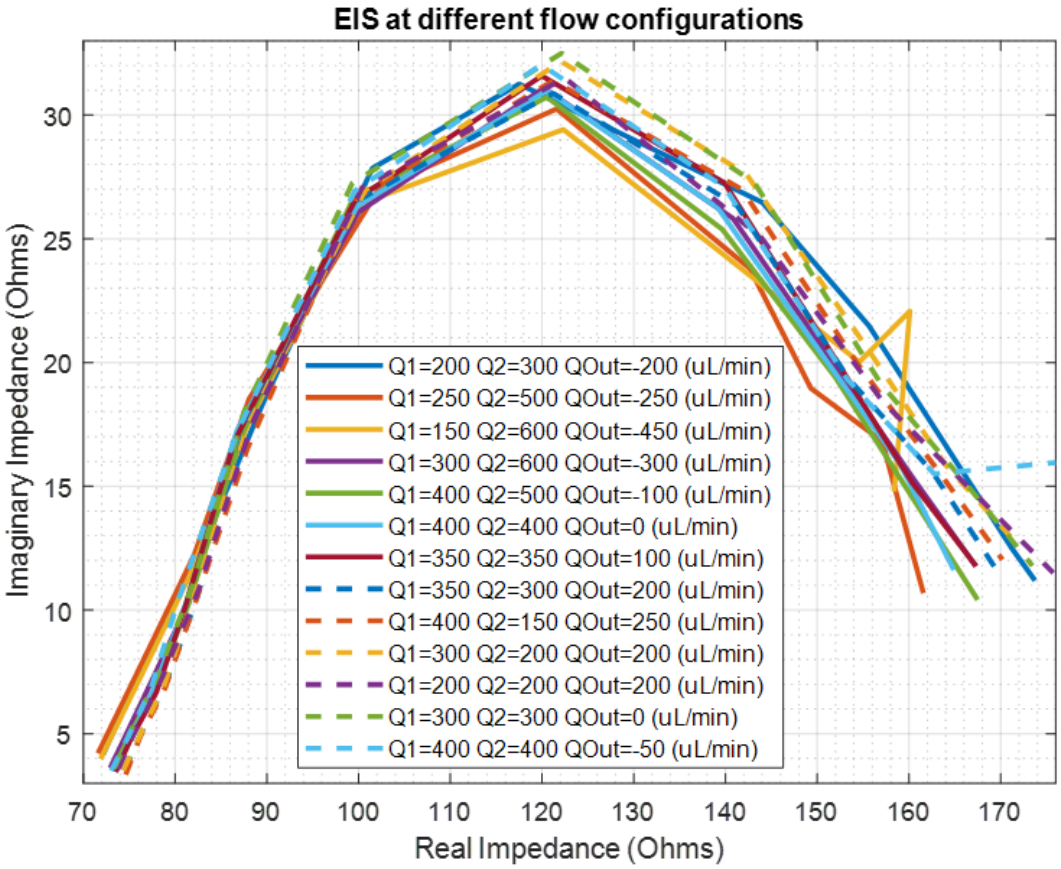

Figure 4.2: Nyquist plot of the collection of EIS experiments performed to measure the battery response under different flow conditions.

The flow configurations and their EIS response are shown in Fig. 4.2 The flow configurations are described by the negative and positive inlets (Q_1 and Q_2 respectively) and the difference of the negative minus the positive outlets ($Q_{out} = Q_3 - Q_4$). The microfluidic operation does not include recirculation in this case to make sure the state of charge is constant between measurements. It can be observed the effect of the noise for lower frequencies, and how at the final values at the right of the graph there are some noisy values even before going below the final frequency of 1 Hz. It is important to highlight that changes in the equivalent electrical elements due to flow configurations would be expected to modify the impedance response at different frequencies. Hence, the entire EIS curve would be distorted if flow configuration affected them.

However, when observing the figure and comparing the data obtained at different flow configurations, it is observed that impedance response is almost the same in all cases. Besides some small deviation, that are common when performing EIS experiments even under the same conditions, the tendencies and significant values of the curves are very similar. Moreover, the identified values for the impedances ($R_0 = 75.33W$, $R_at = 50.96W$, and $C_dl = 12\mu F$) are constant. This means that the fluid dynamics does not significantly affect the impedance

parameters of the circuit.

It can be noted that the identified parameters for this EIS set of experiments give impedance values very distant to the ones expected from an optimal reactor. This is because the cell used for microfluidic evaluation is a control model different from the final design used in the project in which the thesis takes part. As the main objective is to develop and validate an electric modelling scheme and evaluate the relative microfluidic influence this is considered substantiated.

Considering that in real operation it has been observed that changes in the configuration of flow values and the fluid dynamics modify the electrical output prominently. As a straightforward demonstration for this it is designed a constant voltage discharge experiment. In this experiment, all operation conditions are again constant except the flow values. These are the same premises as for the previous EIS experiment. Also, in order to make sure that the state of charge of the electrolytes does not change, the electrolytes are not recirculated to the tanks at the cell outlets, so the volume and the concentrations in the tanks are not renewed.

Throughout the entire test duration, the discharge voltage is fixed at 0.7V (under the open circuit voltage of 1.42V), and the output current is measured. Accordingly, current variations stand directly for output power of the battery. Flow configurations are modified dynamically in steps of around 30 seconds to ensure changes in current are observable.

In this experiment (Fig. 4.3), it becomes evident that there are electrical changes due to flow configuration variations. Both steady state value and the transient time dynamics of the current are driven by the flow steps. Given the electrical equivalent circuit, and since EIS measurements from previous experiment did not show significant changes in impedance value with varying flow configurations, microfluidic influence has to be modelled in the voltage source. This is the reason why the flow was presented as a variable for the voltage source function. Therefore, the current variations measured at the cell output terminals are explained by this net power variation in the source.

4.2 Available Steady State Power

After it has been proven the influence of microfluidics on cell power, and that it can be introduced as a variable for the voltage source function of the equivalent circuit, in this section it is modelled how it affects the steady state value of this power.

I must be considered that the voltage source is also a function of the state of charge of the electrolytes and the cell design. Flow configuration effects are isolated from these other variables from the measurement. To do so, in each experiment the electric power variables are converted to a relative measure from 0 to 1. This means dividing each value by the maximum for that particular SOC and cell design. The maximum power values are measured experimentally at the optimal flow conditions: those obtained with the electrolytes interface cantered and with the maximum necessary electrolyte renovation in the reactor. It is considered for this cell design that 800 $\mu l/min$ is effectively above the maximum renovation needed. Using these relative measurements allows to model the influence of fluid dynamics and how flow operation affects battery performance, rather than modelling absolute power, which is

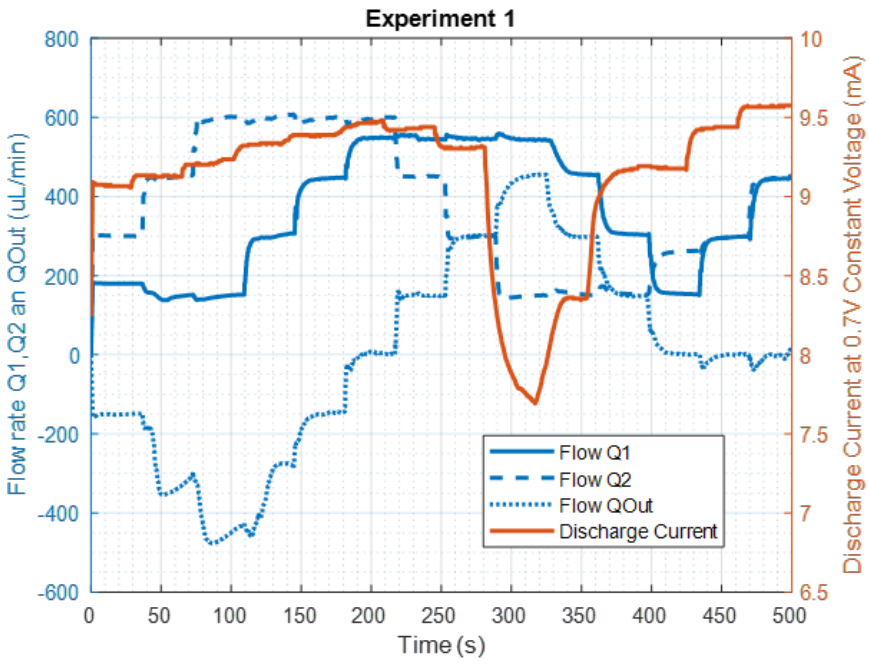

Figure 4.3: Experiment showing microfluidic influence on electric response. Constant voltage (0.7V) discharge, with different flow configurations represented on the left axis by the three flows, and the maximum given electric current on the right axis.

out of the scope of this work and electric model.

On another note, measured power is different from the equivalent power at the equivalent power at the voltage source of the equivalent circuit. This is because the steady-state power measurements are made at the battery output terminals. Therefore, since experiments are performed by measuring the current at constant voltage at the output terminals, the equivalent steady-state source voltage is calculated using:

$$E_0 = V_c + I.Z_{circuit} = V_c + I.(R_0 + R_{at}) \tag{4.5}$$

This means that for constant voltage experiments, both the influence of the fluid on the steady-state source voltage and the battery power can be described and studied from the response of the electric current to the fluid operation.

Model Based on Conventional Approach

Using conventional RFB approach and analytical electrochemical expression it is deduced an expression relating electrical current to flow rate. First, the introduced Nernst´s equation (Eq. 4.1) describes the open-circuit source voltage of the equivalent circuit. Also, Faraday´s law relates the amount of chemical reaction of the active species (i.e., the volume of electrolytes) to the magnitude of the electrical charge passing through the electrodes. Faraday´s expression can be applied to a time differential [135], and obtain an equation that defines the minimum electrolyte flow for a given electric current:

$$Q = \frac{2bN_{cell}I}{zFc_{vanadium}SOC_{min}} \tag{4.6}$$

where Q is the calculated electrolyte flow rate that guarantees the minimum species renovation in the reactor for a desired electric current, b is a sign factor that is 1 for charging and -1 for discharging, N_{cell} is the number of reactor cells, $i(t)$ is the net charge/discharge current, z is the number of electrons in the reaction (1 for the vanadium RFB), and SOC_{min} is the minimum state of charge of the electrolytes entering the reactor (in case they are different for each electrolyte).

This expression can be rearranged to show that the maximum current is limited by the minimum inlet flow rate of the electrolytes:

$$I = Q_m in\frac{zFc_{vanadium}SOC_{min}}{2bN_{cell}} \tag{4.7}$$

Besides this, it is known that the maximum current for (4.7) must match the value obtained from Nernst´s equation (4.1) for the open circuit voltage, and the expression in (4.5) rearranged. Experimentally, as it has been already explained, it is measured using a high minimum inlet flow rate (above 800 $\mu l/min$) so that it does not limit the reaction.

$$I_{max} = \frac{E_{OCV} - V_c}{R_0 + R_a t} \tag{4.8}$$

The expression in (4.7) indicates that, at a specific state of charge, at any instant k, the value of the current depends on the minimum input flow for the renewal of the electrolyte's species multiplied by a constant factor. Considering constant temperature and state of charge, the relative current I_r is proportional to the minimum input flow by a factor K_F. The relative current is defined divided by the maximum current for the working state of charge.

$$I_r(k) = \frac{I}{I_{max}} = Q_{min}(k)K_F \tag{4.9}$$

This approach only considers flow influence as a minimum value for species of the electrolytes renovation. By using only expressions for conventional batteries. Nevertheless, it is intuitively incomplete for microfluidic membraneless designs, where the flows configurations define the interface depletion and positioning. It can be proven in a constant voltage discharge experiment, without recirculation so that the state of charge of the electrolytes entering the reactor remains constant, and where the minimum inlet flow rate is kept at a fixed value while the ratio of the inlets is changed. In this scenario, the current is measured, and if the expression from (4.9) is correct, it should be constant. The results are shown in Fig. 4.4.

It is demonstrated that equation (4.9) is incomplete for the microfluidic membraneless case.

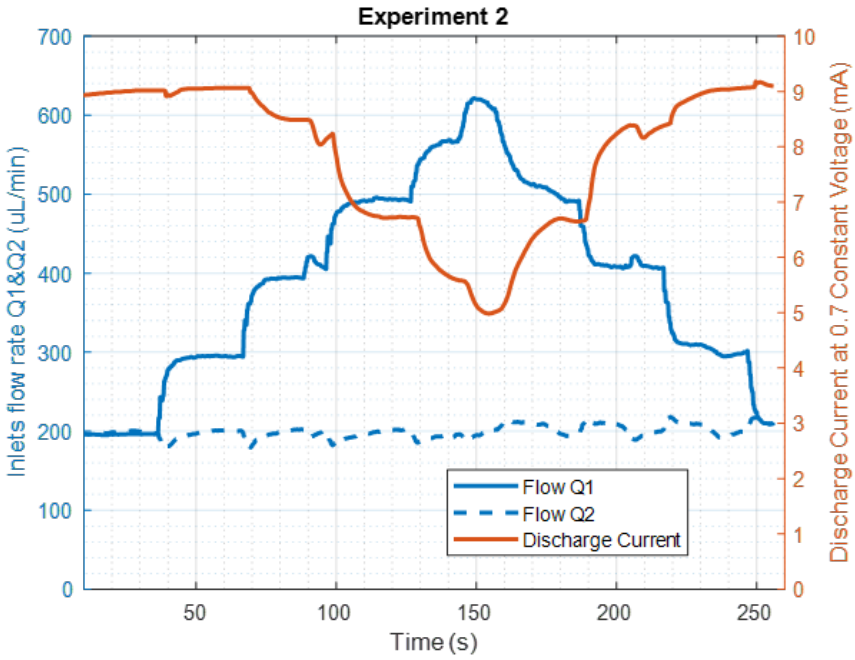

Figure 4.4: Constant voltage discharge experiment, with one of minimum inlet flow rates constant and modifying the fluidic interface by changing the other inlet flow (left axis), and relative current output (right scale).

Microfluidic Membraneless Model

It is deduced that minimum input flow is not the only variable that defines the reactor power and flow analysis must be expanded for the microfluidic membraneless model. In this cell designs, operating the different electrolytes flow at a correct ratio is critical to guarantee that these laminar flows form a centred interface that avoids electrolyte mixing and minimizes advective mixing. Moreover, previous experiment shows that interface deviation due to changes in the ratio between the inlet flows influences the output current and, consequently, the available cell power. Considering this effect, and similarly the effect that flows ratio at the outlets may have, it is proposed an equation that includes interface effects for an instant k relative to the maximum current:

$$I_r(k) = Q_{min}(k).K_F - ratio_{In}(k) * K_{ratioIn} - ratio_{Out}(k) * K_{ratioOut} \tag{4.10}$$

where $K_{ratioIn}$ and $K_{ratioOut}$ are constants to empirically quantify the power losses caused by interface deviation produced by inlet and outlet flow ratios respectively. These ratios at the input and output are defined as:

$$if \left| \frac{Q_1(k) - Q_2(k)}{(Q_1(k) - Q_2(k))/2} \right| > Threshold1: \quad ratio_{In}(k) = \left| \frac{Q_1(k) - Q_2(k)}{(Q_1(k) - Q_2(k))/2} \right|^{exp}$$
$$else: \quad ratio_{In}(k) = 0 \tag{4.11}$$

$$if \left| \frac{Q_{out}(k)}{(Q_1(k) - Q_2(k))/2} \right| > Threshold2: \quad ratio_{Out}(k) = \left| \frac{Q_{out}(k)}{(Q_1(k) - Q_2(k))/2} \right|^{exp}$$
$$else: \quad ratio_{Out}(k) = 0 \tag{4.12}$$

This expression tries to reproduce the empirical behaviour observed in experiment from Fig. 4.4, where it is observed that the interface deflection due to flow ratios differences does not affect the output current until a threshold is reached, at which point an exponential loss occurs. This threshold, as well as the exponential behaviour, and the constants of equation (4.10) are identified from empirical experiments, using grey-box identification methods. The result is a grey-box mechanistic model, which as it was presented in the introduction uses fundamental knowledge of the process and then unknown parameters are estimated from experimental data.

Results of Models

First, the unknown parameters of the greybox model are identified. The regression has been implemented using the adaptive subspace Gauss-Newton search [95] included as a function in the tools for system identification in Matlab. Also, it is defined a fitness function for evaluating the models with real data, that is:

$$fit = 100 \left(\frac{|y - \vec{y}|}{|y - mean(y)|} \right) \tag{4.13}$$

where y is the actual output data vector used as a reference, and $\hat{y}$ is the model output when excited with the actual input data. Regarding the model from the conventional approach and analytical expression from Faraday's law and Nernst´s equation presented in (4.9), its fitness is tested in the experiment from Fig. 4.5.

It is observed that the model only partially reproduces the trend of the actual relative power and fails to model the real response. The best fit is not satisfactory, and even when small corrections to the model (offset values) are introduced in an attempt to mitigate the deviations, it still does no reflects the experimental steady-state power values. The percentage of fit measurement is also low (≈30%).

It becomes evident the need for a more complete model, that includes quantification of the interface positioning. The model proposed in this thesis, detailed in expressions (4.10) to (4.12),

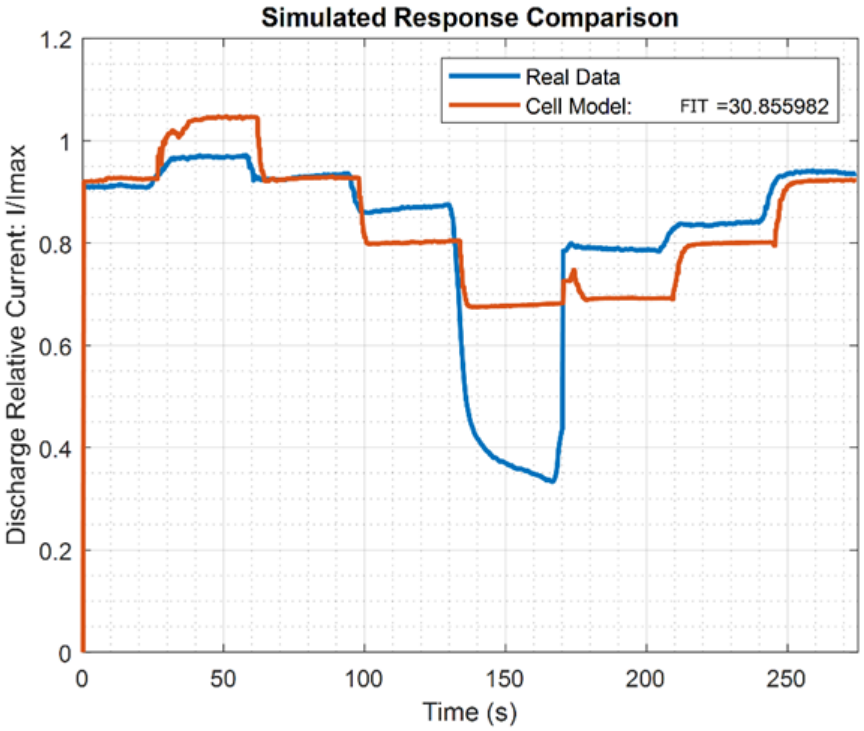

Figure 4.5: Simulated response for the model of equation (4.9) and real experimental data. The goodness of fit measurement is performed and indicated in the legend in percentage.

includes the interface influence added to the factor accounting for the minimum electrolyte renovation. The unknown parameters of the model are identified with the cited Gauss-Newton regression algorithm. Table 4.1 presents the best-found values for the parameters and that are used to evaluate the response with the same real data in Fig. 4.6.

Symbol	Quantity
K_f	$5.5423.10^{-4}(\mu l/min)^{-1}$
$K_{ratioIn}$	0.0928
$K_{ratioOut}$	0.0781
Threshold1	0.5
Threshold2	0.5
Exp	4

Table 4.1: Values of the parameters of the proposed equations

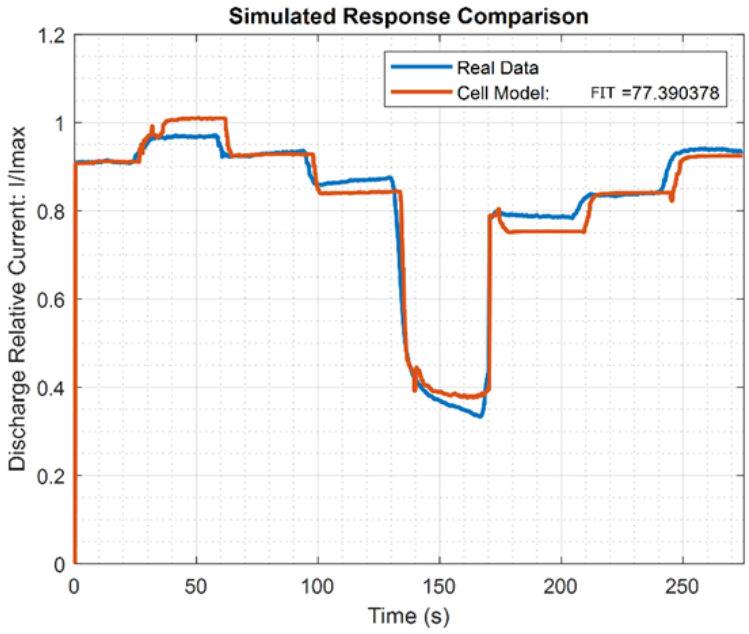

Figure 4.6: Simulated response for the proposed model from equations (4.10)-(4.12) with parameters from Table 4.1, and actual steady-state relative current experimental data. The fitness measure is indicated in the legend.

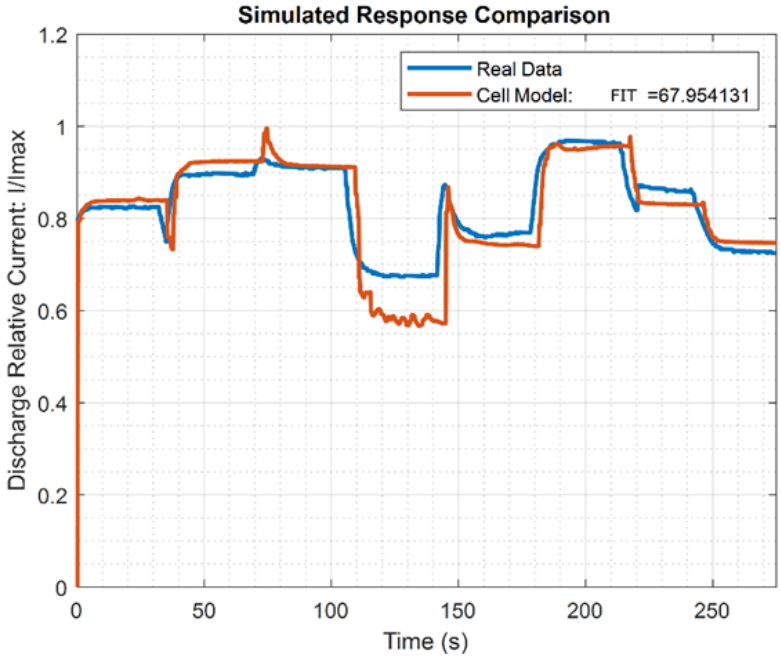

Figure 4.7: Simulated response for the proposed model from equations (4.10)-(4.12) with parameters from Table 4.1, and actual steady-state relative current experimental data in different experiment. The fitness measure is indicated in the legend.

The model with the identified parameters is able to accurately represent the actual relative

current performance of the battery, with fit measurement of around 77%. These parameters are cross-validated with data from a different experiments where flow operation is different and performed to the same cell after hours of operation, which is represented in Fig. 4.7.

The fitness of this second experiment demonstrates that the identified model parameters are extendable for different conditions and after hours of operation time. The fitness measure is slightly lower than for the first experiment of identification and validation, but it is still of the same order and much better than the conventional approach. The model response is considered satisfactory and the parameter values adequate. It should be noted that microfluidic devices, such as the reaction cell used in these experiments, suffer from inconsistency due to multiple factors (bubbles in the porous electrodes, pressure fluctuations, substrate deformation, etc.) [72], [73]. This reinforces the relevance of the proposed model, and the fitness measurements validate the values of the identified parameters. The model is valid for estimating relative electrical power from fluid dynamics operation data.

4.3 Power Dynamic Response

The dynamic response of the output power is studied separately from the steady state value. Based on the proposed equivalent electric circuit, the set of impedances introduce a dynamic response between the voltage source and the measured output. Beyond those dynamics, there is also a dynamic response of the voltage source responding to the microfluidic configuration that has to be modelled. This is because the steady state power values previously modelled do not change instantaneously but are a time dependant function. Therefore, the dynamic response function must include both impedance and voltage source to flow dynamics.

The importance of the dynamic model is that it defines how the fluid dynamics must operate for any desired power transient response. This is how microfluidic operation must adapt to make fast and stably power available in the battery (both supplying it in discharge mode and converting it to energy storage when charging). This becomes all the more relevant in applications that require frequent changes in power demand. This is the case typically for intermittent energy sources such as wind and solar photovoltaic (very common applications for RFB). The power electronics must be designed considering the model of the dynamic response of the battery to integrate it into the particular application.

Regarding the first part of dynamic response, the impedances already defined in the equivalent electric circuit, the transfer function is derived from the circuit from Section 4.1. As a reminder, it is modelled by curve fitting the EIS measurement that parametrizes the resistor and the capacitors of the circuit. This transfer function is:

$$\frac{E_0(s)}{I(s)} = \frac{\frac{R_0+R_{at}}{R_{at}C_{dl}} + R_0 s}{\frac{1}{R_{at}C_{dl}} + s} \tag{4.14}$$

This transfer function of the impedance is used to transform the measured output current function into the curve at the voltage source. Then, this data curve can be used for the modelling of the voltage source dynamics in relation with the fluid dynamics. The transfer

function proposed to model these dynamics is:

$$D_n(s) = \frac{E_s(s)}{E_0(s)} = \frac{1}{1 + \tau.s} \tag{4.15}$$

where E_s is the instantaneous value of the voltage source, E_0 is the steady-state value corresponding to the power as modelled previously in the steady-state part, and τ is the time constant. It has been empirically observed that the parameter τ is different for increasing and decreasing flow rate changes. The equation (4.15) is proposed to imitate a low-pass filter response, due to the experimental behaviour examined in the experimental data.

The proposed model for transient relative electric power dynamics is validated using experimental data. This data is generated performing periodic flow configuration steps. Consequently, this creates power steps at the measured output current. The flow configuration steps are made at different conditions of settling time stability so that the power dynamics are also diverse. These different experimental conditions are used to find the optimal value of the time constant defined in (4.15). Using again Gauss-Newton regression algorithm is found that the fitness is improved when using different values for increasing and decreasing flow dynamics ($\tau = 1$ and $\tau = 1.333$ respectively).

The fit to the different experimental curves is calculated. These experiments are represented in Fig. 4.8, where the minimum inlet flow rate is also plotted graphically for each experiment. This is displayed to better understand the different operating conditions and how their dynamics translate into the power output.

It can be observed that the model fits satisfactorily the real response in the three different experiments (each one representing a different dynamic). The fitness measurements are calculated using equation (4.13), and they have values in the range of 70-80%. It is considered demonstrated that the proposed dynamic model with the two different identified values of the time constant reproduces well the real dynamic response, with overshoot and settling time close to the real ones.

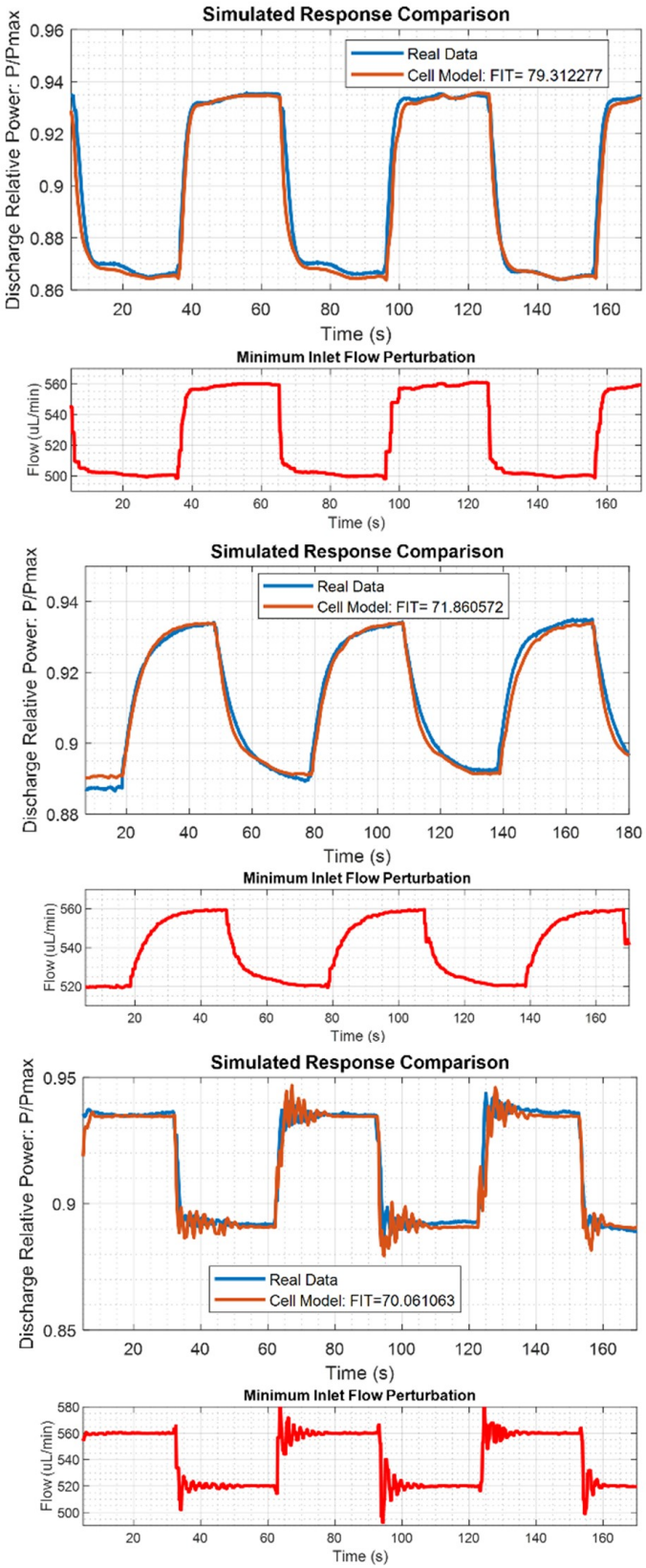

Figure 4.8: Simulated responses for the dynamic model and three real experimental transient power data. The fitness measure is indicated in each legend.

4.4 Mixing Losses

Mixing and self-discharge losses affect severely the efficiency of membraneless RFB operation and modify the state of charge, affecting the electrical response. Although the relation between these losses and microfluidic operation is intuitively direct, previous works as explained in Section 2.2.1 have considered the reaction cell to have always a perfectly centered interface with equilibrated flow rates at the inlets and outlets. These works can provide analytical expressions that bound the crossover diffusion losses [[61], or experimentally measure how the resident time within different cell designs affect them [66], but do not evaluate how different flow configuration and fluid dynamics modify the total capacity loss (due not only to the diffusion self-discharge but also to mixing).

In this thesis, a first approach is made to correlate fluidic operation and mixing and self-discharge. The approach is to consider the measured volume crossover directly proportional to the mixing part of the losses and its change in species concentration in the electrolytes. Diffusion mixing, which occurs at the interface of the two electrolytes due to the difference in species concentration, is also considered and can be identified when the volume mixing is zero. The diffusion part varies with the resident time, decreasing as flow rates increase and this time is smaller. However, previous work from [66] indicates that it has an asymptotic behaviour after exceeding the order of tens of $\mu l/min$. This can be observed in Fig. 4.9.

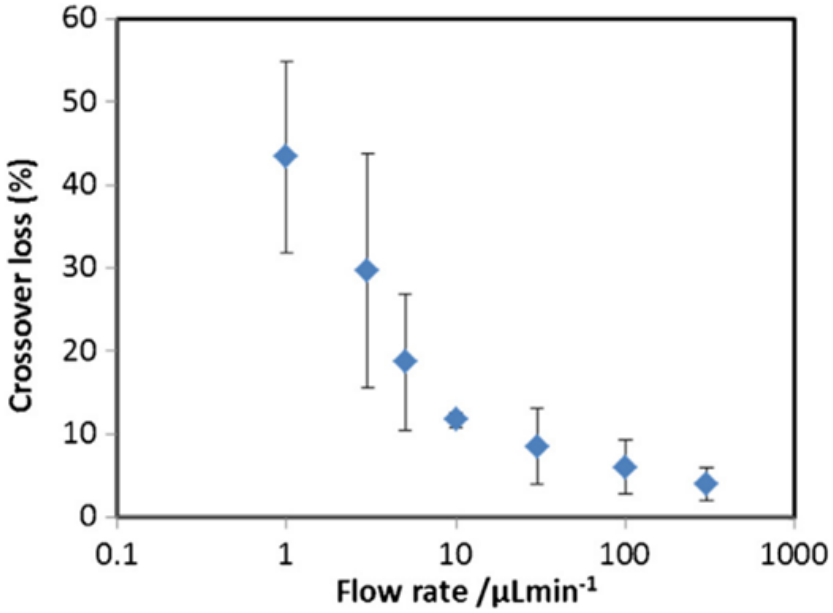

Figure 4.9: Experimental measurements of the self-discharge losses from [66], at different equal inlet flow rates from 0.1 to 300 $\mu l/min$ and at 90% states of charge, using logarithmic scale.

Considering that flow rates used in this work are maintained always above 100 $\mu l/min$ the diffusion effect can be considered constant. Therefore, the equation correlating the state-of-charge loss and self-discharge with volume mixing is determined as:

$$SOC_{loss} = Diff + \%V_{mix} * K_m \tag{4.16}$$

where $Diff$ is the fixed self-discharge loss mainly due to diffusion, K_m is a linear factor representing the proportionality between the state-of-charge loss (SOC_{loss}) and the percentage of mixed liquid volume ($\%V_{mix}$). This percentage is:

$$\begin{aligned} &if (V_{Out1} - V_{Out2}) > (V_{In1} - V_{In2}) : \\ &\qquad \%V_{mix} = \frac{(V_{Out1} - V_{Out2}) - (V_{In1} - V_{In2})}{2 * V_{Out1}} * 100 \\ &else : \\ &\qquad \%V_{mix} = \frac{(V_{Out1} - V_{Out2}) - (V_{In1} - V_{In2})}{2 * V_{Out2}} * 100 \end{aligned} \tag{4.17}$$

Here, V indicates the volumes of the system, and the subscripts indicate whether the volume is measured at the inlet or outlet, and the numbers whether they belong to the negative or positive side (1 and 2 respectively).

The experimental scheme for model validation is illustrated in Fig. 4.10. This configuration allows empirical correlation between volumetric mixing flowmeter data and the change in state of charge provided by spectrophotometers. These devices provide species concentration (state of charge) measurements using spectra calibration reference curves for each vanadium species [67],[136]. Since the electrolytes at the inlets are known to be at a certain state of charge, it is possible to calculate the change in species concentration.

In the experiments using this configuration, electrolytes at oxidation states V^{3+} and V^{4+} have been used for the negative and positive side, respectively, to simplify the spectrum analysis. Consequently, in order to be consistent with equations (4.3) and (4.4), the state of charge for each electrolyte is calculated as the C_3 and C_4 concentrations of those two oxidation states:

$$SOC_{-} = \left(\frac{C_3}{C_3 + V_4}\right) \tag{4.18}$$

$$SOC_{+} = \left(\frac{C_4}{C_3 + V_4}\right) \tag{4.19}$$

The loss of state of charge for equation (4.16) is calculated as the initial state of charge (that is guaranteed to be equal in both electrolytes) minus the minimum of the SOC_{-} and SOC_{+} measured at the outputs.

This proposed mixing experiment is performed with several different flow configurations obtaining diverse electrolyte mixtures. For each configuration, the mixing percentage by

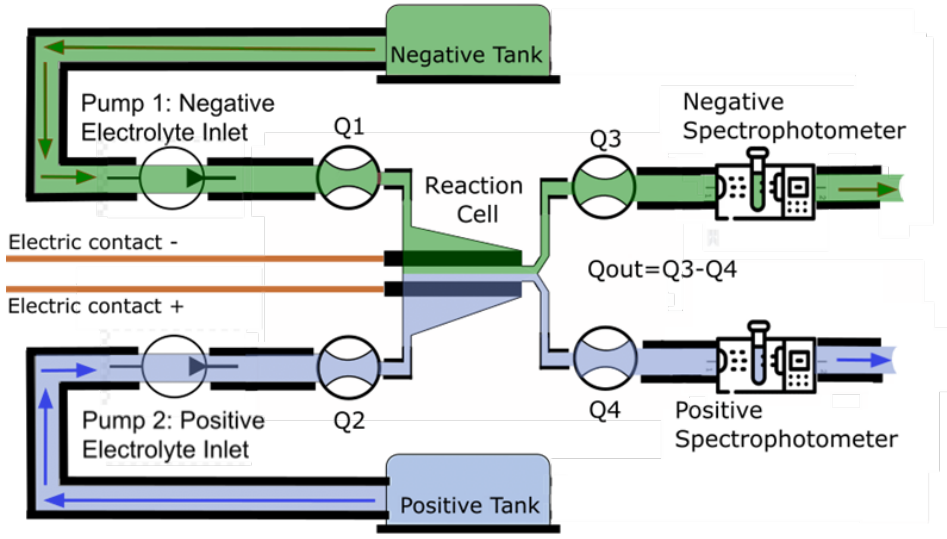

Figure 4.10: System configuration scheme for correlation between flow and mixing and self-discharge, with pumping system, reaction cell, flowmeters, and spectrophotometers. The cell outlets are not recirculated to preserve SOC at the tanks.

volume measured integrating flowmeters values, and state of charges from spectrophotometer are calculated. Considering that the electrolytes at the inlets are at full state of charge, the state-of-charge losses are obtained by subtracting the limiting value of the two SOC values from the spectrophotometer at the outlets.

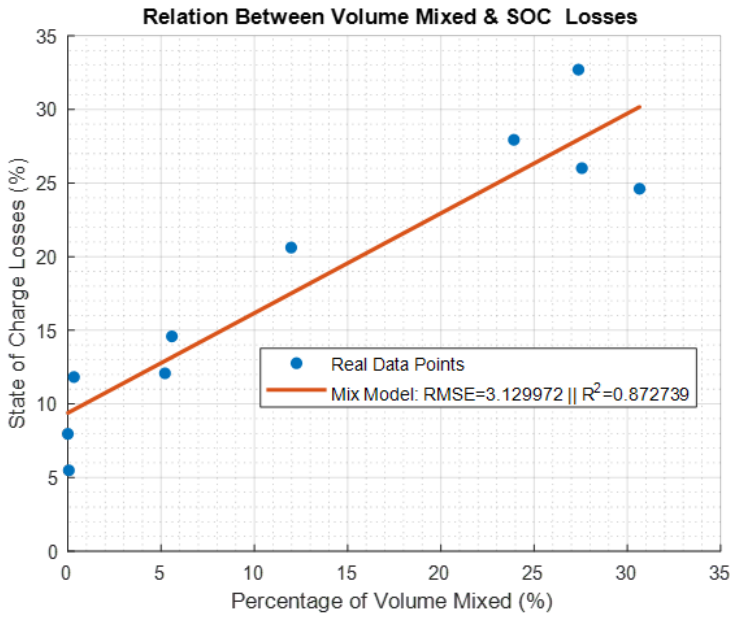

Figure 4.11: Relation between SOC losses and mixed volume, with experimental points and linear curve model fit indicated. Root-mean-square error and R^2 measurements are shown in the legend.

The results of the experiments are shown in Fig. 4.11, together with the plot of the linear equation (4.16) with the parameters $Diff = 9.394$ and $K_m = 0.678$ adjusted to minimize root-mean-square error (RMSE). The value for the R^2 coefficient to the datapoints is close to 0.87, indicating a quality replica of the real response.

It is demonstrated that the model reproduces the actual behaviour of the losses. The volume crossover together with the diffusion of active species can explain the main losses in the state of charge. The constant loss due to diffusion is proved to be one of the main drawbacks of membraneless operation. Furthermore, it is demonstrated that minimizing the volume error with proper flow control is critical for optimal battery performance.

4.5 Conclusions

In this chapter an electrical model for microfluidic membraneless RFBs has been proposed and validated experimentally, with special consideration to the fluidic influence on its response. The main conclusions are:

- This works presents for the first time an electric equivalent circuit model for micro membraneless redox flow batteries. The model is based on conventional RFB references that present similar architecture for the electrical circuit.
- The equivalent circuit consists of a voltage source that emulates the electromotive force of the battery (E_s), an ohmic resistance (R_0) accounting for the internal ohmic losses of the electrical contacts (the electrodes and the electrolytes), and an impedance pair in parallel, consisting of a resistance (R_at), that models the concentration and activation overpotentials, and a capacitance (C_{dl}), that models the electrical double layers at the contacts between the porous electrodes and the liquid electrolytes.
- The voltage source value is defined as a function of state of charge, flow configuration and time.
- The state of charge of the battery is defined as a coefficient of the active species concentration over the total concentration of all vanadium species for each electrolyte. As there are two definitions (one for each electrolyte) that may differ due to unbalancing, it is used the minimum of both in practice.
- The model studies the fluidic dynamic influence on its electrical response, and it demonstrate how critical is for an optimal electric performance by empirically showing high available power variability with respect to changing flows. It studies three metrics specifically: steady state power, power dynamics, and losses due to self-discharge and mixing.
- It demonstrates empirically which elements of the equivalent circuit are affected by this fluid dynamics with electrochemical impedance spectroscopy. This EIS experiment shows no change in the impedance response for a set of diverse flow configurations, which demonstrates that impedances are not the cause for the power variability. Therefore, the voltage source is the only possible element affected by fluidic operation that changes available power.

- Conventional approach for modelling fluidic influence on steady-state available power considers Nernst´s equation and Faraday law. Nernst´s equation defines open circuit potential based on state of charge (and temperature but it is considered constant in this study). Faraday law can be used for correlating electric current with species renovation in the reactor (minimum inlet flow).
- It is demonstrated that the conventional approach for steady state power is incomplete, as for the membraneless scenario available power is not affected only by limiting inlet electrolytes flow, but also by the generated laminar interface of the electrolytes through the reactor.
- The microfluidic membraneless RFB proposed new model for steady state power considers interface depletion using inlet and outlet flows ratios. The effect of the incorrect positioning of the interface is null for small deviations and then presents an exponential loss in the available power. This is a mechanistic greybox model that has some unknown parameters that are identified using Gauss-Newton regression.
- The new proposed model with identified parameters shows a good resemblance for the real steady-state power value. A fitness measurement based on the distance between real and simulated data vectors is defined. The model performs with fit values of 68-77%, more than the double for the conventional model.
- This work also models the dynamics of this available power. The model consist on the dynamics due to the impedances in the defined equivalent circuit and identified with EIS experiments, and the dynamics on the voltage source due to fluidic conditions. The transfer function for the impedance is defined by the electric circuit, and the one for the fluidics is proposed to have similar to a low-pass filter based on observed behaviour. The time constant for this low pass filter is defined as different for increasing minimum inlet flows than for decreasing ones. Both values are identified using Gauss-Newton regression again, and model is validated under different operating conditions that produce different power dynamics conditions in terms of stability and speed. Fitness measurements are calculated using the same expression and are in the range of 70-80
- The third modelled metric refers to discharge losses, including diffusive self-discharge and mixing due to volume crossover. The diffusion is considered constant as previous works empirically demonstrated an asymptotic behaviour for the working flow rates range. The rest of the state of charge losses are considered to be caused by volume mixing. For this second losses data from flowmeters and spectrophotometry is correlated in different single pass experiments, what allows to find the linear relation between flow and SOC losses. The modelled equation joining diffusive constant losses and mixing proportional ones is validated calculating the R^2 coefficient to the real data points ($R^2 \approx 0.87$).
- The proposed model can help for further studies on optimization of membraneless redox flow batteries design and operation, and future power electronics integration.

The design of the proposed electrical equivalent circuit, the model considering fluidic influence on its elements, and its experimental validation is one of the

main contributions of this thesis.

Chapter 5

Fluid dynamic modelling

In Chapter 4, it is studied the electrical model of the battery, and how the microfluidic operation affects it. Now, this chapter is focused on developing a design methodology for a microfluidic model that can emulate the real response of the micro laminar flows in regard to the active elements of the instrumentation setup.

This modelling is important to predict the flow configuration based on the microfluidics actuators operation. This flow configuration itself determines electrical response as previous chapter has demonstrated. It is also relevant to design the control strategy of the active pumping elements, allowing to simulate the system response and to mathematically calculate and adjust the regulation parameters of the control design.

In this chapter, first the system variables are described based on the microfluidic setup explained in Section 3.4. Input and output variables of the system are determined and explained, as well as the state variables for the state space representation. Then, based on theoretical analysis of microfluidics dynamics principles and empirical knowledge of the system, equations describing state variables response are proposed. The unknown parameters of the system are identified for the greybox model. Due to variability and stochasticity of microfluidics, correction factors are proposed to adjust the equations. These correction factors are calculated in real time using Extended Kalman Filter (EKF). The models with and without the real time adjustment are validated experimentally.

5.1 System Configuration

In section 3.4 the system microfluidic setup is presented. As a summary, in this configuration pumps are located at the inlets of the cell, pumping each of the electrolytes from its respective tank in a regulated flow rate. These piezoelectric pumps introduce complexity in the control, but provide flexibility to adapt pumping actions faster, and reduce pulsation compared to syringe ones. The full control of the interface of the liquids is achieved controlling also the flows at the outlets, placing one valve in each of them to regulate the pressure drop. The valves are activated using air pressure regulated by varying the power of a micro air compressor. The flows (inlet negative flow Q_1, inlet positive flow Q_2, outlet negative flow Q_3, and outlet

positive flow Q_4) are measured using the microfluidic flowmeters in each of the inlets and outlets.

The system is modelled in a state space representation, so first variables need to be defined. The inputs are defined as the voltages of the pumps and the differential voltage of the valves, and the state variables, which coincide with the outputs, as the inlets flows and the difference between the outlet flows, as shown in (5.1) and (5.2). The reason for defining the system variables as differences is trivial for the output: the sum of the input flows must be the same as the sum of the output ones, then knowing only three of them fourth is also known. Equivalently, knowing the inputs and the difference between the outputs, the two outputs are calculated in a straightforward manner. The reason for choosing the third input as the differential voltage of the valves is to introduce an additional constraint: at least one of the valves must be always completely opened (power of the air compressor equal to zero). This constraint makes the system compatible determinate (3 variables and 3 equations). The solution of the system also becomes the one that requires least actuator power, as only one valve generate pressure drop, so it is generated the minimum additional pressure drop for the pumps.

$$U = \begin{bmatrix} U_1 \\ U_2 \\ U_3 \end{bmatrix} = \begin{bmatrix} Pump1Voltage \\ Pump2Voltage \\ Valve1Power - Valve2Power \end{bmatrix} \tag{5.1}$$

$$X = \begin{bmatrix} X_1 \\ X_2 \\ X_3 \end{bmatrix} = Y = \begin{bmatrix} Y_1 \\ Y_2 \\ Y_3 \end{bmatrix} = \begin{bmatrix} Q_1 \\ Q_2 \\ Q_3 - Q_4 \end{bmatrix} \tag{5.2}$$

It should be noted that the system has some intrinsic problems that make its operation complex. As it has been mentioned, it is common in stable flow microfluidic applications [72], [73] that bubbles or variable wettability in the surfaces and in the internal porous media of the cell modify the pressure drop across the fluidic channels and elements. Furthermore, these issues produce micro actuators do not have a repeatable response. For example, pumps do not impulse always the same flow at the same operation conditions (applied voltage) and ambient conditions (same electrolyte, room temperature and humidity, etc.). The reason for this is the explained bubbles and wettability, that in the case of the pumps is enhanced due to the fact that they have internal passive valves in the chambers that can fluctuate their micro internal position and response. Besides, the valves membranes have strong inertias and deflection hysteresis. Together with these stochastic conditions, the dynamics also present a nonlinear behaviour. Finally, external conditions of the system can change the dynamic response of the actuators and the liquids, mainly the change in temperature or the state of charge of the electrolytes.

5.2 Equations Definition

Three discrete equations are proposed describing the behaviour of the dynamic of the fluids within the system. These are discrete equations based on theoretical analysis of microfluidics

dynamics principles. The expressions are proposed consistently with momentum and mass conservation principles as stated in continuity and Navier-Stokes equations [137], [138]. Also, it must be considered that in microfluidics the gravitational force terms are neglected, so for incompressible and isothermal fluids, the momentum equations are reduced to Stokes equation [139]. The system is considered to work with incompressible viscous fluids in laminar regime, and to have no changes in density or temperature. Them, the proposed expressions define the relation between flow, viscosity inertia, pressure drop in the conduction and external pumping work. The set of microfluidic ducts that compose the system converge in the reaction cell, so there is influence of each on the others. This influence is related with heuristics and based on experimental observations. Finally, all the relations are simplified in the proposed dynamic equations:

$$Q_1(k+1) = Q_1(k)a_1 + U_1(k)k_{V1} - U_2(k)k_{P2} - |U_3(k)|k_{P3} - c_{P1} \tag{5.3}$$

$$Q_2(k+1) = Q_2(k)a_2 + U_2(k)k_{V2} - U_1(k)k_{P1} - |U_3(k)|k_{P3} - c_{P2} \tag{5.4}$$

$$(Q_3 - Q_4)(k+1) = (Q_3 - Q_4)(k)a_3 + U_3(k)k_{V3} + (Q_1(k) - Q_2(k))c_{Q3} + c_{P3} \tag{5.5}$$

The equations shown in (7.4)-(7.6) represent the discrete evolution of the three state variables, defined also as outputs of the system. The defined parameters in the equations are described in Table 5.1.

Symbol	Meaning	Quantity
K_{V1}	Gain $U_1 \rightarrow Q_1$	$1.1195(\mu l/min.V)$
K_{V2}	Gain $U_2 \rightarrow Q_2$	$1.1904(\mu l/min.V)$
K_{V3}	Gain $U_3 \rightarrow Q_3 - Q_4$	$-0.0124(\mu l/min.V)$
K_{P1}	Gain $U_1 \rightarrow Q_2$	$0.5317(\mu l/min.V)$
K_{P2}	Gain $U_2 \rightarrow Q_1$	$0.3988(\mu l/min.V)$
K_{P3}	Gain $U_3 \rightarrow Q_1 \| Q_2$	$0.0254(\mu l/min.V)$
c_{P1}	Pressure Drop Q_1	$22.4132(\mu l/min)$
c_{P2}	Pressure Drop Q_2	$1.1995(\mu l/min)$
c_{P3}	Pressure Drop $Q_3 - Q_4$	$24.7262(\mu l/min)$
a_1	Inertia-Viscosity ratio Q_1	2.1114
a_2	Inertia-Viscosity ratio Q_2	0.7682
a_3	Inertia between outputs $Q_3 - Q_4$	0.7905
c_{Q3}	Inertia inputs-outputs $Q_1 - Q_2 \rightarrow Q_3 - Q4$	0.9709

Table 5.1: Parameters of the proposed equations

It can be observed that the equations describing the flow at the inlets (Q_1 and Q_2) are symmetrical, and depend on the terms:

1. Inertia of the fluid at the same inlet, which is represented by $Q_i(k)a_i$, where the flow at instant $k+1$ is proportional to the flow at the previous instant k in the same inlet multiplied by the inertia factor a_i, that must be positive and less than 1 as friction slows down flow (ratio between viscous force and inertia).

2. Pump action at the same inlet, represented by $U_i(k)k_{Vi}$, where flow at k+1 is proportional to pump voltage at instant k multiplied by gain factor k_{Vi}, that must be positive as pump action tends to increase flow.

3. Pump pressure generated by pumping the other inlet, represented by $-U_j(k)k_{Pj}$, where flow decrease at instant $k+1$ is proportional to voltage of the pump at the other inlet at instant k multiplied by a gain factor k_{Pj}, that must be positive as this pump action tends to decrease flow.

4. Pressure drop from valves action, $-\|U_3(k)\|k_{P3}$, where the flow decrease at instant $k+1$ is proportional to the absolute value of input 3 (difference in the power of the valves) at instant k multiplied by a gain factor k_{P3}. The valve action being a negative absolute value is because moving away from zero (both valves fully opened) will increase pressure drop, and inlet flows will be reduced. k_{P3} must have a positive value to be consistent with this.

5. Constant pressure drop of the cell inlet, represented by $-c_{Pi}$, where flow is decreased by a constant factor. This term must be positive, and it is not valid when flow is close to zero, as it represents a constant pressure drop at higher flows (the typical working range for the cell).

The equation for the third state variable $(Q_3 - Q_4)$ is different and has the terms:

1. Inertia of the fluids at the outlets, represented by $(Q_3 - Q_4)(k)a_3$, where the difference in outlet flows at instant $k+1$ is proportional to the difference at previous instant k multiplied by the inertia factor a_3. This factor must have a value around 1, as the difference in flows at the outlets tend to stay similar when no other term interacts.

2. Valves action, represented by $U_3(k)k_{V3}$, where flow at instant $k+1$ is proportional to pump voltage at instant k multiplied by gain factor k_{V3}. This gain parameter must be negative as valve action in one inlet tends to decrease flow at this inlet by closing and narrowing fluid conduit, and therefore increase it at the other outlet.

3. Inlet to outlet inertia, $(Q_1(k) - Q_2(k))c_{Q3}$, where difference of outlet flows at instant $k+1$ is proportional to flow difference at the inlets at the previous instant k multiplied by the inertia factor c_{Q3}. The cell structure favors that the negative electrolyte at the inlet tends to flow through the negative outlet, and the same for the positive side. Consequently, c_{Q3} value should be positive.

4. Constant pressure drop difference at cell outlets, represented by c_{P3}, where the difference in flow is modified by a constant factor. This term can have any value, as it represents tendency to flow preferably by one of the outlets due to the constant difference in the pressure drop. It is not valid when the flow in the inlets is close to zero, as at this point the difference would also be zero.

The values for these parameters of the dynamic equations (also shown in Table 5.1) are first identified using nonlinear grey-box model identification, the same methodology as for the unknown parameters of the electric model (Chapter 4). This methodology consists of using the adaptive subspace Gauss-Newton search by means of Matlab. The nonlinearity that

justifies using this method is raised in the equations by the absolute value term of (7.4) and (7.5). It is important to note that the values identifies shown in Table 5.1 are coherent with their definition as referred previously.

The response of the model with the identified parameters is expected to mimic very closely the real response of the same data used for identification. However, when ambient conditions change the system response and stochasticity becomes more evident, it is known that microfluidics models distance themselves from the experimental response, and the model becomes imprecise. In any case, the model should maintain dynamic coherence, so that the grey-box parameter identification is valid as a generalization of the response and consistent with the measured data.

The results of using the proposed equations (7.4)-(7.6) with the identified values from Table 5.1 are shown in Fig. 5.1 and Fig. 5.2 These figures represent two different experiments, the first experiment showing the results of the output of the model compared to the same data used for the identification (with 0,2 s sample time), and the second experiment showing the model compared to data from a different experiment. The experiments from the figures are represented with a percentage value indicating the fitness of the model. This value is calculated as in previous chapter, with the equation (7.4).

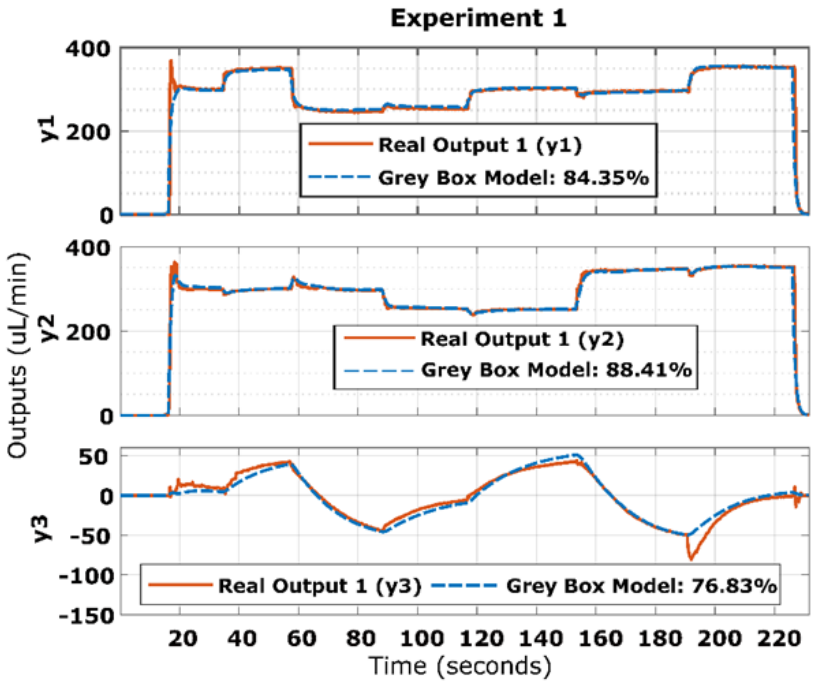

Figure 5.1: System output for model with grey box identified parameters compared to real experimental data for the same experiment as used for identification. Fitness measurement is indicated for each dataset.

The identified model shows good similarity to the same data used for identification, as expected. The fitness values are between 75-90%, which shows that for all three outputs the model follows the real flow dynamics. However, the second experiment repeated in the same

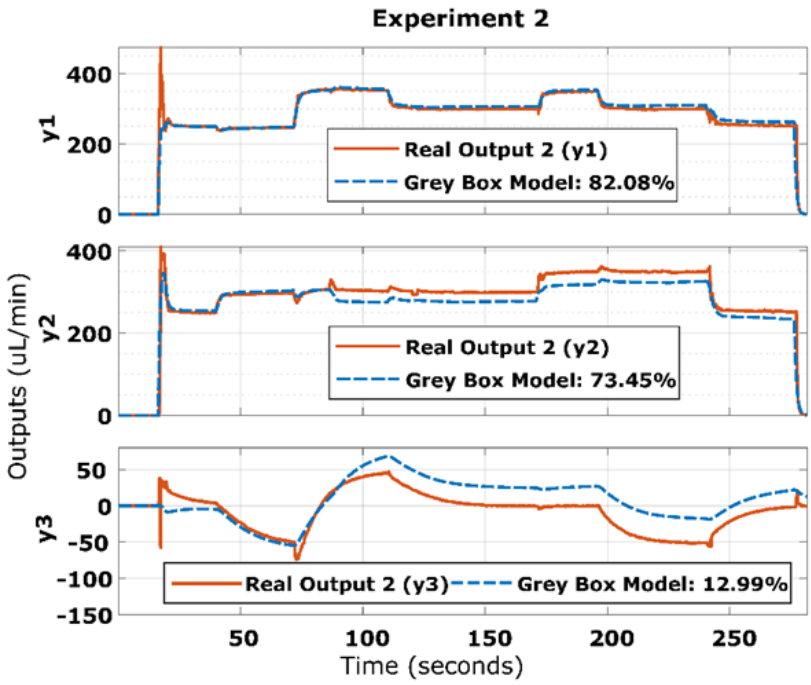

Figure 5.2: System output for model with grey box identified parameters compared with real data for a different experiment. Fitness measurement is indicated for each dataset.

electrolytes and ambient conditions but after several hours of operation, the model is more imprecise. This is mainly explained due to microfluidics stochasticity: change in actuators, wettability, or air bubbles. This second experiment have lower fitness values, especially for the second and third output (which falls to 12%). The first output maintains a good fitness value, which might be caused due to stochastic variability affecting this first output being smaller. Also, it is observed for all outputs of the model to have dynamic coherence between experiments and to real data, this is that although steady state values are not precise the model outputs follow the real flow steps and increase and decrease together with real data. Therefore, these two facts indicate that the proposed model equations are valid, and the aim of this grey-box model identification to have a generalization of the response is proven. However, it is also evident that the strong changing response of the microfluidics elements (as specifically observed for the second and third output for the second experiment) make the model imprecise, and the need of a model adaptation can be concluded.

5.3 Correction Factors Definition

To solve problems encountered in Section 5.2 for model response adaptation for different experiments, it is proposed to add correction factors to the model. These factors should adapt model response for different conditions and therefore make the simulated output more precise to real measured data. The more pronounce variability is observed in the actuators, since it is easily seen that the same actuators conditions do not reflect in the same flow rates. Therefore,

the proposed correction factors are defined applied for the three actuators (f_1,f_2, and f_3), each one applied to negative and positive pumps and to the combined valves action. They are introduced modifying previous parameters from equations (7.4) to (7.6), each one applied to all the actions related with their respective actuator:

$$Pump1 : \begin{Bmatrix} k_{V1} f_1 \\ k_{P1} f_1 \end{Bmatrix} \tag{5.6}$$

$$Pump2 : \begin{Bmatrix} k_{V2} f_2 \\ k_{P2} f_2 \end{Bmatrix} \tag{5.7}$$

$$Valves : \begin{Bmatrix} k_{V3} f_3 \\ k_{P3} f_3 \end{Bmatrix} \tag{5.8}$$

These correction factors are introduced in equations (7.4) to (7.6), which are now modified and expressed as:

$$Q_1(k+1) = Q_1(k)a_1 + U_1(k)k_{V1}f_1 - U_2(k)k_{P2}f_2 - |U_3(k)|k_{P3}f_3 - c_{P1} \tag{5.9}$$

$$Q_2(k+1) = Q_2(k)a_2 + U_2(k)k_{V2}f_2 - U_1(k)k_{P1}f_1 - |U_3(k)|k_{P3}f_3 - c_{P2} \tag{5.10}$$

$$(Q_3 - Q_4)(k+1) = (Q_3 - Q_4)(k)a_3 + U_3(k)k_{V3}f_3 + (Q_1(k) - Q_2(k))c_{Q3} + c_{P3} \tag{5.11}$$

These factors aim to solve the variability in the response of actuators, whether caused by stochasticity or external conditions. Nevertheless, they can also compensate for nonlinearities in the system, as the correction is applied to the linear terms of the expression and can introduce nonlinear behaviour when adapted in real time.

The validity of the use of these factors for compensations is experimentally studied. In order to compare the response of the model with and without the correction, the same data from experiment of Fig. **??** is used. The model parameters are the ones already identified and indicated in Table 5.1 Then, the value of the factors is determined in a new grey-box identification regression for the equations (5.9) to (5.11), where previous parameters are now introduced as known constants. Then, the response is compared in Fig. 5.3 , where real measured data, model without introducing the correction factors, and model with them are compared.

The identification algorithm determines that the values of the factors for the example of the figure are: $f_1 = 1.0216$, $f_2 = 1.0364$, and $f_3 = 1.1471$. The simulations comparison demonstrates that the model adapted with the correction in the actuator factors has a more accurate response of the system for this data. This is indicated by the fitness measurements, which are improved for all three variables. This also means that the correction factors can help to adapt the response with the changing stochastic response of the system. The values of the factors are close to 1 (their initial value), which indicates that small changes in actuators conditions modify notably the system response. Note that all factors affect all outputs, but equations (5.9) to (5.11) indicate that factor f_3 is mainly linked to the third output factor y_3.

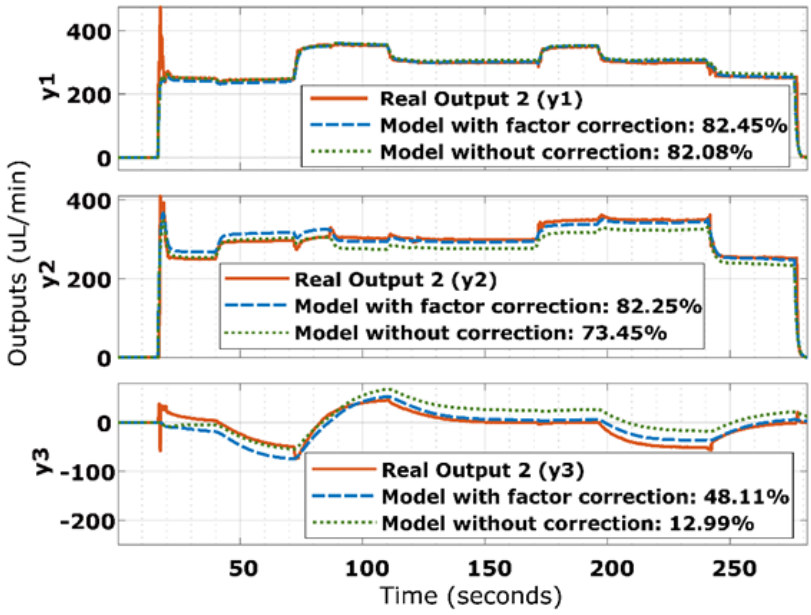

Figure 5.3: Experimental data compared with models with and without factor correction calculated in an offline regression. Fitness measurement is indicated for each dataset.

In this experiment, this output is the more distant in the model without correction, and the factor f_3 is the one with its value further from the initial value 1.

The system model can be rewritten as a state-space system based on dynamic equations described in (5.9) to (5.11). The states are selected to be the same as the outputs, as already defined in (5.2). Considering the nonlinear nature of the equations, the state space system is described as two linear state spaces, each one describing each possible sign for the absolute value. Therefore, the working space is divided in two halves, which are continuous for the case where the action of the valves is equal to zero.

$$A = \begin{bmatrix} a_1 & 0 & 0 \\ 0 & a_2 & 0 \\ c_{Q3} & -c_{Q3} & a_3 \end{bmatrix} C = \begin{bmatrix} 1 & 0 & 0 \\ 0 & 1 & 0 \\ 0 & 0 & 1 \end{bmatrix} D = \begin{bmatrix} -c_{P1} \\ -c_{P2} \\ c_{P3} \end{bmatrix}$$

$$\begin{array}{cc} if \quad U_3 < 0 & if \quad U_3 \geq 0 \\ B = \begin{bmatrix} k_{V1}f_1 & -k_{P2}f_2 & -k_{P3}f_3 \\ -k_{P1}f_1 & k_{V2}f_2 & -k_{P3}f_3 \\ 0 & 0 & k_{V3}f_3 \end{bmatrix} & B = \begin{bmatrix} k_{V1}f_1 & -k_{P2}f_2 & k_{P3}f_3 \\ -k_{P1}f_1 & k_{V2}f_2 & k_{P3}f_3 \\ 0 & 0 & k_{V3}f_3 \end{bmatrix} \end{array} \tag{5.12}$$

This representation described in (5.12), can be used for the design of different control structures, as it is explored in Chapter 6.

5.4 Extended Kalman Filter Correction

The practical use of the defined correction factors for the actuators comes from adjusting them in real time to adapt the response of the model. This adjustment in real time allows to have a more exact estimation of the system state, predict more accurately the microfluidic response, and it also can be used for the controller gains tuning. The chosen algorithm for the calculation is the Extended Kalman Filter (EKF) that recursively approximates the nonlinear set of equations by applying linearized equations in every iteration. It is chosen because it generally works well with non-linear systems, although there are other good alternatives such as the unscented Kalman filter, whose implementation is simpler as it avoids Jacobian calculation but it usually has a higher computational cost [140]. Also, the system nonlinearities are not severe, so the linearization of the EKF is expected to be enough.

EKF is an iterative method that considers a measurement, model and initial estimation variances, with no need to store all previous states. The working flow chart has already been presented in Section 2.3.4, in Fig. 2.23. The state of the filter, $Xf(k)$, is defined as the set of the correction factors, $f_i(k)$, and the process variables defining its evolution are the values of the actuators and the previous values of the flows.

$$Xf(k) = \begin{bmatrix} Xf_1(k) \\ Xf_2(k) \\ Xf_3(k) \end{bmatrix} = \begin{bmatrix} f_1(k) \\ f_2(k) \\ f_3(k) \end{bmatrix} \tag{5.13}$$

$$u(k) = \begin{bmatrix} u_1(k) \\ u_2(k) \\ u_3(k) \\ u_4(k) \\ u_5(k) \\ u_6(k) \end{bmatrix} = \begin{bmatrix} U_1(k) \\ U_2(k) \\ U_3(k) \\ Q_1(k-1) \\ Q_2(k-1) \\ Q_3(k-1) - Q_4(k-1) \end{bmatrix} \tag{5.14}$$

The measurement vector, $Z(k)$, is built with the measurement of the flows from the sensors in the current instant:

$$Z(k) = \begin{bmatrix} Q_1(k) \\ Q_2(k) \\ Q_3(k-1) - Q_4(k) \end{bmatrix} \tag{5.15}$$

It is considered that the best estimation of state evolution, expressed in function g, is that factors have the same value plus unknown random process noise w. Estimated variables are noted with superscripted symbol "$^-$". Symbol " $\hat{}$ " notes internal auxiliar variables of the filter algorithm.

$$\widehat{Xf}^-(k) = g(\widehat{Xf}(k-1), u(k-1), w(k-1)) = \begin{bmatrix} f_1(k-1) \\ f_2(k-1) \\ f_3(k-1) \end{bmatrix} + w(k-1) \tag{5.16}$$

For the h function defining measures estimation, equations of the system from (5.9) to (5.11) are used, since the prediction of the measure is that it will follow the proposed model dynamics plus the measurement noise v.

$$\widehat{Z}^{-}(k) = h(\widehat{Xf}(k), v(k)) = \begin{bmatrix} u_4(k-1)a_1 + u_1(k)k_{V1}\widehat{Xf_1}^{-}(k) - u_2(k)k_{P2}\widehat{Xf_2}^{-}(k) - |u_3|k_{P3}\widehat{Xf_3}^{-}(k) - c_{P1} \\ u_5(k-1)a_2 + u_2(k)k_{V2}\widehat{Xf_2}^{-}(k) - u_1(k)k_{P1}\widehat{Xf_1}^{-}(k) - |u_3|k_{P3}\widehat{Xf_3}^{-}(k) - c_{P2} \\ u_6(k-1)a_3 + u_3(k)k_{V3}\widehat{Xf_3}^{-}(k) + (u_4(k-1) - u_5(k-1))c_1 - c_{P2} \end{bmatrix} + v(k) \tag{5.17}$$

Once variables and functions are defined and applying the definitions of the algorithm, Jacobian matrices of partial derivatives are calculated. For the partial derivatives of equation (5.16) it is obtained:

$$A_{[i,j]}(k) = \frac{\partial g_{[i]}}{X_{f[j]}}(\widehat{Xf}^{-}(k-1), u(k-1), 0) = I \tag{5.18}$$

$$W_{[i,j]}(k) = \frac{\partial g_{[i]}}{W_{f[j]}}(\widehat{Xf}^{-}(k-1), u(k-1), 0) = I \tag{5.19}$$

Where I is de identity matrix. Then, the partial derivatives of equation (5.17) are:

$$H_{[i,j]}(k) = \frac{\partial h_{[i]}}{X_{f[j]}}(\widehat{Xf}^{-}(k-1), 0) = \begin{bmatrix} k_{V1}u_1(k) & -k_{P2}u_2(k) & -k_{P3}|u_3(k)| \\ -k_{P1}u_1(k) & k_{V2}u_2(k) & -k_{P3}|u_3(k)| \\ 0 & 0 & k_{V3}u_3(k) \end{bmatrix} + v(k) \tag{5.20}$$

$$V_{[i,j]}(k) = \frac{\partial h_{[i]}}{v_{f[j]}}(\widehat{Xf}^{-}(k-1), 0) = I \tag{5.21}$$

After defining all functions and Jacobian matrices, the steps of the algorithm are detailed. First, the prediction step, where $P^{-}(k)$ is an a priori estimation of the covariance of the error between estimated and real state vectors, $P(k-1)$ is the a posteriori estimation of the covariance of the error between estimated and real state vectors from previous instant $k-1$, and $Q_f(k-1)$ is the covariance matrix of process noise w. Also, considering the best prediction using equation (5.16) with null noise (unknown), the equations are:

$$\widehat{Xf}^{-}(k) = g(\widehat{Xf}^{-}(k-1), u(k), 0) \tag{5.22}$$

$$P^{-}(k) = A(k)P(k-1)A^{T}(k) + W(k)Q_f(k-1)W^{T}(k) \tag{5.23}$$

After obtaining the value of the state in instant k, predicted from the values in $k-1$, the correction step is made. In this step, the calculated gain $K(k)$ is applied to the estimation from the prediction step to correct the state and $R_f(k)$ is the covariance matrix of the measurement noise v. The corrected state, that is the output of the filter, is calculated in this step:

$$K(k) = [P^{-}(k)H^{T}(k)(H(k)P^{-}(k)H^{T}(k) + V(k)R_f(k)V^{T}(k))]^{-1} \tag{5.24}$$

$$\widehat{Xf}(k) = \widehat{Xf}^{-}(k) + K(k)(Z(k) - h(\widehat{Xf}^{-}(k,0)) \tag{5.25}$$

$$P(k) = (I - W(k)H(k))P^{-}(k) \tag{5.26}$$

The final step of the algorithm is updating the values for the next iteration, where values of instant k become $k-1$. Values for $Q_f(k-1) = I * 0.01$ (covariance matrix of process noise) and $R_f(k) = I$ (covariance matrix of the measurement noise) are selected based on prior confidence on process change and measurements respectively. The estimation algorithm and model with real time adaptation are validated through two tests. For the first experiment, the same real data already used in previous experiments in Sections 5.2 and 5.3 is again the reference for comparing the accuracy of the model. Now, the response of the real-time EKF application with its estimated factors is compared to the model without any correction. The responses of this first experiment are represented in Fig. 5.4.

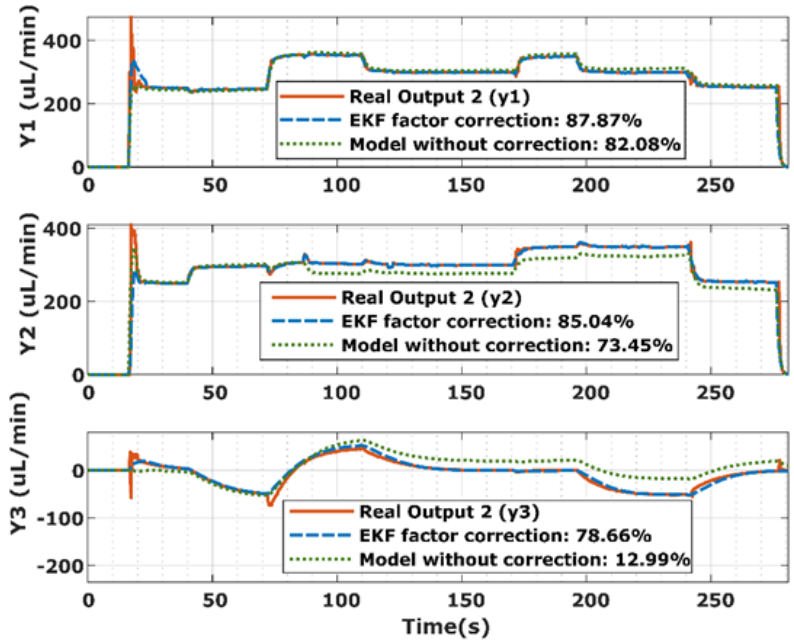

Figure 5.4: Comparison of real data system response with the model with online EKF factor correction and the model without factor correction. Fitness measurement is indicated for each dataset.

It is demonstrated that real-time correction with EKF achieves a very precise simulation of the real response. It has fitness measurements between 78% to 88%, which far outperforms the model with no correction, and it also improves significantly the model with the correction factors calculates offline. The second test consist of a simulated model built with equations from (5.9) to (5.11). In this simulation the correction factor values change in real time by externally forcing their value with white noise added. The model is excited with a sequence of inputs in the actuators similar to the sequences from real experiments. In these conditions the EKF estimation is applied. The random evolution of the factors values is compared with the estimated values from the EKF to check how far from the introduced perturbations are the values calculated by the algorithm. The results are presented in Fig. 5.5.

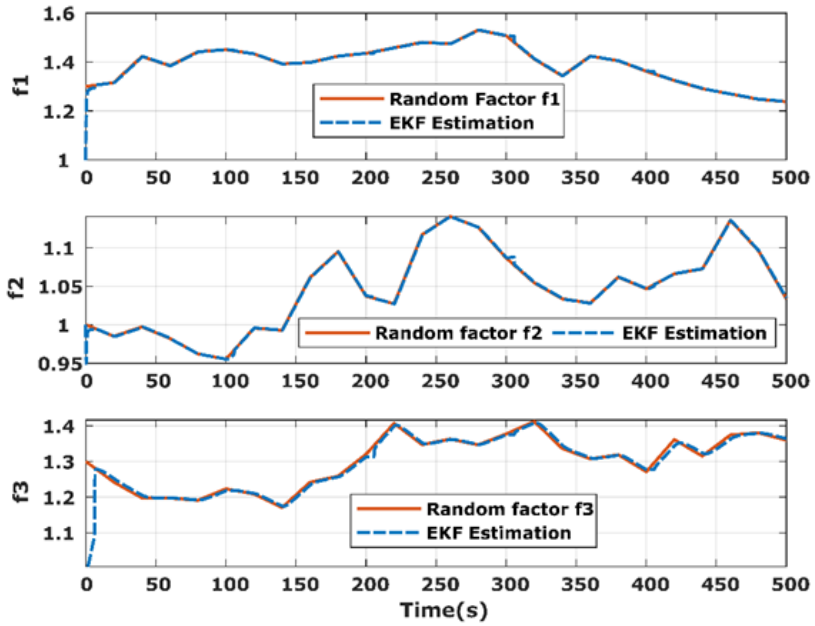

Figure 5.5: Random factor values fed to the simulated model of the system and EKF online estimation of these values. Estimated values are adjusted precisely to random changes in the factors fed to the model.

The result shows that the estimated values match the evolution of the factors fed to the model, with almost no deviation. The estimation rapidly converges to the values and then is able to mimic the introduced simulated perturbation. This means that the algorithm is able to properly quantify the correction factors, and since the equations with the adjusted correction factors reproduces accurately the real response, the methodology is proven to achieve an enhanced modelling for the microfluidics of the membraneless RFB system.

5.5 Conclusions

In this chapter a microfluidic dynamic model for microfluidic membraneless RFBs has been proposed and validated experimentally, proposing the dynamic discrete equations that describe

the response, the correction factors applied to the actuators to account for stochasticity, and the real time estimation algorithm for these factors. The main conclusions are:

- The system variables are chosen in the state space, and considering the microfluidic setup presented in Chapter 3. The states and outputs are the flows at the inlets and the difference of the flows at the outlets, since using one flow more would be redundant. The inputs for the state space representation are the action of the two pumps, and the combination of the valves action (one of them is forced to be always completely open and the other one is regulated). Therefore, the solution for the operation of the actuators for any desired microfluidic configuration is guaranteed to be the one with minimum pumping power and is unique.
- The proposed equations reflecting the general dynamics of the system are based on theoretical principles of mass and momentum conservation, and on relation between actuators and cell flow rates observed empirically.
- The equations are based on terms accounting for pumping gains, valve restriction, fluids inertia in each conduction, pressure drops caused by flows coupling influence, and inertia-viscosity ratios terms. They are reflected in a multiple input multiple output system with coupling between the different actuators and the state variables.
- The values for the specific terms are unknown and identified using Gauss-Newton regression algorithm. The sign and order of the values are checked to have consistency with the theoretical principles in which they are based.
- The equations with the identified values are proven to be a good generalization of the dynamics, but to have deviation with different experiments after several hours of operation time, when stochasticity due to wettability, actuators hysteresis, bubbles or any other system condition effect becomes relevant.
- It is proposed to use some factors correcting proportionally the actuators effect. Consequently, proposed equations are modified including these three correction factors, each one associated with one actuator.
- The correction factors are calculated offline with a new regression. This allows to check that the model augmented with the factors is able to adapt the response to the different stochastic conditions.
- The real time calculation is performed using Extended Kalman Filter, linearizing the system and defining the Jacobian matrixes of the partial derivatives of the proposed augmented equations.
- The EKF algorithm is proven to be able to estimate the change in the factors in simulation, and to experimentally adapt the model to adjust it to the real system conditions.
- The model methodology performs a precise and accurate estimation of the microfluidic response which can be used to simulate and estimate the derived battery electrical response, and to design and optimize the microfluidic control and regulation method for the actuators.

The proposed microfluidic dynamic equations, the parameters identification, the proposed augmented equations with the corrections factors, the real time estimation of them, and the whole methodology experimental validation is one of the main contributions of this thesis.

Chapter 6

System control

Microfluidic operation has been demonstrated to be critical for optimal membraneless RFB, as Chapter 4 electrical modelling shows its influence in the power, mixing and self-discharge losses. Also, to operate the setup described in Chapter 3, which incorporates more elements to have a deeper control of the flow configuration, a modelling methodology of the active microfluidics elements and how they interact with liquid interface and its flow within the cell has been presented in Chapter 4.

All this work leads to allows the design of a precise control strategy that allows to operate in recirculation the battery with an optimal interface positioning and adapting to power demands. This precise regulation can overcome problems and operation limitations of the previous existing references, as explained in Section 2.1, and allow the project in which this thesis takes place to demonstrate the first microfluidic membraneless RFB with recirculation and charge/discharge cycling.

This chapter explores different control strategies and designs. First, it is detailed the operation with no microfluidic modelling, using conventional Proportional Integral Derivative (PID) controllers, and combining them as independent Single Input Single Output (SISO) systems to make the multivariable control. Also, it is explained this strategy different possible approaches of use. For example, to avoid operation changes with power demand, it can be chosen to flow at a high constant flow rate so that there always enough species available at the reactor. This mentioned approach drawbacks (higher pump consumption) and general problems of using independent PID controllers (actuators coupling) are demonstrated and explained.

Consequently, and given the availability of the proposed microfluidic modelling, the main object of study in this chapter is model-based control strategies. This multiple input multiple output (MIMO) controllers using the state space designed model can be expected to perform a better regulation. The proposed controllers include optimal LQR with integral action (LQRI), optimal control with incremental state, and model predictive control (MPC), which is divided into a nonlinear approach and an adaptive linearized one.

This chapter describes all these controllers and explains its designs. Their flow response is tested in simulation and experimentally, and the microfluidic results are displayed. The electrical performance resulting from each controller microfluidic operation is detailed in

Chapter 7.

6.1 Model-Free Control Strategy

Model-free control methods are relevant in addressing control challenges in systems where precise modelling may not be available or necessary, requires too many efforts, or is imprecise. Their adaptability, robustness, real-time capabilities, and data-driven nature make them valuable tools for real-world problems.

There are different modern control strategies that allow to design the system regulation without a model. However, usually these techniques depend on complex methodologies that rely on implementations to learn, adapt, and make control decisions without explicit knowledge of the system's mathematical model. These methodologies are often grounded in machine learning and optimization techniques, as they need to cope with the inherent complexity and uncertainty of real-world system.

PID control is notably simpler to understand and implement compared to many complex model-free techniques. It does not require sophisticated algorithms or extensive data-driven training. Also, PID controllers can be tuned with engineering expertise and practical experimentation. In contrast, complex model-free techniques often demand extensive parameter tuning, data collection, and algorithm development. Finally, PID also offers real-time responsiveness and resource efficiency, as it typically involves low computational cost and can run on resource-constrained hardware. This allows to use limited computing resources to provide immediate real-time responses to system changes or disturbances. Some complex model-free techniques may require significant computation time or offline learning before deployment.

6.1.1 Multiple Independent PID-Controllers

The model-free approach for the system using classical PID controllers is designed as several independent PID controllers working as SISO systems. This is the initial approach for controlling the flows within the cell. Besides evaluating it as a valid control strategy, this structure also allows to have a fast first control design for different experiments and to collect data. This has been used as the first basic control for the modelling experiments stated in previous chapters. This architecture is shown in Fig. 6.1.

The architecture consists of three independent PIDs, each of them being a single-input single-output (SISO) system that is adjusted alone and considered to work alone. It is true that from the observed response of the system, it can be deduced that problems because of coupling between controllers can occur: as the proposed equation from the microfluidic modelling from Chapter 5 indicates, all inputs affect all outputs, and this state variables are also coupled between them. Nevertheless, if influence of every actuator in each of the outputs is observed, it is indicated that the first pump (U_1) has the main influence on flow at the first inlet ($Y_1 = Q_1$), the second pump (U_2) in flow at the second inlet ($Y_2 = Q_2$), and the combined action of the valves (U_3), written as the difference between their power, has a more direct relationship with flows at the outlets ($Y_3 = Q_3 - Q_4$). These correlations can be deduced from intuitive study of the system, but they are also demonstrated by equations

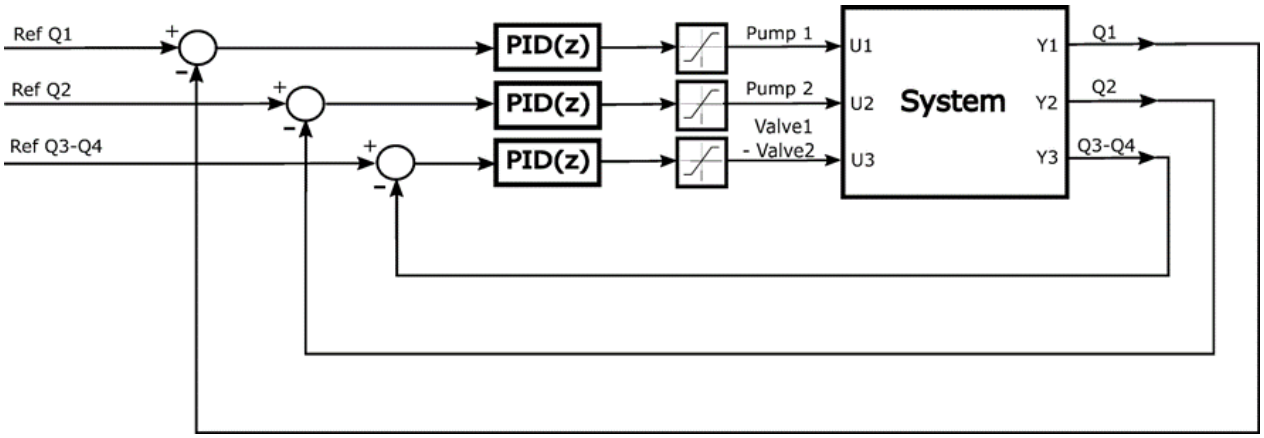

Figure 6.1: Model-free control architecture based on three independent SISO PID controllers by assigning one input for the actuators to one measured output of the system.

(5.9) to (5.11), and specially evaluating the values of the constants of the model obtained by identification in section 5.2 and shown in Table 6.1. It can be checked that values of k_{V1}, k_{V2} and k_{V3} are significantly larger (2 or 3 times) than the rest of parameters that apply to each flow. The discrete expression for each controller expressed as a Z transform is:

$$U(z) = K_p + k_i \frac{T_s(z-1)}{1(z-1)} + k_d \frac{N(z-1)}{(z-1)+NT_s} \tag{6.1}$$

Where T_s is the sampling time, k_p is the proportional gain, k_i is the integral gain whose term is calculated in the trapezoidal approach, and k_d is the derivative gain whose term has the constant N adjusted to act as a low-pass filter. Note that, as indicated in Fig. 6.1 the inputs have saturations that limits the actuators to their working ranges.

Values of the PIDs are adjusted empirically by trial and error. They are written in Table 6.1. The process for this adjustment is: first in a real experiment get some broad values and have the system working for collecting more data, second with the model and simulating the response values are adjusted, and finally the values are validated in the real setup again and slightly modified when needed.

Symbol	PID 1	PID 2	PID 3
K_p	0.1	0.1	-0.2
K_i	0.2	0.2	-0.3
K_d	0.02	0.02	-0.1

Table 6.1: Values of the parameters of the proposed PID controllers

The method is validated in simulation using the proposed model (although this method implementation was made before its development), and experimentally in the real system. In both validations it is used a sampling time of 1ms, and N=10. However, it must be noted that in following sections where the this set of PID regulators are compared to other control

methods, the sampling time is 0.2ms in order to match the one use for them. Therefore, the constant N is also changed to 1, and the low pass filter is implemented in the measurement of the flow sensors directly. The results for an example of these experiments are shown in figures Fig 6.2 and Fig. 6.3.

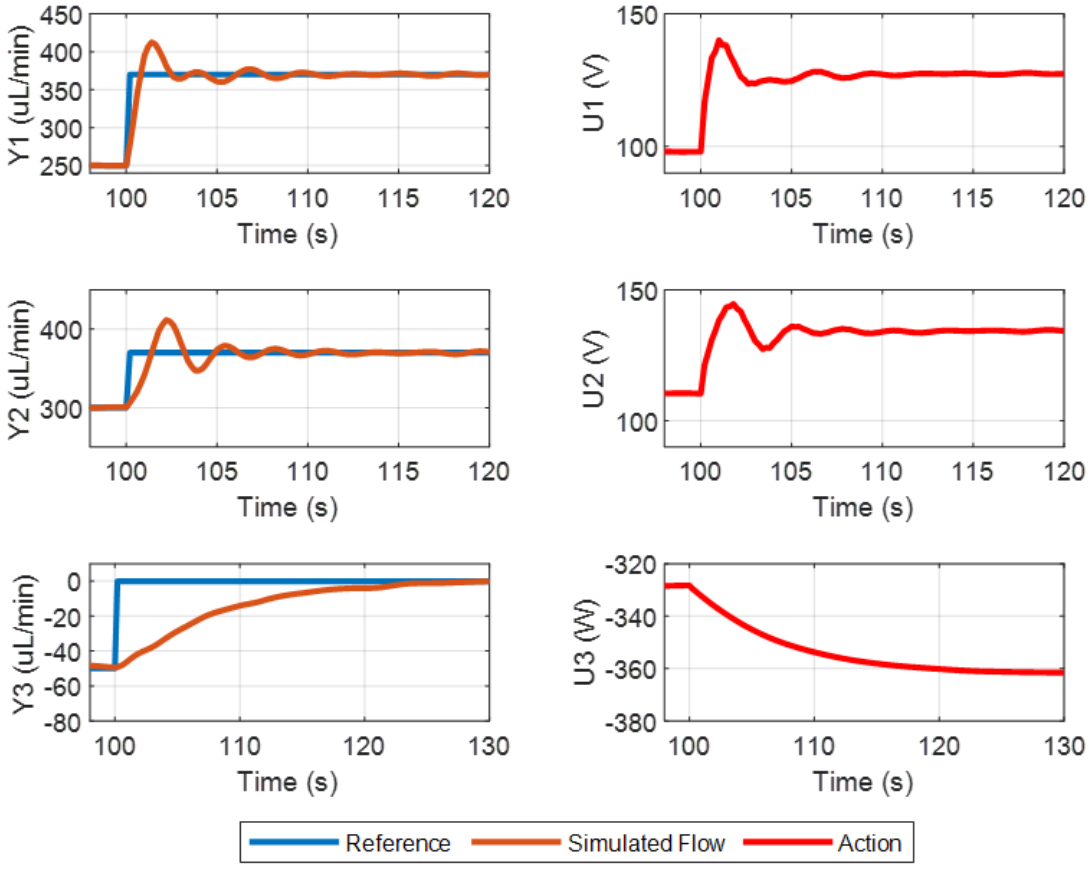

Figure 6.2: Simulated response for the control architecture with 3 PIDs controllers.

The response for the simulated and experimental response shows that the controller is not optimal. It presents overshoot for the two first outputs, that stabilizes after more than 10 seconds. Regarding the third output it has a slow response with around 30 seconds of settling time. The computational cost of this algorithm is very low (the whole computer application acting as SCADA run with this control algorithm in less than 10ms). The results for simulation are similar to the ones in the real experimentation, but the real system shows more coupling between variables, which increases overshoot and extends settling time. Note that for simulation is used the system model, although this control strategy does not require it, and it was temporally earlier. It is true that system model can help in the parameter tuning for PID controllers.

The overshoot of the response can be mitigated using other control gains, at the cost of making response to slow (more than 20s of settling time for Y_1 and Y_2, and more than 50 s

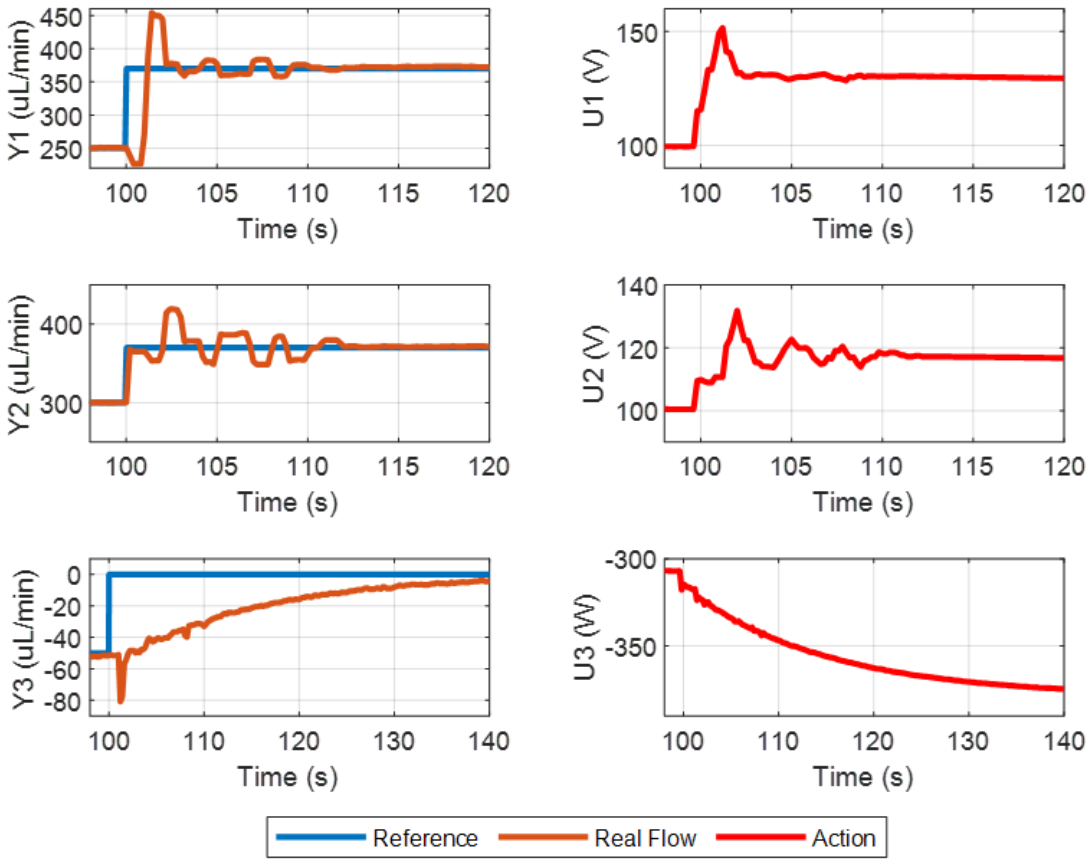

Figure 6.3: Real response for the control architecture with 3 PIDs controllers.

for Y_3). This is the reason that has been chosen to present the result with these gains, as those settling times do not comply with the system requirements, and, also, because here it is easier to observe coupling between variables which as an important effect to understand the need for a MIMO approach.

This 3-independent PIDs control architecture can be used in different ways. It can be considered that since the response to changes in the setpoint is not optimal (whether it has overshoot or is made too slow), it is better to minimize this require changed. This can be done by equilibrating the interface with the maximum inlet flows so that it is not necessary to rapidly adapt them to meet power demands. Obviously, this has the cost of using more pumping power than required, which for experimental validation of the battery might not be critical, but it is for real battery operation. These two approaches (using the PID controllers and flowing at the maximum inlet flows) are analysed using the electrical model in order to be evaluated and compared to the rest of the control designs.

6.2 Model Based Strategies

The simplest approach has shown to have limitations to adapt the flow rates to reference step changes. These steps are expected to be needed during operation of the battery to meet power demands. Consequently, other control methodologies are explored taking advantage of the proposed model. Since model capture the relationships between inputs, outputs, and states, it provides a detailed understanding of how the system responds, and it can be used for mathematically design and calculate control laws.

In this section, different control laws are explained and its implementation detailed, in order to perform regulations that comply with each algorithm optimality function or specific objectives of precision, speed and stability. The proposed algorithms are divided in optimal algorithms with augmented system implementation added to compensate for steady-state error, and model predictive controllers. Each control is validated in simulation and real experiments individually, and finally all actions are compared by displaying them together (including the model-free design from previous section).

6.2.1 LQR with Integral Action

The first proposed control method using the microfluidic model is an optima control based on the linear quadratic regulator (LQR). This method is a widely applied and influential control strategy in the field of control theory and engineering. LQR is designed to find the optimal control action of linear dynamic systems, making it particularly well-suited for applications considering precise control and performance optimization. At its core, LQR aims to find control inputs that minimize a weighted combination of two key objectives: the control effort (energy or cost) and the deviation of the system state from a desired reference trajectory. By formulating the control problem in this way, LQR controllers can achieve a delicate balance between achieving desired performance and minimizing control effort. However, this control law is vulnerable to model deviations, and can not guarantee zero steady-state error when the model differs even slightly from the real system [122]. Since it has been already discussed that microfluidic systems in general and the membraneless RFB in particular have a stochastic variability in their response, it is necessary to add an integral action that compensates for these possible deviations in the steady-state besides the EKF correction of the model.

The most common strategy for addressing this limitation is augmenting the system matrix with integration of error in the outputs, as described in [141]. This modification introduces an additional term to the control law that integrates the error signal over time. This addresses the inability of common LQR to eliminate steady-state errors in the system's response. Integral control is particularly effective in systems with non-zero setpoints or reference values. It continuously accumulates the error between the desired and actual system states, gradually driving the steady-state error to zero. This enhancement ensures that the controlled system can achieve precise and accurate tracking of desired trajectories or reference signals, achieving both optimal transient response and steady-state accuracy.

The augmented system introduces the integral error as a new system variable for the state space representation of the system. This new state variable, ϵ, is defined as the sum of errors as:

$$\epsilon(k+1) = \epsilon(k) + T_s(r(k) - C.X(k)) \tag{6.2}$$

Where r is the reference setpoint vector of flows. And the augmented state space representation is now written as:

$$\begin{bmatrix} X(k+1) \\ \epsilon(k+1) \end{bmatrix} = \begin{bmatrix} A & 0 \\ -C & I \end{bmatrix} \begin{bmatrix} X(k) \\ \epsilon(k) \end{bmatrix} + \begin{bmatrix} B \\ 0 \end{bmatrix} U(k) + \begin{bmatrix} 0 \\ I \end{bmatrix} r(k) \tag{6.3}$$

Therefore, system dynamics are now defined by augmented system matrices, $\tilde{A}$ and $\tilde{B}$, that are:

$$\tilde{A} = \begin{bmatrix} A & 0 \\ C & I \end{bmatrix} \quad \tilde{B} = \begin{bmatrix} B \\ 0 \end{bmatrix} \tag{6.4}$$

Optimal control for these new dynamics is calculated to solve the well known LQR process, that minimizes the cost function J defined as:

$$J = \sum_{x=0}^{\infty} ((X(k) - X_r)^T Q(X(k) - X_r)) + (U(k)^T R U(k)) \tag{6.5}$$

Where Q and R matrices are defined to ponderate error versus action in the cost. Then, control action U is defined as a gain applied to the state:

$$U(k) = K(X_r - X(k)) \tag{6.6}$$

The solution for obtaining the K gain is calculated as:

$$K = (R + \tilde{B}^T P \tilde{B})^{-1} \tilde{B}^T P \tilde{A} \tag{6.7}$$

Where P is the solution to the discrete algebraic Riccati equation:

$$P = \tilde{A}^T P \tilde{A} - (\tilde{A} P \tilde{B})(R + \tilde{B}^T P \tilde{B})^{-1} (\tilde{B}^T P \tilde{A}) \tag{6.8}$$

This process for obtaining the optimum control gain is calculated using augmented matrices described in (6.3), and since state space representation is adaptive and changes in real time with EKF estimation of the correction factors, solution of the Riccati equation has to be found at every instant. Because of this the best approach is to have an iterative process that approximates and converges to the solution. The used iterative equations derived from [142] are:

$$K(k) = (R + \tilde{B}^T(k) P(k-1) \tilde{B}(k))^{-1} . \tilde{B}^T(k) P(k-1) \tilde{A}(k) \tag{6.9}$$

$$P(k) = Q + K^T(k)RK(+) + (\tilde{A}(k) - \tilde{B}(k)K(k))^T P(k-1)(\tilde{A}(k) - \tilde{B}(k)K(k)) \quad (6.10)$$

Finally, reference tracking gain is added apart from the integral part to adjust the action to the flow setpoints that are different from zero.

$$K_{ref}(k) = K(k) - \tilde{B}(k)^{-1}(\tilde{A}(k) - I) \quad (6.11)$$

The scheme for this control architecture is shown in Fig. 6.4.

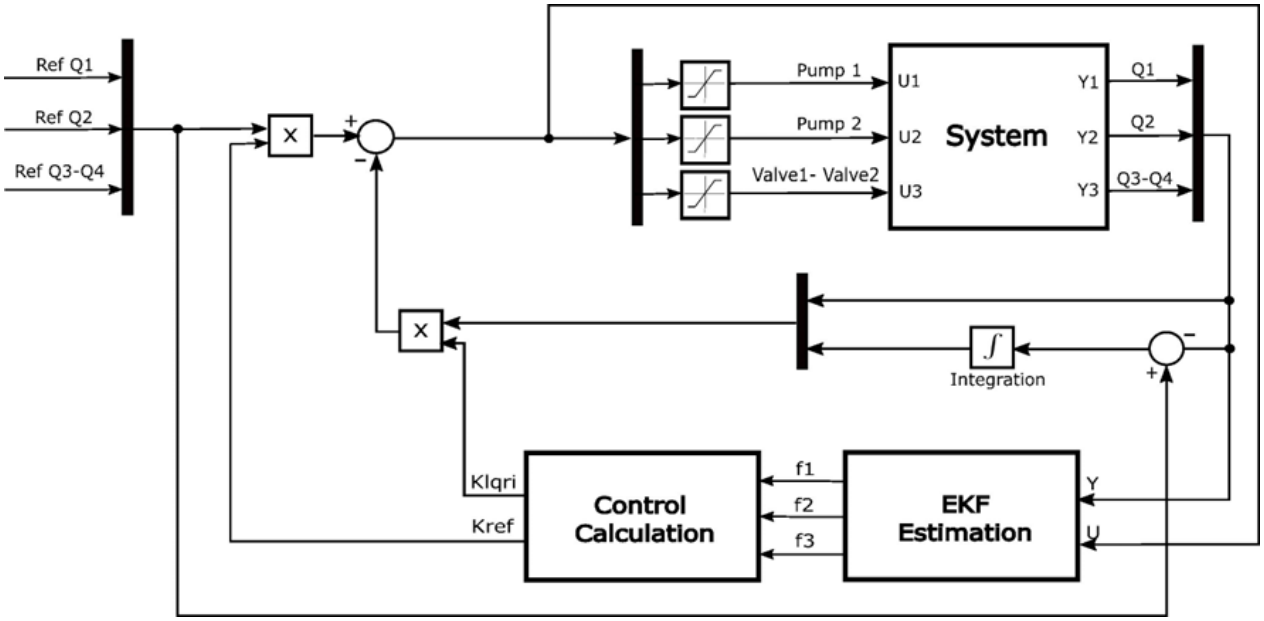

Figure 6.4: Control scheme of the LQR with integral action, with factors from the EKF estimation for the adaptive model of the control calculation, and the iteratively calculated control gains.

In the microfluidic membraneless RFB system, outputs are the state variables, so augmenting state with output error is equivalent to incorporating error in states. Building new system matrices with equations in (6.4) applied to state space definition from section 5.3 is written as:

$$\tilde{A} = \begin{bmatrix} a_1 & 0 & 0 & 0 & 0 & 0 \\ 0 & a_2 & 0 & 0 & 0 & 0 \\ c_{Q3} & -c_{Q3} & a_3 & 0 & 0 & 0 \\ -1 & 0 & 0 & 0 & 0 & 0 \\ 0 & -1 & 0 & 0 & 0 & 0 \\ 0 & 0 & -1 & 0 & 0 & 0 \end{bmatrix}$$

$$\tilde{B} = \begin{matrix} if \quad U_3 < 0 \\ \begin{bmatrix} k_{V1}f_1 & -k_{P2}f_2 & k_{P3}f_3 \\ -k_{P1}f_1 & k_{V2}f_2 & k_{P3}f_3 \\ 0 & 0 & k_{V3}f_3 \\ 0 & 0 & 0 \\ 0 & 0 & 0 \\ 0 & 0 & 0 \end{bmatrix} \end{matrix} \qquad \tilde{B} = \begin{matrix} if \quad U_3 \geq 0 \\ \begin{bmatrix} k_{V1}f_1 & -k_{P2}f_2 & -k_{P3}f_3 \\ -k_{P1}f_1 & k_{V2}f_2 & -k_{P3}f_3 \\ 0 & 0 & k_{V3}f_3 \\ 0 & 0 & 0 \\ 0 & 0 & 0 \\ 0 & 0 & 0 \end{bmatrix} \end{matrix} \tag{6.12}$$

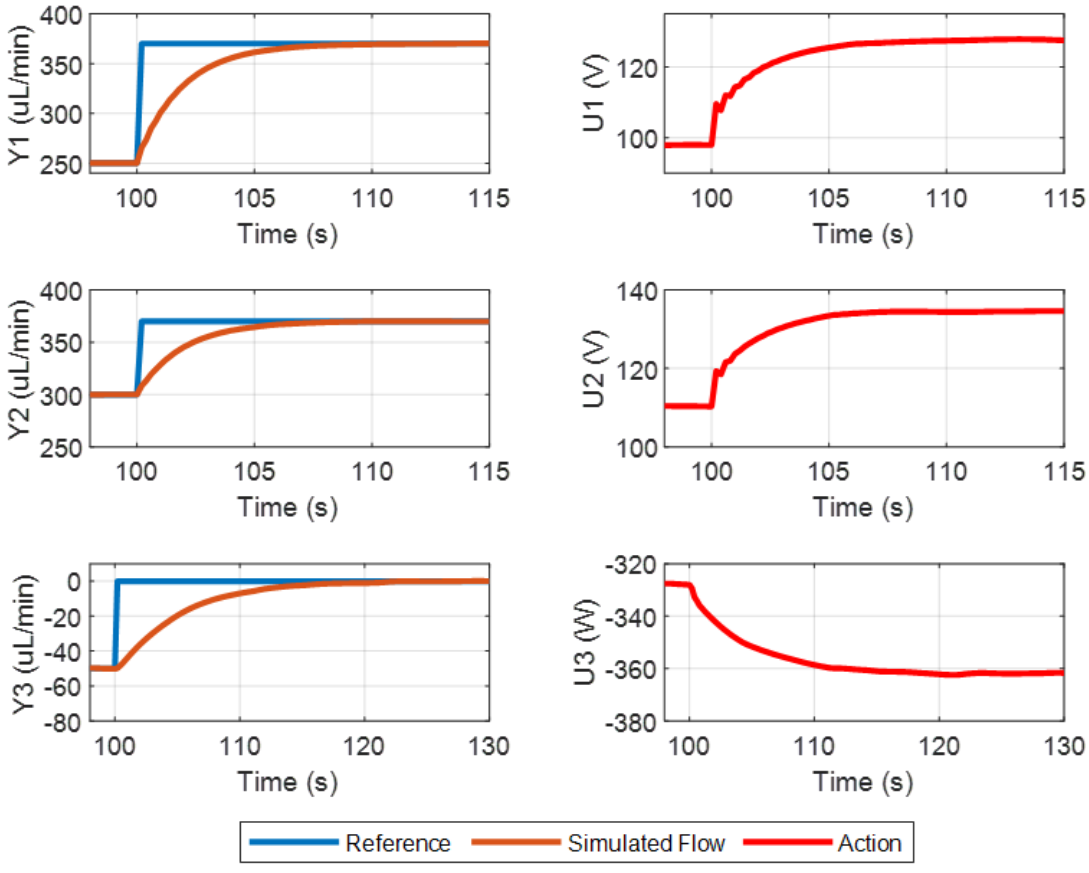

Figure 6.5: Simulated response for the LQR with integral action control architecture.

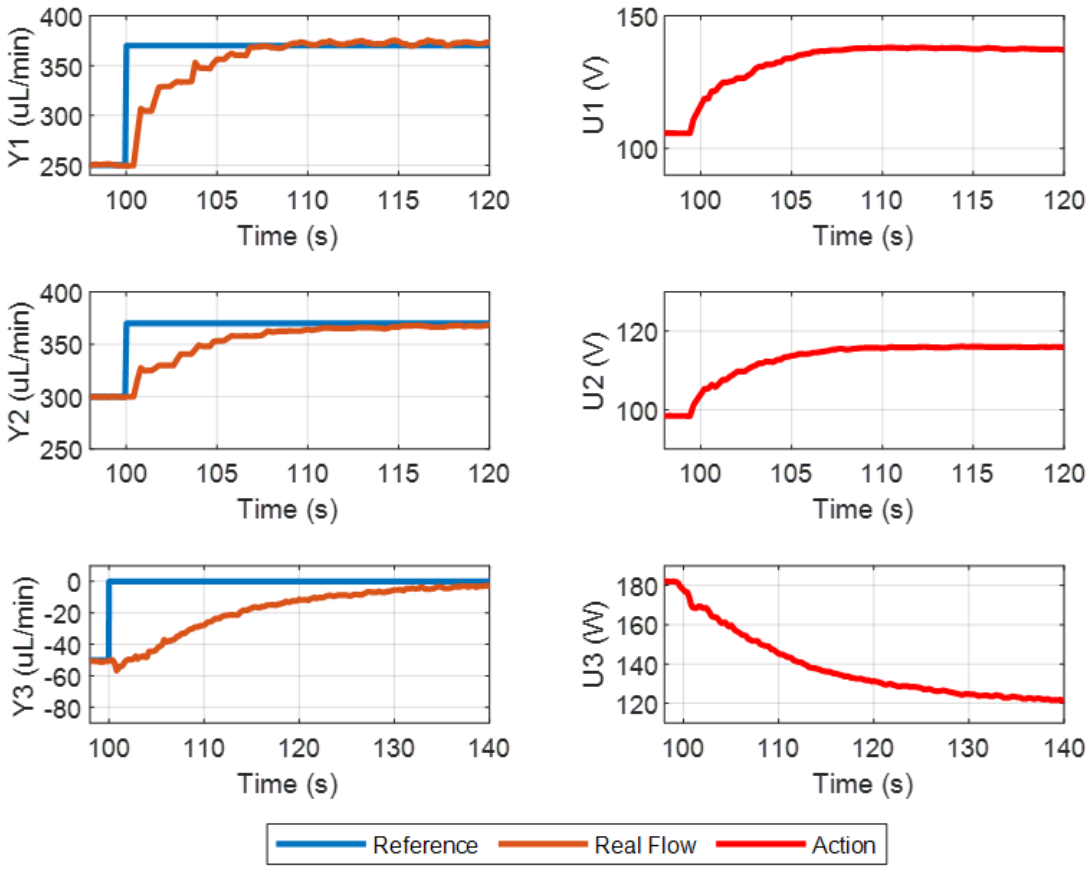

Figure 6.6: Real response for the LQR with integral action control architecture.

The method is validated in simulation and experimentally in the real system. The values for the system matrixes are selected by trial and error in simulation and then validated and adjusted again if necessary in real experiment tests. The values are $Q = I.10^{-3}$ and $R = I.10^{3}$, as a more aggressive control action introduces instabilities and oscillations. The sampling time is 0.2ms. The results for an example of these experiments are shown in figures Fig. 6.5 and Fig. 6.6.

The response for the simulated and experimental response shows that the controller is capable to improve the model-free response. It presents a smooth response with less settling time for all the outputs. For the two first outputs it stabilizes in less than 10 seconds. Regarding the third output it has again a slower response with around 30 seconds of settling time, which is not a remarkable improvement compared to the previous PID based controller. However, in general the controller has a good response, faster and more stable with no coupling affecting the transient response and producing big oscillation as in for the PID based case. The computational cost of this algorithm is low (the whole computer application acting as SCADA run with this control algorithm in less than 40ms).

The results for simulation are similar to the ones in the real experimentation, except for

two differences. First, there are small perturbations in real operation that do not appear in simulation, due to noise from real tests. Then, and more remarkably, there are differences in the control action, especially for the third variable value. There, the simulated expected value and the real control action differ in hundreds of units. The two first control action variables are also different in tens of units. This is caused for all of them by the stochasticity of the system. This variability changes the working point where the desired flow configuration is achieved. This proves that the EKF correction of the model, which is linked mainly to the actuators, is able to adapt the model in real operation in real time to adjust the control action and have produce output dynamics as expected from simulation.

6.2.2 Optimal with Incremental State

The second proposed control technique based on system model is also an optimal control augmented to incorporate a steady-state correction. In this case, it is an optimal control with incremental state. It has similar characteristics to the integral action, as it combines the minimization of a function cost index to find an optimal between error and control effort for the dynamics, with an incremental implementation for a zero error for the steady state.

This incremental state optimal control uses the state space linear implementations from Section 5.3. The state is expressed in an incremental form as presented in [143], for adding an integral action that removes the steady-state error together with the dynamic response of an LQR optimal control [144].

The general expressions of the converted state space are:

$$\tilde{X}(k) = \begin{bmatrix} Y(k) \\ \Delta X(k) \end{bmatrix} \qquad \tilde{Y}(k) = \begin{bmatrix} I & 0 \end{bmatrix} \begin{bmatrix} Y(k) \\ \Delta X(k) \end{bmatrix} \tag{6.13}$$

$$\begin{bmatrix} Y(k+1) \\ \Delta X(k+1) \end{bmatrix} = \begin{bmatrix} I & CA \\ 0 & A \end{bmatrix} \begin{bmatrix} Y(k) \\ \Delta X(k) \end{bmatrix} + \begin{bmatrix} CB \\ B \end{bmatrix} \Delta U(k) \tag{6.14}$$

The control action is defined also as an incremental function and control gain K separated into two partial matrices (K_x and K_y):

$$U(k) = U(k-1) + \Delta U(k) \tag{6.15}$$

$$\Delta U(k) = K(\tilde{X}_r(k) - \tilde{X}(k)) = \begin{bmatrix} K_y & K_x \end{bmatrix} \begin{bmatrix} Y_r(k) - Y(k) \\ -\Delta X(k) \end{bmatrix} \tag{6.16}$$

$$\tilde{X}_r(k) = \begin{bmatrix} Y(k) \\ 0 \end{bmatrix} \tag{6.17}$$

Where Y_r and X_r are reference output and reference state (which increment part is zero). The feedback gain is calculated with new state matrices that, as in (6.14), now are expressed as:

$$\tilde{A} = \begin{bmatrix} I & CA \\ 0 & A \end{bmatrix} = \begin{bmatrix} 1 & 0 & 0 & a_1 & 0 & 0 \\ 0 & 1 & 0 & 0 & a_2 & 0 \\ 0 & 0 & 1 & c_{Q3} & -c_{Q3} & a_3 \\ 0 & 0 & 0 & a_1 & 0 & 0 \\ 0 & 0 & 0 & 0 & a_2 & 0 \\ 0 & 0 & 0 & c_{Q3} & -c_{Q3} & a_3 \end{bmatrix}$$

$$\begin{array}{cc} if \quad U_3 < 0 & if \quad U_3 \geq 0 \\ \tilde{B} = \begin{bmatrix} CB \\ B \end{bmatrix} = \begin{bmatrix} k_{V1}f_1 & -k_{P2}f_2 & k_{P3}f_3 \\ -k_{P1}f_1 & k_{V2}f_2 & k_{P3}f_3 \\ 0 & 0 & k_{V3}f_3 \\ k_{V1}f_1 & -k_{P2}f_2 & k_{P3}f_3 \\ -k_{P1}f_1 & k_{V2}f_2 & k_{P3}f_3 \\ 0 & 0 & k_{V3}f_3 \end{bmatrix} & \tilde{B} = \begin{bmatrix} CB \\ B \end{bmatrix} = \begin{bmatrix} k_{V1}f_1 & -k_{P2}f_2 & -k_{P3}f_3 \\ -k_{P1}f_1 & k_{V2}f_2 & -k_{P3}f_3 \\ 0 & 0 & k_{V3}f_3 \\ k_{V1}f_1 & -k_{P2}f_2 & -k_{P3}f_3 \\ -k_{P1}f_1 & k_{V2}f_2 & -k_{P3}f_3 \\ 0 & 0 & k_{V3}f_3 \end{bmatrix} \end{array} \tag{6.18}$$

The optimal control for this new dynamic model is defined to minimize again the index from (6.5), It is calculated, as already presented, using the same expressions (6.7) to (6.10) for the discrete algebraic Riccati equation, but for the new K gain (divided afterwards in K_x and K_y as (6.16) indicates). The scheme for this controller architecture is shown in Fig. 6.7.

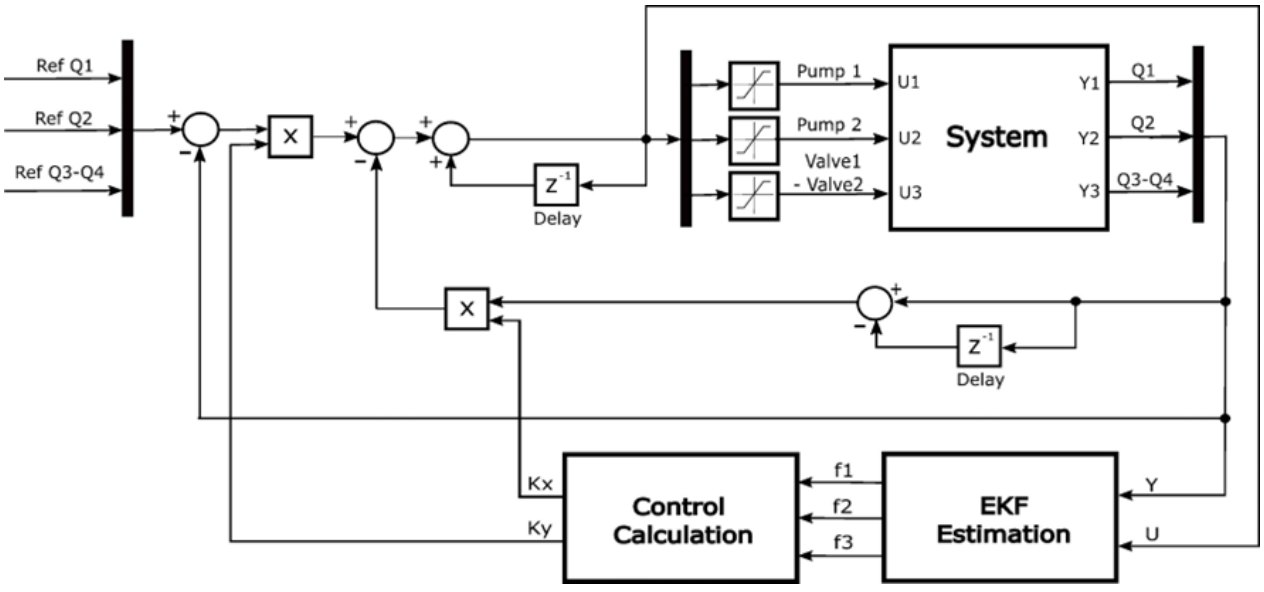

Figure 6.7: Scheme for the optimal controller with incremental state, with factors from the EKF estimation for the adaptive model of the control calculation, and the iteratively calculated control gains.

The method is validated in simulation and experimentally in the real system. The values for the system matrices are selected again with the same process: by trial and error in simulation

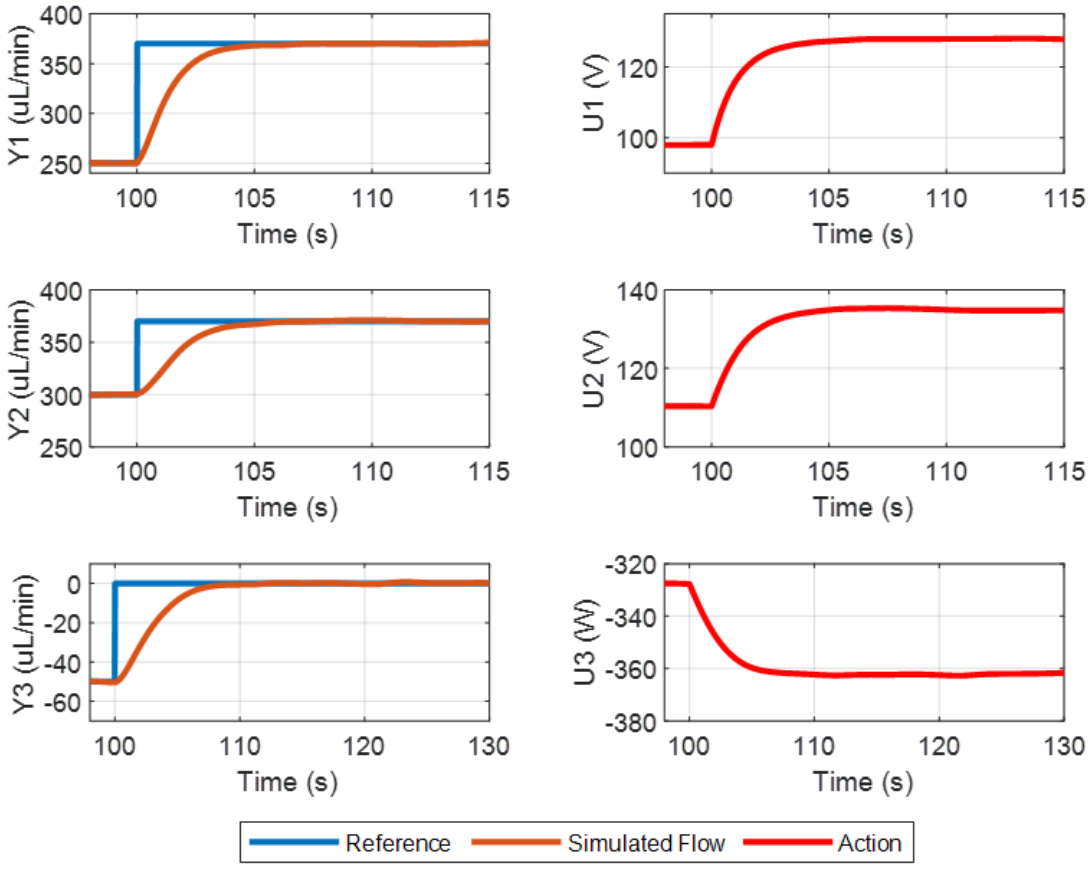

Figure 6.8: Simulated response for the optimal control with incremental state architecture.

and then validated and adjusted again if necessary in real experiment tests. The values are $Q = I$ and $R = I * 10^2$ as this implementation allows to use a more aggressive weights for the control action than the LQR with integral action. The sampling time is 0.2 ms. The results for an example of these experiments are shown in figures Fig. 6.8 and Fig. 6.9.

The response for the simulated and experimental response shows that the controller has a good response. It presents a smooth and fast response with less settling time for all the outputs, especially for the third output, than the LQR with integral action. For the two first outputs it stabilizes in less than 5 seconds. Regarding the third output it has again a slower response with around 20 seconds of settling time (10 in simulation), which is now a significant improvement. In general, the controller has a good response, although in the transient dynamics of the real response the oscillations are slightly bigger than for the LQR with integration. The computational cost of this algorithm is low (the whole computer application acting as SCADA run with this control algorithm in less than 40ms).

Again, there are small differences between real operation and simulation. The small perturbations in real operation that do not appear in simulation, the mentioned different settling time for the third output, and again the differences in the control action. These differences appear

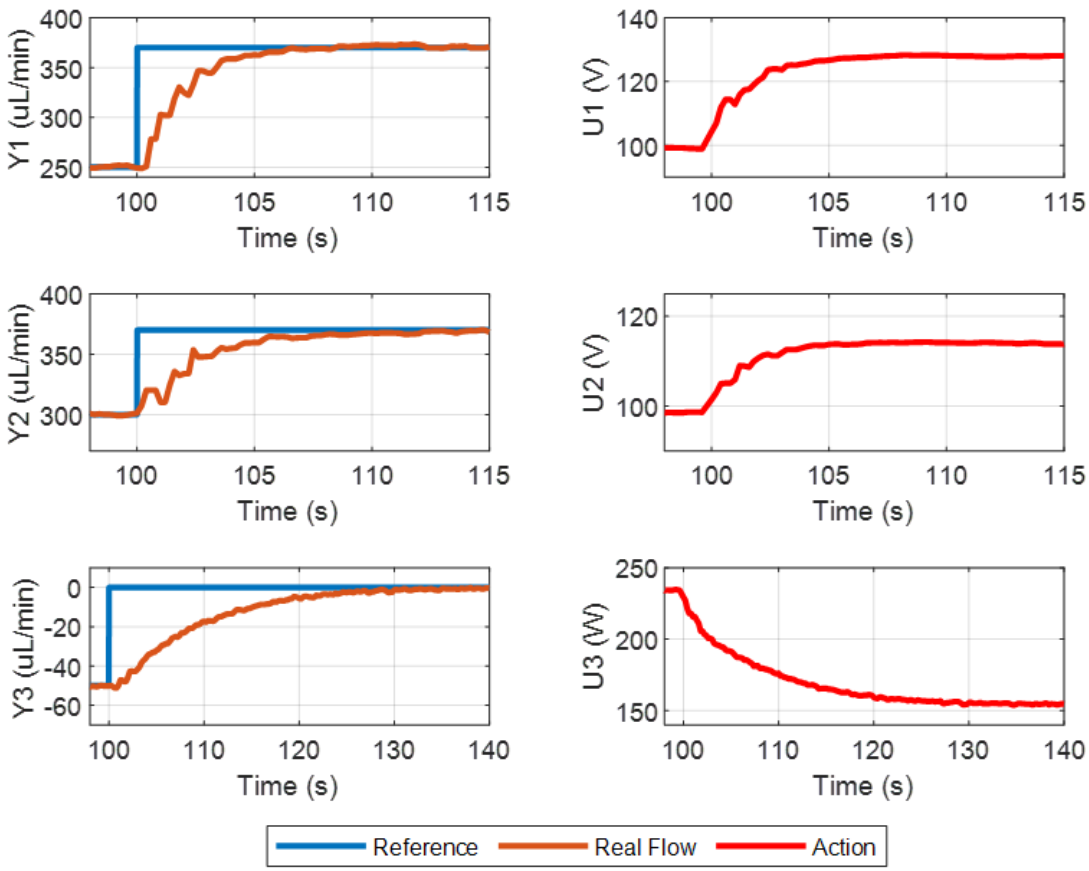

Figure 6.9: Real experiment response for the optimal control with incremental state architecture.

in the second and third inputs, and again especially the third variable differs in hundreds of units. The reason is again the stochasticity of the system, and the model capability to adapt and the control to recalculate the control gains based on the EKF correction are proven, producing a, adequate methodology for the microfluidic control.

6.2.3 Adaptive Nonlinear Model Predictive Control

It is proposed a control method that considers the trajectory of the states to control in a time horizon. This is made using model prediction control (MPC), in this case using the proposed model equations from Section 5.3 and its nonlinearity, and the real time correction for its adaptation. Therefore, the architecture of the used MPC is an adaptive nonlinear model predictive control (ANLMPC). Model predictive control is also an optimization problem, that tries to minimize the defined cost function over a time horizon using a set of controlled variables for a control time horizon, and with a set of inputs and states constraints. This is represented in Fig. 6.10 as already presented in Section 2.4.1. Note that if the control horizon is less than the prediction horizon the output predictions are selected by maintaining the last

computed input.

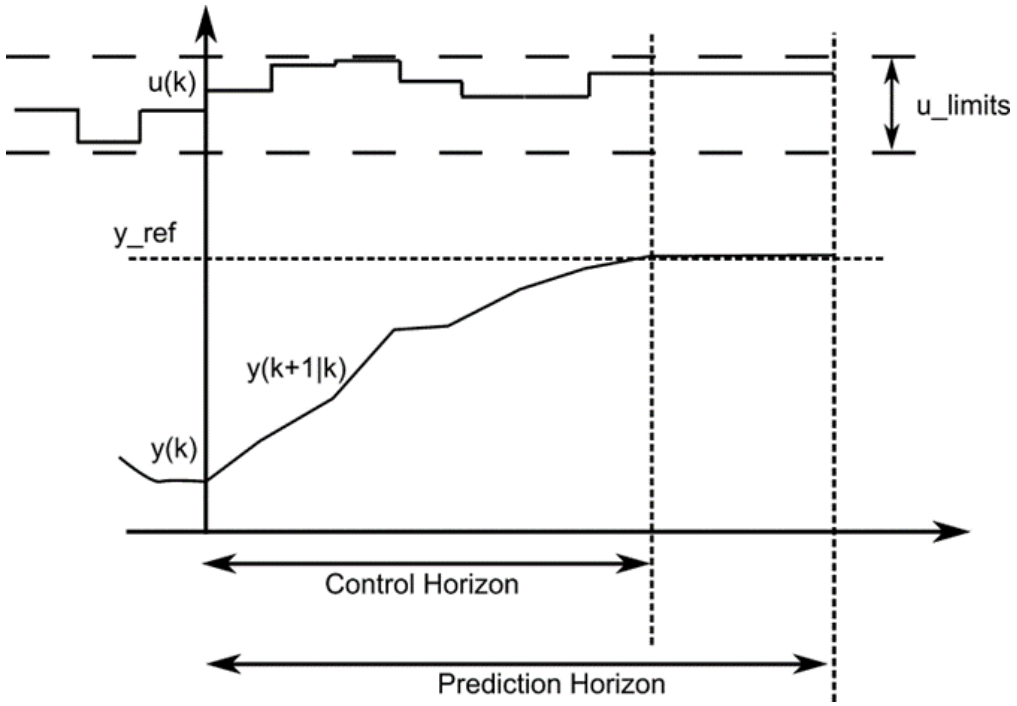

Figure 6.10: Time horizon strategy for general MPC with the moving prediction and control horizons, the set of control actions u, and the reference and expected outputs.

The nonlinear MPC defines an optimal control problem for every instant, solves it and updates it moving the time horizons for the next instant implementation. The optimal control problem has been detailed in many works as [145] and [146]. Here it is presented in the form:

$$
\begin{aligned}
&min \quad J \\
&s.t.: \\
&x(k+i) = f(x(k+i-1), u(k+i-1)) \quad | \quad x(k+1) = f(x(k), u(k)) \\
&y(k) = h(x(k+i-1), u(k+i-1)) \\
&y_{min} \leq y(k+i) \leq y_{max} \\
&u_{min} \leq u(k+i) \leq u_{max} \\
&\Delta u_{min} \leq \Delta u(k+i) \leq \Delta u_{max}
\end{aligned}
\tag{6.19}
$$

Where the cost function J is defined as:

$$J = J_y + J_u + J_{\Delta u} + J_\varepsilon \tag{6.20}$$

That is divided in four terms, each one considering one part of the total cost. First, J_y is the cost of the reference tracking that is:

$$J_y = \sum_{j=1}^{n_y} \sum_{i=1}^{p} \left\{ w_{i,j}^{y} . (r_j(k+i|k) - (y_j(k+i|k)) \right\}^2 \tag{6.21}$$

In which k is the control interval, p is the prediction horizon, n_y is the number of plant output variables, $y_j(k+i|k)$ is the predicted value of jth plant output at ith prediction horizon step, $r_j(k+i|k)$ is the reference value for jth plant output at ith prediction horizon step, and $w_{i,j}^{y}$ is the tuning weight for jth plant output at ith prediction horizon step. Then, there is the manipulated variable tracking term. This is used in some applications where it is desired to keep selected manipulated variables at specified values. The term is written as:

$$J_u = \sum_{j=1}^{n_u} \sum_{i=1}^{p} \left\{ w_{i,j}^{u} . (u_j(k+i|k) - (u_{j,target}(k+i|k)) \right\}^2 \tag{6.22}$$

Where n_u is the number of manipulated variables, $u_{j,target}(k+i|k)$ is the target value for jth manipulated variable at ith prediction horizon step, and $w_{i,j}^{u}$ is the tunning weight for jth manipulated variable at ith prediction horizon step.

Also, there is a term accounting for variations in the manipulated variables, used for smoothing the response of the actuators and produce smaller input steps. It is written as:

$$J_\Delta u = \sum_{j=1}^{n_u} \sum_{i=1}^{p-1} \left\{ w^{\Delta} u_{i,j} . (u_j(k+i|k) - (u_j(k+i-1|k)) \right\}^2 \tag{6.23}$$

Where $w^{\Delta} u_{i,j}$ is the tuning weight for jth manipulated variable movement at ith prediction horizon step. Finally, there is a term to reinforce constraints where there are situations that made them unavoidable and is preferred to introduce them as this soft constraint conditions. They are written as:

$$J_\varepsilon = \rho_\varepsilon \varepsilon_k^2 \tag{6.24}$$

Where ε_k is the slack variable at control interval k and ρ_ε is the constraint violation penalty weight.

For solving this minimization problem, it is used the sequential quadratic programming (SQP) algorithm as presented in [147], [148] . This SQP method divide the nonlinear optimization problem in a set of iterative linear subproblems. For each of these subproblems it is used a linearization of the constraints for a quadratic model. The subproblems are solved using quadratic programming (QP), and the stop condition for the iteration is when it is considered that the solution has converged with a stable value. The algorithm is considered a quasi-Newton method as sometimes the Newton-Raphson steps cannot be computed directly, and it decides a search direction and iterates until this step is achieved.

This minimization algorithm is made for simulation using the Matlab implemented function *'fmincon'*. This function is also exported to C code to integrate it in the developed SCADA software by adding it as a dynamic link library (DLL) of the rest of the *C#* application.

This method is applied to the microfluidic control of the membraneless RFB by using the model equations from 5.3, defining the input constraints in the range of the real actuators as explained in Section 3.2 (this is 0-260V for the pumps and -1000 to 1000 mW for the valves), and the states constraints are defined to not allow negative flows (this means that the two first states cannot be negative). As the minimization algorithm uses Jacobians of the f and h functions, they are derived from proposed equations. As the states and outputs are the same, for the h function the Jacobian is the identity matrix, and for the f function the Jacobians in respect to the state and the inputs are:

$$\frac{\partial f}{\partial x} = \begin{bmatrix} a_1 & 0 & 0 \\ 0 & a_2 & 0 \\ c_{Q3} & -c_{Q3} & a_3 \end{bmatrix} \tag{6.25}$$

$$\begin{matrix} if \quad U_3 < 0 \\ \frac{\partial f}{\partial u} = \begin{bmatrix} k_{V1}f_1 & -k_{P2}f_2 & k_{P3}f_3 \\ -k_{P1}f_1 & k_{V2}f_2 & k_{P3}f_3 \\ 0 & 0 & k_{V3}f_3 \end{bmatrix} \end{matrix} \qquad \begin{matrix} if \quad U_3 \geq 0 \\ \frac{\partial f}{\partial u} = \begin{bmatrix} k_{V1}f_1 & -k_{P2}f_2 & -k_{P3}f_3 \\ -k_{P1}f_1 & k_{V2}f_2 & -k_{P3}f_3 \\ 0 & 0 & k_{V3}f_3 \end{bmatrix} \end{matrix} \tag{6.26}$$

The control architecture scheme is presented in Fig. 6.11:

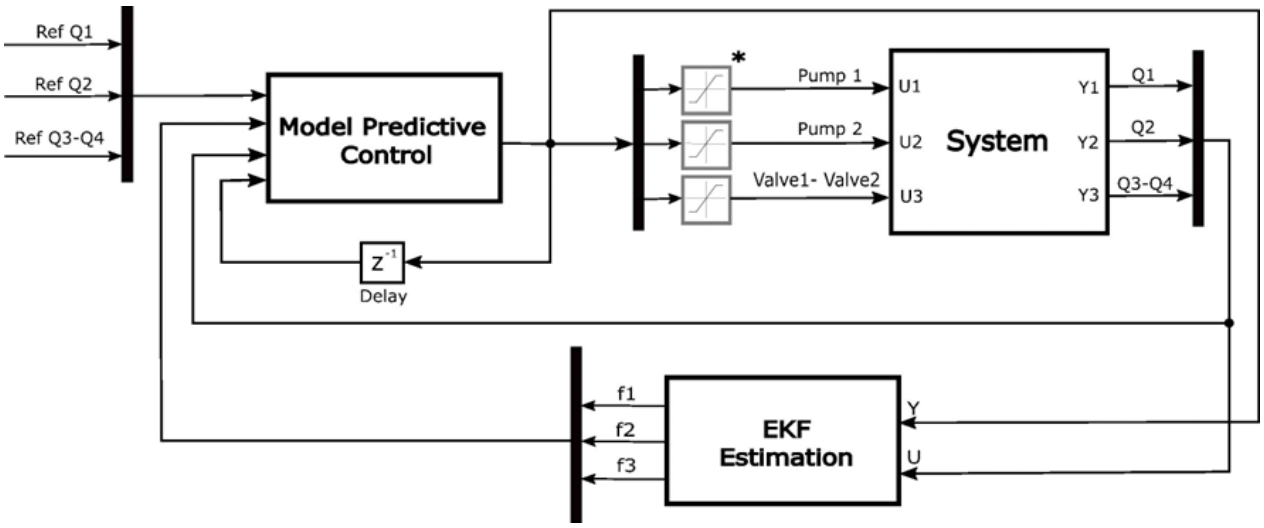

Figure 6.11: Scheme for the adaptive nonlinear MPC, with factors from the EKF estimation for the adaptive model of the control calculation, and the calculated manipulated variables. Note that saturations for the inputs are marked to indicate that are not necessary since the MPC calculation already considers the operation range as a constraint.

As it has been mentioned, for the practical implementation the constraints are defined. Also, the weights for the different cost functions, the sample time, and the control and prediction horizons. Since there are no references for the manipulated variables the weights for (6.22) are zero, and for their rates taking account of their variability in equation (6.23) the values

are $w_1^{\Delta u} = 800$, $w_2^{\Delta u} = 800$ and $w_3^{\Delta u} = 200$. For the outputs from functions cost (6.21) the weights are $w_1^{y} = 290$, $w_2^{y} = 290$ and $w_3^{y} = 40$ respectively. Soft constraints are not used for function cost (6.24) so there is no need to specify these weights. The sample time is 0,2 s, the prediction horizon is 10 samples and the control horizon is 3 samples.

All these values are adjusted by trial and error in experimental test and cross-validated in simulation. The results for the simulation and experimental response of the controller to an example reference step are presented in Fig. 6.12 and 6.12.

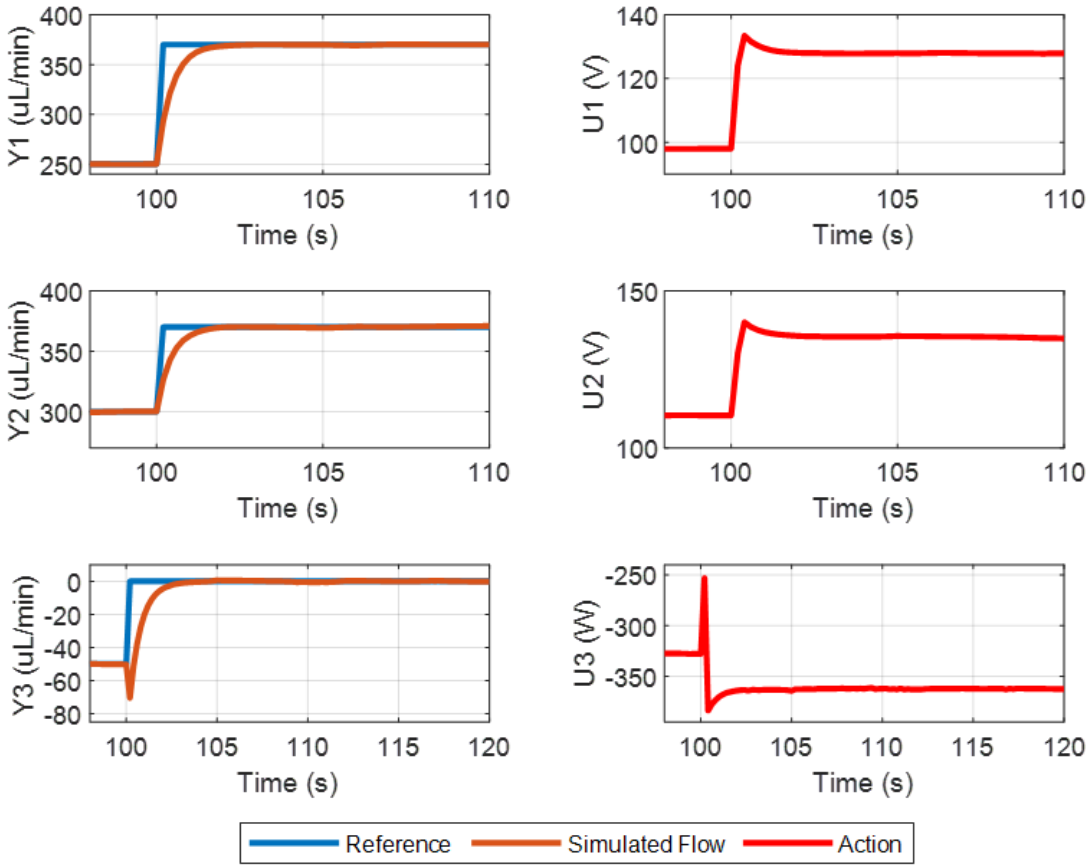

Figure 6.12: Simulated response for the adaptive nonlinear MPC architecture.

The response for the simulated and experimental response shows that the controller is capable to control fast the flows, but in real experiments appears a little overshoot that does not appear in simulation. This can indicate a small discrepancy between the model and the real system, or an exceeding change in the actuators due to stochasticity. The control can be adjusted in real operation by modifying the used weights so that the increment in the manipulated variables is smaller and the input action less aggressive. Besides this, in general It presents a good response with a short settling time for all the outputs. For the two first outputs it stabilizes in less than 5 seconds, although again the response is worst in the real experiment and the zero steady state error takes a little bit more of time. Regarding the

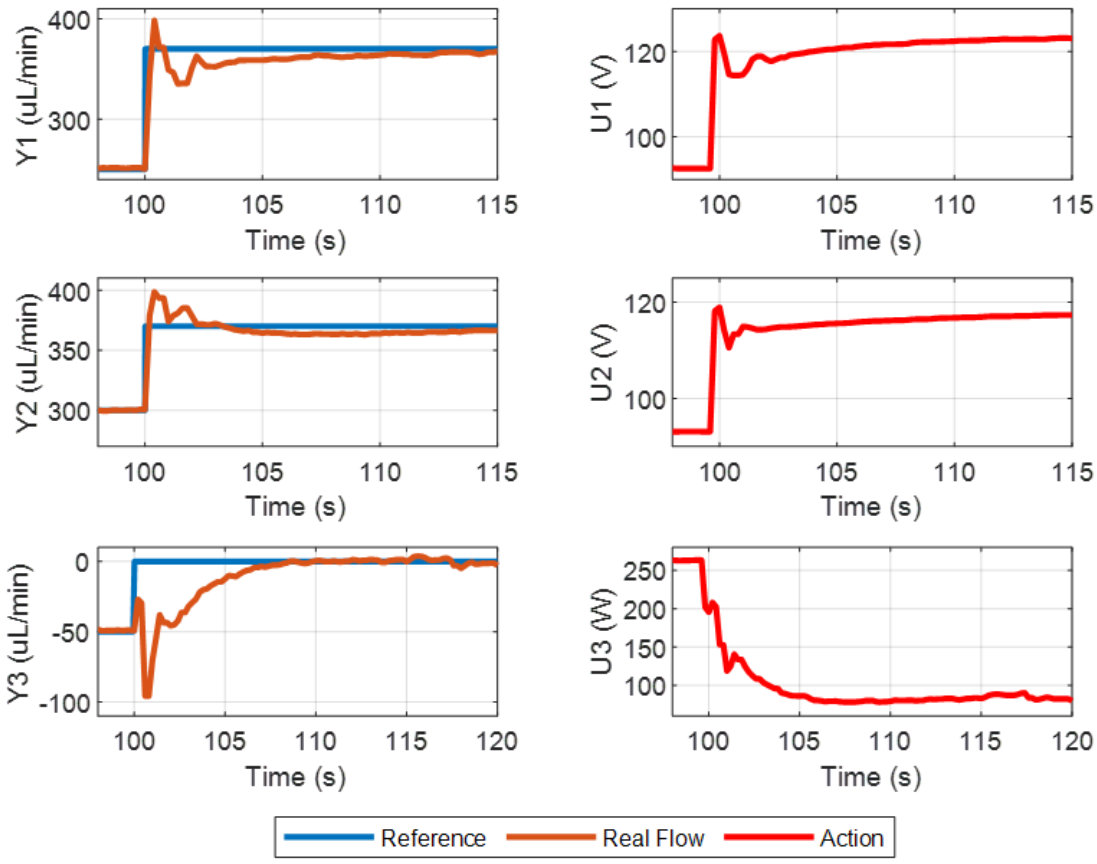

Figure 6.13: Real experiment response for the adaptive nonlinear MPC architecture.

third output it has again a slower response, but this time is close to the other with less than 30 seconds of settling time, which is a remarkable improvement compared to the previous optimal with integral and incremental controllers. However, now this output presents a peak at the start of the transient response, that although being short it represents a high error than is expected to produce a significant mixing in the electrolytes. The controller has a good response, improving previous ones in some features such as speed, but worsening in others like the observed perturbations and its most reliance on an exact modelling. The computational cost of this algorithm is high compared to the other (the whole computer application acting as SCADA run with this control algorithm in about 95 ms).

The results for simulation are less similar to the ones in the real experimentation for this controller than to the others. This is caused by the explained higher dependency of this method on a precise modelling. This is a weakness that is present even when the correction factors are applied in real time using the EKF estimation. As other methods, there are also differences in the steady state values of the input actions. The chosen weights can be modified to improve the overshoot at the cost of losing the gained speed, so the current ones are kept to better show this method capability to accelerate the response, and to better observe the problem of the differences between simulation and real response.

6.2.4 Adaptive Incremental Model Predictive Control

Another methodology proposed for the microfluidic control based on model predictive control techniques is made using the incremental implementation of the state space model, as it was described in Section 6.2.2. This regulation strategy aims to add to the previous mentioned advantages of MPC (an optimal search taking into account state, output and input trajectories, with constraints definition, for a moving time horizon), an incremental approach that accounts for an integral type of action. This incremental implementation is expected to help to reduce the steady state error seen in the transient response of the previous nonlinear adaptive MPC. Therefore, it should achieve faster the zero error than this previous regulation method where modelling discrepancies made the controller to take significant time.

The MPC part of the regulation consist again in a moving time horizon optimization of a cost function. The procedure representation is also depicted in Fig. 6.10, and the function cost to minimize is described in equations (6.19) to (6.24). However, the state space representation is now the one presented in equations (6.13) to (6.18) in Section 6.2.2.

Since the state space definition is now made using this equation (6.13) to (6.18), it can be observed that the manipulated variables that are optimized within the process account for the increment in the inputs of the original not augmented system (equation 6.15). Also, the state prediction and measured are written as increments of the original ones. Consequently, the control architecture is defined as represented in Fig. 6.14. Note that in this architecture the external input saturations are now needed due to the explained usage of the manipulated variables calculation within the MPC algorithm.

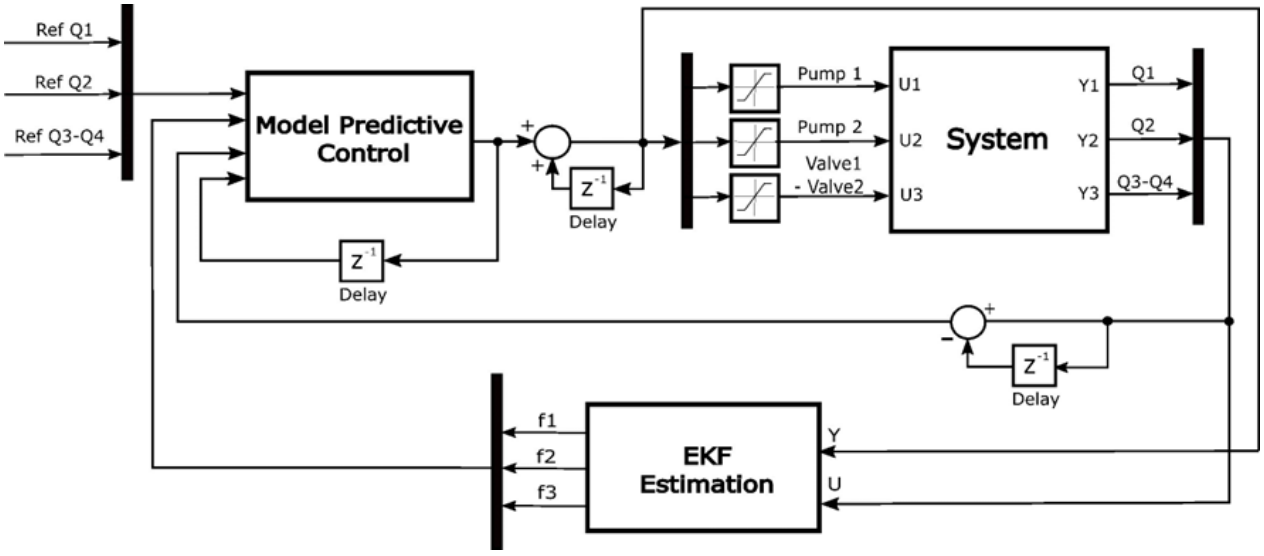

Figure 6.14: Scheme for the adaptive incremental MPC, with factors from the EKF estimation for the adaptive model of the control calculation, and the calculated increment in the manipulated variables.

The minimization problem is again solved using the same sequential quadratic programming (SQP) algorithm. It once more divides the problem in a set of subproblems where a linearization of the constraints and model are made. As it is applied for adaptive nonlinear MPC, the

Matlab implemented function *'fmincon'* is used for simulation and it is exported to C code for the real experiments, where it is integrated in the application software as a dynamic link library (DLL).

This method is applied to the microfluidic control of the membraneless RFB by using the model equations from 6.18, defining now the input constraints as -10 to 10 for the increment of the pumps values, and -20 to 20 as the range for the increment in the input regulating the valves. The states as defined in (6.15) are constrained also for the output part of the original system, in order to avoid negative inlet flows. The incremental part of the state have no constraints. The Jacobians of the f and h functions from equation (6.19), as derived from proposed equations, and are:

$$\frac{\partial h}{\partial y} = \begin{bmatrix} I \\ 0 \end{bmatrix} \tag{6.27}$$

$$\frac{\partial f}{\partial x} = \begin{bmatrix} 1 & 0 & 0 & a_1 & 0 & 0 \\ 0 & 1 & 0 & 0 & a_2 & 0 \\ 0 & 0 & 1 & c_{Q3} & -c_{Q3} & a_3 \\ 0 & 0 & 0 & a_1 & 0 & 0 \\ 0 & 0 & 0 & 0 & a_2 & 0 \\ 0 & 0 & 0 & c_{Q3} & -c_{Q3} & a_3 \end{bmatrix} \tag{6.28}$$

$$\begin{array}{cc} if \quad U_3 < 0 & if \quad U_3 \geq 0 \\ \frac{\partial f}{\partial u} = \begin{bmatrix} k_{V1}f_1 & -k_{P2}f_2 & k_{P3}f_3 \\ -k_{P1}f_1 & k_{V2}f_2 & k_{P3}f_3 \\ 0 & 0 & k_{V3}f_3 \\ k_{V1}f_1 & -k_{P2}f_2 & k_{P3}f_3 \\ -k_{P1}f_1 & k_{V2}f_2 & k_{P3}f_3 \\ 0 & 0 & k_{V3}f_3 \end{bmatrix} & \frac{\partial f}{\partial u} = \begin{bmatrix} k_{V1}f_1 & -k_{P2}f_2 & -k_{P3}f_3 \\ -k_{P1}f_1 & k_{V2}f_2 & -k_{P3}f_3 \\ 0 & 0 & k_{V3}f_3 \\ k_{V1}f_1 & -k_{P2}f_2 & -k_{P3}f_3 \\ -k_{P1}f_1 & k_{V2}f_2 & -k_{P3}f_3 \\ 0 & 0 & k_{V3}f_3 \end{bmatrix} \end{array} \tag{6.29}$$

The values for the weights, and control and prediction time horizons are adjusted by trial and error in experimental test and cross-validated in simulation. This time, as the manipulated variables are increments of the inputs of the real system, they have weights to limit the increment, so the weights for (6.22) are $w_1^u = 0,1$, $w_2^u = 0,1$ and $w_3^u = 0,1$. This values are modulated with their rates, that take account also of their variability in equation (6.23) (the variability of the increment) the values are $w_1^{\Delta u} = 100$, $w_2^{\Delta u} = 100$ and $w_3^{\Delta u} = 20$. For the outputs from functions cost (6.21) the weights are $w_1^y = 1$, $w_2^y = 1$ and $w_3^y = 1$ respectively. Soft constraints are not used for function cost (6.24) so there is no need to specify these weights. The sample time is 0,2 s, the prediction horizon is 10 samples and the control horizon is 2 samples. The results for the simulation and experimental response of the controller to an example reference step are presented in Fig. 6.15 and 6.16.

The simulation and real experiment show a good response, with a fast stabilization and less overshoot than the previous MPC method. For the two first outputs it stabilizes in less than

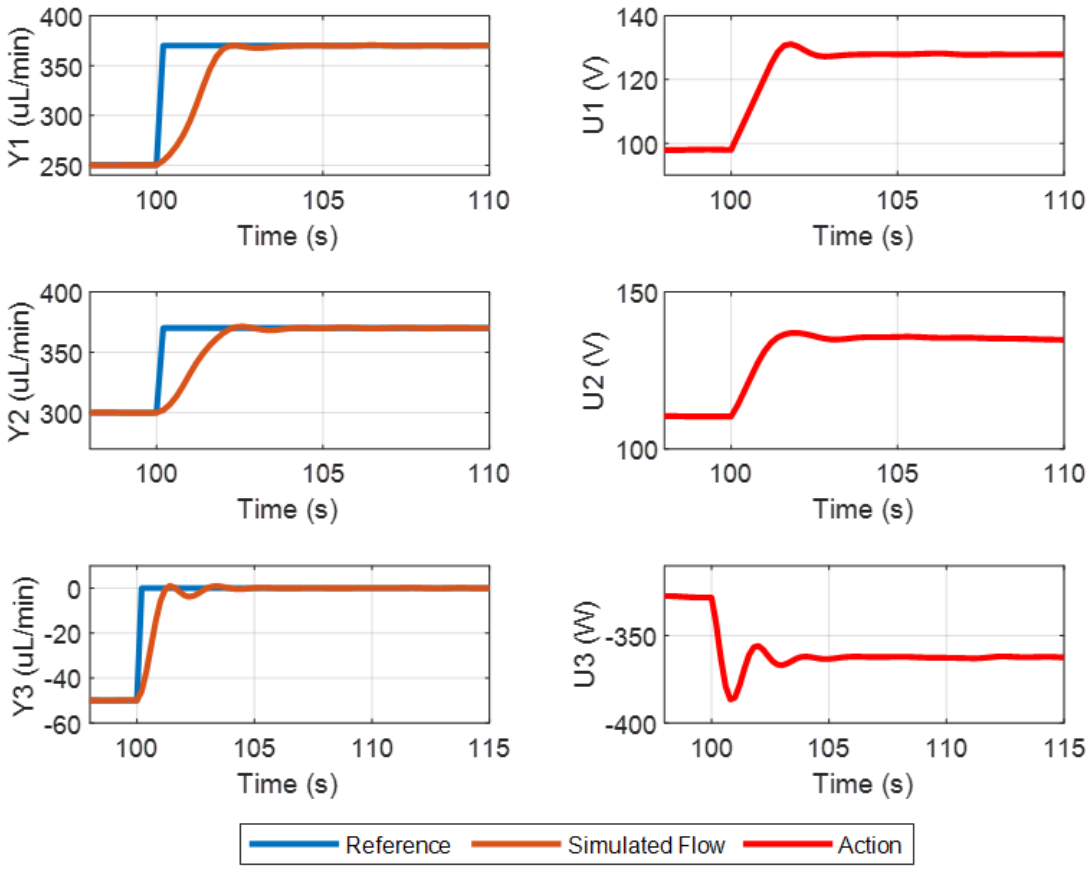

Figure 6.15: Simulated response for the adaptive incremental MPC architecture.

5 seconds and the overshoot is below 5% in real experiments (in simulation is even smaller although still present). Regarding the third output, as seen in all controllers the response is slower, but in this case is closer to the two first outputs, and this cause a small oscillation. These oscillations are larger and longer in time for the real experiment, but it is still the best obtained response for this variable. Also, regarding this output, the observed peak at the start of the transient response for the adaptive nonlinear MPC is smaller in this controller. The controller has a good response, improving previous ones in most features specially for the third output where it is faster and despite appearing small oscillations, they are less pronounced than previous MPC. This also proves less reliance on an exact modelling for this control method. The computational cost of this algorithm is high but lower than previous MPC (the whole computer application acting as SCADA run with this control algorithm in about 70ms).

The results for simulation are very similar to the ones in the real experimentation. The oscillations and overshoot for the two first outputs of the real experiment exceed slightly the ones from simulation. However, it is the third output the one that shows higher discrepancies in these values, and more significantly the period time of this oscillations. This difference in the period of oscillations is also observed in the third input, where a similar tendency occurs.

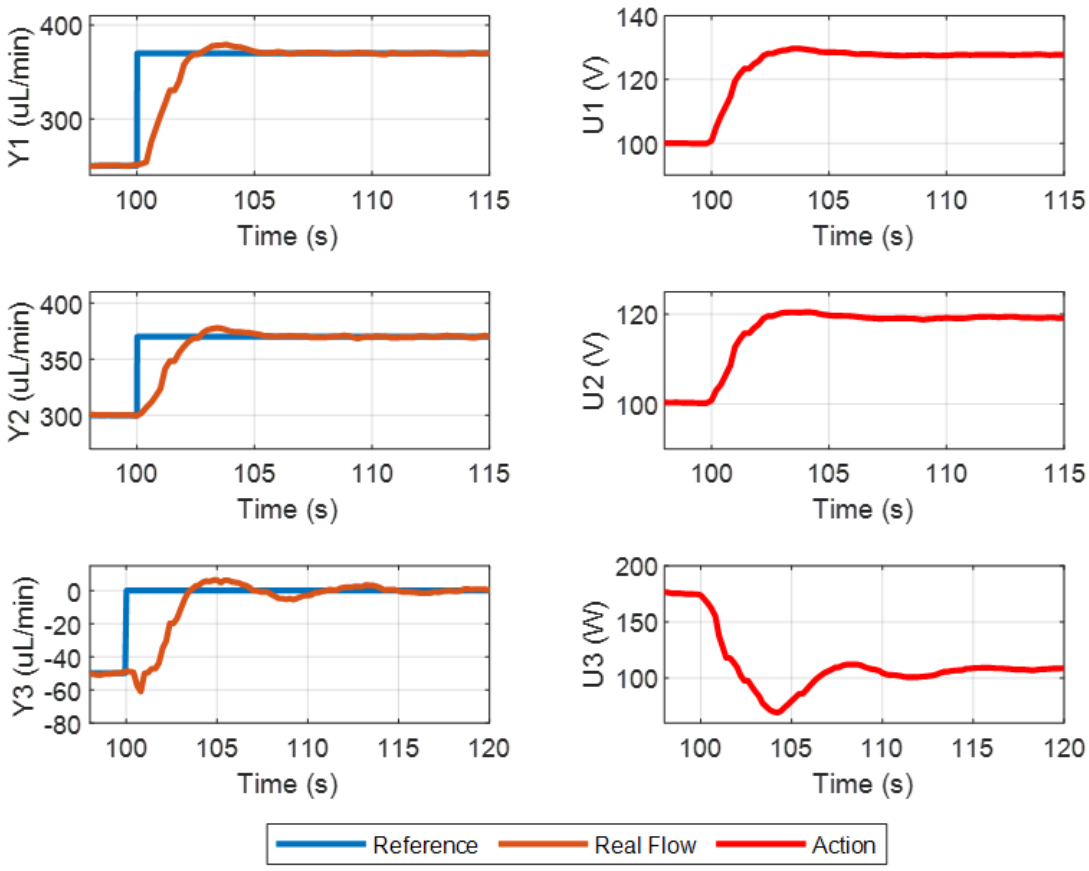

Figure 6.16: Real experiment response for the adaptive incremental MPC architecture.

These input values, as it is seen in other methods, show differences in the steady state values due to the stochasticity that the models adapt with the correction factors of the actuators.

6.3 Conclusions

In this chapter several control methods are proposed, its implementation described and tested in simulation and real experiments. These results are explored through all the chapter, but hereunder are presented together to better compare them in an step example. The simulations and real experiments for all of them are depicted in Fig. 6.17 and Fig. 6.18 respectively. Also, a sequence of references steps is presented in Fig. 6.19, so that result to different changes are also shown in a longer real experiment. The conclusions deduced from these comparisons and from the study of each of them are summarized as follows:

- Model free strategy based on independent PIDs acting as SISO systems can be implemented. This is a simple approach that do not requires high implementation or computational effort and can make the system converge to the desired references with zero steady state error. However, the transient response is not good, with oscillations,

high settling time and high overshoots.

- There are several control strategies than can be designed based on the model proposed in Chapter 5 and its real time factor correction based on EKF.
- One of these techniques is a LQR with integral action, which is proposed as a control strategy. This method considers a classical LQR approach for the augmented state space system to include the integral action for accounting for the steady state error. It improves the oscillations of the independent PIDs, showing a smooth but slow response. The implementation is easy with a limited computational cost.
- Other adaptive method based on an optimization is the adaptive incremental optimal control. This method modifies the state space system by written it in an incremental form. This is a similar to integral action that drives the system to a zero steady state error, and it is able to accelerate to a small extend the transient response compared to the LQR with integral action. The computational cost is also limited.
- The model with the real time correction is also used in model predictive approaches where for a moving time horizon the trajectory of the states, outputs and manipulated variables are considered for optimizing a cost function with explicit constraints.
- The first implementation of the MPC approach uses the nonlinear adapted model as it is to minimize the cost function. This allows to obtain a fast response that differs in real experiments more from simulation than other controllers. This is caused by model inaccuracies that are more critical in this method that relies on more on the model. This dependency causes that real response has oscillations and peak that produce errors. Also, the algorithm implementation is more computationally costly.
- The second MPC implementation is based on the incremental augmentation of the state space representation. This incorporates an integral like action to the MPC algorithm. The control architecture has to be reorganized to consider state, input and outputs as increments. The obtained response has a speed in the same order as the previous MPC, but sacrifices it slightly to be able to reduce errors due to oscillations and peaks, and achieves more smoothly zero steady state error. The computational cost is similar but lighter than previous MPC.
- The electrical response of using each controller is evaluated in next chapter so that they can be selected based on an electrical battery performance criterion.

The design of the five proposed control strategies, its simulation using the proposed fluidic model, and its experimental validation is one of the main contributions of this thesis.

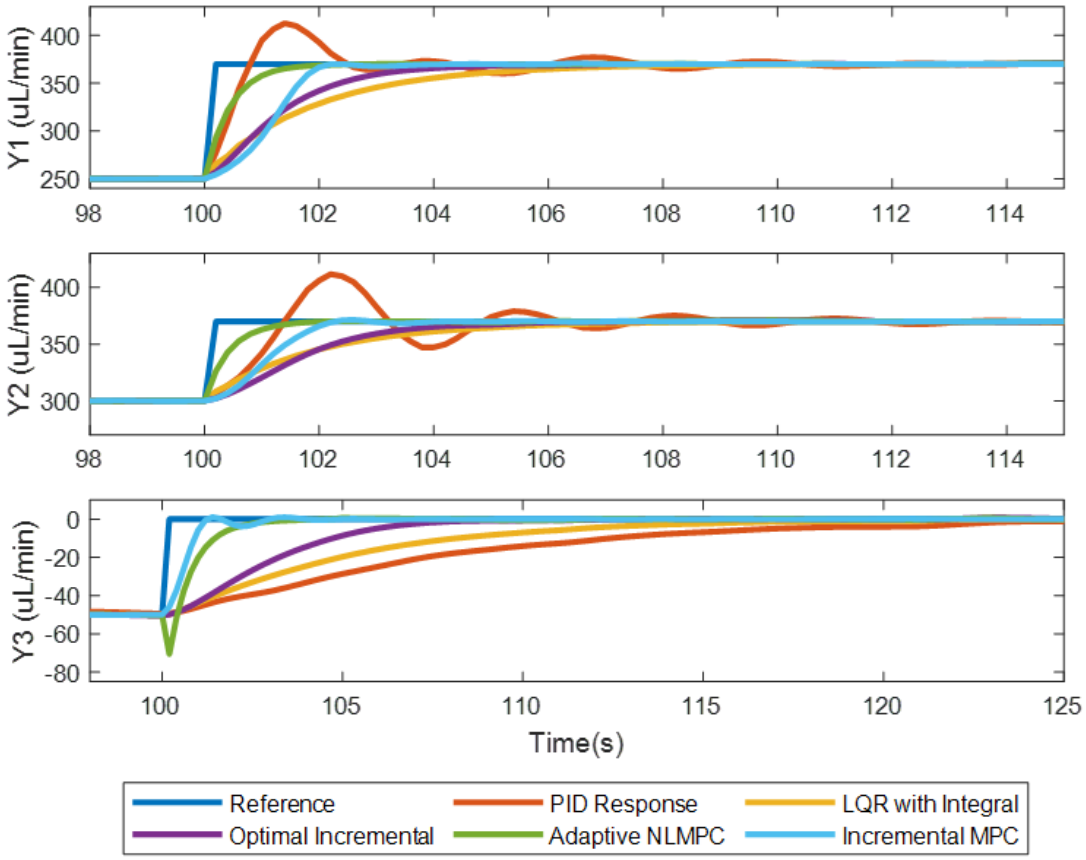

Figure 6.17: Simulated response to a single reference step. Comparison of all the proposed control methods.

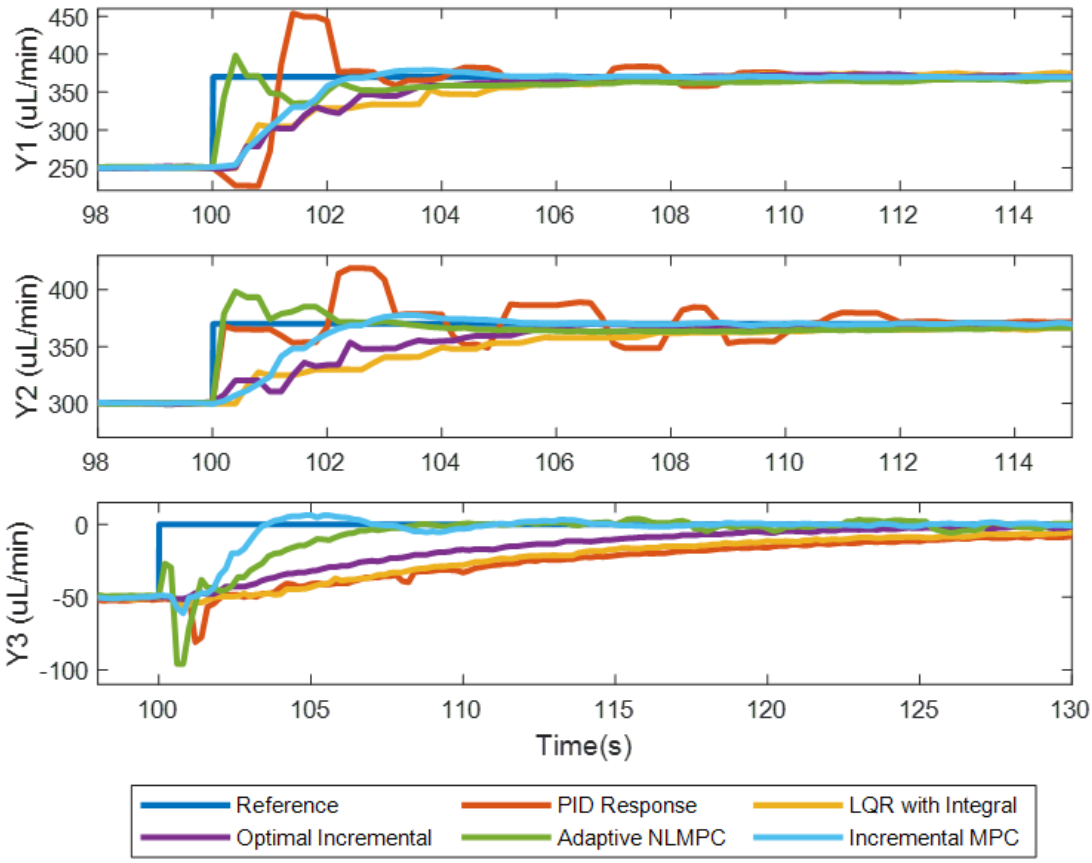

Figure 6.18: Real experiments response to a single reference step. Comparison of all the proposed control methods.

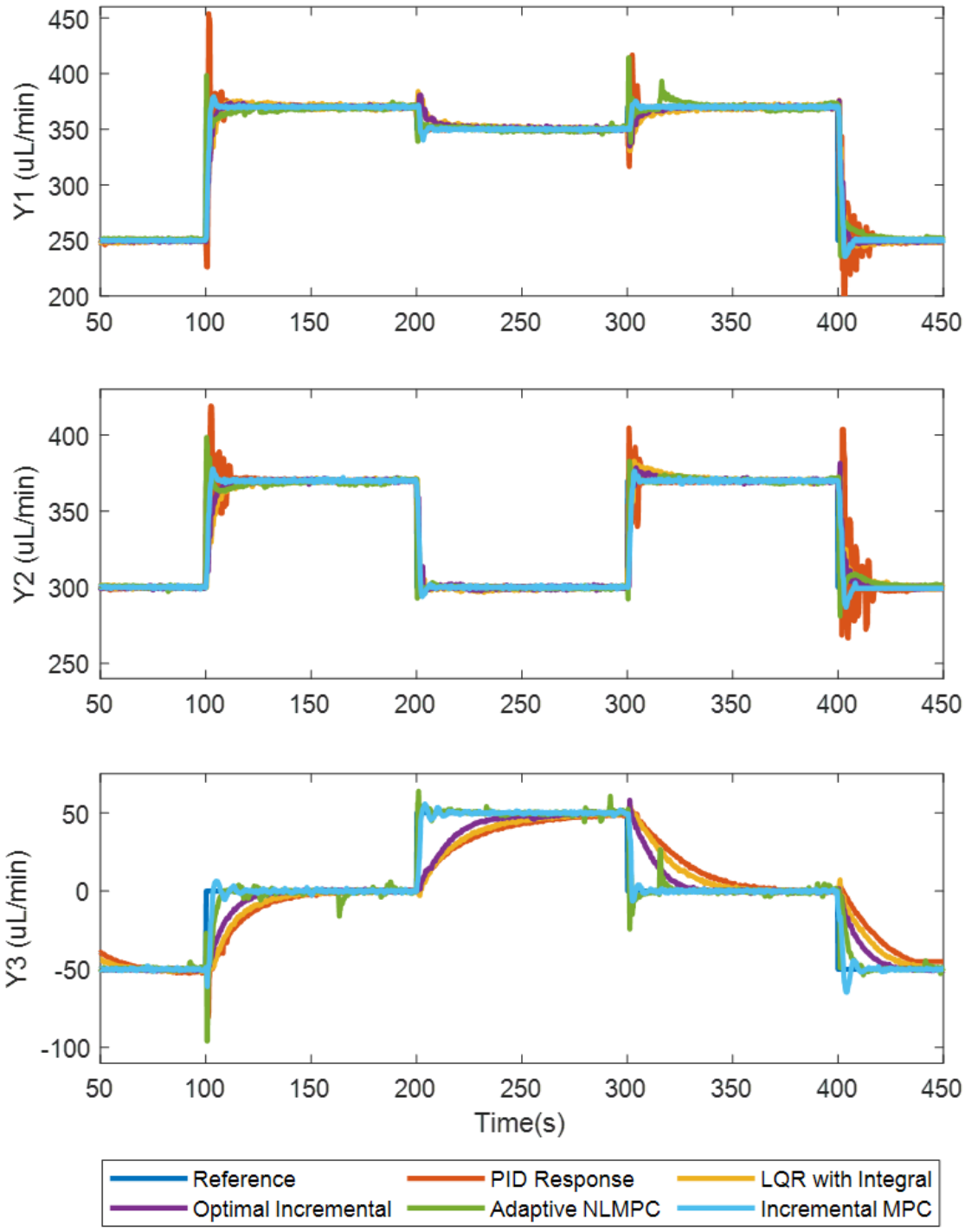

Figure 6.19: Real experiments response to a sequence of different steps. Comparison of all the proposed control methods.

Chapter 7

Control strategies evaluation

The results of the control strategies presented in Chapter 6 have been only evaluated with an example step change in their reference and showing their flows and inputs responses. However, this can only give an approximate idea of the battery performance during operation with each of these regulation methods. It is necessary to evaluate the electrical response of the battery when the microfluidic dynamics are determined by each controller, and to do such task the electrical model from Chapter 4 is used in this chapter. This way, different measured real flow responses can be evaluated electrically applying the electrical model, without the need for real electrical measurements. These electrical measurements have the problem that they would be influenced by other variables and would need long operation times so that the measurements obtained with each control strategy would be considered valid and analogous.

The control methods are going to be evaluated using a benchmark power profile that would determine the required flow configuration. Within this benchmark, the strategies are going to be evaluated testing their available power response, the SOC losses due to mixing and self-discharge, and finally a microfluidic actuators power consumption term is also evaluated.

7.1 Power Profile Definition

Membraneless RFB must adapt their flow configuration to maintain the liquids interface properly positioned while renewing the electrolyte species within the reactor. Therefore, with changing power references the flow configuration setpoints also vary. These changing references during the charge or discharge process depend on the application where the battery is used. As it has been explained in the introduction of this thesis, RFB properties made them especially useful in applications with intermittent operation, where their long cycle life, depth of discharge and low degradation made them outperform other energy storage technologies. This is the case of renewable power sources, the most common application for RFB that are characterized for their continuous power variability. An example of this intermittent available source power is presented in [149], where an example of rooftop photovoltaic installation is analysed, and the power profile for a sunny and partially cloudy day are presented.

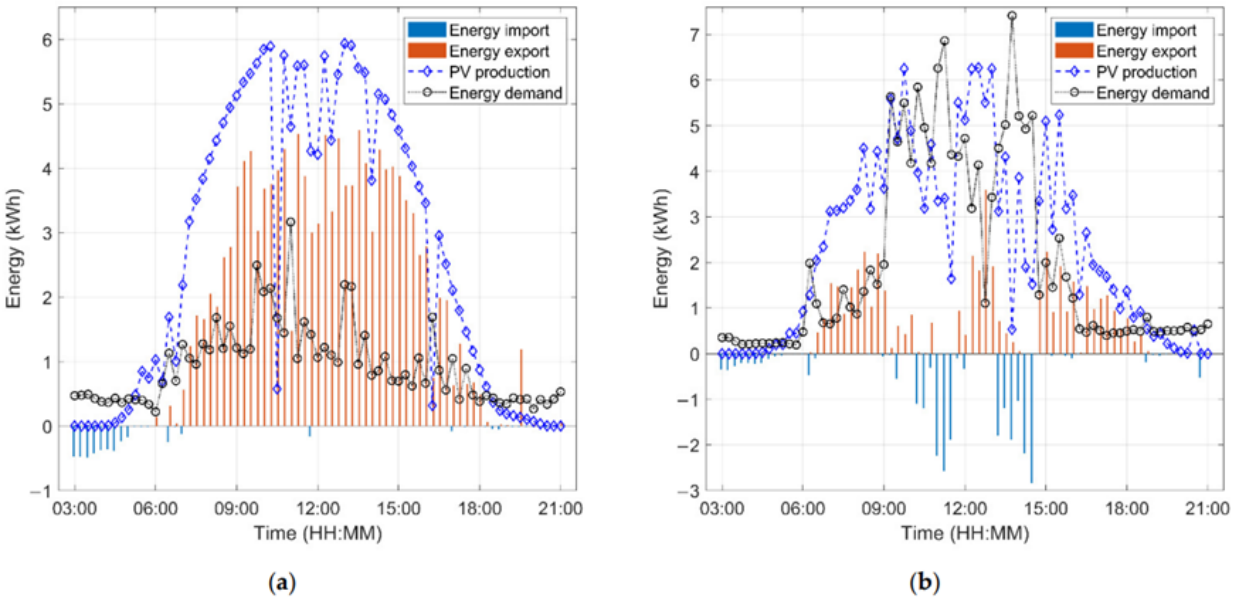

Figure 7.1: Profiles from [149] where energy production, load, energy import, and export are presented for a sunny day of July 2020 (a) and a partly cloudy day of July 2020 (b).

In Fig. 7.1 and the referenced work it can be observed that even for sunny days there are heavy intermittent changes that require a significant change in the power of the hypothetical battery working with this source. In the case of the microfluidic membraneless RFB, that would be mean either flowing continuously over the required minimum inlet flow for species renewal to assure battery power is always available (increasing pumping losses), or adapting the flow configuration to each condition using the designed microfluidic control methods. Therefore, to evaluate these methods and based on the observed typical variability it is defined an example power setpoint steps profile. This profile is shown in Fig 7.2.

The proposed power profile considers relative power from the cell, as considered in the modelling from Chapter 4, and defines power steps around one third to two thirds of the maximum power of the cell. The sequence of step is defined for 450 seconds and is defined with steps 100 seconds apart from one another. These time ranges are selected to be as frequent as they could be in a real intermittent application, and separated enough to make sure all control strategies are settled in their setpoints.

This power profile determines an equivalent flow configuration profile that is the one that acts as the setpoint for the controllers. These flow setpoints are derived from equations (4.10) to (4.12) that establish a minimum inlet flow for each demanded power value, and the ratios of the inlets and outlets to stay within the limits that do not generate any power loss. Therefore, the flow configuration profile has the same shape as the power profile from Fig. 7.2 but with the equivalent flow rate for the inlets, and the proper difference ratio between the outlets.

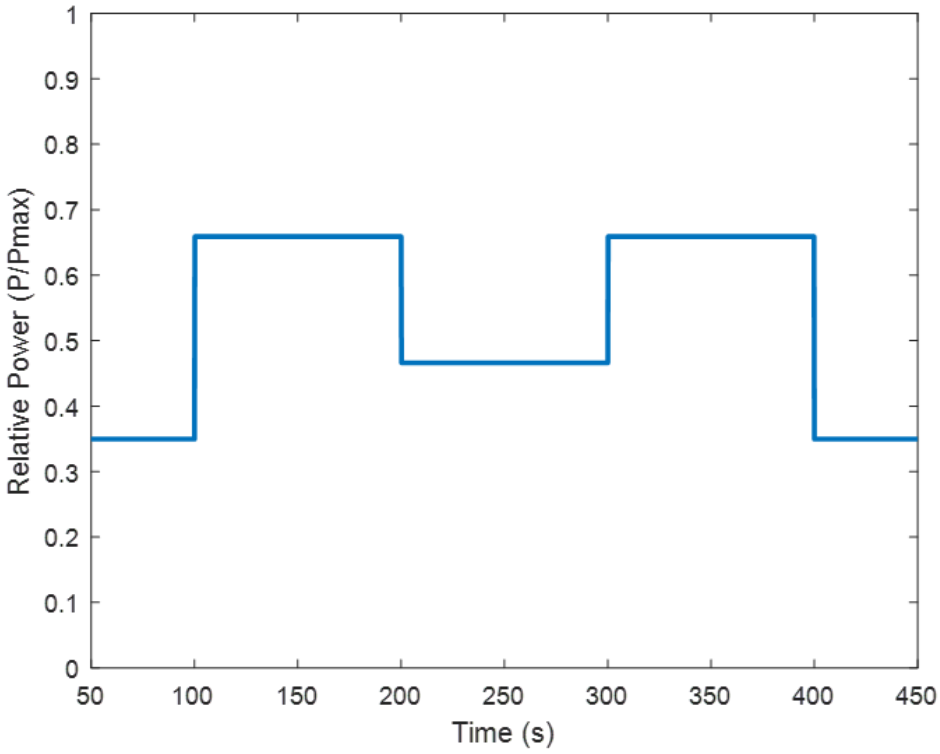

Figure 7.2: Benchmark power profile defined for control strategies electric evaluation.

7.2 Control Strategies Evaluation

Given the defined power benchmark, the strategies are evaluated testing their available power response, the SOC losses due to mixing and self-discharge, and their actuators power consumption.

7.2.1 Available Relative Cell Power

The first electrical measurement that control strategies must comply with is adapt the microfluidic configuration to the required power. In this section, it is analysed how fast and stably can the different control methods adapt their available power. Based on these responses, it must be defined the power electronics transient actuation, a safety factor for the flow to over provide the minimum species renewal, or other actions to consider battery response limitations. However, in this evaluation the control strategies references are set to the instantaneous power demand to evaluate their response before any engineering factor is afterwards applied to comply with real operation requirements. This way, it can be better observed which strategies are able to meet the power demands more efficiently.

Electrical model equations (4.10) to (4.12) give the relative power steady state value for determined SOC and temperature, while equations (4.14) and (4.15) define the dynamic transient response of this relative power. Using the values for these equations identified in Chapter 4, and using the same setup for the different control strategies, the measured flow

configurations are introduced as the input for the electrical model, and the power outputs are obtained as presented in Fig. 7.3.

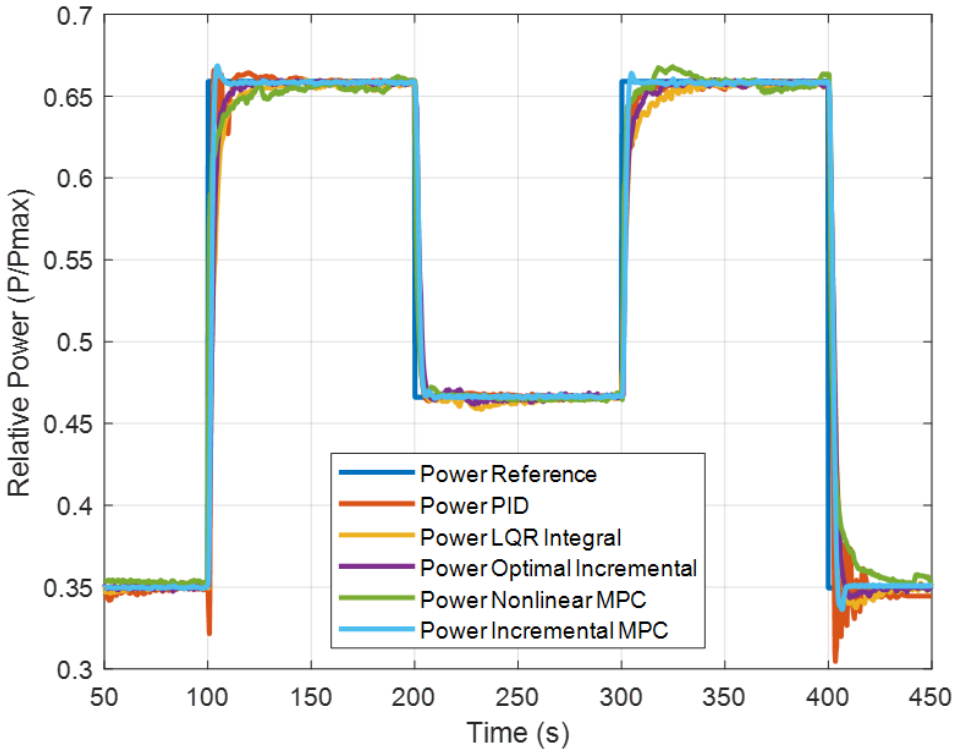

Figure 7.3: Benchmark power profile with the relative power response of each of the control strategies.

This figure shows that the different controllers adapt the power similarly, with differences in the transient responses and some more evident instabilities. These instabilities are mainly seen in the PID controller with the power oscillating, and the adaptive nonlinear MPC where available power distances from the reference at specific moments. These errors in the nonlinear MPC are explained by the previously mentioned stronger reliance of this method in an exact modelling which causes it to be affected more severely by stochasticity. It can be also observed that for the steps increasing the power the differences between controllers are more pronounced and more critical, since for the steps of decreasing power the power dynamics themselves are slower and there is no problem in the available power being over the required one except for the pumping power surplus. As a detailed view for better observing the transient response, single steps increasing and decreasing power are presented in Fig. 7.4 and Fig. 7.5.

The increasing power demand shows that the adaptive incremental MPC has the fastest and more precise response, combining the MPC trajectory optimization with the incremental representation for adding an integral action. Nonlinear MPC shows a slow response, with power increasing rapidly but taking quite time to settle to the reference exactly. This is caused by the peak error at the flow of the outlets and despite the flows at the inlets showing a fast response. This controller also shows the mentioned problems with stochasticity. The

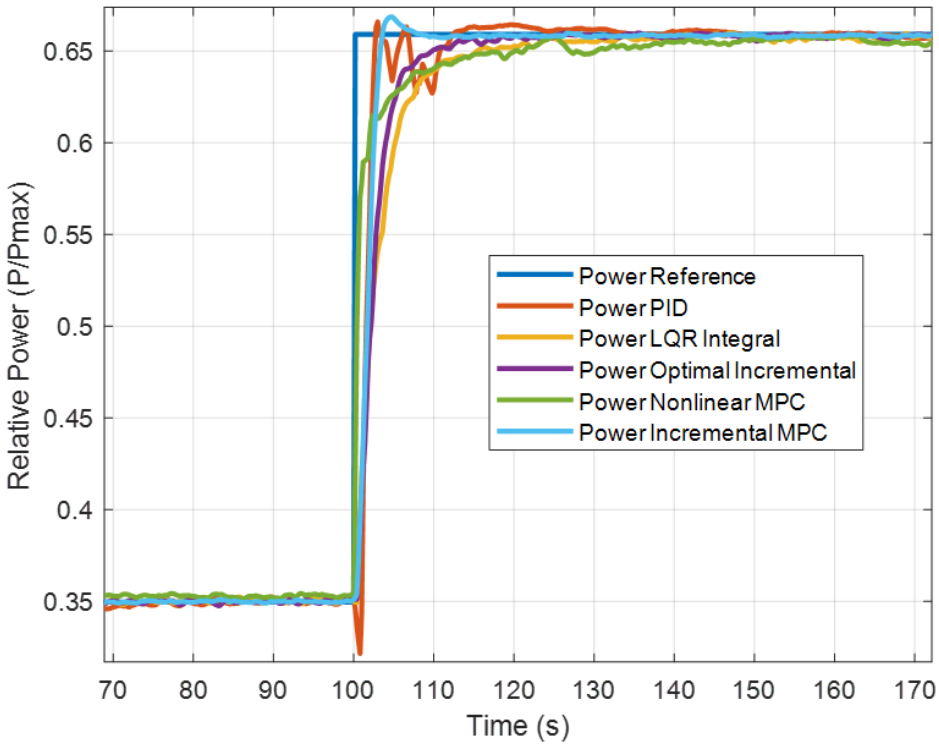

Figure 7.4: Detail of the benchmark power profile with a single step increasing the reference and the relative power response of each of the control strategies.

PID controller shows a oscillated response, but the oscillations in this case are smaller than shown in the flows in previous chapter due to power dynamics damping (the model dynamics in equation (4.15) act as a low pass filter). Both LQR with integral action and optimal with incremental implementation show a smooth power response like their flow responses.

The decrease in power reference shown in Fig. 7.5 shows similar results than the increase in power reference but with important differences in the responses and its and implications. Adaptive incremental MPC still has the best power response, although the peak in the increasing step is now converted in a valley that would produce an available power the required. That would be solved using a safety factor for the minimum inlet flows as already explained. The nonlinear MPC is again slow but is not a problem more than an excessive pumping power usage for a limited time. The three independent PID controllers working together now produce a higher oscillation that significantly influences available power even with the damping of the intrinsic power dynamics. LQR with integral action and the optimal with incremental state control have a consistent smooth response like in the power increase steps. It can be deduced that besides each controller response, it could be used parameters for each of them that slow down their response, decreasing available power gradually and with a limited pumping power excess.

In order to quantify the fitness of the controllers, it is measured the relative percentage of power that each controller is under the required one. This index is defined in equation (7.1).

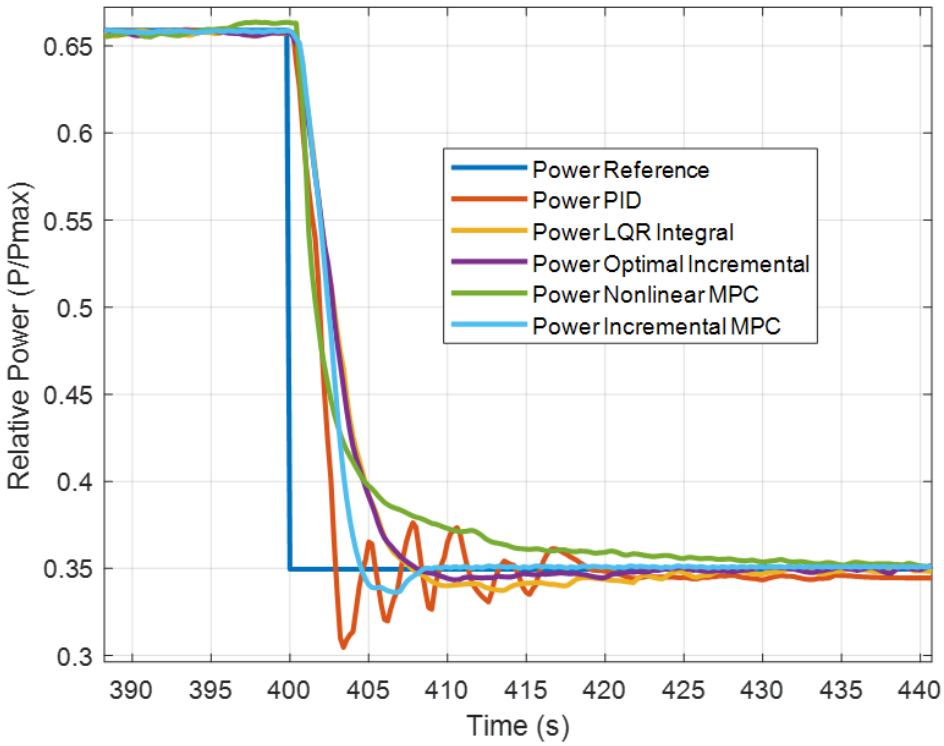

Figure 7.5: Detail of the benchmark power profile with a single step decreasing the reference and the relative power response of each of the control strategies.

$$I_i = \frac{\int P_{u,i}(t)}{\int P_{ref}(t)}.100 \tag{7.1}$$

$$\begin{array}{ll} if \quad P_{ref}(t) > P_i(t) & else \\ P_{u,i}(t) = P_{ref}(t) - P_i(t) & P_{u,i}(t) = 0 \end{array}$$

Where I_i is the index for each control strategy i, P_{ref} is the reference power from the power profile benchmark, and $P_{u,i}$ is the relative power under P_{ref} for each controller i. This value is only used as a reference, as it has been explained that safety factors and slower decreasing response would be implemented in real operation to limit available powers under the demand. However, this value is useful to compare the controllers. The result of applying this index to the defined power profile benchmark are presented in Table 7.1.

This index shows again that the adaptive incremental MPC has the minimum value of power under the reference. It is remarkable the adaptive nonlinear MPC which apparently had a slow response, has a good value. This is because its power increases fast and then there is an error until reaching the reference in steady state, but this error is small and therefore its integral value is limited. The LQR with integral action has the worst index due to the slow

Indep. PIDs	LQR with Integral	Optimal with Incremental State	Adaptive Nonlinear MPC	Adaptive Incremental MPC
0.92%	1.08%	0.87%	0.69%	0.54%

Table 7.1: Percentage of power under demanded reference power for each control method

power response and bigger settling time. The optimal control with incremental state improves the PID response but still is conditioned by the smooth increase in power. This independent PIDs have an unexpectedly good index value, since as mentioned before the implicit power dynamics damp the oscillations of this controller. These oscillations do affect mixing losses as detailed in the next section and are important in the whole evaluation of the designed control methods.

7.2.2 Mixing Losses

Losses in the state of charge due to diffusion and mixing are an important metric to consider when evaluating control strategies to be used in the microfluidic membraneless RFB. These losses affect directly battery efficiency as state of charge losses is energy that is not stored. Also, it has to be considered that volume mixing generates tanks volume unbalancing, what reduces total energy capacity (net usable volume is reduced), and also reduces time before a balancing cycle is required. This balancing is a maintenance process that is required after some operation time to compensate for the differences of volume in the tanks and reset the electrolyte species to their original oxidation states. Reducing the mixing and postponing this maintenance can translate into saving costs.

The control strategies are evaluated for this criterion using the same benchmark power profile experiments, and now measuring the volumes mixed from the flowmeters. Using the expression from (4.17) the volume mixed is calculated integrating flowmeter instantaneous values and considering the outlet where the mixing is occurring. The evolution of the mixing for the different control methods is presented in Fig. 7.6.

The final mixing values for the benchmark experiment are presented in Table 7.2. It must be noted that these results are for a limited time and limited reference steps, and hence the mixing volume would increase with time as Fig. 7.6 tendency shows, and it would be more pronounced the more intermittent or variable power the application requires.

Indep. PIDs	LQR with Integral	Optimal with Incremental State	Adaptive Nonlinear MPC	Adaptive Incremental MPC
$77.46\mu l$	$68.40\mu l$	$44.18\mu l$	$12.88\mu l$	$9.3\mu l$

Table 7.2: Volume mixed during benchmark operation for each control method

This table shows that independent PIDs have the more amount of volume mixed, and observing the curve from Fig. 7.6 and the previous flow response it can be explained to oscillations in the inlet flows and slow response in the flow of the outlets. This same slow response at the outlets is the same one that causes that LQR control with integral action to also have high

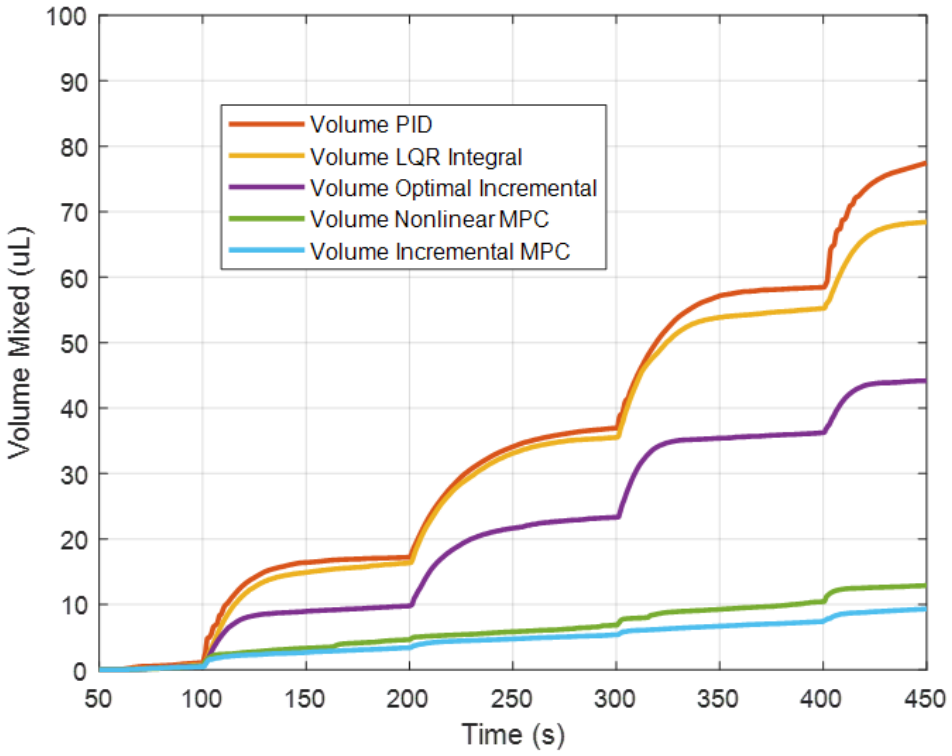

Figure 7.6: Volume mixed evolution in benchmark power profile experiment for the different designed control strategies.

volume mixed. Actually, for these two control methods have a similar mixing evolution except when PID oscillates, where its mixing volume increases faster. The optimal control with incremental state has again a reasonable value with a significant improvement to model free and LQR with integral regulations. Both variants of MPC control have a really low mixing value. Incremental implementation for MPC is again the best control method for this metric. Adaptive nonlinear MPC produces a small mixed volume despite its problems dealing with stochasticity, what can be explained because the errors in flow although being quite frequent are of a small value.

Regarding state of charge losses linked with the volumes mixed, it is used the modelling from (4.16) to calculate the equivalent loss. The values are presented in Table 7.3.

Indep. PIDs	LQR with Integral	Optimal with Incremental State	Adaptive Nonlinear MPC	Adaptive Incremental MPC
0.26%	0.22%	0.15%	0.04%	0.03%

Table 7.3: Increment in state of charge losses during benchmark operation for each control method

The values show a similar distribution compared to the table of mixed volumes, as equation (4.16) shows the linear proportionality term between them. The conclusion and causes for

each of them are hence the same. It must be again noted that these are values for the limited running time and reference steps of the experiment. Therefore, these losses would be much more significant with more frequent reference steps, which are the conditions where the main volume mixing occurs, as seen in Fig. 7.6.

Another consideration that must be analysed is the relative impact of the mixing in the state of charge losses. Even if limiting the mixing is critical to avoid tanks unbalancing, regarding SOC losses it is more influential the diffusion term. This diffusion is considered constant for the working flow ranges as explained in Section 4.4 and as stated in equation (4.16), and with an impact of around 5% to 10% (from experimental measurement in this thesis and in previous works as [66]). Therefore, cell design that minimizes this diffusion term by limiting contact area or any other strategy, can impact more the SOC losses reduction than optimization from microfluidic control. However, looking into tanks unbalancing the control optimization is still crucial for microfluidic membraneless RFB operation.

7.2.3 Actuators Consumption

Pumps and valves power affects auxiliar power and therefore condition battery efficiency. In the laboratory scale where this thesis took part and to demonstrate the first microfluidic membraneless RFB charge and discharge cycles with electrolyte recirculation, actuators consumption was a secondary criterion, as proper operation and electrochemical and electrical responses were prioritised. All efficiency calculations and optimizations in the project are calculated excluding this auxiliar power. However, for future development of a prototype, and for scaling up the battery design it is important to evaluate which control methods make a more efficient use of the pumping system.

Hence, real operation is used for calculating pump consumption from input actions measurements. For pump consumption evaluation first pump and valves consumption profiles are obtained. For each actuators curves are obtained correlating input value (pump voltage or valve power) with the consumption of its respective electronic driver. Note that as explained in Section 3.3.1, there are two pump drivers used to extend the pump working range. The values for the two pump drivers are presented in Table 7.4.

Voltage	Low Driver Power	High Driver Power
10V	60mW	-
50V	80mW	-
100V	120mW	650mW
150V	190mW	650mW
200V	-	950mW
250V	-	1275mW
260V	-	1275mW

Table 7.4: Consumption of pump drivers

Electronic board always uses the low driver when possible, to minimize consumption, and actually for the operation during the defined benchmark power profile this driver is always

the one used. The driver for the high voltage range is usually only activated to overcome air bubbles or any other transient clogging in the line. Hence, this driver usage does not distort the consumption calculation. These measured values for the low driver are presented Fig. 7.7 together with the model curve for the pumps that is expressed in equation (7.2), where P_{pump} is the power consumption of the pump driver in milli-Watts, and U_{pump} is the used voltage of the pump in volts.

$$P_{pump} = 0.005U_{pump}^2 - 0.125U_{pump} + 59.54 \tag{7.2}$$

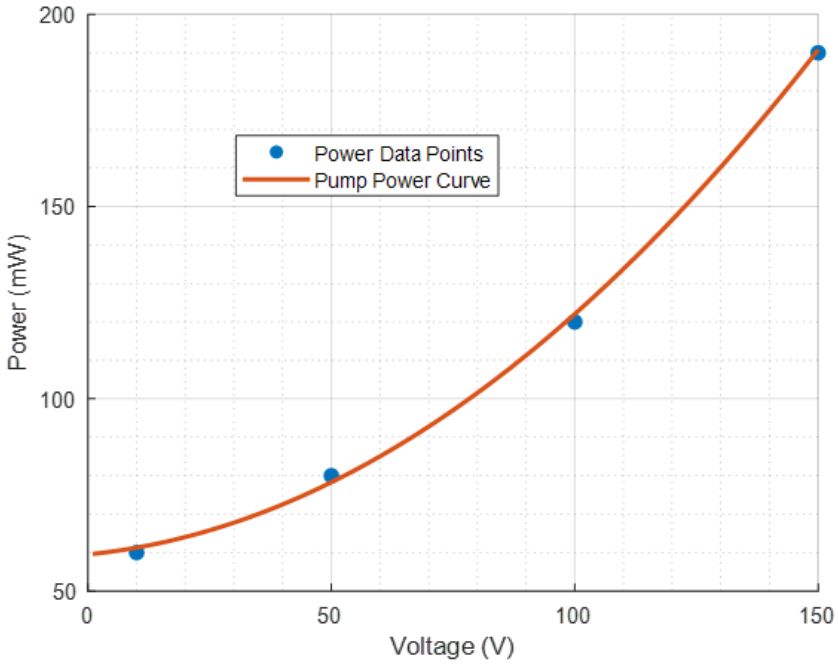

Figure 7.7: Pump driver power data points and curve from equation (7.2).

An equivalent process is made for the valves action used as input in the state space representation of the system and the measured power of the micro compressor driver. These values are presented in Table 7.5.

These measured values for the low driver are presented Fig.(7.8) together with the model curve for the pumps that is expressed in equation (7.3), where P_{valve} is the power consumption of the pump driver in milli-Watts, and U_{valve} is the used voltage of the pump in volts.

$$P_{valve} = 1.1634U_{valve} + 164.03 \tag{7.3}$$

Using these two expressions (7.2) and (7.3) in the registered action of actuators during the real experiment for the benchmark power profile the total power consumption of each control method can be calculated. The real measured action curves are presented in Fig. 7.9.

Voltage	Valve Driver Power	Voltage	Valve Driver Power
10V	180mW	550V	790mW
50V	240mW	600V	850mW
100V	290mW	650V	910mW
150V	345mW	700V	975mW
200V	400mW	750V	1035mW
250V	455mW	800V	1095mW
300V	505mW	850V	1155mW
350V	560mW	900V	1220mW
400V	620mW	950V	1290mW
450V	670mW	1000V	1345mW
500V	730mW	-	-

Table 7.5: Consumption of valve driver

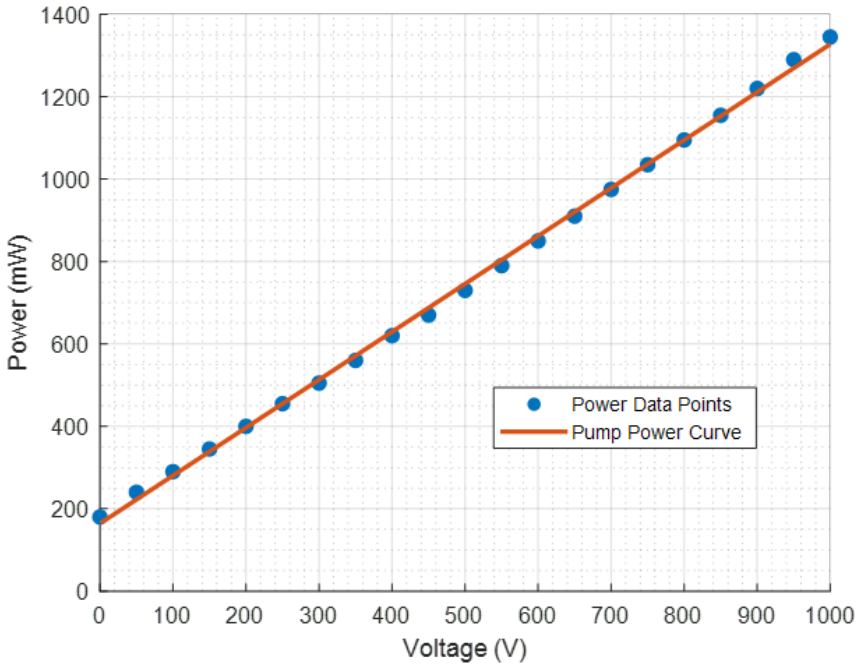

Figure 7.8: Pump driver power data points and curve from equation (7.3).

The figure shows that the actions for achieving the same flow profiles are disparate. Since these real measurements are affected by stochasticity and other conditions that vary between experiments, the actuators actions are not equivalent between controllers. Therefore, the measured consumptions are skewed. This is the cause for using the microfluidic model detailed in Section 5.2, expressed in the equations (7.4) to (7.6) and the identified values shown in Table 5.1. This model is used inversely to calculate an equivalent voltage for the actuators based on each controller real flows profile. These equivalent voltages are defined as the reference voltages that each controller would use for producing its flow profile if all of them would have

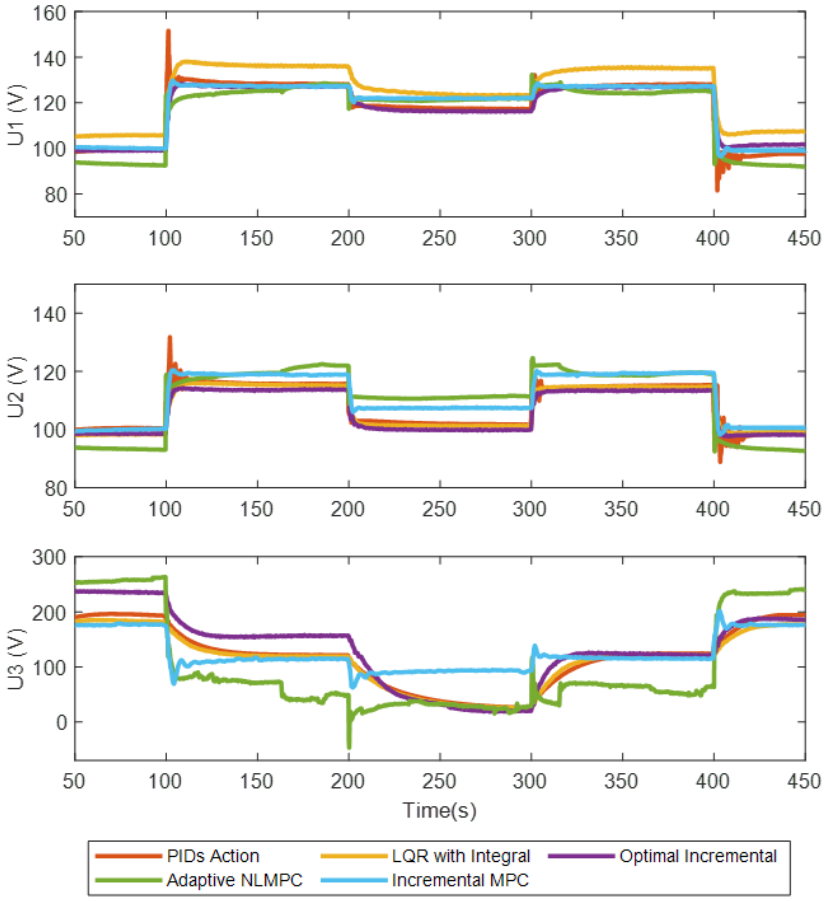

Figure 7.9: Inputs actions from all control strategies during real experiment performing the benchmark power profile.

performed under the same ideal conditions for the actuators. The inverse expression to obtain the equivalent values of the actuators for each of the flow profiles of the controllers are:

$$U_3(k) = \frac{(Q_3(k+1) - Q_3(k)a_3 - (Q_1(k) - Q_2(k)c_{Q3}) - c_{P3})}{k_{V3}} \tag{7.4}$$

$$U_2(k) = \frac{Q_2(k+1) - Q_2(k)a_2) + [Q_1(k+1) - Q_1(k)a_1 + |U_3(k)|\, k_{P3} + c_{P1}]\frac{k_{P1}}{k_{V1}} + |U_3(k)|\, k_{P3} + c_{P2}}{k_{V2} - \frac{k_{P1}.k_{P2}}{k_{V1}}} \tag{7.5}$$

$$U_1(k) = \frac{Q_1(k+1) - Q_1(k)a_1) + U_2(k)k_{P2} + |U_3(k)|\, k_{P3} + c_{P1}}{k_{V3}} \tag{7.6}$$

Using these calculated equivalent flow rates, also equivalent power consumption is obtained

from (7.2) and (7.3) expressions. The results for the equivalent power consumption during the benchmark experiments are shown in Table 7.6.

Indep. PIDs	LQR with Integral	Optimal with Incremental State	Adaptive Nonlinear MPC	Adaptive Incremental MPC
79.75mWh	79.66 mWh	79.64mWh	79.72mWh	79.69mWh

Table 7.6: Total equivalent action consumption for each control method

The table manifests that the optimal control with incremental state has the least actuators consumption, as it has the smoother response. The LQR with integral action which has also smooth transitory response in the steps, has the second lower consumption. The higher consumption comes from the independent PIDs, which can be explained because its oscillations where an excessive actuator power may be used until stabilising the outputs. Finally, both MPC methods have an intermediate consumption, with the adaptive nonlinear design being slightly higher, partially due to the correction it needs to apply when it loses the reference promptly because stochasticity and its reliance on an exact model.

These results show that the power consumption for a single cell is too high, and in order to achieve an effective working battery with a limited auxiliary pump power is necessary to either reduce the pumping power by increasing pumps efficiency or scale up the cell power and the number of cells. Another conclusion that is deduced is that the difference between controllers is not very significant compared to the differences in performance due to volume mix or power profiles, which are the most critical metrics for evaluating the control strategies. Although not presented in the table, the strategy of fixing the inlets flows at the equivalent rate for the maximum required power during the test is also calculated. This strategy allows to avoid flow steps and transitory mixing, but in this case the energy used during the benchmark experiment is 85,28 mW.h, what it is a significant difference compared to adapting the flow configuration to the power demand with any of the control strategies (around 7% increase compared to the worst control strategy in terms of consumption). If the inlet flows are fixed at the equivalent flow rates for the maximum power of the battery, and not the maximum required for the benchmark test, the consumption would be increased to 95,86 mW.h (20,2% more actuators power than the worst designed control method). These values help to understand the energy losses of using a fixed flow rates strategy, and why it is not feasible.

7.3 Conclusions

In this chapter, the designed control strategies from Chapter 6 are evaluated based on electrical parameters of the microfluidic membraneless RFB. A benchmark power profile is defined to be used as the reference for all the real experiments of the controllers, defining the power requirements and hence the flow configurations profiles they use as setpoints. This benchmark power profile defines power demand steps between one third to two thirds of the total battery power during 450s of experiment. After measuring real responses from each control method, the electrical model metrics proposed in Chapter 4 are calculated.

The calculated electrical response includes the available power curve for each controller. Using the steady state and transient dynamics of power from Section 4.2 and 4,3 respectively, power curves are obtained from the microfluidic configuration in the benchmark experiment. These curves can be used to observe the real time available power of each control and how each control is able to meet the demand in terms of settling time and stability. These power responses give an insight into the electrical power differences between controllers already observed in the flow responses from Chapter 6. Also, a measure of the percentage of not available power for each controller is obtained, so that the power adequacy intuited from the curves is quantitatively expressed. The MPC strategies, especially the adaptive incremental approach has the best performance for this metric. Optimal control with incremental state also has an acceptable power profile, and the independent PIDs and the LQI with integral action show the greater power losses.

When adapting the flow configuration to power demand step it is also important to avoid volume mixing that produce state of charge losses and tanks unbalancing that shortens maintenance times. This mixing is measured for the benchmark experiments, calculating the crossover volume for each real response. The resulting values are that adaptive incremental MPC has the least mixing, then the nonlinear MPC, the optimal control with incremental state has again an intermediate value, and LQR with integral action improves the independent PID that produce now the most mixing. Then, the model from Section 4.4 is used to obtain the equivalent SOC loss for the mixed volumes. These SOC losses have the same distribution as the volumes for the different controllers, however, the difference of percentage of loss is not very significant, since diffusion losses are more prominent for this state of charge variation.

Finally, an actuators consumption metric is calculated. This metric is based on the pumps and valves consumption curves interpolated from the different actuation points. These curves are applied to equivalent values for the actuators from their flow profiles. These equivalent values are used to erase stochasticity influence in working conditions during real experiments, that may cause actuators output to be very different. Therefore, actuators actions are comparable. Optimal control with incremental state has the lowest consumption due to its smooth flow response, similar to LQR with integral action which has a close value. MPC strategies have slightly higher consumptions, as well as independent PID which have the highest. The consumption are higher and indicate the need for more efficient pumps, higher power density cell or scale up them in stacks. Also, the difference between controllers is very low, but they make a big difference compared to the strategy of fixing constant maximum inlet flows.

All the evaluated metrics are summarized in Table 7.7, and together with implementation complexity and computational cost explained in Chapter 6 can help to select the best control strategy. For example, using adaptive incremental MPC can result in the more precise control, with less power and mixing losses, although being more complex and consuming slightly more power and computational resources. Nonlinear MPC has good similar properties but slightly inferior with the same complexity. Optimal control with incremental state has acceptable properties for all metrics in a simpler implementation with less computational and actuators consumption costs than the MPC approaches. Finally, the LQR with integral action have modest properties that improve just slightly the independent PIDS, that although generally having the worst values, are the simplest and lightest solution.

	Indep. PIDs	LQR with Integral	Optimal with Increm. State	Adaptive Nonl. MPC	Adaptive Increm. MPC
% of P_{loss}	0.92%	1.08%	0.87%	0.69%	0.54%
Volume Mixed	77.46μl	68.40μl	44.18μl	12.88μl	9.3μl
% of SOC loss	0.26%	0.22%	0.15%	0.04%	0.03%
Aux. Act. P. Consump.	79.75mWh	79.66 mWh	79.64mWh	79.72mWh	79.69mWh

Table 7.7: Summary of Control Strategies Electrical Evaluation

The electrical evaluation of the proposed control strategies, including power loss, volume mixed, SOC loss and auxiliary power consumption, is one of the main contributions of this thesis.

Chapter 8

Conclusions and outlook

The main contribution of this thesis has been to develop a microfluidic modelling for a micro scale membraneless RFB, consisting of an electric model including the microfluidic influence and a microfluidic dynamics model that is used to also design different microfluidic control strategies. The thesis is divided into four parts. The first part consists of a detail study of the background of the topic. This background is explored in the introduction and the study of the state of the art chapters. The second part focuses on the modelling of the microfluidic membraneless RFB. First of all it dedicates a chapter to explaining the system configuration, the actuators and sensors selection, and the electronics developments including hardware and software. Then, an electric model for the battery is presented and experimentally validated in another chapter. Finally, the microfluidic dynamics are addressed in the final chapter of this part. Throughout the third part different control strategies are proposed, using the microfluidic dynamics model for its design, and the electrical one for evaluating them. The fourth and final part consists of the conclusions, contributions and future work descriptions.

The introduction explains the context of global energy transition, and the prominent role that energy storage solutions play in the integration of renewable intermittent power sources. Then, it explains the working principles and properties of redox flow batteries, and how their cyclability, low degradation and long cycle life make this type of batteries very suitable in this context. A comparison of this type of batteries to other technologies is offered. Microfluidic membraneless RFB are also introduced, explaining how this concept can enhance the performance and reduce costs. Their working and operation particularities are detailed.

These microfluidic membraneless RFB are explained more thoughtfully in the second chapter, the study of the state of the art. Here, all previous relevant microfluidic cell reactor works are detailed, explaining their cell design and their microfluidic setup and operation. The limitations of each work and the reasons for not completing a battery capable of charge-discharge operation with recirculation are explored. Secondly, there is a study on existing model for membraneless RFB regarding electrochemical, hydraulic, thermal and electrical dimensions. The electrochemical dimension includes works on concentration profiles, mass transport, diffusive mixing and self-discharge; the hydraulic dimension works on fluid control of active elements and pumping power; and the electrical dimension is focused on equivalent electrical circuits. As previous works on microfluidic membraneless RFB models are limited,

some of the dimensions include models applied to conventional RFBs as the more similar existing reference. Then, study of the state of the art on modelling techniques is made. This study classifies the techniques on analytical models, blackbox models and greybox models. The characteristics of each approach are described, and in which applications each one is more useful is explained. Also, real time filters and corrections for the models are introduce, detailing different existing algorithms for this task. Finally, control design methods are studied, first explaining how they are categorised and which general characteristics they may have (continuous or discrete time, open or closed loop, linear or nonlinear, etc.). Some of the more common control strategies are presented, divided in model free and model based methods.

Chapter 3 describes the system configuration for microfluidic membraneless redox flow batteries operation. It begins explaining the manufacturing process of the used cell reactor, in order to better understand the parts it consist of and the internal structure. Then, the available instrumentation is presented and the reason why each of them is selected are detailed. This includes the pumping technologies, the regulation valves that need to be self-developed, and the sensors (flow meters and pressure sensors). It is also detailed how tanks are monitored for real operation. The developed electronics for the operation of the instrumentation are described, both explaining hardware structure and the developed softwares (embedded and SCADA computer application).

In Chapter 4 the modelling of the battery tackles the electrical dimension. It begins proposing an equivalent electrical circuit. It is experimentally studied which elements of this circuit are affected by microfluidic operation, for which electrochemical impedance spectroscopy experiment are performed, testing impedance variation for different flow configurations. Moreover, electrical output response (current and voltage) is measured during flow variations experiments. An expression for modelling steady state power value is proposed, substituting conventional expressions based on Faraday´s law and Nernst´s equation. This proposed expression includes liquid electrolytes interface positioning. Similarly, transient power dynamics are modelled by joining impedance dynamics from the identified equivalent circuit and proposed power source dynamics. These two models are validated with experimental data and fitness measurements are calculated. A third electrical metric is modelled, the mixing and self-discharge losses. This is achieved using spectrophotometry measurements that can give a precise species concentration value (state of charge). This SOC information is then correlated with volume mixing data in a non-recirculation experiment and it is modelled their relationship. The modelled power and SOC losses are introduced into the equivalent circuit as variables for the power source.

Chapter 5 continues with the battery modelling, now addressing the microfluidic dynamics model. System variables are defined for the state space representation: inlet flows and difference between the outlet flows are states and outputs of the system, and inputs are defined as pumps voltages and difference between the valves actions. Then, the model is built based on a set of proposed equations that combine the empirically observed behaviour of the flow configurations and to be consistent with momentum and mass conservation principles as stated in continuity and Navier-Stokes equations. The parameters of the terms of the equations are identified from experimental data to complete this greybox approach. Stochasticity present

in microfluidic applications makes the model deviate from real response when conditions change, so correction factors are added to the actuator terms of the model. This correction factors are proved to adjust the model response for different stochastic conditions, and they are introduced as real time correction into the model calculating their value with the extended Kalman filter algorithm. This real time adaptation is again experimentally tested.

The proposed model is used for designing different control strategies in Chapter 6. As a baseline method, first it is designed a model free method, using independent PID controllers as SISO systems. Then, the mentioned model-based techniques include LQR with integral action, optimal control with incremental implementation, adaptive nonlinear model predictive control, and adaptive incremental model predictive control. Each control method architecture is presented, its implementation explained, and its working parameters selected and detailed. Thus, for independent PIDs it is explained each SISO subsystem and the proportional, integral and derivative terms of each one. Regarding the LQR with integral action and the optimal control with incremental implementation, the weight matrices for output error and input action are presented, beyond the particular system augmentation and state representation of each one. Similarly, for the MPC approaches in addition to the algorithm sequence and their cost functions, it is presented for each one their state and input constraints, their control and prediction horizons, and their cost for their reference and manipulated variables tracking. Simulated and experimental response of the microfluidic dynamics are shown for each control strategy.

The measured experimental response of each control strategy is evaluated in more depth in Chapter 7. In this chapter, the electrical model from Chapter 4. is used to obtain the power response, mixing and self-discharge losses, and actuators consumption of each controller. All control strategies are evaluated using a benchmark power profile that makes them comparable and performs different step changes to reproduce the expected usage of the microfluidic membraneless RFB when integrated with an intermittent power source.

In summary, this thesis has identified the characteristics of microfluidic membraneless RFB and their possible impact in the energy storage sector in the global energy transition context. Previous works and their microfluidic setup and operation are identified and explained. Also, the different existing models for the different dimensions of the battery are studied. It has been explained the limitations of this previous works and models. In this work, a new microfluidic setup that allows to precisely control the microfluidic configuration within the cell and a recirculation operation is presented. Then, an equivalent electrical circuit is presented for the first time, together with a modelling of the microfluidic influence on the different circuit elements. This model covers available power steady-state value and power dynamics, and mixing and self-discharge losses influence in the state of charge. Also, a microfluidic dynamics model is detailed, using proposed equations based on observed behaviour and consistent with theoretical principles. This is an adaptive model that includes correction factors calculated in real time to adjust system behaviour to existing stochasticity. Control strategies are designed using this model and validated both at simulation and experimental levels. The experimental response is further validated using the electrical model to obtain electrical performance metrics.

As it has been justified along the thesis, the designed and implemented microfluidic setup

allows to make a precise operation of the battery flows in recirculation. Moreover, the proposed electrical model provides the first electrical equivalent circuit for this type of battery, and it demonstrates which elements of the circuit are dependent on microfluidic configuration. Microfluidic modelling and the control strategies designed allow for a precise flow control, that as the electrical model can quantify, can enhance battery performance and its critical for future integration. The proved enhancement, together with the microfluidic setup configuration, allows the project where this thesis takes part to be the first to demonstrate a complete charge and discharge cycling with electrolytes recirculation.

8.1 Summary of Contributions

The contributions of this thesis are:

- An exhaustive review of the previous works on microfluidic membraneless reactors, explaining their microfluidic setup and operation and how the condition the electrochemical performance, and the existing models on the different dimensions of the membraneless RFBs. The review also explores modelling techniques (analytical, blackbox and greybox approaches and real time filter and state estimation algorithms), and control methods.
- The proposed microfluidic setup that allows electrolytes recirculation and precise operation, including the selection of the pumping system, valve development and manufacturing, control board design, and integration and software programming of the instruments.
- The proposed electrical modelling, presenting for the first time an electric equivalent circuit model for micro membraneless redox flow batteries, focused on fluidic dynamic influence. Also, the empirically demonstration of which elements of this equivalent circuit are affected by this fluid dynamics using electrochemical impedance spectroscopy.
- The electrical model demonstrates that for the membraneless scenario available power is not affected only by limiting inlet electrolytes flow but also by the generated laminar interface of the electrolytes. It also models the dynamics of this power and SOC losses due to mixing and self-discharge, which are modelled using spectrophotometry measurements.
- The first microfluidic dynamic model for micro membraneless redox flow batteries, based on the proposed dynamic equations that describe general behavior of the micro-fluid dynamics. This model relies on parameters whose specific values are identified from experimental data, in a grey-box model structure.
- The correction factors to be added to the proposed general equations to correct the system model due to microfluidic stochasticity, and the proposed methodology for real time estimation of this correction factors.
- This modelling methodology experimental validation and its state-space representation that allows for control design.
- The design of different control strategies and their simulation and experimental tests.

These strategies include independent SISO PIDs, LQR with integral action, optimal control with incremental state representation, adaptive nonlinear MPC, and adaptive incremental MPC.

- The electrical evaluation and comparison of the designed control methods using the proposed electrical model and obtaining different electrical quantitative metrics.

8.2 Future Work

The work started in this thesis can be continued in different aspects. First, regarding the microfluidic setup, when the cell reactor design is considered mature enough to its scale up into a stack of cells, it will be necessary to redefine the instrumentation architecture. Then, the proposed methodologies for modelling and control can be replicated for this scenario. The future planned expansion to new battery chemistries will also require to replicate this proposed methodologies for the electric and microfluidics dynamic modelling and control.

Regarding the electrical modelling, as future work, it is proposed to refine the flow ratios describing the interface effect on steady-state power by modelling minor effects such as viscosity changes and small nonlinearities due to state-of-charge variations. For the equivalent electrical circuit, it is also planned to study other equivalent circuit configurations, such as fractional order-based models using other impedance terms as constant phase elements. For mixing and self-discharge losses, further spectrophotometry experiments are planned to refine the diffusion effects in the model and describe its smaller variations with state of charge.

For the microfluidic dynamics modelling, it is proposed to refine the proposed equations with more complex relations, expanding some terms or also introducing more account for nonlinearities, either explicitly or using a composition of subspaces (for example using fuzzy or polytopic models) for combining terms and parameters values and create a nonlinear space. This should also cause the need to redefine the correction factors and their filter estimation. It will be analysed the effect of adding new parameters to model stochasticity. If the model dynamics equations are modified and reflect stronger nonlinearities, other estimation algorithms will be studied to modify the estimation algorithm, such as the unscented Kalman filter that preserves mean and covariance of the nonlinearities in its calculations.

Besides, different new controllers can also be designed, or the same methods redefined to the modified proposed model equations or the cell stack reactor. The electrical evaluation will be contrasted with long real operation experiments when the cell real performance can be considered consistent enough for long periods of time.

As a final consideration, the proposed microfluidic setup, electrical and microfluidic dynamics models and control methods constitute the framework architecture that will be used for any further research in other areas, such as testing other electrolytes chemistries different from vanadium, other cell designs or perform any desired electrochemical experiment.

8.3 Dissemination

8.3.1 Direct Contributions

Articles

- A. B. De Quirós, A. E. Quintero, A. Francés and J. Uceda, "Adaptive Microfluidic Modeling of a Membraneless Micro Redox Flow Battery Using Extended Kalman Filter," in IEEE Access, vol. 11, pp. 100207-100217, 2023, doi: 10.1109/ACCESS.2023.3313416.
- A. B. D. Quirós, A. E. Quintero, A. Francés, A. A. Maurice and J. Uceda, "Electrical Model of a Membraneless Micro Redox Flow Battery—Fluid Dynamics Influence," in IEEE Access, vol. 11, pp. 46132-46143, 2023, doi: 10.1109/ACCESS.2023.3273927.

Conference Papers / Book Chapters

- A.B. de Quirós, M. de las Heras, A.E. Quintero, "Microfluidic Flow Rate Control Device: From Concept to Product Through Additive Manufacturing" In: Lachmayer, R., Bode, B., Kaierle, S. (eds) Innovative Product Development by Additive Manufacturing 2021. (2023). Springer, Cham. https://doi.org/10.1007/978-3-031-05918-6_17.

8.3.2 Other Works and Collaborations

Patents

- Submitted patent: Microfluidic Flow Rate Control Device and Method. Micro Electrochemical Technologies S.L. Inventors: Alberto Bernaldo de Quirós, Alberto E. Quintero, Beatriz Oraá. Submission number 300387703. Application number EP20382985.8. 13 November 2020. International application published under the PCT. International publication number: WO 2022/101477 A1. International publication date: 19 May 2022.
- Submitted patent: Redox Microfluidic Energy Storage System and Method. Micro Electrochemical Technologies S.L. Inventors: Alberto Bernaldo de Quirós, Alberto E. Quintero, Beatriz Oraá, Miguel de las Heras. Submission number 300415349. Application number EP21382584.7. 1 July 2021. International application published under the PCT. International publication number: WO 2023/275349 A1. International publication date: 05 January 2023.

Conference Papers

- A.A. Maurice, A. Bernaldo de Quirós, S. Sevilla, V. Muñoz, P.A. Prieto-Diaz, A.E. Quintero, M. Vera, "Monitoring the State of Charge Imbalance of Vanadium Redox Flow Batteries Via Dual Online UV/Visible Spectroscopy", ECS Meeting Abstracts, MA2023-01 2493, DOI: 10.1149/MA2023-01462493mtgabs.
- B. Oraá-Poblete, A. Bernaldo de Quirós, M. de las Heras, B. Ruiz, J. Palma, A. E. Quintero. "Microfluidics applied to redox flow batteries: a membraneless break-

throug technology" IFBF—International Flow Battery Forum Virtual Conference from 19th—21st January 2021.

- B. Oraá, A. Bernaldo, E. Serrano, A. E. Quintero. Membraneless micro flow batteries: a disruptive technology. EChemCONSTORE, I Meeting on Electrochemical Energy Conversion and Storage Devices. January 2021.
- B. Oraá, A. E. Quintero, A. Bernaldo de Quirós, J. Palma, "Microfluidica aplicada a baterías de flujo redox: una tecnología disruptiva sin membrana" V Workshop de la Red E3TECH / I Workshop Iberoamericano a Distancia 'Aplicaciones Medioambientales y Energéticas de la Tecnología Electroquímica') 28-31 October, 2020.

Projects

- Industrial Doctorate Program of the Comunidad de Madrid under Grant IND2018/AMB-9616.
- NATO Industrial Advisory Group: Naval DC Power Systems Architecture (Study Group 244). Workshop Lines of Power Control and Energy Storage/Cogeneration. Funding entity: NATO / OTAN Industrial Advisory Group (NIAG) Call: Year 2020.
- ESA Business Incubation Program. Madrid Region. Project: "Micro Fuel Cell". Funding entity: Fundación Madri+d. ESA BIC Madrid Region. Call: Year 2020.
- Research and Development Project. Project: Module Level Energy System – MLES Identification file: EXP – 00111738. Funding entity: Center for Industrial Technological Development (CDTI). Call: Year 2018-2020.

Bibliography

[1] Stephen F. Lincoln. "Fossil Fuels in the 21st Century". In: *JSTOR* 34.8 (2005), pp. 621–627. DOI: http://www.jstor.org/stable/4315666.

[2] Dolf Gielen et al. "The role of renewable energy in the global energy transformation". In: *Energy Strategy Reviews* 24 (2019), pp. 38–50. DOI: https://doi.org/10.1016/j.esr.2019.01.006.

[3] INTERNATIONAL ENERGY AGENCY. *Renewables 2021 Analysis and forecast to 2026, Revised version, December 2021*. URL: http://www.oecd.org/about/%20publishing/corrigenda.html. (accessed: 29.07.2023).

[4] A.A. Mohamad J. Mitali S. Dhinakaran. "Energy storage systems: a review". In: *Energy Storage and Saving* 1.3 (2019), pp. 166–216. DOI: https://doi.org/10.1016/j.enss.2022.07.002.

[5] Roberto Bocca. *Wind and solar hit record levels of power generation in 2022. What you need to know about the global energy transition this week, 18 Apr 2023*. URL: https://www.weforum.org/agenda/2023/04/wind-solar-record-global-energy-transition-17-april/. (accessed: 27.07.2023).

[6] John Farrell. *The Challenge of Reconciling a Centralized v. Decentralized Electricity System. DATE: 17 OCT 2011*. URL: https://ilsr.org/challenge-reconciling-centralized-v-decentralized-electricity-system/. (accessed: 29.07.2023).

[7] C. Mills A. Makhijani and M.V. Ramana. *Renewable Minnesota: a technical and economic analysis of a 100% renewable-energy based electricity system for Minnesota*. URL: http://%20ieer.org/resource/reports/renewable-minnesota-technica/. Institute for Energy and Environmental Research (IEER) (accessed: 30.07.2023).

[8] M.C. Argyrou, P. Christodoulides, and S.A. Kalogiro. "Energy storage for electricity generation and related processes: Technologies appraisal and grid scale applications". In: *Renewable and Sustainable Energy Reviews* 94 (2018), pp. 804–821. DOI: 10.1016/j.rser.2018.06.044.

[9] W. Kangro. *Verfahren zur Speicherung von elektrischer Energie*. Germany Patente 914264. May 1949.

[10] W. Kangro and H. Pieper. "Zur frage der speicherung von elektrischer energie in flüssigkeiten". In: *Renewable and Sustainable Energy Reviews* 7.4 (1962), pp. 435–448.

[11] L.H. Thallerr. "Electrically rechargeable redox flow cells". In: *NASA TM X-71540, Lewis Research Center* (1974), pp. 1–5.

[12] M. Skyllas-Kazacos. "New All-Vanadium Redox Flow Cell". In: *Journal of The Electrochemical Society* 133(5).1057 (1986).

[13] B. Huskinson et al. "A metal-free organic–inorganic aqueous flow battery". In: *Nature* 505 (2014), pp. 195–198.
[14] P. Singh. "Application of non-aqueous solvents to batteries". In: *J. Power Sources* 11 (1984), pp. 135–142.
[15] L. F. Arenas et al. "The characteristics and performance of hybrid redox flow batteries with zinc negative electrodes for energy storage". In: *Renewable and Sustainable Energy Reviews* 90 (2018), pp. 992–1016.
[16] Dapeng Zhang, Qinghua Liu, and Yongdan Li. *Reactor and Process Design in Sustainable Energy Technology Pages, Chapter 3 - Design of flow battery, 61-97*. Elsevier, 2014. ISBN: 9780444595669.
[17] Ltd. LE SYSTEM CO. *About VRFB*. URL: https://www.lesys.jp/english/redox/.
[18] Z. Gary Yang and James Provost. *It´s big and long-lived, and it won´t catch fire: The Vanadium Redox-Flow Battery: Move over, lithium ion: Vanadium flow batteries finally become competitive for grid-scale energy storage.* URL: https://spectrum.ieee.org/its-big-and-longlived-and-it-wont-catch-fire-the-vanadium-redoxflow-battery. 26 OCT 2017.
[19] Zhangxing He et al. "Electrode materials for vanadium redox flow batteries: Intrinsic treatment and introducing catalyst". In: *Chemical Engineering Journal* 427 (2022). DOI: https://doi.org/10.1016/j.cej.2021.131680.
[20] Qiang Ye et al. "Design trade-offs among shunt current, pumping loss and compactness in the piping system of a multi-stack vanadium flow battery". In: *Journal of Power Sources* 296 (2015), pp. 352–36. DOI: https://doi.org/10.1016/j.jpowsour.2015.06.138.
[21] C.H.L. Tempelman et al. "Membranes for all vanadium redox flow batteries". In: *Journal of Energy Storage* 32.101754 (2020). DOI: https://doi.org/10.1016/j.est.2020.101754.
[22] M. Moore et al. "An analysis of the contributions of current density and voltage efficiency to the capital costs of an all vanadium redox-flow battery". In: *J. Chem. Eng. Process Technol.* 7 (2016), p. 5.
[23] L. Tang et al. "Capital cost evaluation of conventional and emerging redox flow batteries for grid storage applications". In: *Electrochimica Acta* 437 (2023). DOI: https://doi.org/10.1016/j.electacta.2022.141460.
[24] Michael Dieterle et al. "Life cycle assessment (LCA) for flow batteries: A review of methodological decisions". In: *Sustainable Energy Technologies and Assessments* 53 (2022). DOI: https://doi.org/10.1016/j.seta.2022.102457.
[25] Sukriti Gupta, Tuti M. Lim, and Samir H. Mushrif. "Insights into the solvation of vanadium ions in the vanadium redox flow battery electrolyte using molecular dynamics and metadynamics". In: *Electrochimica Acta* 270 (2018), pp. 471–479. DOI: https://doi.org/10.1016/j.electacta.2018.03.008.
[26] M. Skyllas-Kazacos et al. "Progress in Flow Battery Research and Development". In: *Journal of The Electrochemical Society* 158.8 (2011), R55. DOI: 10.1149/1.3599565.
[27] Zainul Abdin and Kaveh Rajab Khalilpour. "Polygeneration with Polystorage for Chemical and Energy Hubs". In: Academic Press, 2019. Chap. Chapter 4 - Single and Polystorage Technologies for Renewable-Based Hybrid Energy Systems.

[28] David A.J. Rand and Patrick T. Moseley. "Electrochemical Energy Storage for Renewable Sources and Grid Balancing". In: Elsevier, 2015. Chap. Chapter 13 - Energy Storage with Lead–Acid Batteries.

[29] Wei Chen et al. "Nickel-hydrogen batteries for large-scale energy storage". In: *Proceedings of the National Academy of Sciences* 115 (2018). DOI: 10.1073/pnas.1809344115.

[30] Johnson Mattey Battery System. *Johnson Mattey Battery System, Our Guide to Batteries*. URL: http://www.chemwinfo.com/private_folder/Uploadfiles2015_March/JMBS-Guide-to-Batteries.pdf..

[31] M. Dassisti et al. "Vanadium: A Transition Metal for Sustainable Energy Storing in Redox Flow Batteries". In: *Reference Module in Materials Science and Materials Engineering* (2016). DOI: https://doi.org/10.1016/B978-0-12-803581-8.04007-8.

[32] Anil D. Pathak et al. "A review on battery technology for space application". In: *Journal of Energy Storage* 61 (2023). DOI: https://doi.org/10.1016/j.est.2023.106792.

[33] E. Sánchez-Díez et al. "Redox flow batteries: Status and perspective towards sustainable stationary energy storage". In: *Journal of Power Sources* 481 (2021).

[34] K.T. Cho et al. "High performance hydrogen/bromine redox flow battery for grid-scale energy storage". In: *J. Electrochem. Soc.* 159 (2012). DOI: 10.1149/2.018211jes.

[35] T. Liu et al. "A total organic aqueous redox flow battery employing a low cost and sustainable methyl viologen anolyte and 4-HO-TEMPO catholyte". In: *Adv. Energy Mater* 6 (2016). DOI: 10.1002/aenm.201501449.

[36] E. Zanzola et al. "Redox solid energy boosters for flow batteries: polyaniline as a case study". In: *Electrochim. Acta* 235 (2017). DOI: 10.1016/j.electacta.2017.03.084.

[37] L. Madec et al. "Surfactant for enhanced rheological, electrical, and electrochemical performance of suspensions for semisolid redox flow batteries and supercapacitors". In: *ChemPlusChem* 80 (2015). DOI: 10.1002/cplu.201402042.

[38] P. Navalpotro et al. "A membrane-free redox flow battery with two immiscible redox electrolytes". In: *Angew. Chem. Int. Edit.* 129 (2017), pp. 12634–12639. DOI: 10.1002/anie.201704318.

[39] R. Ferrigno et al. "Membraneless vanadium redox fuel cell using laminar flow". In: *J Am Chem Soc* 124.44 (2002), pp. 12930–12931. DOI: 10.1021/ja020812q..

[40] P. J. A. Kenis, R. Ismagilov, and G. M. Whitesides. "Microfabrication inside capillaries using multiphase laminar ow patterning". In: *Science* 285.5424 (1999), pp. 83–85. DOI: 10.1126/science.285.5424.83.

[41] E. R. Choban et al. "Microfluidic fuel cell based on laminar flow". In: *Journal of Power Sources* 128.1 (2004), pp. 54–60. DOI: https://doi.org/10.1016/j.jpowsour.2003.11.052.

[42] R. S. Jayashree et al. "Air-Breathing Laminar Low-Based Microfluidic Fuel Cell". In: *J. Am. Chem. Soc* 127.48 (2005), 1675816759. DOI: https://doi.org/10.1021/ja054599k.

[43] E. Kjeang et al. "Planar and three-dimensional microfluidic fuel cell architectures based on graphite rod electrodes". In: *Journal of Power Sources* 168.2 (2007), pp. 379–390. DOI: 10.1016/j.jpowsour.2007.02.087.

[44] E. Kjeang et al. "A microfluidic fuel cell with flow-through porous electrodes". In: *J. Am. Chem. Soc* 130.12 (2008), pp. 4000–4006. DOI: https://doi.org/10.1021/ja078248c.

[45] J. W. Lee and E. Kjeang. "Chip-embedded thin film current collector for microfluidic fuel chip". In: *International Journal of Hydrogen Energy* 37 (2012), pp. 9359–9367. DOI: 10.1016/j.ijhydene.2012.02.155.

[46] J. W. Lee, M. A. Goulet, and E. Kjeang. "Microfluidic redox battery". In: *International Journal of Hydrogen Energy* 13.13 (2013), pp. 2504–2507. DOI: https://doi.org/10.1039/C3LC50499A.

[47] J. Marschewski et al. "On the mass transfer performance enhancement of membraneless redox flow cells with mixing promoters". In: *International Journal of Heat and Mass Transfer* 106 (2017), pp. 884–894. DOI: 10.1016/j.ijheatmasstransfer.2016.10.030.

[48] M. A. Goulet et al. "Maximizing the power density of aqueous electrochemical flow cells within operando deposition". In: *Journal of Power Sources* 339 (2017), pp. 80–85. DOI: https://doi.org/10.1016/j.jpowsour.2016.11.05.

[49] K. Marques-Lisboa and R. Machado-Cotta. "On the mass transport in membraneless flow batteries with flow-by configuration". In: *International Journal of Heat and Mass Transfer* 122 (2018), pp. 954–966. DOI: https://doi.org/10.1016/j.ijheatmasstransfer.2018.02.002.

[50] M. Suss et al. "Membraneless flow battery leveraging flow-through heterogeneous porous media for improved power density and reduced crossover". In: *RSC Adv.* 122 (2016). DOI: https://doi.org/10.1039/C6RA22608F.

[51] K. Marma, J. Kolli, and K.T. Cho. "Membrane-Less Hydrogen Iron Redox Flow Battery". In: *ASME. J. Electrochem. En. Conv. Stor.* 16(1) (2019). DOI: https://doi.org/10.1115/1.4040329.

[52] J. T. Davis et al. "Floating Membraneless PV-Electrolyzer Based on Buoyancy-Driven Product Separation". In: *International Journal of Hydrogen Energy* 43 (2018), 12241238. DOI: https://doi.org/10.1016/j.ijhydene.2017.11.086.

[53] E. Ortiz-Ortega et al. "A Flow-Through Membraneless Microfluidic Zinc-Air Cell". In: *ACS Appl. Mater. Interfaces* 12.37 (2020), 4118541199. DOI: https://doi.org/10.1021/acsami.0c08525.

[54] J. P. Esquivel et al. "Microfluidic Fuel Cells on Paper: Meeting the Power Needs of next Generation Lateral Flow Devices". In: *Energy and Enviromental Science* 7 (2014), 17441749. DOI: https://doi.org/10.1039/C3EE44044C.

[55] Deepak Krishnamurthy et al. "Computational modeling of microfluidic fuel cells with flow-through porous electrodes". In: *Journal of Power Sources* 196(23) (2011), pp. 10019–10031. DOI: 10.1016/j.jpowsour.2011.08.024.

[56] L. Li et al. "Vanadium microfluidic fuel cell with novel multi-layer flow-through porous electrodes: Model, simulations and experiments". In: *Applied Energy* 177 (2016), pp. 729–739. DOI: 10.1016/j.apenergy.2016.05.072.

[57] K.M. Lisboa and R.M. Cotta. "Analysis of the mass transport in corrugated membraneless flow batteries". In: *Appl Math Model* 77 (2020), pp. 1512–1530. DOI: 10.1016/j.apm.2019.09.001.

[58] H. Park et al. "In operando visualization of redox flow battery in membrane-free microfluidic platform". In: *Proceedings of the National Academy of Sciences* 119.9 (2022). DOI: https://doi.org/10.1073/pnas.2114947119.

[59] M.N. Nasharudin et al. “Mass transfer and performance of membrane-less micro fuel cell: A review”. In: *International Journal of Hydrogen Energy* 39 (2014), pp. 1039–1055. DOI: https://doi.org/10.1016/j.ijhydene.2013.09.135.

[60] M. Tanveer and K.Y. Kim. “Effects of geometric configuration of the channel and electrodes on the performance of a membraneless micro-fuel cell”. In: *Energy Conversion and Management* 136 (2017), pp. 372–381. DOI: 10.1016/j.enconman.2017.01.027.

[61] S.E. Ibáñez et al. “Effects of the diffusive mixing and self-discharge reactions in microfluidic membraneless vanadium redox flow batteries”. In: *International Journal of Heat and Mass Transfer* 170 (2021). DOI: https://doi.org/10.1016/j.ijheatmasstransfer.2021.121022.

[62] A. Tang, J. Bao, and M. Skyllas-Kazacos. “Dynamic modelling of the effects of ion diffusion and side reactions on the capacity loss for vanadium redox flow battery”. In: *J Power Sources* 196 (24) (2011), pp. 10737–10747. DOI: https://doi.org/10.1016/j.jpowsour.2011.09.003.

[63] M. Skyllas-Kazacos and L. Goh. “Modeling of vanadium ion diffusion across the ion exchange membrane in the vanadium redox battery”. In: *J Memb Sci* 399 (2012), pp. 43–48. DOI: https://doi.org/10.1016/j.memsci.2012.01.024.

[64] K.W. Knehr et al. “A transient vanadium flow battery model incorporating vanadium crossover and water transport through the membrane”. In: *J Electrochem Soc* 159.9 (2012). DOI: 10.1149/2.017209jes.

[65] A.A. Shah, M.J. Watt-Smith, and F.C. Walsh. “A dynamic performance model for redox-flow batteries involving soluble species”. In: *Electrochim. Acta* 53 (2008), pp. 8087–8100. DOI: 10.1016/j.electacta.2008.05.067.

[66] M.A. Goulet and E. Kjeang. “Reactant recirculation in electrochemical co-laminar flow cells”. In: *Electrochim. Acta* 140 (2014), pp. 217–224. DOI: 10.1016/j.electacta.2014.03.092.

[67] A. Maurice, A. Quintero, and M. Vera. *A comprehensive guide for measuring total vanadium concentration and state of charge of vanadium electrolytes using UV-Visible spectroscopy*. Version 1. July 28, 2023. arXiv: https://doi.org/10.48550/arXiv.2307.15009.

[68] S. Ressel et al. “State of charge monitoring of vanadium redox flow batteries using half cell potentials and electrolyte densit”. In: *Journal of Power Sources* (2018). DOI: 10.1016/j.jpowsour.2018.01.006.

[69] J.W. Haverkort A. Bhadra. “The optimal electrode pore size and channel width in electrochemical flow cells”. In: *Journal of Power Sources* 579 (2023). DOI: https://doi.org/10.1016/j.jpowsour.2023.233240.

[70] V. Viswanathan et al. “Cost and performance model for redox flow batterie”. In: *Journal of Power Sources* 247 (2014), pp. 1040–1051. DOI: https://doi.org/10.1016/j.jpowsour.2012.12.023.

[71] A. Trovò, F. Picano, and M. Guarnieri. “Comparison of energy losses in a 9kW vanadium redox flow battery”. In: *Journal of Power Sources* 440 (2019). DOI: https://doi.org/10.1016/j.jpowsour.2019.227144.

[72] O. J. Dressler et al. “Reinforcement Learning for Dynamic Microfluidic Control”. In: *ACS Omega* 3(8) (2018), pp. 10084–10091. DOI: https://doi.org/10.1021/acsomega.8b01485.

[73] J. T. Elliott G. A. Cooksey and A. L. Plant. "Reproducibility and Robustness of a Real-Time Microfluidic Cell Toxicity Assay". In: *Analytical Chemistry* 83(10) (2011), pp. 3890–3896. DOI: https://doi.org/10.1021/ac200273f.

[74] A. Tang, J. Bao, and M. Skyllas-Kazacos. "Studies on pressure losses and flow rate optimization in vanadium redox flow battery". In: *Journal of Power Sources* 248 (2014), pp. 154–162. DOI: https://doi.org/10.1016/j.jpowsour.2013.09.071.

[75] T. Wang et al. "Dynamic control strategy for the electrolyte flow rate of vanadium redox flow batteries". In: *Applied Energy* (2017). DOI: https://doi.org/10.1016/j.apenergy.2017.07.065.

[76] B. Xiong et al. "Thermal hydraulic behavior and efficiency analysis of an all-vanadium redox flow battery". In: *Journal of Power Sources* 242 (2013), pp. 314–324. DOI: https://doi.org/10.1016/j.jpowsour.2013.05.092.

[77] J. Marschewski et al. "Enhancement of Mass and Heat Transfer Using Herringbone-Inspired Microstructures for Application in Microfluidic Redox Flow Cells". In: *ASME 2016 14th International Conference on Nanochannels, Microchannels, and Minichannels* (2016). DOI: https://doi.org/10.1115/ICNMM2016-7920.

[78] J. Marschewski et al. "3D-printed fluidic networks for high-power-density heat-managing miniaturized redox flow batteries". In: *Energy Environ. Sci.* 10(3) (2016), pp. 780–787. DOI: https://doi.org/10.1039/c6ee03192g.

[79] Z. Wei et al. "Dynamic thermal-hydraulic modeling and stack flow pattern analysis for all-vanadium redox flow battery". In: *Journal of Power Sources* 260 (2014), pp. 89–99. DOI: https://doi.org/10.1016/j.jpowsour.2014.02.108.

[80] Y. Zhang et al. "A comprehensive equivalent circuit model of all-vanadium redox flow battery for power system analysis". In: *Journal of Power Sources* 290 (2015), pp. 14–24. DOI: https://doi.org/10.1016/j.jpowsour.2015.04.169.

[81] A. Bhattacharjee and H. Saha. "Design and experimental validation of a generalised electrical equivalent model of Vanadium Redox Flow Battery for interfacing with renewable energy sources". In: *Journal of Energy Storage* 13 (2017), pp. 220–232. DOI: https://doi.org/10.1016/j.est.2017.07.016.

[82] B. Xiong et al. "An Enhanced Equivalent Circuit Model of Vanadium Redox Flow Battery Energy Storage Systems Considering Thermal Effects". In: *IEEE Access* 7 (2019), pp. 162297–162308. DOI: https://doi.org/10.1109/access.2019.2952212.

[83] M. Guarnieri A. Trovò W. Zamboni. "Multichannel Electrochemical Impedance Spectroscopy and equivalent circuit synthesis of a large-scale vanadium redox flow battery". In: *Journal of Power Sources* (2021). DOI: https://doi.org/10.1016/j.jpowsour.2021.229703.

[84] W. Guan and X. Huang. "A Modular Active Balancing Circuit for Redox Flow Battery Applied in Energy Storage System". In: *IEEE Access* 9 (2021), pp. 127548–127558. DOI: https://doi.org/10.1109/ACCESS.2021.3112902.

[85] M.S. Yesilyurt MS and H.A. Yavasoglu. "An All-Vanadium Redox Flow Battery: A Comprehensive Equivalent Circuit Model". In: *Energies* 16(4):2040 (2023). DOI: https://doi.org/10.3390/en16042040.

[86] G. S. Watson. "Linear Least Squares Regression". In: *The Annals of Mathematical Statistics* 38.6 (1967), pp. 1679–99. DOI: http://www.jstor.org/stable/2238648.

[87] D.R. Brillinger. "A Generalized Linear Model With "Gaussian" Regressor Variables". In: *Selected Works of David Brillinger. Selected Works in Probability and Statistics* (2012). DOI: https://doi.org/10.1007/978-1-4614-1344-8_34.

[88] S. Coxe, S.G. West, and L.S. Aiken. "The Oxford handbook of quantitative methods". In: 2013. Chap. Generalized linear models. p26-51.

[89] Gallant. "Nonlinear Regression". In: *The American Statistician* 29.2 (1975), pp. 73–81. DOI: https://doi.org/10.1080/00031305.1975.10477374.

[90] J.O. Ogutu abd T. Schulz-Streeck and H.P. Piepho. "Genomic selection using regularized linear regression models: ridge regression, lasso, elastic net and their extensions". In: *BMC Proceedings* 6 (2012). DOI: https://doi.org/10.1186/1753-6561-6-S2-S10.

[91] Jeffrey D. Hart and Thomas E. Wehrly. "Kernel Regression Estimation Using Repeated Measurements Data". In: *Journal of the American Statistical Association* 81:396 (1986), pp. 1080–1088. DOI: https://doi.org/10.1080/01621459.1986.10478377.

[92] A.J. Smola and B. Schölkopf. "A tutorial on support vector regression". In: *Statistics and Computing* 14 (2014), pp. 199–222. DOI: https://doi.org/10.1023/B:STCO.0000035301.49549.88.

[93] P. Geladi and B.R. Kowalski. "Partial least-squares regression: a tutorial". In: *Analytica Chimica Acta* 185 (1986), pp. 1–17. DOI: https://doi.org/10.1016/0003-2670(86)80028-9.

[94] L. Marquez et al. "Neural network models as an alternative to regression". In: *Proceedings of the Twenty-Fourth Annual Hawaii International Conference on System Sciences* 4 (1986), pp. 129–135. DOI: https://doi.org/10.1109/HICSS.1991.184052.

[95] T. Bohlin. *Practical Grey-box Process Identification. Theory and Application*. Advanced in Industrial Control. Springer, 2006. ISBN: https://doi.org/10.1007/1-84628-403-1.

[96] B. Sohlberg and E.W. Jacobsen. "Grey Box Modelling – Branches and Experiences". In: *IFAC Proceedings* 41.2 (2008), pp. 11415–11420. DOI: https://doi.org/10.3182/20080706-5-kr-1001.01934.

[97] H.H. Afshari, S.A. Gadsden, and S. Habibi. "Gaussian filters for parameter and state estimation: A general review of theory and recent trends". In: *Signal Processing* 135 (2017), pp. 218–238. DOI: https://doi.org/10.1016/j.sigpro.2017.01.001.

[98] B. Efron and C. Morris. "Limiting the Risk of Bayes and Empirical Bayes Estimators—Part I: The Bayes Case". In: *Journal of the American Statistical Association* 66:336 (1971), pp. 807–815. DOI: https://doi.org/10.1080/01621459.1971.10482348.

[99] S.A.U. Islam and D.S. Bernstein. "Recursive Least Squares for Real-Time Implementation [Lecture Notes]". In: *IEEE Control Systems Magazine* 39.3 (2019), pp. 82–85. DOI: https://doi.org/10.1109/MCS.2019.2900788.

[100] V. Gómez. "Wiener-Kolmogorov Filtering and Smoothing for Multivariate Series With State–Space Structure". In: *Journal of Time Series Analysis* 28.3 (2007), pp. 361–385. DOI: https://doi.org/10.1109/MCS.2019.2900788.

[101] G. Welch and G. Bishop. *An introduction to the Kalman filter*. Univ. North Carolina Chapel Hill, Chapel Hill, NC, USA, Tech. Rep. TR 95-041, May 1995.

[102] E.A. Wan, R. Van Der Merwe, and S. Haykin. "Wiener-Kolmogorov Filtering and Smoothing for Multivariate Series With State–Space Structure". In: *Kalman Filtering*

Neural Netw. 5 (2001), pp. 221–280. DOI: https://doi.org/10.1111/j.1467-9892.2006.00514.x.

[103] P. M. Djuric et al. "Particle filtering". In: *IEEE Signal Processing Magazine* 20.5 (2003), pp. 19–38. DOI: https://doi.org/10.1109/MSP.2003.1236770.

[104] B. Xia et al. "Strong Tracking of a H-Infinity Filter in Lithium-Ion Battery State of Charge Estimation". In: *Energies* 11 (2018). DOI: https://doi.org/10.3390/en11061481.

[105] S.R. Habibi, R., and Burton. "The Variable Structure Filter". In: *ASME. J. Dyn. Sys., Meas., Control.* 125(3) (2003), pp. 287–293. DOI: https://doi.org/10.1115/1.1590682.

[106] S. Challa, Y. Bar-Shalom, and V. Krishnamurthy. "Nonlinear filtering via generalized Edgeworth series and Gauss-Hermite quadrature". In: *IEEE Transactions on Signal Processing* 48.6 (2003), pp. 1816–1820. DOI: https://doi.org/10.1109/78.845944.

[107] J. Liu et al. "Predictive Control for Unknown Dynamics With Observation Loss: A Temporal Game-Theoretic Approach". In: *IEEE Transactions on Industrial Electronics* 71(3) (2023), pp. 2965–2977. DOI: https://doi.org/10.1109/TIE.2023.3266574.

[108] K.J. Astrom and T. Hagglund. *PID controllers: Theory, design, and tuning.* Research Triangle Park, NC: Instrument Society of America. ISA - The Instrumentation, Systems and Automation Society, 1995. ISBN: 1-55617-516-7.

[109] M. Fliess and C. Join. "Intelligent PID controllers". In: *2008 Mediterranean Conference on Control and Automation - Conference Proceedings* (2008), pp. 326–331. DOI: https://doi.org/10.1109/MED.2008.4601995.

[110] L. Thamir. "A Comparative Study of Various Intelligent Controllers' Performance for Systems Based on Bat Optimization Algorithm". In: *Engineering and Technology Journal* 38 (2020), pp. 938–950. DOI: https://doi.org/10.30684/etj.v38i6A.622.

[111] K.J. Åström et al. "Towards intelligent PID control". In: *Automatica* 28.1 (1992), pp. 1–9. DOI: https://doi.org/10.1016/0005-1098(92)90002-w.

[112] L. Qu, Y. Huang, and L. Ling. "Design of Intelligent PID Controller Based on Adaptive Genetic Algorithm and Implementation of FPGA". In: *Advances in Neural Networks Part of the Lecture Notes in Computer Science book series* 5264 (2008), pp. 542–551. DOI: https://doi.org/10.1007/978-3-540-87734-9_62.

[113] M.H. Demir and M. Demirok. "Designs of Particle-Swarm-Optimization-Based Intelligent PID Controllers and DC/DC Buck Converters for PEM Fuel-Cell-Powered Four-Wheeled Automated Guided Vehicle". In: *Appl. Sci.* 13.5 :2919 (2023). DOI: https://doi.org/10.3390/app13052919.

[114] H. Khleaf, A. Nahar, and A. Subhi. "Intelligent control of DC-DC converter based on PID-neural network". In: *International Journal of Power Electronics and Drive Systems (IJPEDS)* 10.2554 (2023). DOI: https://doi.org/10.11591/ijpeds.v10.i4.pp2254-2262.

[115] W. Jiang and X. Jiang. "Design of an Intelligent Temperature Control System Based on the Fuzzy Self-Tuning PID". In: *Procedia Engineering* 43 (2012), pp. 307–311. DOI: https://doi.org/10.1016/j.proeng.2012.08.053.

[116] X. You et al. "Model-free control for soft manipulators based on reinforcement learning". In: *International Conference on Intelligent Robots and Systems (IROS)* (2017), pp. 2909–2915. DOI: https://doi.org/10.1109/IROS.2017.8206123.

[117] E. Pasta et al. "Collaborative strategy for model-free control of arrays of wave energy converters: A genetic algorithm approach". In: *OCEANS 2021* (2021), pp. 1–7. DOI: https://doi.org/10.23919/OCEANS44145.2021.9705877.

[118] Z. Wang, L. Liu, and H. Zhang. "Neural Network-Based Model-Free Adaptive Fault-Tolerant Control for Discrete-Time Nonlinear Systems With Sensor Fault". In: *IEEE Transactions on Systems, Man, and Cybernetics: Systems* 47.8 (2017), pp. 2351–2362. DOI: https://doi.org/10.1109/TSMC.2017.2672664.

[119] M. Nauman, W. Shireen, and A. Hussain. "Model-Free Predictive Control and Its Applications". In: *Energies* 15.5131 (2022). DOI: https://doi.org/10.3390/en15145131.

[120] H.E. Glida et al. "Optimal model-free fuzzy logic control for autonomous unmanned aerial vehicle". In: *Proceedings of the Institution of Mechanical Engineers Part G: Journal of Aerospace Engineering* 236.5 (2022), pp. 952–967. DOI: https://doi.org/10.1177/09544100211025379.

[121] J. Marinus van Ast, R. Babuška, and B. De Schutter. "Novel ant colony optimization approach to optimal control". In: *International Journal of Intelligent Computing and Cybernetics* 2.3 (2009), pp. 414–434. DOI: https://doi.org/10.1108/17563780910982671.

[122] E. Lavretsky and K. A. Wise. "Optimal Control and the Linear Quadratic Regulator". In: *Robust and Adaptive Control. Advanced Textbooks in Control and Signal Processing* (2013). DOI: https://doi.org/10.1007/978-1-4471-4396-3_2.

[123] K. Holkar, K. Wagh, and L. Waghmare. "An Overview of Model Predictive Control". In: *International Journal of Control and Automation* 3.4 (2011), pp. 47–64.

[124] L. Grüne and J. Pannek. "Nonlinear Model Predictive Control. In: Nonlinear Model Predictive Control". In: *Communications and Control Engineering* (2017). DOI: https://doi.org/10.1007/978-3-319-46024-6_3.

[125] M. Tanaskovic, L. Fagiano, and V. Gligorovski. "Adaptive model predictive control for linear time varying MIMO system". In: *Automatica* 105 (2019), pp. 237–245. DOI: https://doi.org/10.1016/j.automatica.2019.03.030.

[126] V.A. Ugrinovskii. "Robust H infinity control in the presence of stochastic uncertainty". In: *International Journal of Control* 71.2 (1998), pp. 219–237. DOI: https://doi.org/10.1080/002071798221849.

[127] A.T. Nguyen et al. "Fuzzy Control Systems: Past, Present and Future". In: *IEEE Computational Intelligence Magazine* 14.1 (2019), pp. 56–68. DOI: https://doi.org/10.1109/MCI.2018.2881644.

[128] F. Massa et al. "Finite element analysis of frictionless contact problems using fuzzy control approach". In: *Engineering Computations* 32 (2015), pp. 585–606. DOI: https://doi.org/10.1108/EC-11-2013-0289.

[129] R.A. DeCarlo, S.H. Zak, and G.P. Matthews. "Variable structure control of nonlinear multivariable systems: a tutorial". In: *Proceedings of the IEEE* 76.3 (1988), pp. 212–232. DOI: https://doi.org/10.1109/5.4400.

[130] M.M. Mahmouh and M. Khater. "Robust Chatter-Free Sliding Mode Observer of Sensorless Induction Motor Drives". In: *Engineering Research Journal (ERJ)* 30.1 (2007), pp. 9–15. DOI: https://doi.org/10.21608/erjm.2007.69889.

[131] M.A. Unger et al. "Monolithic microfabricated valves and pumps by multilayer soft lithography". In: *Science* 288.5463 (2000), pp. 113–116. DOI: https://doi.org/10.1126/science.288.5463.113.

[132] an Elvesys brand © 2023 Elveflow. *Microfluidic low-flow liquid flow meter: a review*. URL: https://www.elveflow.com/microfluidic-reviews/microfluidic-flow-control/microfluidic-low-flow-liquid-flow-meters-a-review/. (accessed: 12.09.2023).

[133] Y. Yao et al. "Assessment methods and performance metrics for redox flow batteries". In: *Nature Energy* (2021). DOI: https://doi.org/10.1038/s41560-020-00772-8.

[134] C. Iliescu, D. P. Poenar, and S. T. Selvan. "Frequency dependence on the accuracy of electrical impedance spectroscopy measurements in microfluidic devices". In: *Journal of Micromechanics and Microengineering* 20.2 (2010). DOI: https://doi.org/10.1088/0960-1317/20/2/022001.

[135] M.O. Bamgbopa, S. Almheiri, and H. Sun. "Prospects of recently developed membraneless cell designs for redox flow batteries". In: *Renewable and Sustainable Energy Reviews* 70 (2017), pp. 506–518. DOI: https://doi.org/10.1016/j.rser.2016.11.234.

[136] K.H. Shin et al. "Real-time monitoring of the state of charge (SOC) in vanadium redox-flow batteries using UV–Vis spectroscopy in operando mode". In: *Journal of Energy Storage* 27 (2020). DOI: https://doi.org/10.1016/j.est.2019.101066.

[137] H. Bruus. *Theoretical microfluidics*. Oxford Master Series in Physics. Oxford university press, 2007. ISBN: 9780199235087.

[138] N.T. Nguyen, S.T. Wereley, and S.A.M. Shaegh. *Fundamentals and applications of microfluidics*. Integrated Microsystem Series. Artech house, 2019. ISBN: 9781630813642.

[139] O.A. Ibrahim et al. "Microfluidics for Electrochemical Energy Conversion". In: *Chemical Reviews* (2022). DOI: https://doi.org/10.1021/acs.chemrev.1c00499.

[140] C. Yang, W. Shi, and W. Chen. "Comparison of Unscented and Extended Kalman Filters with Application in Vehicle Navigation". In: *The Journal of Navigation* 70.2 (2017), pp. 411–431. DOI: https://doi.org/10.1017/S0373463316000655.

[141] H.G. Malkapure and M. Chidambaram. "Comparison of Two Methods of Incorporating an Integral Action in Linear Quadratic Regulator". In: *IFAC Proceedings* 47.1 (2017), pp. 55–61. DOI: https://doi.org/10.3182/20140313-3-IN-3024.00105.

[142] B.D.O. Anderson and J.B. Moore. *Optimal control: linear quadratic methods*. Prentice-Hall, 1990. ISBN: 9780486457666.

[143] B.M. Al-Hadithi, A. Jiménez, and J. Perez-Oria. "New incremental Takagi-Sugeno state model for optimal control of multivariable nonlinear time delay systems". In: *Eng. Appl. Artif. Intell.* 45 (2015), pp. 259–268. DOI: https://doi.org/10.1016/j.engappai.2015.07.006.

[144] J.M. Adánez, B.M. Al-Hadithi, and A. Jiménez. "Wind Turbine Multivariable Optimal Control Based on Incremental State Model". In: *Asian Journal of Control* (2018). DOI: https://doi.org/10.1002/asjc.1720.

[145] L.O. Santos et al. "On-line implementation of nonlinear MPC: an experimental case study". In: *Control Engineering Practice* 9.8 (2001), pp. 847–857. DOI: https://doi.org/10.1016/s0967-0661(01)00049-1.

[146] S. Yu et al. "A revisit to MPC of discrete-time nonlinear systems". In: *IEEE 2015 IEEE International Conference on CYBER Technology in Automation, Control, and*

Intelligent Systems (CYBER) (2015), pp. 7–12. DOI: https://doi.org/10.1109/cyber.2015.7287901.

[147] P. Spellucci. "A new technique for inconsistent QP problems in the SQP method". In: *Journal of Mathematical Methods of Operations Research* 47.3 (1998), pp. 255–400. DOI: https://doi.org/10.1007/BF01198402.

[148] K. Tone. "Revisions of constraint approximations in the successive QP method for nonlinear programming problems". In: *Journal of Mathematical Programming* 26.2 (1983), pp. 144–152. DOI: https://doi.org/10.1007/BF02592051.

[149] S. Gulkowski. "Specific Yield Analysis of the Rooftop PV Systems Located in South-Eastern Poland". In: *Energies* 15.10 (2022). DOI: https://doi.org/10.3390/en15103666.